# AN UNCOOLED INFRARED MICROBOLOMETER DETECTOR ARRAY USING SURFACE MICROMACHINED MEMS TECHNOLOGY

A THESIS SUBMITTED TO
THE GRADUATE SCHOOL OF NATURAL AND APPLIED SCIENCES
OF
MIDDLE EAST TECHNICAL UNIVERSITY

BY

MAHMUD YUSUF TANRIKULU

IN PARTIAL FULFILMENT OF THE REQUIREMENTS
FOR
THE DEGREE OF DOCTOR OF PHILOSOPHY
IN
ELECTRICAL AND ELECTRONICS ENGINEERING

AUGUST 2007

Approval of the thesis:

**AN UNCOOLED INFRARED MICROBOLOMETER DETECTOR ARRAY USING SURFACE MICROMACHINED MEMS TECHNOLOGY**

submitted by **MAHMUD YUSUF TANRIKULU** in partial fulfillment of the requirements for the degree of **Doctor of Philosophy in Electrical and Electronics Engineering Department**, **Middle East Technical University** by,

Prof. Dr. Canan Özgen
Dean, Graduate School of **Natural and Applied Sciences** _____

Prof. Dr. İsmet Erkmen
Head of Department, **Electrical and Electronics Engineering** _____

Prof. Dr. Tayfun Akın
Supervisor, **Electrical and Electronics Engineering Dept., METU** _____

**Examining Committee Members:**

Prof. Dr. Cengiz Beşikçi
Electrical and Electronics Engineering Dept., METU _____

Prof. Dr. Tayfun Akın
Electrical and Electronics Engineering Dept., METU _____

Assoc. Prof. Dr. Sencer Koç
Electrical and Electronics Engineering Dept., METU _____

Asst. Prof. Dr. Haluk Külah
Electrical and Electronics Engineering Dept., METU _____

Prof. Dr. Ekmel Özbay
Electrical and Electronics Engineering Dept., Bilkent University _____

**Date**: 31.8.2007

**I hereby declare that all information in this document has been obtained and presented in accordance with academic rules and ethical conduct. I also declare that, as required by these rules and conduct, I have fully cited and referenced all material and results that are not original to this work.**

Name, Last Name: Mahmud Yusuf TANRIKULU

Signature :

# ABSTRACT

## AN UNCOOLED INFRARED MICROBOLOMETER DETECTOR ARRAY USING SURFACE MICROMACHINED MEMS TECHNOLOGY

TANRIKULU, Mahmud Yusuf

Ph. D., Department of Electrical and Electronics Engineering

Supervisor: Prof. Dr. Tayfun AKIN

August 2007, 163 pages

This thesis presents the design, fabrication, and characterization of a surface micromachined uncooled infrared resistive microbolometer detector along with the implementation of a 320x240 focal plane array (FPA) using this detector. The detector design includes the selection of the detector active material as Yttrium Barium Copper Oxide (YBaCuO), modeling of the detector as cascaded transmission lines (CTL) for absorptance calculations, optimization of the pixel and electrode structures, and the simulation of the thermal and the mechanical properties. The detector is designed to have a pixel pitch of 50 μm with a fill factor of 64 %. The absorptance is calculated to be 66 % in 8-12 μm wavelength region, and the thermal conductance ($G_{th}$) of the detector is simulated to be $9.4 \times 10^{-8}$ W/K.

The fabrication steps of the detector and the layers used in these steps are optimized separately during the realization of the detector. The active material, YBaCuO, is optimized to have minimum resistivity and maximum temperature coefficient of resistance (TCR) in order to achieve the highest performance parameters. The absorber layer, titanium nitride (TiN), is also optimized to have a sheet resistance value of 377 Ω/□ to have the highest infrared absorptance.

The characterization of the detector includes TCR, $G_{th}$, noise, and responsivity measurements. TCR is measured to be -3.4 %/K which is one of the highest TCR values among YBaCuO detectors with a reasonable resistivity. The $G_{th}$ value is extracted to be $9.0x10^{-8}$ W/K from the test detector measurements. Also the 1/f noise corner frequency is measured to be 1.6 kHz at 27 μA bias current which is compatible with the values in the literature. Finally, the responsivity value is extracted as 400000 V/W at 10 μA current bias from the test detector characterization. Using these measurement results the NETD value of a 320x240 FPA consisting of these detectors is estimated as 55 mK.

A 320x240 FPA is fabricated on CMOS wafers together with the readout circuitry using the designed pixels and the first infrared images are obtained using an in-house built test setup. The obtained images show that the detectors are successfully fabricated monolithically with the CMOS readout circuit and the FPA is working properly.

The research completed under the scope of this thesis is a very important example of the development of MEMS and infrared imaging systems in Turkey. The fabricated FPA, which is the first surface micromachined uncooled infrared microbolometer array in Turkey, can be used for applications requiring high performance. With the development of this FPA Turkey has become the $4^{th}$ country that has developed its own technology to fabricate uncooled microbolometer FPAs.

Keywords: Uncooled infrared detectors, high performance microbolometer detectors, surface micromachining MEMS technology, Yttrium Barium Copper Oxide (YBCO) microbolometers, uncooled infrared focal plane arrays.

# ÖZ

## YÜZEY MİKROİŞLEME MEMS TEKNOLOJİSİ İLE SOĞUTMASIZ KIZILÖTESİ MİKROBOLOMETRE DETEKTÖR DİZİNİ

TANRIKULU, Mahmud Yusuf

Doktora, Elektrik ve Elektronik Mühendisliği Bölümü

Tez Yöneticisi: Prof. Dr. Tayfun AKIN

Ağustos 2007, 163 sayfa

Bu tezde yüzey mikroişleme teknolojisi ile üretilen soğutmasız kızılötesi direnç tipi mikrobolometre detektörünün tasarımı, üretimi ve karakterizasyonu ve bu detektörler kullanılarak üretilen 320x240 odak düzlem matrisinin (ODM) gerçeklenmesi anlatılmaktadır. Tasarım, detektör aktif materyalinin Yitriyum Baryum Bakır Oksit (YBaCuO) olarak seçilmesini, emilim miktarının bulunabilmesi için detektörlerin birleştirilmiş iletim hatları olarak modellenmesini, piksel ve detektör yapısının tasarımını ve detektörlerin ısıl ve mekanik simülasyonlarını kapsamaktadır. Tasarlanan detektörün büyüklüğü 50 µm ve doluluk oranı % 64'tür. Detekörün 8-12 µm dalgaboyu aralığındaki emilimi % 66 olarak hesaplanmış ve ısıl iletkenliği ($G_{th}$) $9.4x10^{-8}$ W/K olarak simüle edilmiştir.

Detektörün fabrikasyon basamakları ve bu basamaklarda kullanılan katmanlar ayrı ayrı optimize edilmiştir. Aktif materyal olan YBaCuO, en yüksek performansı elde

etmek için, özdirenci minimum ve direncin sıcaklıkla değişim katsayısı (TCR) maksimum olacak şekilde optimize edilmiştir. Emilim katmanının yüzey direnç değeri en yüksek kızılötesi emilimi sağlayacak olan 377 Ω/□ değerine getirilmiştir.

Detektörün karakterizasyonu için TCR, $G_{th}$, gürültü ve tepkisellik değerleri ölçülmüştür. TCR -3.4 %/K olarak ölçülmüştür ve bu değer makul özdirençli YBaCuO detektörleri içinde ölçülen en yüksek değerlerden biridir. ısıl iletkenlik değeri test detektörlerinin ölçümleri sonucunda $9.0x10^{-8}$ W/K olarak bulunmuştur. Yine yapılan ölçümlerde 1/f gürültüsünün köşe frekansı 27 μA akım altında 1.6 kHz olarak bulunmuştur. Bu değer literatürdeki değerler ile uyumludur. Son olarak tepkisellik değeri, test detektörlerinin karakterizasyonu sonucu 10 μA akım altında 400000 V/W olarak bulunmuştur. Bu ölçüm sonuçlarına göre gürültü eşlenikli sıcaklık farkı (NETD) 55 mK olarak tahmin edilmektedir.

Tasarlanan detektörler kullanılarak 320x240 boyutlarında ODM CMOS plakalar üzerinde okuma devreleri ile beraber üretilmiş ve laboratuvarlarımızda kurulan bir test düzeneği ile ilk kızılötesi görüntüler elde edilmiştir. Elde edilen bu görüntüler detektörlerin CMOS okuma devreleri ile monolitik bir şekilde başarılı olarak üretildiğini göstermektedir.

Bu çalışma Türkiye'de MEMS ve kızılötesi görüntü sistemlerinin geldiği noktayı gösteren çok önemli bir örnektir. Üretilen bu ODM yüksek performans gerektiren uygulamalar için kullanılabilecek Türkiyede üretilen ilk yüzey mikroişlenmiş soğutmasız kızılötesi mikrobolometre matrisidir. Bu teknolojinin geliştirilmesi ile Türkiye özgün olarak soğutmasız kızılötesi ODM üretebilen 4. ülke olmuştur.

Anahtar Kelimeler: Soğutmasız kızılötesi detektörler, yüksek performanslı mikrobolometre tipi detektörler, yüzey mikroişleme MEMS teknolojisi, Yitriyum Baryum Bakır Oksit (YBaCuO) mikrobolometreler, soğutmasız kızılötesi odak düzlem matrisleri.

*To My Family*

# ACKNOWLEDGMENTS

I would like to express my appreciation and thanks to my thesis advisor Prof. Dr. Tayfun Akın for his supervision, invaluable guidance, and endless support during this study and also my undergraduate and graduate life. It is an exceptional opportunity for me to work with him.

I would also like to thank Prof. Dr. Cengiz Beşikçi and Prof. Dr. Ekmel Özbay for their ideas, comments, and suggestions throughout the progress of this thesis. I would also like to acknowledge Asst. Prof. Dr. Haluk Külah for his help and support during this Ph. D. study.

I want to thank Murat Tepegöz not only for his help in detector design and testing and his tremendous efforts to operate the imaging system, but also for his great friendship for the past seven years. I also want to thank Fehmi Çivitci for his priceless support and help during the fabrication processes and his patience and friendship during the hard times in cleanroom. I want to thank Orhan Akar for his support, incredible patience and sharing his wide experience whenever I needed.

I would like to thank Dr. Said Emre Alper, Dr. Kağan Topallı, and Mehmet Ünlü for their valuable suggestions for the detector fabrication and for their friendship. I also would like to acknowledge my roommate Mustafa Seçmen for his help during the mathematical formulation of absorption calculations and thermal conductance measurements and for his friendship. I wish to thank the former and current members and staff of the METU MEMS group and METU BIO-MEMS group members whose names are not listed here, for creating a very pleasant and friendly

working environment. I specially thank Özge Zorlu (currently at EPFL) for his support and encouragement through his e-mails.

I want to thank Harun Tanık, Murat Ünal, Ebru Topallı and other employees of METU-MET facilities for all their help during this study and support during the fabrication processes. I want to thank Zeki Topçu and Yılmaz Ünal from Aselsan for their suggestions and help during the detector tests. I also would like to thank the members of III-V research group especially to Dr. Selçuk Özer and Dr. O. Orkun Cellek for their help during this study.

I would like to thank Prof. Dr. Zeynep Çelik-Butler and Prof. Dr. Donald Butler for their collaboration and help during my visit to UTA. I also want to thank Aamer Mahmood and Aasutosh Dave for their support and friendship during this visit. This visit was supported by TÜBİTAK BAYG (currently TÜBİTAK BİDEB) within joint Ph. D. programme.

I also want to thank all the members of METU TaeKwonDo team, especially to the master trainers Ali Mete and Dr. Genco Çetinkanat, for all their support and encouragement during this study.

Last but not least I would like to thank to my family members for their continuous support, encouragement, help and patience during this study and my whole life.

This work is supported by Research and Development Department of the Ministry of Defense (MSB Arge) and partially supported by TÜBİTAK.

# TABLE OF CONTENTS

ABSTRACT ..... iv
ÖZ ..... vii
DEDICATION ..... ix
ACKNOWLEDGMENTS ..... x
TABLE OF CONTENTS ..... xii
LIST OF TABLES ..... xv
LIST OF FIGURES ..... xvi
CHAPTER
1. INTRODUCTION ..... 1
1.1. Infrared Spectrum ..... 2
1.2. Overview of Infrared Detectors ..... 4
1.3. Uncooled Infrared Detectors ..... 6
1.3.1. Thermoelectric (Thermopile) Detectors ..... 8
1.3.2. Pyroelectric Detectors ..... 10
1.3.3. Microbolometers ..... 12
1.3.4. Microcantilever Detectors and Other Approaches ..... 17
1.4. Previous Work on Microbolometers at METU ..... 18
1.5. Research Objectives and Thesis Organization ..... 21
2. FIGURE OF MERITS FOR UNCOOLED INFRARED DETECTORS ..... 24
2.1. Temperature Sensitivity ..... 24
2.2. Thermal Conductance ($G_{th}$) ..... 25
2.3. Responsivity ..... 27

2.4. Noise Equivalent Power (NEP) ..... 29
2.5. Noise Equivalent Temperature Difference (NETD) ..... 32
2.6. Detectivity (D*) ..... 33
2.7. Fundamental Limitations ..... 34
2.8. Conclusions ..... 35
3. DESIGN OF THE MICROBOLOMETER PIXEL ..... 36
3.1. Determination of the Active Detector Material ..... 36
3.2. Detector Resistance Value and Structure ..... 42
3.3. Structure of the Detector and Pixel Size ..... 45
3.4. Absorption Calculations of the Detector ..... 50
3.4.1. Theory ..... 51
3.4.2. Absorption Simulations ..... 58
3.5. Thermal simulations ..... 63
3.6. Mechanical Simulations ..... 65
3.7. Conclusions ..... 68
4. PROCESS OPTIMIZATION AND FABRICATION OF A SINGLE PIXEL MICROBOLOMETER ..... 69
4.1. Design of the Fabrication Process ..... 69
4.2. Optimization of the Process Steps ..... 79
4.2.1. Optimization of the Sacrificial Layer ..... 83
4.2.2. Optimization of the Mirror Metal ..... 85
4.2.3. Optimization of the Structural Layer ..... 86
4.2.4. Optimization of Interconnect Metal and the Electrode Metal ..... 88
4.2.5. Optimization of the YBaCuO Layer ..... 89
4.2.6. Optimization of the Absorber Layer ..... 93

4.2.7. Fabrication Results of the Single Pixel Microbolometer Detector ..... 94
4.3. Conclusions ..... 95
5. TEST RESULTS OF FABRICATED SINGLE PIXEL MICROBOLOMETER DETECTORS ..... 97
5.1. TCR Measurements ..... 97
5.2. Thermal Conductance Measurements ..... 98
5.3. Noise Measurements ..... 105
5.4. Responsivity Measurements ..... 106
5.5. Conclusions ..... 111
6. FABRICATION OF 320X240 MICROBOLOMETER FOCAL PLANE ARRAY AND INITIAL MEASUREMENTS ..... 113
6.1. Fabrication of 320x240 FPAs ..... 113
6.2. Initial Measurements and the First Images from 320x240 FPA ..... 125
6.3. Conclusions ..... 132
7. CONCLUSIONS AND FUTURE WORK ..... 133
REFERENCES ..... 139
APPENDICES
A. DERIVATION FOR EQUATION 3.14 ..... 150
B. MATLAB CODE FOR ABSORPTION SIMULATIONS ..... 152
C. DETAILED FABRICATION PROCESS FLOW ..... 156
CURRICULUM VITAE ..... 162

# LIST OF TABLES

TABLES

Table 3.1: The summary of the regions, layer combinations and the areas of the regions. Total area is the sum of the areas of these regions. ..... 56

Table 3.2: The summary of the thermal properties of the layers used in the simulations..... 64

Table 3.3: The summary of the mechanical properties of the layers used in the support arms..... 65

Table 3.4: The maximum displacement and stress results in all direction for an acceleration of 1000 g. The maximum stress values in all directions are less than the yield strength values of silicon nitride and titanium which are 14 GPa and 170 MPa, respectively. ..... 66

Table 3.5: The resonance frequencies and maximum displacement values of the first five modes. The results show that any mechanical input with frequency less than 60 kHz is acceptable for the designed microbolometer detector. ..... 68

Table 5.1: Summary of the properties of *pixel_v1* and expected performance values. ..... 112

# LIST OF FIGURES

FIGURES

Figure 1.1: The infrared spectrum and its sub-regions in the whole electromagnetic spectrum [5]. ..... 2

Figure 1.2: The detailed version of atmospheric transmission and the absorbing molecules with respect to wavelength [6]. ..... 3

Figure 1.3: The spectral exitance with respect to wavelength for different temperatures [8]. The straight line given in the figure shows the wavelength of maximum exitance at different temperatures. ..... 5

Figure 1.4: The principal structure of the uncooled infrared detectors [19]. The incident infrared radiation is absorbed by the sensor which is connected to the substrate via the supporting legs. ..... 7

Figure 1.5: The basic structure of a thermocouple detector. The temperature difference between hot junction ($T_h$) and the cold junction ($T_c$) results in a self induced voltage ($V_{ind}$) ..... 8

Figure 1.6: Representative view of pyroelectric detectors. ..... 11

Figure 1.7: Representative perspective view of a microbolometer detector. The infrared radiation is absorbed by the absorber layer resulting in an increase in the temperature of the detector. This temperature increase causes a change in the electrical property of the detector material. This change is readout by the monolithically integrated CMOS circuitry. ..... 13

Figure 1.8: SEM pictures of some example detectors. (a) shows a 50 µm pixel from BAE systems [41] while (b) shows a 25 µm pixel from Raytheon [42]. ..... 14

Figure 1.9: SEM pictures of some 17 µm detectors. (a) Raytheon's detector [49] (b) DRS's detector [51]. ..... 14

Figure 1.10: Infrared images taken with FPAs of 17 µm detectors. (a) shows the image from BAE Systems' FPA [50], while (b) shows the image from DRS's FPA [51]. ..... 15

Figure 1.11: Mitsubishi's diode type microbolometer detectors. (a) pixel structure and (b) an SEM picture (b). ..... 17

Figure 1.12: SEM picture of the successfully fabricated array composed of n-well detectors. ..... 19

Figure 1.13: Successfully fabricated array pixels. (a) shows the top view while (b) shows the bottom view. ..... 20

Figure 2.1: Thermal analogue circuit for a microbolometer detector with thermal conductance $G_{th}$ and thermal capacitance $C_{th}$. ..... 28

Figure 3.1: The XRD test results obtained from the samples taken from UTA. From the measurements it is found that the material on both of the wafers is amorphous as desired. ..... 39

Figure 3.2: The resistance variation of a 570 kΩ YBCO resistor with the varying temperature. The measured results are fit into a third order polynomial and the TCR value of the resistor is found as -2.9 %/K at room temperature. ..... 40

Figure 3.3: The noise measurement results of the YBCO resistor at different bias currents. 1/f noise corner frequencies are found as 40 Hz and 100 Hz at 0.61 µA and 1.24 µA, respectively. ..... 41

Figure 3.4: The change of NETD with the changing resistance value when the self-heating of the detector is totally cancelled. NETD value decreases as the resistance value is reduced. ..... 43

Figure 3.5: The change of NETD value with the changing resistance when the self-heating effect is partially cancelled. ..... 44

Figure 3.6: The designed finger type electrode structure; (a) top view and (b) the perspective view. The distance between the electrodes determines the length of the resistor (L), while the total length of the fingers determines the width of the resistor (W). ..... 45

Figure 3.7: Top view of some different detector structures. The important variables are given in (a) as pixel pitch, support arm width, spacing, and active area. ..... 47

Figure 3.8: The variation of NETD with the pixel pitch for different minimum feature sizes. In this simulation only the structural dimensions are changed according to the minimum feature size. ..... 49

Figure 3.9: The layout of the designed microbolometer detector pixel. The metal interconnects on the support arms, the spacing and the finger size of the electrodes are designed to be 1.5 µm which is the minimum feature size in our facilities. ..... 49

Figure 3.10: Representative perspective view of a part of a microbolometer detector (a) and its transmission line model (b). ..... 50

Figure 3.11: The modified version of the transmission line model of microbolometer structure after some assumptions. ..... 54

Figure 3.12: Different regions of the microbolometer detector structure. ..... 56

Figure 3.13: The layout of the pixel developed in [18]. The pixel has dimensions of 40 µm x 40 µm fabricated in 0.35 µm CMOS technology and post-CMOS processed in METU facilities [18]. ..... 57

Figure 3.14: Measured refractive index and extinction coefficient of the structural layer (silicon nitride, $Si_3N_4$). ..... 58

Figure 3.15: Measured refractive index and extinction coefficient of the active material (YBCO). ..... 59

Figure 3.16: Variation of the absorption with respect to cavity and structural layer thicknesses. ..... 60

Figure 3.17: Variation of the thermal conductance with respect to structural layer thickness. ..... 61

Figure 3.18: Variation of the absorption with the surface resistance of the absorber layer. ..... 62

Figure 3.19: Absorption simulation of the modeled microbolometer structure. The total absorption value at 10 μm wavelength is not very low when compared with the data in literature [67] and can be increased if the areas of Regions 2 and 3 are reduced. ..... 63

Figure 3.20: The result of the thermal simulation performed using Coventorware. The temperature of the pixel increases 1061 mK with an applied power of 100 nW. This results in a thermal conductance value of $9.4x10^{-8}$ W/K..... 64

Figure 3.21: The variation of the pixel temperature with time. The thermal time constant of the pixel is found as 15.4 ms from this simulation result. ..... 65

Figure 3.22: The simulation results for the displacement (a) and the stress (b) for the acceleration of 1000 g in -z direction. ..... 67

Figure 4.1: The representative cross-sectional view of the detector after each step of the designed process flow. ..... 74

Figure 4.2: The 3-D views of the detector pixel after each process step. The views are obtained from the model used in the Coventorware software. ..... 78

Figure 4.3: The layout of the designed mask set which is used for the optimization of the fabrication steps. ..... 80

Figure 4.4: The layouts of some different pixels from the mask set. ..... 82

Figure 4.5: The SEM view of the successfully patterned polyimide layer. The edge of the polyimide layer is upright as desired..... 84

Figure 4.6: The SEM views of the suspended aluminum bridges verifying that the polyimide layer can be successfully etched. The bridges are bended due to the internal stress of the aluminum layer..... 85

Figure 4.7: Successfully patterned chromium/gold mirror of the microbolometer pixel. ..... 86

Figure 4.8: The SEM pictures of the suspended nitride bridges patterned in detector shape. As can be seen the layer is stress free and can be used as the structural layer of the detector..... 87

Figure 4.9: Successfully patterned titanium as the interconnect metal and the gold fingers as the electrode metal. ..... 89

Figure 4.10: The variation of the resistivity of YBCO layer with the oxygen amount change. A minimum resistivity of 255 Ω/cm is obtained for an oxygen amount of 5 %. ..... 90

Figure 4.11: The change of the TCR value of the YBCO layer with the oxygen amount variation. As can be seen from the figure the TCR values are very close to each other. The highest measured TCR value is -3.6 %/K with an oxygen ratio of 7.4 %. ..... 92

Figure 4.12: The change of the NETD value with the oxygen amount variation. As can be seen from the figure, the optimum oxygen amount to have the highest performance is 5 % for the finger type electrodes when the resistivity and TCR of the YBCO layer are considered together ..... 93

Figure 4.13: Microscopic view of a successfully fabricated microbolometer detector..... 94

Figure 4.14: The SEM views of the fabricated detectors. As can be seen from the views, the detectors are suspended and thermally isolated from the substrate. Also the detectors are standing without any buckling since there is no stress in the arms due to the stress free nitride layer. .... 96

Figure 5.1: The sample and the temperature sensor used in TCR measurements. .. 99

Figure 5.2: Resistance and TCR variation with the changing temperature. The TCR value at the room temperature (25 °C) is measured approximately as - 3.4 %/K..... 99

Figure 5.3: The vacuum dewar used in the thermal conductance measurements. 100

Figure 5.4: The layout of the pixel used in thermal conductance measurements (*pixel_v2*). This pixel also has a pixel pitch of 50 µm, but the support arm width and the spacing is different than the pixel used in the array. The support arm width is 4 µm where the interconnect metal width is 2 µm and the spacing is 3 µm. The length of the arms is 80 µm which is 0.5 µm shorter than the pixel used in the array. ..... 103

Figure 5.5: The result of the thermal simulation of *pixel_v2* performed using Coventorware software. The thermal conductance value is simulated as $1.35x10^{-7}$ W/K which is higher than the simulated value of *pixel_v1* due to the wider support arms. ..... 104

Figure 5.6: The thermal conductance value of *pixel_v2* with the changing vacuum level. The minimum measured thermal conductance is $1.27x10^{-7}$ W/K which is smaller than the simulated value. ..... 104

Figure 5.7: The power spectral density of a detector having 106 kΩ resistance at room temperature (this measurement is done by Mr. Murat Tepegöz). The corner frequencies for 27 μA and 54 μA are 1.6 kHz and 4.3 kHz respectively. ..... 106

Figure 5.8: The test setup that is used to measure the responsivity of the fabricated detector. (a) shows the whole setup while (b) shows the zoomed view of the dewar and chopper. ..... 108

Figure 5.9: The responsivity measurement of *pixel_v2* and the fitted curve. The DC responsivity of the detector is found as 665 V/W from the fitting..... 110

Figure 5.10: The result of the absorption simulation performed using cascaded transmission line method. The absorptance at 10 μm is 21.5 %. This pixel have high area ratio of Region 2 and Region 3, so the absorptance of the pixel at 10 μm is low. The discrepancy between the measurements and simulations comes from the fabricated thicknesses of the layers ..... 111

Figure 6.1: The 6" CMOS wafer and a zoomed view of one of the readouts. There are 30 readout chips in a 6" wafers..... 114

Figure 6.2: The layout of the designed mask set for fabrication of 320x240 FPAs on 6" wafers. There are 8 masks in the set since the process steps are the same as the process of the single pixel microbolometer detector..... 115

Figure 6.3: The microscope views of the detectors after each process step. ..... 119

Figure 6.4: The SEM views of the successfully released detectors in 320x240 FPAs. ..... 124

Figure 6.5: The dewar used for the initial tests and the wirebonded FPA chip. .... 126

Figure 6.6: NETD measurement result for the FPA. The mean value of NETD is measured as 450 mK. ..... 128

Figure 6.7: Infrared images obtained from several FPAs. These images are raw images and only one point correction is applied. ..... 130

Figure 6.8: Filtered version of Figure 6.7 (b). The single dead pixels are replaced by the surrounding pixels and the background noise is eliminated by some software filtering. (the iamge processing is performed by Emre Kültürsay) ..... 131

# CHAPTER 1

# INTRODUCTION

The talent to see under adverse conditions like darkness or obscured visibility has always been a desire for the mankind. The reason for this desire is clear: to be able to do the things that can be done under daylight [1, 2]. The daylight is reflected from the objects in the environment, and this reflected light is converted to image by the eyes and the brain. So in order for the eyes and the brain to see, some kind of information should come from the target. In darkness, this information can come in different ways. First way is the illumination of the target with an artificial light source. Light sources have limited capacity to illuminate under certain conditions, and it is not always wanted to illuminate the target of interest, especially in military applications. The second way is to detect the radiation emitted by the target, which is known as *infrared imaging*. Everything that has a temperature above 0 K emits infrared radiation, and this information can be used to see the target. There are many applications of infrared imaging. The most common application areas are military applications such as rifle sights, targeting, missile seekers, smart munitions, etc. and civilian applications such as driver's night vision enhancement, fire fighting, predictive maintenance, nondestructive testing, medical imaging, etc [3]. This thesis reports the development of a 320x240 uncooled microbolometer focal plane array which can be used in both military and civilian applications.

The rest of this chapter gives more detailed explanations about infrared radiation and infrared detectors. Section 1.1 gives information about infrared spectrum as a

part of electromagnetic spectrum, while Section 1.2 makes an overview of the infrared detectors which are grouped as cooled and uncooled detectors. Section 1.3 explains the uncooled infrared detectors, and Section 1.4 gives the history of uncooled microbolometer studies at METU. Finally, Section 1.5 summarizes the objectives of this research and the organization of this thesis.

## 1.1. Infrared Spectrum

Infrared radiation is a form of electromagnetic wave whose spectrum is a part of electromagnetic spectrum lying in the wavelength range of 0.75-1000 μm [4]. In 1800's Herschel verified the occurrence of this radiation with his glass thermometer, which is accepted as the first infrared detector [1]. Figure 1.1 shows the infrared spectrum and its sub-regions in the whole electromagnetic spectrum [5].

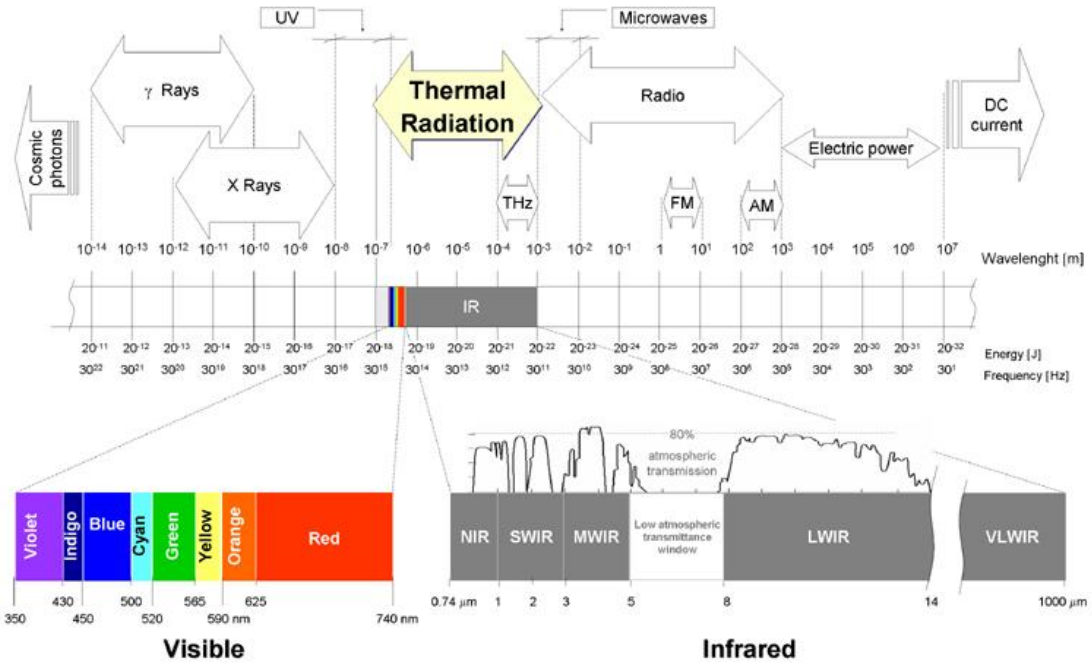



Figure 1.1: The infrared spectrum and its sub-regions in the whole electromagnetic spectrum [5].

As shown in Figure 1.1, the atmospheric transmission is not same for every wavelength in the infrared region. This difference is caused by the absorption of some molecules in the air. Figure 1.2 gives the detailed version of atmospheric transmission and the absorbing molecules in infrared region with respect to wavelength [6]. As can be seen from the figure, in some regions the transmittance is nearly zero which makes infrared detection unattainable, and in some regions the absorption percentage of molecules is very low making all the infrared information available for detection. The infrared detectors are designed to detect the infrared signals at the regions where atmospheric transmission is maximum. The most common of these regions are 3-5 µm and 8-12 µm sections of infrared spectrum.

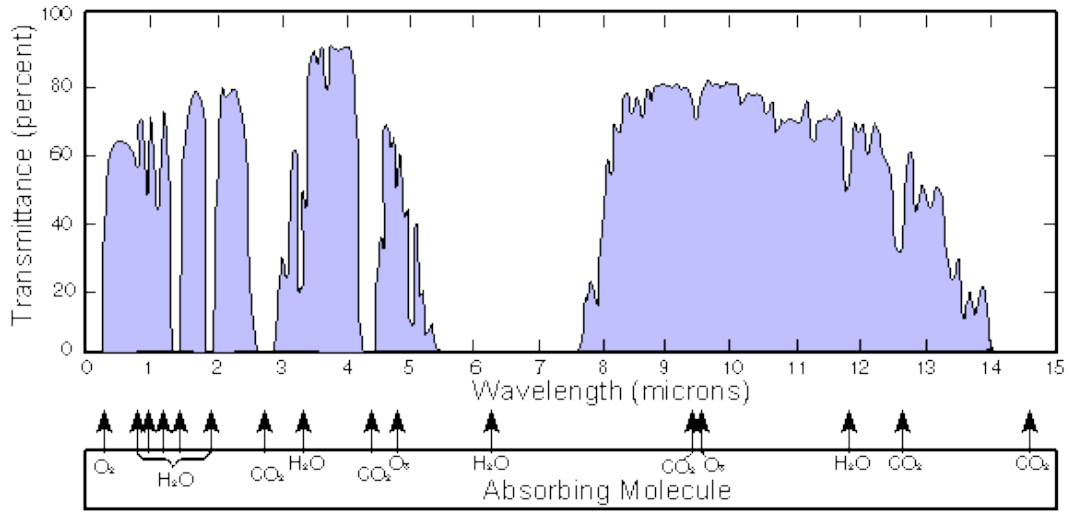



Figure 1.2: The detailed version of atmospheric transmission and the absorbing molecules with respect to wavelength [6].

Another important aspect for the choice of the spectral region to be detected is the temperature range of the target. It is known that the radiation that an object emits depends on the temperature of the object, and as the temperature increases the radiation level also increases [7]. For a blackbody object the spectral exitance is given as

$$M(\lambda,T)=\frac{2\pi hc^2}{\lambda^5(e^{hc/\lambda kT}-1)} \tag{1.1}$$

where $M(\lambda,T)$ is the spectral exitance, $h$ is the Planck's constant, $c$ is the speed of the light, $\lambda$ is the wavelength, and $T$ is the temperature of the object. Figure 1.3 shows the spectral exitance with respect to wavelength for different temperatures [8]. The straight line given in the figure shows the wavelength of maximum exitance at different temperatures. As can be seen from the figure, the maximum exitance occurs at smaller wavelengths as the temperature increases, which is known as the Wien's displacement law and expressed as

$$\lambda_{max}=\frac{2898}{T} \tag{1.2}$$

where $\lambda_{max}$ is the wavelength of maximum exitance in μm and $T$ is the temperature of the object in K. For the objects at 300 K, i.e., the room temperature, the wavelength of maximum exitance is around 10 μm. For this reason the detectors used to sense the objects at room temperature are designed to sense the wavelength range of 8-12 μm. For hotter objects such as airplanes or missiles, the detectors are designed for the wavelength range of 3-5 μm since the maximum exitance occurs in that region. The types of the detectors used in these wavelength regions will be explained in the next section.

## 1.2. Overview of Infrared Detectors

There are two principal types of infrared detectors: photon (cooled) detectors and thermal (uncooled) detectors [9]. In photon detectors, the photons in the absorbed radiation interact with the electrons in the detector material. In thermal detectors, the absorbed radiation produces a change in the temperature of the detector which changes a temperature dependent property of the detector.

Photon (cooled) detectors can be divided into four main groups depending on the nature of interaction. These are intrinsic detectors, extrinsic detectors, photoemissive detectors (schottky barriers), and quantum well detectors. It is also possible to make the grouping depending on the development of electric and magnetic fields. In this case the detectors are grouped as photoconductive, photovoltaic, photoelectromagnetic, and photoemissive detectors [10].

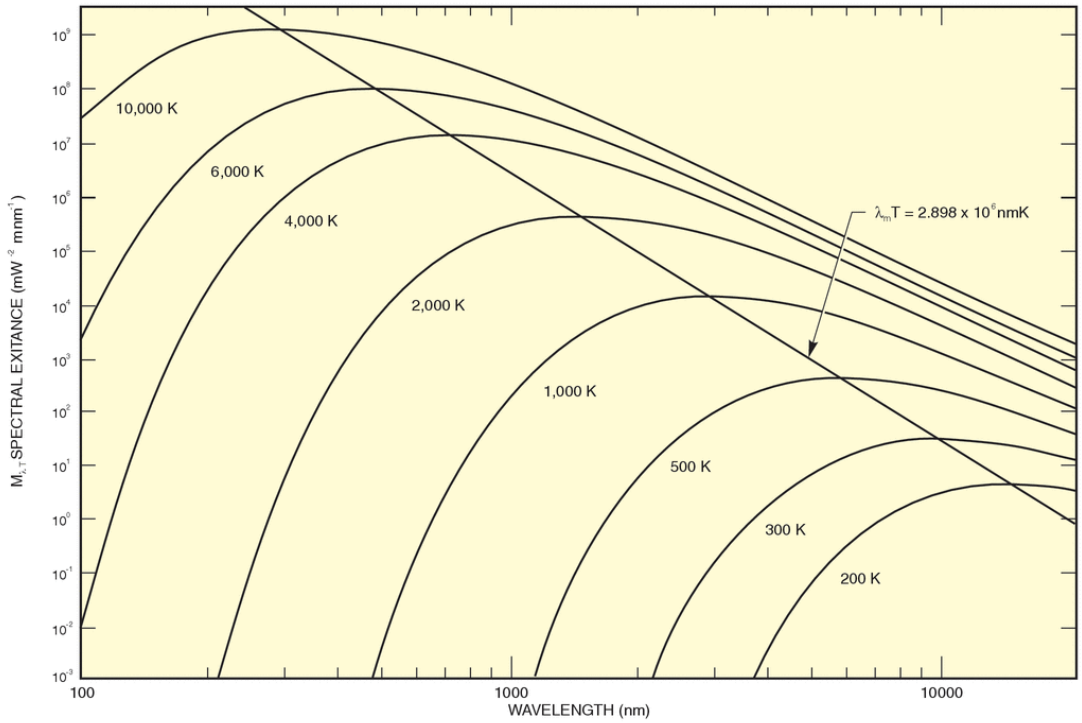



Figure 1.3: The spectral exitance with respect to wavelength for different temperatures [8]. The straight line given in the figure shows the wavelength of maximum exitance at different temperatures.

Photon detectors have very high signal-to-noise ratio and very fast response. They also exhibit good wavelength selectivity which enables the production of multiband detectors [11]. But in order for the photon detectors to achieve these properties, they should be cooled down to cryogenic temperatures, such as 77 K or below. This

is necessary in order to distinguish the generated carriers due to infrared radiation from the thermally generated carriers. This cooling requirement increases the cost and weight of the system and prevents the extensive use of photon detectors [10]. Due to this cooling requirement photon detectors are also called as cooled detectors.

The most common photon detectors are mercury cadmium telluride (HgCdTe or MCT), indium antimonide (InSb), quantum well infrared photodetectors (QWIP) and superlattice type-II detectors [12-17]. All of these detectors require complicated fabrication steps increasing the cost of these detectors. Due to this cost issue they are mainly used in military, astronomy, and special medical instruments in which the performance is more important than the cost [18].

Thermal detectors are mainly divided into three groups. These are thermoelectric detectors (thermopiles), pyroelectric detectors, and microbolometers. Opposing to cooled detectors, thermal detectors do not need to be cooled down to cryogenic temperatures, so they are also called as uncooled detectors. The details of uncooled infrared detectors will be given in the next section.

## 1.3. Uncooled Infrared Detectors

Uncooled infrared detectors perceive the incident infrared radiation via a change in one of the temperature dependent electrical properties of the detector. Figure 1.4 shows the principal structure of uncooled infrared detectors [19]. As can be seen from the figure, the detector has mainly three parts: the sensor part, the supporting legs, and the substrate. The incident infrared radiation is absorbed by the sensor which is connected to the substrate via the supporting legs. This absorbed portion of the infrared power heats the sensor part of the detector and causes a temperature increase in the detector. An electrical property of the detector, which

depends on the temperature, changes due to this temperature increase. This property change is detected and converted to electrical signal via the readout circuit.

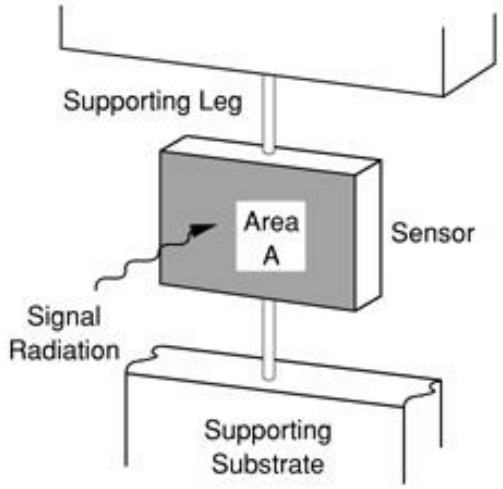



Figure 1.4: The principal structure of the uncooled infrared detectors [19]. The incident infrared radiation is absorbed by the sensor which is connected to the substrate via the supporting legs.

When compared to the cooled detectors, uncooled ones neither have high performance parameters nor high response times. The popularity of the uncooled infrared detectors comes from the fact that they do not need cryogenic coolers, so they allow the implementation of small, light, low-cost, and low power infrared camera systems.

As mentioned in the previous section, there are mainly three types of uncooled detectors, i.e., thermoelectric detectors (thermopiles), pyroelectric detectors, and microbolometers. There are also some relatively new approaches such as microcantilever type detectors. These different detectors are introduced in the following subsections.

### 1.3.1. Thermoelectric (Thermopile) Detectors

Thermoelectric detectors or thermopiles are sensors consisting of a junction of two materials that have different *Seebeck coefficients* [20]. Seebeck coefficient of a material is the measure of the stimulated thermoelectric voltage in response to a temperature difference across that material [21]. Due to the difference in the Seebeck coefficients, the voltage induced across the junction materials is different, and this voltage can be used by the readout circuit and converted to an infrared image. If only one junction of materials is used the structure is called as a thermocouple, and the combination of thermocouples is called as thermopiles. Figure 1.5 shows the basic structure of a thermocouple detector.

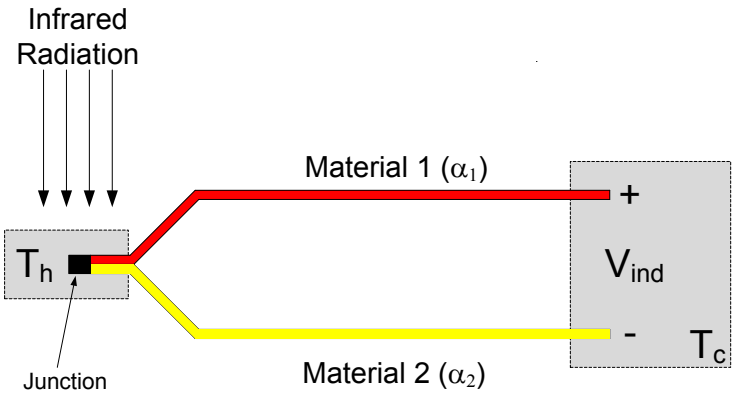



Figure 1.5: The basic structure of a thermocouple detector. The temperature difference between hot junction ($T_h$) and the cold junction ($T_c$) results in a self induced voltage ($V_{ind}$)

The voltage induced at the ends of the materials is expressed as

$$V_{ind} = \alpha_{12}(T_h - T_c) = (\alpha_1 - \alpha_2)(T_h - T_c) \quad (1.3)$$

where $V_{ind}$ is the output voltage induced at the thermocouple, $\alpha_{12}$ is the relative Seebeck coefficient of materials, $\alpha_1$ and $\alpha_2$ are the Seebeck coefficients of material 1 and material 2, respectively, $T_h$ is the temperature of the heated

junction, and $T_c$ is the temperature of the cold end of the materials. As the relative Seebeck coefficient increases, the voltage at the output of the thermocouple increases. Due to this reason, the materials that have large relative Seebeck coefficient are selected as the thermocouple materials. Since semiconductors have higher Seebeck coefficients [22], they are preferred in the fabrication of thermocouples [23-29].

In thermocouples, the induced voltage is generally not enough to detect the infrared radiation. For this reason a number of thermocouples are combined to form the *thermopile* structure. In thermopiles, the induced voltage is found as

$$V_{tp} = NV_{ind} = N\alpha_{12}(T_h - T_c) \tag{1.4}$$

where $V_{tp}$ is the output voltage induced across the thermopile, $N$ is the number of thermocouples used, and $V_{ind}$ is the output voltage induced at one of the thermocouples.

The most important advantage of thermopile detectors is that they do not need temperature stabilizers because of their differential operation. Also, they do not need electrical bias for the induction of the output voltage. But, the responsivity of the thermopiles is lower than the other uncooled detectors, and the pixel sizes of the thermopiles are very large (100 µm - 250 µm). These two disadvantages limit the use of thermopile detectors in large format infrared focal plane arrays [22]. In literature it is possible to see thermopile array sizes as large as 128 x 128 [28] or 120 x 90 [29], however, typical array sizes for thermopiles are 16 x 16 [23] and 32 x 32 [25].

### 1.3.2. Pyroelectric Detectors

Every material is polarized if an electric field is applied upon it. The amount of this polarization is determined by the permittivity and dielectric constant of the material [9]. Some of the materials can be spontaneously polarized even when there is no electric field. The temperature dependence of the polarization is called *pyroelectric effect*. The spontaneous temperature change induces charge on the opposite plates of the detector. This charge generates a current which is given by [18]

$$i_P = pA\frac{dT}{dt} \tag{1.5}$$

where, $i_P$ is the current generated by the induced charge, $p$ is the pyroelectric coefficient, $A$ is the detector area, and $T$ is the detector temperature. As can be seen from the equation, if the temperature is constant, the generated current is zero. Hence, there should be a change in the detector temperature for the current generation. Due to this reason, a chopper should be used with the pyroelectric detectors, and the radiation should be modulated [18, 30, 31]. Figure 1.6 shows the representative view of pyroelectric detectors [4].

The pyroelectric effect disappears above some specific temperature which is called the *Curie temperature*. For improved responsivity, it is better to operate the pyroelectric detectors just below Curie temperature. The Curie temperature is a material property and can be adjusted with the process conditions and the material compositions.

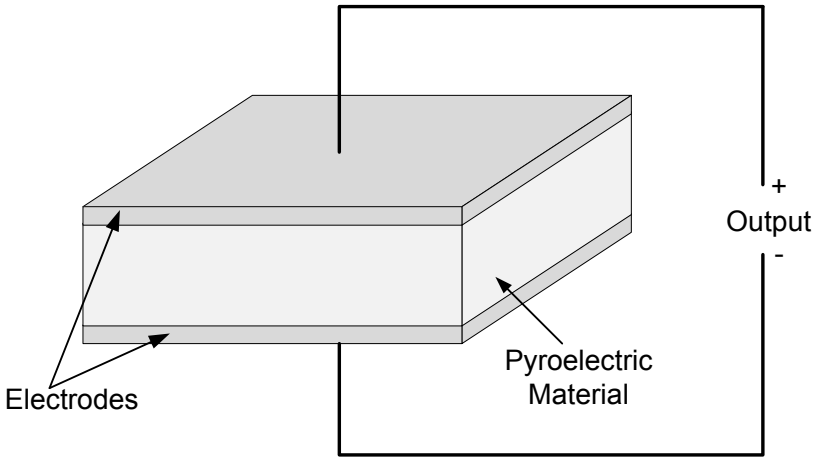



Figure 1.6: Representative view of pyroelectric detectors.

The pyroelectric effect is seen in many materials such as ferroelectrics. If the spontaneous polarization can be inverted by the application of a suitable electric field, the material is called *ferroelectric material*. Although there are other types of pyroelectric detectors, ferroelectrics are the most common group among them. Widely used ferroelectrics are barium strontium titanate ($Ba_xSr_{1-x}TiO_3$), strontium barium niobate ($Sr_{1-x}Ba_xNb_2O$), lithium tantalate ($LiTaO_3$), and lead titanate ($PbTiO_3$) [32]. These materials cannot be fabricated monolithically with CMOS readout circuits, so the detectors are fabricated on a different substrate and bonded onto CMOS readout circuits separately.

Currently, there are 320x240 format pyroelectric detector focal plane arrays (FPAs) with 50 µm pixels on the market [33]. However, the use of pyroelectric detectors is limited due to the disadvantages such as the need for choppers, not working under vibration circumstances, and non-monolithic fabrication process [34]. Although, there are still continuous efforts to fabricate the pyroelectric detectors monolithically with the CMOS readout circuits, it is not exhibited yet.

### 1.3.3. Microbolometers

Bolometers are sensors that measure the amount of the incident infrared radiation like the other thermal detectors [35]. The first bolometer was introduced in 1880s by Langley, who was able to detect a cow from a quarter mile distance [34]. His first bolometer consisted of two platinum strips covered with *lampblack*. One of the strips was exposed to infrared radiation, while the other was shielded. The strips formed a Wheatstone bridge, and the infrared radiation was measured. Although there had been an effort to improve this bolometer structure [36], the size of the detectors was 1 mm or larger making the fabrication of large arrays impossible [9]. In 1980s, Johnson and Higashi fabricated 100 µm sensors having a micromachined silicon nitride bridge structure of 1 µm thickness [9]. In 1983, R. A. Wood demonstrated the first small arrays consisting of micromachined *microbolometers* [9]. After that, a very fast progress was achieved in the array fabrication of microbolometers and large format arrays were demonstrated [37].

Figure 1.7 shows the representative perspective view of a microbolometer detector. The infrared radiation is absorbed by the absorber layer resulting in an increase in the temperature of the detector. This temperature increase causes a change in the electrical property of the detector material. This change is readout by the monolithically integrated CMOS circuitry.

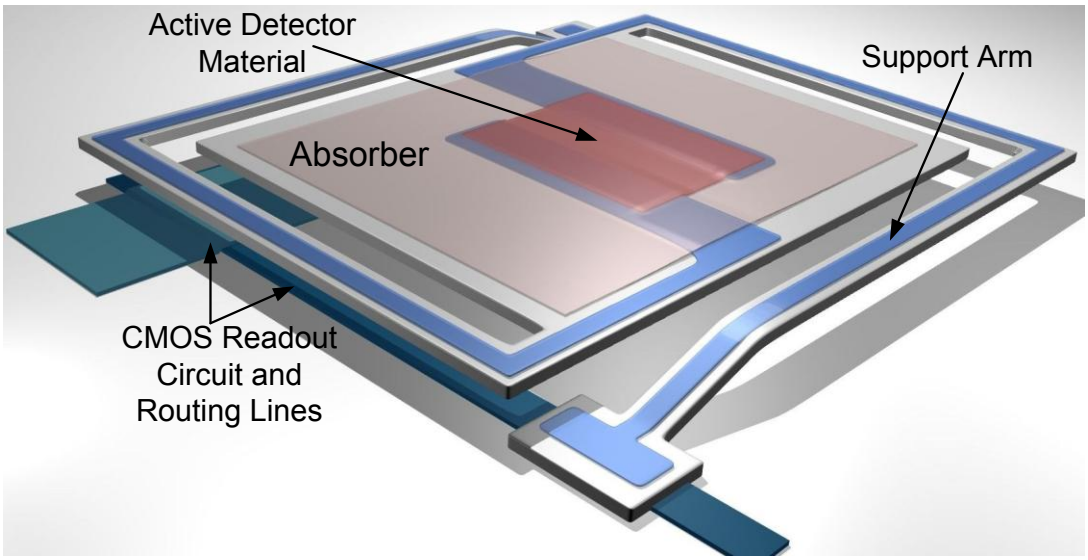
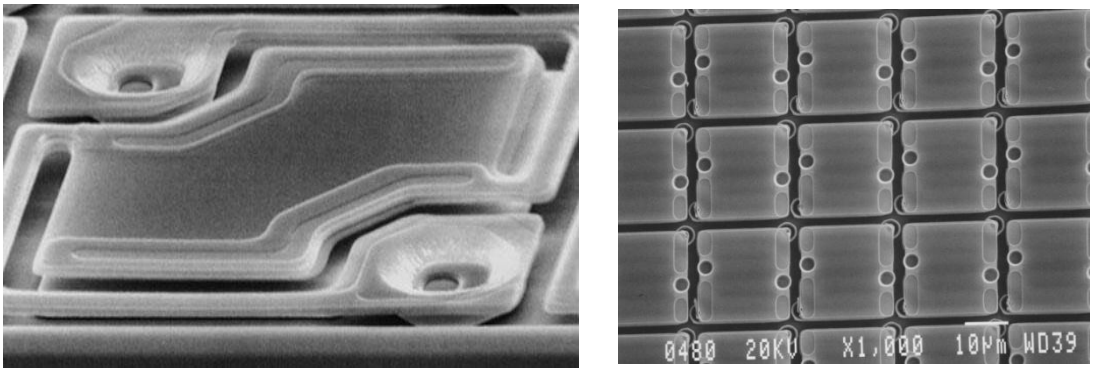



Figure 1.7: Representative perspective view of a microbolometer detector. The infrared radiation is absorbed by the absorber layer resulting in an increase in the temperature of the detector. This temperature increase causes a change in the electrical property of the detector material. This change is readout by the monolithically integrated CMOS circuitry.

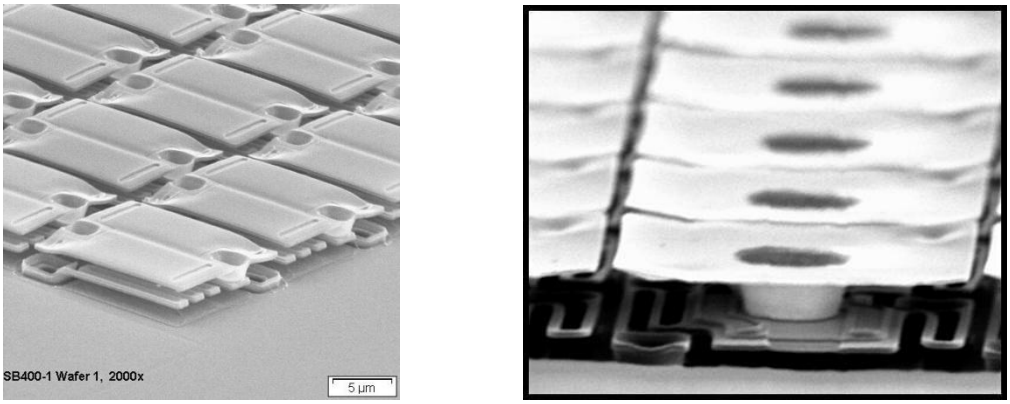
The first and the most widely used detector active material is vanadium oxide ($VO_x$), which was developed and patented by the Honeywell Research Labs [37, 38]. $VO_x$ having a temperature coefficient of resistance (TCR) value of 2-3 %/K (negative) is used as the resistor element in the detectors. The material was licensed to different companies for commercialization. Today, the most important companies developing uncooled infrared microbolometer imagers with $VO_x$ are Raytheon and BAE Systems. Also DRS, SCD, Indigo, and NEC are fabricating FPAs using $VO_x$ detectors. 320x240 format FPAs with 50 µm pixel pitch and 640x480 format FPAs with 25 µm pixel pitch have been realized by these companies [39-48]. Figure 1.8 shows the SEM pictures of some example detectors. Recently, some companies have developed detectors with 17 µm pixel pitch and fabricated 640x480 format FPAs [49-51]. The noise equivalent temperature difference (NETD) values of these FPAs are less than 50 mK (not precisely given) which shows that the uncooled detectors are going to catch the performances of cooled detectors in the near future. Figure 1.9 gives the SEM pictures of some 17 µm detectors, while

Figure 1.10 gives infrared images taken with FPAs consisting of 17 µm detectors. It is announced that 1024x768 format FPAs will soon be presented [52, 53].




(a) (b)

Figure 1.8: SEM pictures of some example detectors. (a) shows a 50 µm pixel from BAE systems [41] while (b) shows a 25 µm pixel from Raytheon [42].




(a) (b)

Figure 1.9: SEM pictures of some 17 µm detectors. (a) Raytheon's detector [49] (b) DRS's detector [51].




(a) (b)

Figure 1.10: Infrared images taken with FPAs of 17 µm detectors. (a) shows the image from BAE Systems' FPA [50], while (b) shows the image from DRS's FPA [51].

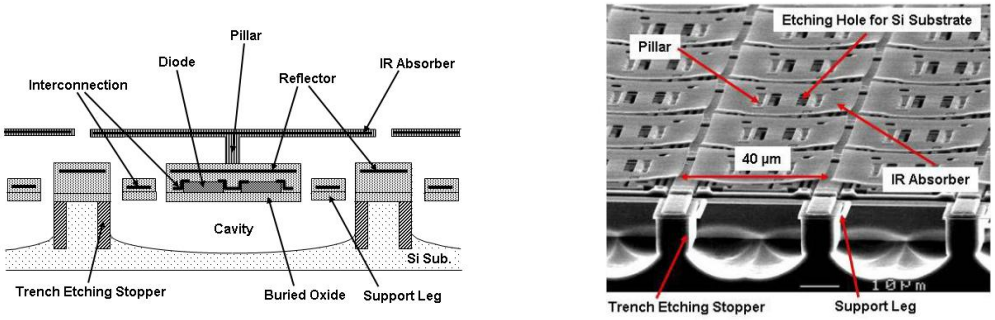
Although $VO_x$ has a high TCR value of 2-3 %/K, it is not a standard material in integrated circuit (IC) fabrication technology, since it is not CMOS line compatible, and it requires dedicated systems for the fabrication process. Also, it is patented, and there are not many process specifications in the literature. Due to these reasons, other materials were tried to be used as resistive element in the detector, including amorphous silicon (a-Si), polycrystalline silicon germanium (poly SiGe), metals, and yttrium barium copper oxide (YBaCuO or YBCO).

Amorphous silicon is a CMOS compatible material with high TCR values like 2-3 %/K, but it requires high temperature annealing processes, making the monolithic integration difficult. But this difficulty can be overcome by process optimizations. Companies and institutions like ULIS, LETI, and Raytheon uses a-Si to fabricate large format uncooled infrared imagers. ULIS has realized 320x240 format FPAs with 50 µm pixel pitch and 640x480 format FPAs with 25 µm pixel pitch. They have also developed detectors with 35 µm pixel pitch as a transition dimension from 50 µm to 25 µm [54-56]. In addition to these FPAs, ULIS also developed 160x120 format FPAs with 25 µm pixel pitch to be used in low-cost applications [57]. Raytheon also fabricated 160x120 format FPAs with a-Si detectors for low cost applications [58].

The other CMOS compatible materials are poly SiGe and metals. Like a-Si, poly SiGe has high TCR value such as 2-3 %/K, but it also requires high temperature annealing making the monolithic integration difficult [18, 59, 60]. It exhibits large 1/f noise and it has internal stress making the array fabrication difficult [22]. There are also efforts to fabricate microbolometers using metal layers such as titanium and platinum [61, 62]. Although metal layers are fully CMOS compatible, they have very low TCR values such as 0.3 %/K, limiting their use in imaging FPAs.

A relatively new material that is used for the fabrication of infrared detectors is YBCO. This material is a superconductor if it is fabricated as a crystal structure. But when it is fabricated as amorphous structure, it behaves as a semiconductor material with a high TCR value of larger than 3 %/K. YBCO is deposited at room temperature and have low 1/f noise making it an attractive choice as a detector material. This material is studied at Mitsubishi Electric Corporation and in University of Texas at Arlington [63-68]. Mitsubishi have demonstrated a 320x240 format FPA with 40 µm pixel size consisting of YBCO detectors.

Apart from the surface micromachined resistive microbolometers, a different approach is to make bulk micromachined diode type microbolometer detectors, where the p-n diode is used as the temperature sensitive element. In these detectors diode forward voltage is affected from the temperature change and this change is readout by the CMOS electronics. Most effort regarding this type of detectors has been spent in Mitsubishi and various detectors having 40 µm and 25 µm pixel pitches and 320x240 and 640x480 format FPAs have been realized [68-70]. These detectors are fabricated in an SOI-CMOS process which makes the cost of the detectors much lower than the other types of the detectors. Figure 1.11 gives the pixel structure and an SEM picture of the fabricated detectors. There have been some efforts regarding diode type microbolometers in METU which will be given in Section 1.4 in detail.




(a) (b)

Figure 1.11: Mitsubishi's diode type microbolometer detectors. (a) pixel structure and (b) an SEM picture (b).

### 1.3.4. Microcantilever Detectors and Other Approaches

In the recent years there are efforts to develop detectors having a cantilever structure. The detectors include two different materials with different bending amounts depending on the temperature change. The detectors can be readout electrostatically or optically [71]. There are difficulties with the process and the uniformities of the detectors, especially due to the internal stress of the materials. When first suggested, the detector arrays would have an NETD of 5 mK. But the published results are above 1 K [72-74].

Another detector that has an optical readout is composed of thermally tunable thin film membranes [75, 76]. A CCD camera is used to readout the output and convert it into image. This approach is reported to be a candidate for low-cost camera applications.

## 1.4. Previous Work on Microbolometers at METU

The microbolometer research started in 1997 at METU. The motivation of the research was to fabricate a very low-cost uncooled infrared imager which can be used in commercial applications. The detectors were fabricated using bulk micromachining technology on CMOS dies. The CMOS die included the detectors and the electronic readout circuit together, allowing the cost of the imager to be as low as a CMOS chip.

The first detectors realized were using the CMOS n-well layer as the resistive detector element. The n-well layer has the highest TCR value of 0.65%/K among the other CMOS layers. The silicon underneath the detector was etched away with an anisotropic silicon etching solution, and the etching of the n-well was prevented by the electrochemical etch-stop technique. First fabricated array was in 16x16 format composed of detectors with 80 μm pixel pitch [34, 77-80]. Figure 1.12 shows the SEM pictures of the successfully fabricated array composed of n-well detectors.

As can be seen from the pictures the fill factor of the detectors is very small. This is due to the fabrication limitations of the design. Also, the effective TCR of the pixel is less than the TCR of the n-well due to the negative effect of the polysilicon resistors at the support arms. In order to increase the fill factor and the performance of the detector, a new structure and fabrication method was developed, and using this method the detectors were fabricated. This method used the $p^+$-active/n-well diode as the detector sensing element. Also, it used the CMOS metal layers as the mask in order to define the etch openings. Several arrays including 64x64 and 128x128 were successfully realized [2, 18, 82-87]. Figure 1.13 shows successfully fabricated array pixels. Although there were successfully fabricated arrays, the post-CMOS process of these pixels was still difficult due to the use of the electrochemical etch-stop process. Another approach which had been tried is the use of the SOI diodes. In this approach there is no need for the

etch-stop because the diodes were on the oxide layer [88]. Arrays of 64x64 composed of this kind of detectors were successfully fabricated. The research on this concept is still continuing.

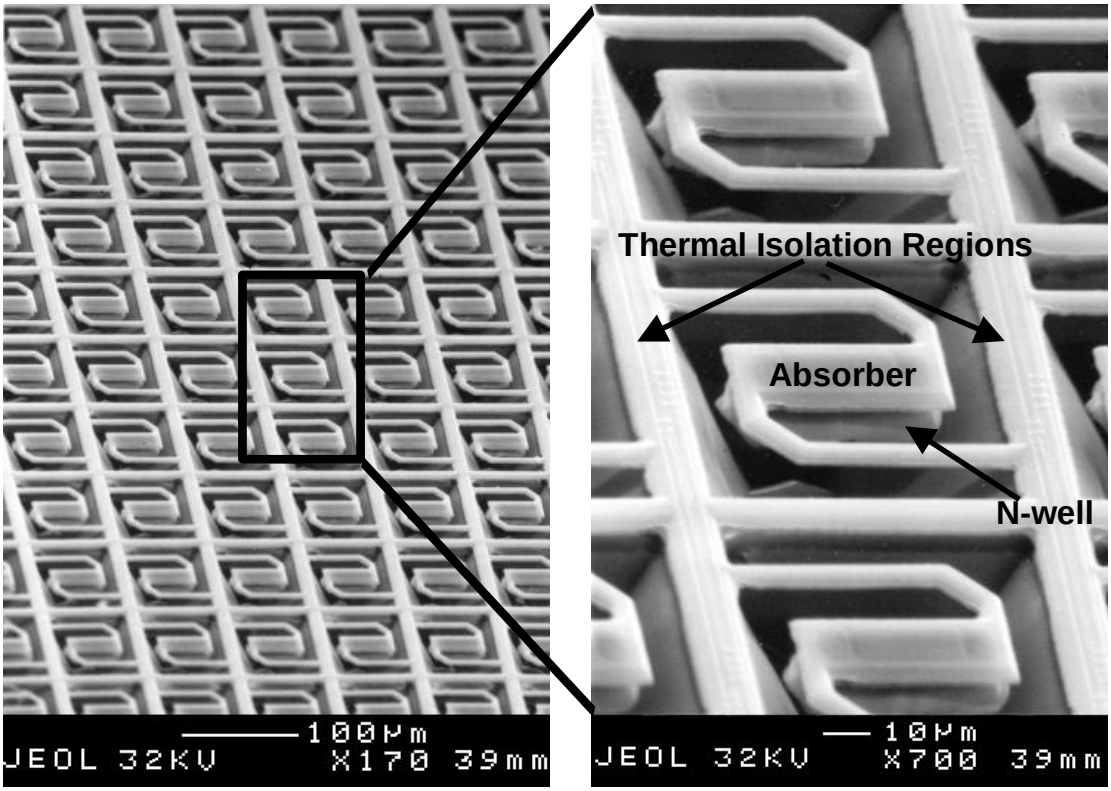
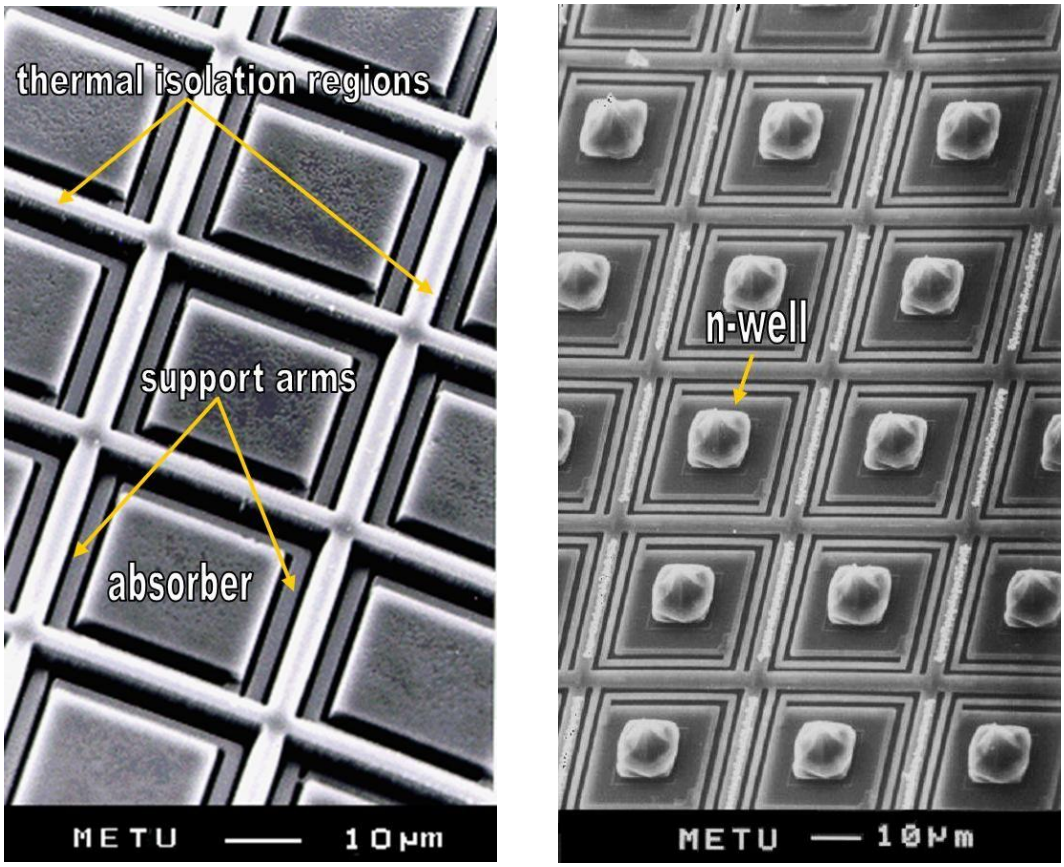



Figure 1.12: SEM picture of the successfully fabricated array composed of n-well detectors.




(a) (b)

Figure 1.13: Successfully fabricated array pixels. (a) shows the top view while (b) shows the bottom view.

Uncooled infrared microbolometer FPAs using the methods above are very promising for the commercial applications where the cost is more important than the performance. This kind of detectors cannot be used in applications requiring high performance imagers such as military applications. So in this Ph. D. study, surface micromachined resistive microbolometer detectors and FPAs are developed in order to be used in applications needing high performance.

## 1.5. Research Objectives and Thesis Organization

The goal of this Ph. D. research is to develop an uncooled infrared microbolometer type detector and focal plane array (FPA) monolithically integrated with its CMOS readout circuit. The FPAs will be fabricated using surface micromachined MEMS technology and will be used in applications requiring high performance. The specific objectives of this research are listed as follows:

1. *Optimization of the detector active material for high performance*. The active material of the detector should be chosen such that it is compatible with the CMOS process i.e., it does not require any high temperature processes. The deposition and the patterning of the active material should not require complex processes. The resistivity of the material should be low enough to achieve desired resistance value and the TCR value of the material should be high enough to be used in a high performance detector. The deposition conditions of the material should be optimized to minimize the resistivity and to maximize the TCR.

2. *Modeling of the detector to increase the performance.* The detector should be designed to have high performance with proper modeling for the performance parameters. The absorptance of the detector should be modeled electromagnetically in order to find the optimum thicknesses of the layers used in the fabrication. Also the detector should be modeled thermally and mechanically in order to determine the thermal isolation of the detector and maximum stress on the support arms, so that the materials are chosen properly.

3. *Development of a fabrication process.* The fabrication process flow of the detectors should be optimized for the fabrication of the designed detectors.

The steps of the process flow should be optimized separately, and the fabrication of the detectors should be completed.

4. *Fabrication of the 320x240 format FPAs and tests.* The fabrication of the 320x240 format FPAs should be completed with the developed process flow monolithically integrated with the CMOS readout circuit. The fabricated FPAs can be used in a system to demonstrate the infrared imaging capability of the FPA.

The organization of this thesis and the contents of the following chapters can be summarized as:

Chapter 2 gives the figure of merits for the uncooled infrared detectors. It gives the definition of the parameters like TCR, thermal conductance, and responsivity. It defines the noise sources in the detector and gives definitions of NETD and detectivity. It also explains the fundamental limitations of the performance of the detectors.

Chapter 3 defines the design cycle of the microbolometer detector. The chapter starts with the selection of the active detector material and the optimization of the electrode structure. The pixel structure optimization is followed by the electromagnetic modeling of the detector and the absorption calculations. Finally the thermal and mechanical simulations are introduced.

Chapter 4 explains the optimization of the process flow. The steps of the process flow are optimized separately. The optimization of the active material is also performed. The pictures of the successfully fabricated detectors are given at the end of the chapter.

Chapter 5 gives the measurement results of the fabricated detectors. The performed measurements are TCR measurements, thermal conductance measurements, noise measurements, and responsivity measurements. The comparison of the measurement results with the expectations is also given.

Chapter 6 presents the fabrication of the 320x240 microbolometer FPA monolithically integrated with the CMOS circuitry. It gives the pictures of the successfully fabricated arrays, and presents the results of the NETD measurements and the first infrared images obtained from the FPA.

Finally, Chapter 7 summarizes the results and the achievements obtained throughout this Ph. D. study, and gives suggestions for the possible future work related to this study.

# CHAPTER 2

# FIGURE OF MERITS FOR UNCOOLED INFRARED DETECTORS

This chapter presents the figure of merits that are used to evaluate the performance of the uncooled infrared detectors, as well as to compare their performances with the cooled detectors. The most important parameters are temperature sensitivity, thermal conductance, responsivity, noise equivalent power, noise equivalent temperature difference, and detectivity. Section 2.1 to Section 2.6 will introduce these parameters and their importance in optimization. Then Section 2.7 will present the fundamental limitations of the uncooled detectors, including temperature fluctuation noise limit and background fluctuation noise limit. Finally, Section 2.8 will summarize the chapter.

## 2.1. Temperature Sensitivity

Temperature sensitivity is the parameter of the uncooled detector which is used to quantify the temperature dependence of the related detector property. For resistive type microbolometers the related property is the resistance of the detector, while for diode type microbolometers, it is the diode voltage. The detailed analysis of the temperature dependence of the diode voltage is given in previous works, so it will not be repeated here [2, 18, 87, 88].

The resistance of the detector changes as the temperature varies. Temperature dependence of the detector resistance is called the temperature coefficient of resistance (TCR), which is given as [9]

$$\alpha = \frac{1}{R}\frac{dR}{dT} \tag{2.1}$$

where $\alpha$ is the TCR of the detector resistance in %/K, $R$ is the detector resistance at the temperature of interest. TCR is a property of the active detector material and can be positive or negative depending on the material used in the detector. Generally metals have positive TCR and semiconductors have negative TCR values [9]. TCR values of the semiconductors depend on the bandgap of the material and can be given as

$$\alpha = -\frac{\Delta E}{\mathrm{kT}^2} \tag{2.2}$$

where $\Delta E$ is the activation energy which is equal to the half of the bandgap, k is the Boltzmann constant, and $\mathrm{T}$ is the temperature of interest.

The absolute value of the TCR of the detector can be increased by the variation of the process conditions of the active material. But the increase in the TCR value can cause undesired changes in resistivity and noise; therefore, TCR, resistivity, and noise of the material should be considered all together during the optimization of the performance parameters.

## 2.2. Thermal Conductance ($G_{th}$)

Thermal conductance ($G_{th}$) is the most important structural parameter that affects the performance of the detector. As explained in Chapter 1, the detectors should be thermally isolated from the substrate which they are fabricated on, in order to

increase their performance. This isolation is determined with the value of thermal conductance. As thermal conductance decreases, the isolation gets better.

There are three components of the total thermal conductance of the detector. These are the thermal conductance of the support arms, thermal conductance of the gas environment surrounding the detector, and radiative thermal conductance. The total thermal conductance can be found with the addition of these components.

Thermal conductance of the support arms ($G_{arm}$) resembles the electrical conductance and is given as

$$G_{arm} = \sigma A/L \tag{2.3}$$

where $\sigma$ is the thermal conductivity of the material used in the support arm, $A$ is the cross sectional area of the support arm, and $L$ is the length of the support arm. Generally, the detectors have more than one support arm, so the value of the conductance of one support arm must be multiplied by the number of the support arms. In addition to this, all of the materials that form the support arm should be taken into account during the calculation of the thermal conductance. Since the thermal isolation gets better as the thermal conductance decreases, materials with low thermal conductivity should be used in the support arms. Also, the cross sectional area should be decreased and the length should be increased as the structure and the process parameters permit.

Radiative thermal conductance ($G_{rad}$) is the loss of heat due to the radiation and is given as [18]

$$G_{rad} = 4A_D\eta\sigma T^3 \tag{2.4}$$

where $A_D$ is the active detector area, $\eta$ is the absorptance of the detector (equivalently emissivity), $\sigma$ is the Stefan's constant, and $T$ is the detector and the surrounding temperature.

Since the detectors are generally used in vacuum conditions, the thermal conductance of the gas environment surrounding the detector becomes negligible. Also, since the radiative thermal conductance is much smaller than the thermal conductance of the support arms, it is often neglected, and the total thermal conductance becomes equal to the thermal conductance of the support arms.

## 2.3. Responsivity

Responsivity is the ratio of the output signal of the detector to the incident infrared radiation. The output of the detector can either be voltage or current depending on the application and readout method; hence, the responsivity is either expressed as Volts/Watt (V/W) or Amps/Watt (A/W).

Figure 2.1 shows the thermal analogue circuit for a microbolometer detector with thermal conductance $G_{th}$ and thermal capacitance $C_{th}$. The infrared power is equivalent to a modulated current source with a modulation frequency of $\omega$. The absorbed infrared power is $\eta P_{0,}$ where $P_0$ is the incident infrared power and $\eta$ is the absorptance of the detector.

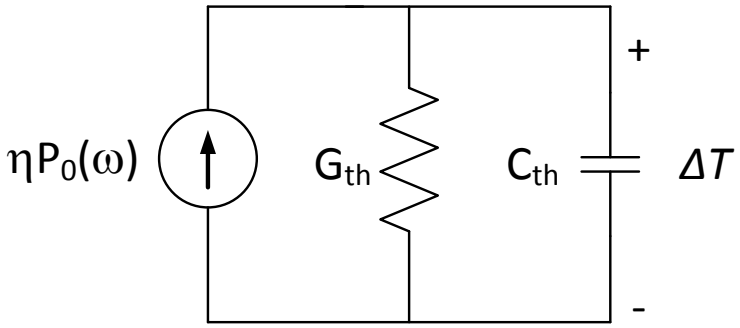



Figure 2.1: Thermal analogue circuit for a microbolometer detector with thermal conductance $G_{th}$ and thermal capacitance $C_{th}$.

From the circuit, the temperature change $(\Delta T)$ on the microbolometer can be written as

$$\Delta T = \frac{\eta P_0}{G_{th}\sqrt{1+(\omega\tau)^2}} \tag{2.5}$$

where $\eta$ is the absorptance of the detector, $P_0$ is the incident infrared power, $G_{th}$ is the thermal conductance of the detector, $\omega$ is the modulation frequency of the infrared power, and $\tau$ is the thermal time constant of the detector which is expressed as

$$\tau = \frac{C_{th}}{G_{th}} \tag{2.6}$$

where $C_{th}$ and $G_{th}$ are the thermal capacitance and thermal conductance of the detector, respectively. For a current biased microbolometer detector, the change in the output voltage $(\Delta V)$ is given as

$$\Delta V = I_d \Delta R = I_d \alpha R_d \Delta T \tag{2.7}$$

where $\alpha$ is the TCR of the detector, $R_d$ is the detector resistance, $I_d$ is the bias current of the detector, and $\Delta T$ is the temperature change. On the other hand, if

the detector is biased with voltage, the change in the detector current ($\Delta I$) is given as

$$\Delta I = \frac{V_d}{R_d} - \frac{V_d}{R_d - \alpha R_d \Delta T} \approx -\frac{V_d}{R_d}\alpha \Delta T \tag{2.8}$$

where $V_d$ is the bias voltage of the detector, $\alpha$ is the TCR of the detector, $R_d$ is the detector resistance, and $\Delta T$ is the temperature change. Then the voltage responsivity ($\Re_V$) and current responsivity ($\Re_I$) of the detector are expressed as

$$\Re_V = \frac{\Delta V}{P_0} = \frac{\eta I_d \alpha R_d}{G_{th}\sqrt{1 + (\omega\tau)^2}} \tag{2.9}$$

$$\Re_I = \frac{\Delta I}{P_0} = \frac{V_d \alpha \eta}{R_d G_{th}\sqrt{1 + (\omega\tau)^2}} \tag{2.10}$$

As can be seen from Equations 2.9 and 2.10, the responsivity of the detector is proportional to absorption coefficient, bias parameter, and TCR; while it is inversely proportional to thermal conductance. So, in order to maximize the responsivity, bias, TCR, and absorptance should be increased while $G_{th}$ should be decreased.

## 2.4. Noise Equivalent Power (NEP)

The noise equivalent power (NEP) is the power incident on the detector that produces an output signal equal to the total root-mean-square (rms) noise of the detector. NEP is expressed in units of Watts (W) and given as

$$NEP = \frac{V_n}{\Re_V} \tag{2.11}$$

where $V_n$ is the total rms noise voltage, and $\Re_V$ is the voltage responsivity of the detector. NEP value of a detector should be accompanied by the electrical bandwidth and the refresh rate of the system [18].

There are four noise sources for a resistive microbolometer detector [32]. These are thermal (Johnson) noise, flicker noise (1/f power law noise), temperature fluctuation noise, and background fluctuation noise.

Thermal (Johnson) noise occurs due to the thermal agitation of the charge carriers in a resistor. This noise source can either be expressed in voltage or current form depending on the readout method of the detector. The rms thermal noise voltage $(V_{n,th})$ is given as

$$V_{n,th} = \sqrt{4kTR_dB} \tag{2.12}$$

where $k$ is the Boltzmann constant, $T$ is the temperature in K, $R_d$ is the detector resistance, and $B$ is the electrical bandwidth of the system. It should be noted that thermal noise exist under both bias and no-bias conditions and has a flat characteristics (white noise) over the entire band.

The second noise source, i.e., the *flicker noise*, occurs due to various reasons all of which depend on the detector material properties. The rms value of flicker noise $V_{n,1/f}$ is given by the expression [32]

$$V_{n,1/f} = \sqrt{\int_B \frac{V_d^2 n}{f} df} = \sqrt{V_d^2 n ln\left(\frac{f_2}{f_1}\right)} \tag{2.13}$$

where $V_d$ is the detector voltage, $B$ is electrical bandwidth, $f_1$ and $f_2$ are the lower and upper frequency limits of the electrical bandwidth, respectively, and $n$ is the 1/f noise parameter. There is no analytical expression for the 1/f noise parameter, but

it is known that it strongly depends on the deposition techniques and dimensions of the detector material, electrical contacts, etc. It should be noted that flicker noise exists under bias conditions, and it is zero if there is no bias on the detector.

The third noise source is the *temperature fluctuation noise* which originates from the random fluctuations in the temperature of the detector. These fluctuations occur since the detector is in contact with the environment by means of conduction and radiation [32]. The rms value of temperature fluctuation noise ($V_{n,TF}$) is given as [32]

$$V_{n,TF} = \Re_V \sqrt{\frac{4kTG_{th}}{\eta}} \tag{2.14}$$

where $\Re_V$ is the voltage responsivity, $k$ is the Boltzmann constant, $T$ is the temperature, $G_{th}$ is the thermal conductance, and $\eta$ is the absorptance of the detector.

The fourth and the last noise source is *background fluctuation noise* generated by the random fluctuations in the radiation power incident on the detector from the environment and the fluctuations in the radiation emitted by the detector itself. The rms value of this noise ($V_{n,BF}$) is given by

$$V_{n,BF} = \Re_V \sqrt{8A_D\eta\sigma k(T_D^5 + T_B^5)} \tag{2.15}$$

where $\Re_V$ is the voltage responsivity, $A_D$ is the active detector area, $\eta$ is the absorption coefficient of the detector, $\sigma$ is the Stefan's constant, $k$ is the Boltzmann constant, $T_D$ is the temperature of the detector, and $T_B$ is the background temperature.

Considering all these noise sources the total rms noise voltage becomes

$$V_n = \sqrt{V_{th}^2 + V_{1/f}^2 + V_{TF}^2 + V_{BF}^2} \tag{2.16}$$

In state of the art detectors thermal noise and flicker noise are dominant compared to other noise sources. So, only thermal noise and flicker noise are generally taken into account during the performance calculations of the detectors.

## 2.5. Noise Equivalent Temperature Difference (NETD)

Noise equivalent temperature difference is the temperature change in the target that generates a signal at the output of the detector which is equal to the total rms noise. NETD is a performance parameter of the focal plane array which also includes the information about the optics. It has the unit of K and can be expressed as [32]

$$NETD = \frac{4F^2 V_n}{\tau_o A_D \Re_V (\Delta P/\Delta T)_{\lambda_1-\lambda_2}} \tag{2.17}$$

where $V_n$ is the total rms noise voltage, $\tau_o$ is the transmission of the optics, $A_D$ is the active detector area, $\Re_V$ is the voltage responsivity of the detector, $(\Delta P/\Delta T)_{\lambda_1-\lambda_2}$is the change of power per unit area radiated by a blackbody at temperature T, measured within the spectral band of $\lambda_1$- $\lambda_2$, and $F$ is a function of distance from the optics to the target. When the target is at infinity, $F$ can be found from the expression

$$4F^2 = 4(f/D)^2 + 1 \tag{2.18}$$

where $f$ is the focal length of the optics and $D$ is the diameter of the optics. For an f/1 optic, i.e., $(f/D)$ ratio is equal to 1, $4F^2$ is taken as 5 in the NETD calculations. For 8-14 µm spectral band interval, the parameter $(\Delta P/\Delta T)_{\lambda_1-\lambda_2}$ for a 295 K blackbody is given as

$$(\Delta P/\Delta T)_{\lambda_1-\lambda_2} = 2.62 \times 10^{-4} \frac{W}{cm^2 K} \tag{2.19}$$

NETD is one of the important parameters that indicate the performance of different focal plane arrays. A small NETD shows that the detector can sense very small temperature variations in the target. In order to obtain such small NETD values, the noise of the detector should be decreased, while the responsivity and the active detector area should be increased. Also the $F$ parameter of the optics can be decreased in order to have lower NETD values. But one should know that, as the $F$ parameter decreases the dimensions of the optics get larger.

## 2.6. Detectivity (D*)

Detectivity is a parameter which is used to compare the performances of different types of detectors having varying pixel sizes and different scanning rates. Detectivity has the unit of $cm\sqrt{Hz}/W$ and given as

$$D^* = \frac{\Re_V \sqrt{A_D B}}{V_n} = \frac{\sqrt{A_D B}}{NEP} \tag{2.20}$$

where $\Re_V$ is the voltage responsivity of the detector, $A_D$ is the active detector area, $B$ is the electrical bandwidth of the system, $V_n$ is the total rms noise voltage, $NEP$ is the noise equivalent power of the detector.

There are two ways to express detectivity; one of them is spectral detectivity ($D^*_\lambda$) while the second one is blackbody detectivity (D*(T), where T is the blackbody temperature) [32]. These expressions are important, since the detectivity of the cooled detectors depend on the wavelength. So, while giving the detectivity of the cooled detectors, the wavelength of interest should be indicated. For the uncooled detectors, the detectivity is relatively independent of the wavelength, so the detectivity is simply denoted by D*. But in reality, it is needed to indicate the

blackbody temperature during the presentation of D*, due to the spectral absorptance property of the uncooled detectors.

## 2.7. Fundamental Limitations

The performance of the uncooled detectors is limited by the thermal fluctuation noise and background fluctuation noise, independent of their detection mechanism. [32, 106-108]. These limits appear due to the statistical nature of the incident infrared radiation. The detailed expressions of the thermal fluctuation noise and background fluctuation noise are given in Section 2.4. Considering these expressions the temperature fluctuation noise limited NETD ($NETD_{TF}$) and background fluctuation noise limited NETD ($NETD_{BF}$) can be written as

$$NETD_{TF} = \frac{8F^2 T_D \sqrt{kG_{th}B}}{\tau_o A_D \eta (\Delta P/\Delta T)_{\lambda_1-\lambda_2}} \tag{2.21}$$

$$NETD_{BF} = \frac{8F^2 \sqrt{2\sigma kB(T_D^5 + T_B^5)}}{\tau_o \sqrt{A_D \eta} (\Delta P/\Delta T)_{\lambda_1-\lambda_2}} \tag{2.22}$$

where $\tau_o$ is the transmission of the optics, $A_D$ is the active detector area, $(\Delta P/\Delta T)_{\lambda_1-\lambda_2}$ is the change of power per unit area radiated by a blackbody at temperature T, measured within the spectral band of $\lambda_1$- $\lambda_2$, $F$ is a function of distance from the optics to the target, $k$ is the Boltzmann constant, $G_{th}$ is the thermal conductance, $\eta$ is the absorptance of the detector, $\sigma$ is the Stefan's constant, $T_D$ is the temperature of the detector, and $T_B$ is the background temperature. For the detectors to achieve background fluctuation noise limit, the thermal conductance value of the detectors should be decreased below the radiation thermal conductance value. So the state of the art detectors are limited with temperature fluctuation noise.

## 2.8. Conclusions

This chapter briefly presented the figure of merits for the evaluation of the performance of the uncooled infrared detectors, as well as to compare the performance with the cooled detectors. The presented parameters are temperature sensitivity, thermal conductance, responsivity, noise equivalent power, noise equivalent temperature difference, and detectivity. The fundamental limitations of the uncooled detectors, including temperature fluctuation noise limit and background fluctuation noise limit are briefly explained. It is concluded that state of the art detectors are limited with the temperature fluctuation noise limit.

# CHAPTER 3

# DESIGN OF THE MICROBOLOMETER PIXEL

This chapter presents the structural design and optimization the microbolometer detector pixel, which is a resistive type microbolometer fabricated using the surface micromachined MEMS technology. Section 3.1 presents the determination of the active detector material while Section 3.2 gives the simulations for the optimum resistor value and the optimization of the electrode structure. Section 3.3 presents the optimization of the pixel pitch and structure of the detector pixel, while Section 3.4 tells the absorption optimization, where the thicknesses of the layers are the major parameters. Section 3.5 and Section 3.6 summarize the thermal and mechanical simulations of the detector. Finally, Section 3.7 summarizes the results of the optimizations and simulations and concludes the chapter.

## 3.1. Determination of the Active Detector Material

The active material is the most crucial part of the microbolometer detector. It should be chosen before the structural design of the detector pixel, since the properties of this material affect the design considerations. There are various properties that should be considered during the choice of the active material. The most important properties of the layer are its resistivity, TCR and the noise value. Resistivity value of the material is important because the material should be suitable to be used in the designed resistor value. The TCR value of the material should be as high as possible, while the noise value should be low for the detector to have high performance. In addition to these properties, the process of active

material should not require complex steps, and it should not affect the other parts of the detector.

It is stated in Chapter 1 that the companies and research centers are focused mainly on four materials as the active material of the microbolometer detectors: $VO_x$, a-Si, poly SiGe, and metals. $VO_x$ is not a standard material in IC fabrication technology and is not CMOS compatible, and it requires dedicated systems for the fabrication process. Also since it is patented, there are not many process specifications about $VO_x$ in the literature. The next two materials, a-Si and poly SiGe require high temperature annealing processes making the CMOS integration difficult. The last group of material which is the metals is compatible with CMOS process but has very low TCR value when compared to the other materials and not suitable to be used in high performance detectors. Due to these drawbacks none of these materials were chosen as the first choice of active microbolometer material.

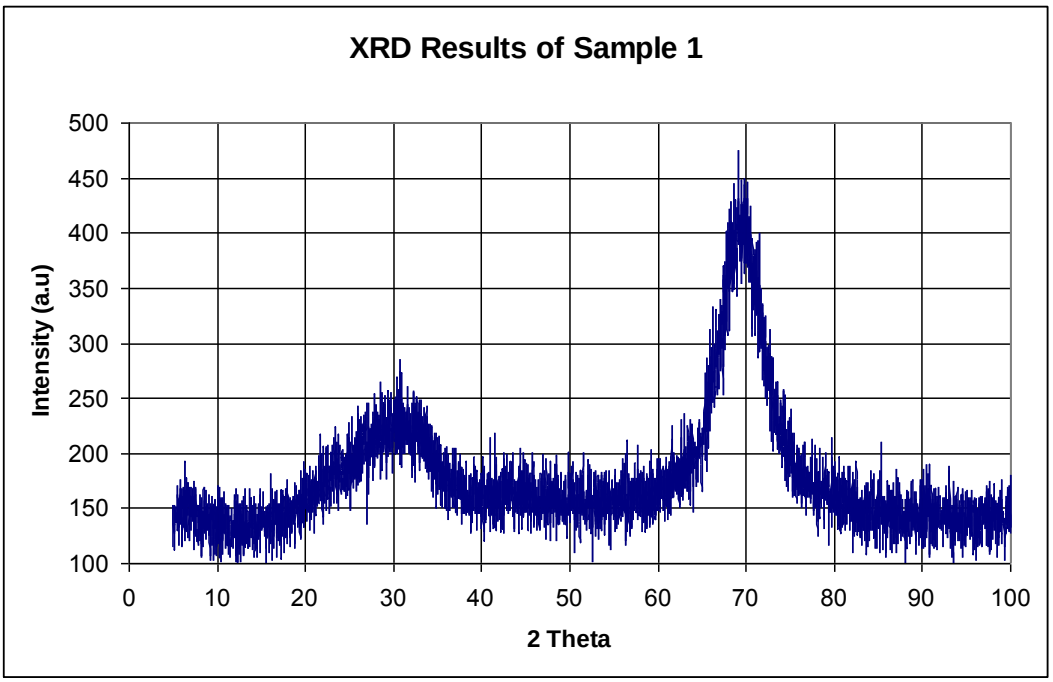
The other material that is being used in the microbolometers is YBaCuO (YBCO) material. The data for this material given in literature shows that it has a TCR value of ~3%/K, which is higher than the other materials [63-67]. The growth of the material is performed by standard RF sputtering techniques at room temperature not requiring high temperatures, and the patterning of this material is performed in diluted aluminum etchant easily. It also exhibits low 1/f noise, making it suitable to be used in high performance microbolometer detectors. Due to these advantages YBCO has become the first choice to be used in the detectors throughout this study.

There are mainly one company (namely Mitsubishi Inc.) and one research center (namely University of Texas at Arlington) working on YBCO as microbolometer material [63-67]. As YBCO became the first choice for the active material, both institutions were contacted to make cooperation to expedite the research. Mitsubishi Inc. could not help us since they were working on this material for defense purposes, but UTA accepted the cooperation and send two YBCO coated

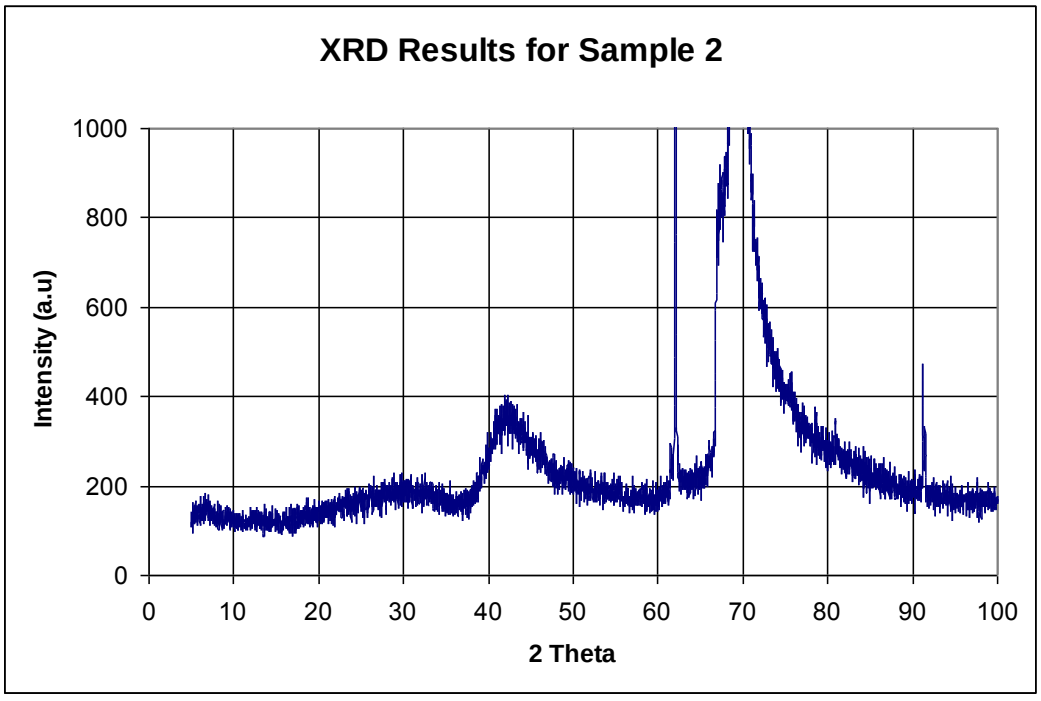
wafers for analysis and measurements. Several tests were performed on the samples from these wafers in order to understand whether the material can be used as the active material in our detectors.

The first test that had been performed on the samples is the x-ray diffraction (XRD) analysis. This analysis is performed in order to understand whether the material is amorphous or not. This is important because in order this material to be used as a high TCR microbolometer material, it should be amorphous [63]. Figure 3.1 shows the XRD test results of the two samples taken from the sample wafers that UTA has sent. From the measurements it is found that the material on both of the wafers is amorphous as desired. The result is also in accordance with the data in literature.

The second test that had been performed is the TCR test, which has been carried out with the resistors fabricated using pieces from the wafers. The YBCO material is patterned using diluted aluminum (Al) etchant, and gold is evaporated onto the patterned YBCO structures. Gold is used as the contact material because it is one of the materials that make ohmic contact with YBCO material (the other two are platinum and silver) [89]. The TCR measurements are carried out in the environmental chamber whose temperature can be adjusted. The details of the test setup are given in Section 5.1. Figure 3.2 shows the resistance variation of a 570 kΩ YBCO resistor with the varying temperature. The measured results are fit into a third order polynomial and the TCR value of the resistor is found as -2.9 %/K at room temperature. This value is a bit lower than the reported values in literature [63-67], probably due to the adhesion problem of gold to YBCO layer. This adhesion problem causes the formation of contact resistances between gold and YBCO, decreasing the TCR of the resistor. It is considered that this TCR value can further increase when the adhesion and the contacts are improved.




(a)




(b)

Figure 3.1: The XRD test results obtained from the samples taken from UTA. From the measurements it is found that the material on both of the wafers is amorphous as desired.

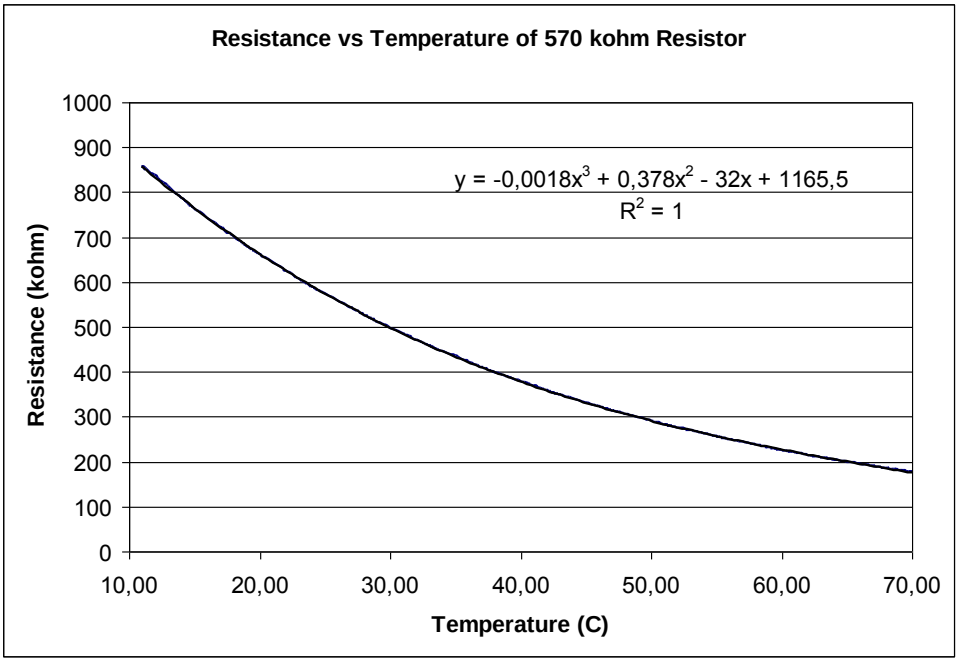



Figure 3.2: The resistance variation of a 570 kΩ YBCO resistor with the varying temperature. The measured results are fit into a third order polynomial and the TCR value of the resistor is found as -2.9 %/K at room temperature.

The third test was the noise measurement of the fabricated resistors. Noise is one of the key parameters that affect the performance of the detectors. Although the detector noise has many components as given in Chapter 2, two of them are the most dominant among the others especially when the resistor is not suspended. These components are the thermal noise (Johnson noise) and the 1/f noise. Having a low 1/f noise value is one of the advantages of YBCO material when compared to a-Si and poly Si-Ge. Figure 3.3 shows the noise measurement results of the YBCO resistor at different bias currents. The noise is measured with the technique suggested in [18]. The measurement without bias application is very close to the theoretical value which is in fact the thermal noise of the resistor. For the biases 0.61 μA and 1.24 μA the 1/f corner frequencies are 40 Hz and 100 Hz, respectively. The contact resistance problem also affects the noise characteristics of the resistor and there will be an improvement in 1/f noise characteristics of the resistors when the contact problem is solved. The noise measurements together with the other

measurements show that this material can be used as the active detector material in the microbolometers.

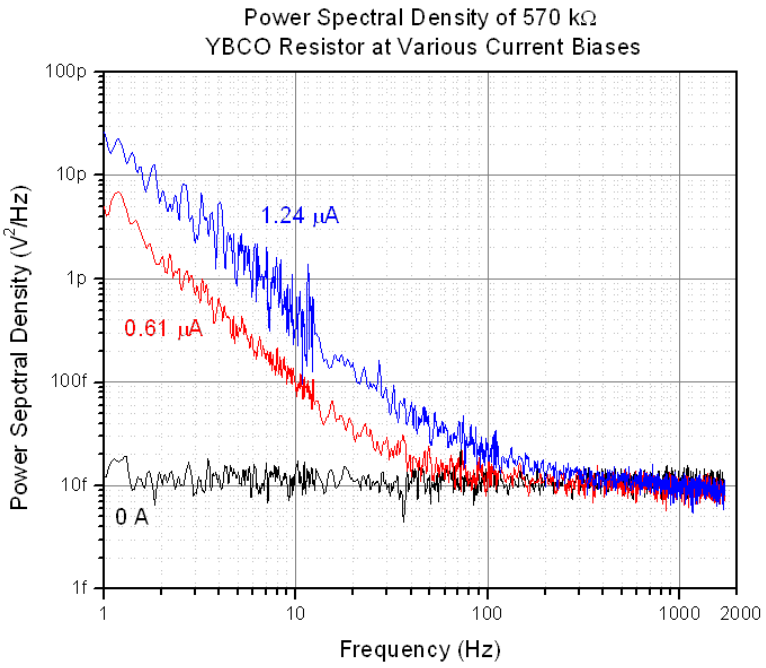



Figure 3.3: The noise measurement results of the YBCO resistor at different bias currents. 1/f noise corner frequencies are found as 40 Hz and 100 Hz at 0.61 µA and 1.24 µA, respectively.

As the part of the cooperation, the author went to UTA laboratories to gain an experience on the growth of YBCO material and fabrication of microbolometer detectors. He studied there under the supervision of Prof. Dr. Zeynep Çelik-Butler and Prof. Dr. Donald Butler for four months. During this study he joined the fabrication steps of the microbolometers and the measurements performed with the fabricated detectors.

## 3.2. Detector Resistance Value and Structure

The resistance value is another parameter that affects the performance of the detector and should be optimized. Chapter 2 explains the effects of this value on the performance parameters such as responsivity, NETD, and detectivity. When the expressions of these performance parameters are investigated, it can be seen that the resistance value affects these parameters in a similar manner. For simplicity only NETD value will be considered in the resistance value optimization simulations. During the simulations the structural parameters of the detector are fixed at some generic values [9]. The pixel size is taken as 50 µm x 50 µm, the fill factor is 70 %, the thermal conductance is 1 x $10^{-7}$ W/K, thermal time constant is 10 ms, the absorptance is 0.5, and the bias voltage is 2 V. The electrical bandwidth is 4.8 kHz that the detectors are in an array of 320 x 240 format and the noise of the readout is assumed to be 100 pA rms. Figure 3.4 shows the change of NETD with the changing resistance value. As can be seen from the figure NETD value decreases as the resistance value is reduced. This means that the resistivity of the active material should be as low as possible to be able to decrease the resistance value. Together with the resistivity the structure of the contact electrodes is also important to decrease the resistance value.

Another effect in the resistance optimizations is the *self-heating effect* which is the heating of the detector due to the electrical bias power. The detector heats up due to the applied electrical bias, and assuming constant voltage bias, this effect increases as the resistance value of the detector decreases. In order to distinguish self-heating from the effect of infrared power, it should be cancelled by a *reference detector,* which has the same electrical properties with the normal detector and is infrared blind. In Figure 3.4 it is assumed that this effect is totally cancelled. But practically, this effect cannot be totally cancelled, and for low resistance values the bias voltage should be decreased in order for the readout circuit not to be *saturated*. Figure 3.5 shows the change of NETD value with the changing resistance

when the self-heating effect is partially cancelled. As can be seen from the figure NETD value becomes minimum at 100 kΩ resistance value, which depends on the self-heating cancellation ratio determined by the properties of the reference detector. For the resistance values larger than 100 kΩ, the self-heating effect is low enough and it can be totally cancelled for maximum bias voltage. However, the resistance values smaller than 100 kΩ should be biased with smaller voltages in order to decrease the self-heating effect. It should be noted that, the resistivity of the active material should be optimized in order to get this resistance value.

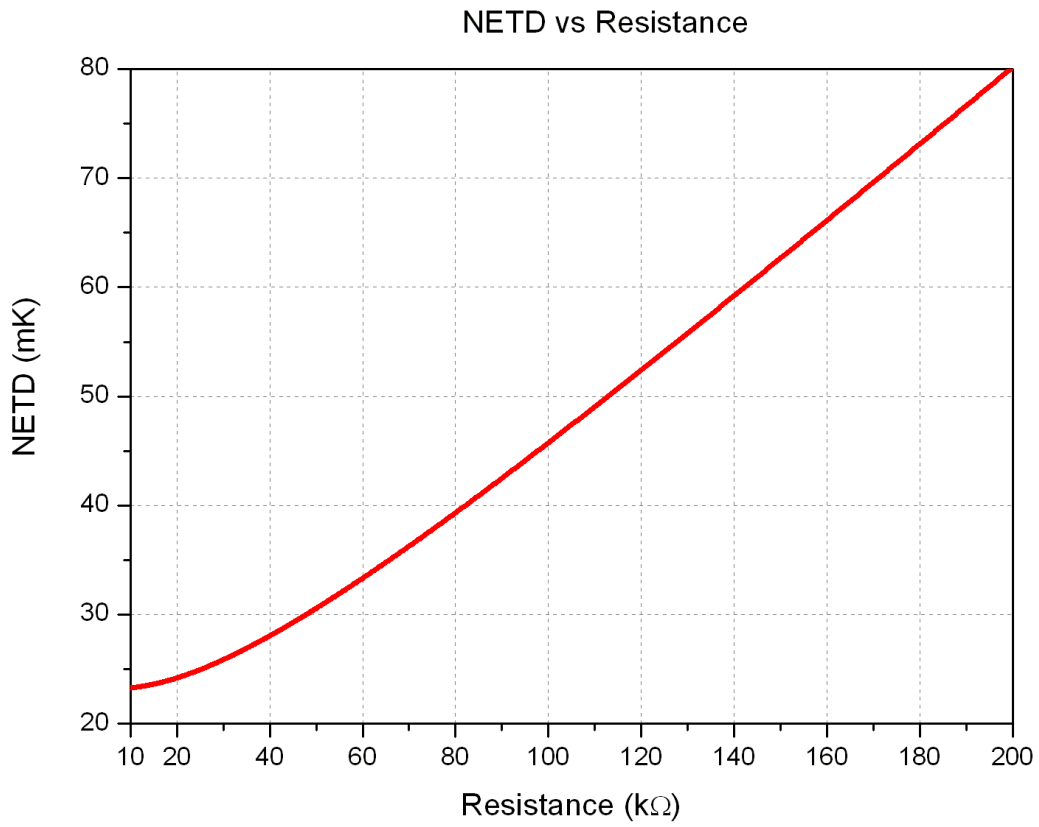



Figure 3.4: The change of NETD with the changing resistance value when the self-heating of the detector is totally cancelled. NETD value decreases as the resistance value is reduced.

The resistivity value of the YBCO material depends on the amount of the oxygen content, and is generally high. For this reason structure of the contact electrodes should be designed in order to decrease the resistance value of the detector. In the designed structure, the length of the resistor should be decreased while the width of the resistance should be increased. Figure 3.6 shows the top view and the perspective view of the designed *finger* type electrode structure [67, 90]. The distance between the electrodes determines the length of the resistor (L), while the total length of the fingers determines the width of the resistor (W). The resistivity values obtained during the process optimizations show that the W/L ratio of the detector resistance should be made as large as possible in order to obtain a resistance of 100 kΩ. The process optimizations will be explained in detail in Chapter 4.

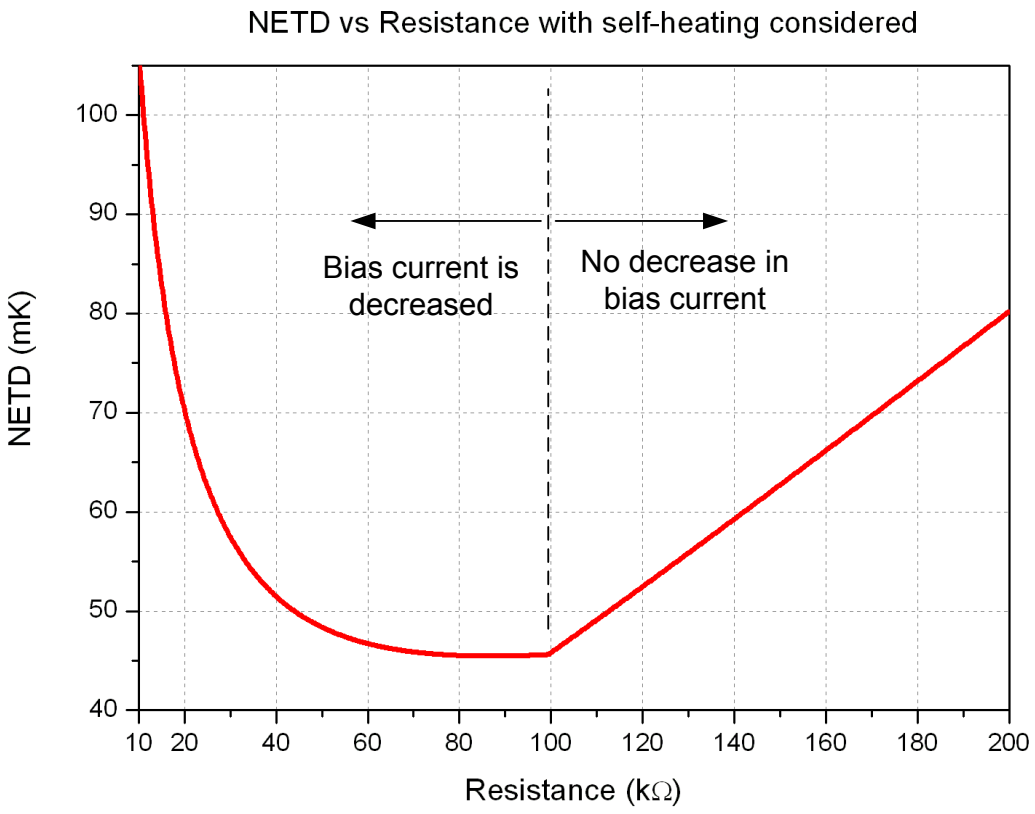



Figure 3.5: The change of NETD value with the changing resistance when the self-heating effect is partially cancelled.

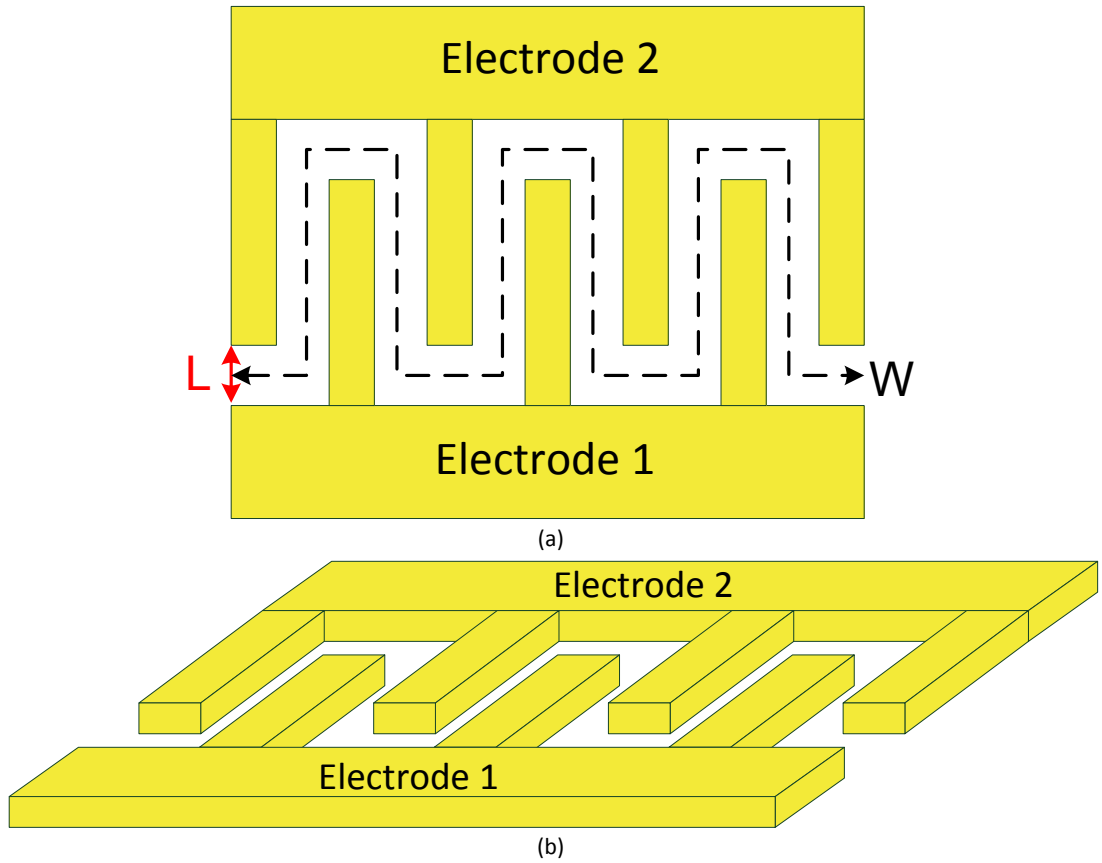



Figure 3.6: The designed finger type electrode structure; (a) top view and (b) the perspective view. The distance between the electrodes determines the length of the resistor (L), while the total length of the fingers determines the width of the resistor (W).

## 3.3. Structure of the Detector and Pixel Size

Structure of the detector and the pixel size are essential parameters that must be optimized during the design of a microbolometer detector. There are mainly two criteria for the structure of the detector: 1) the bridge that the active material lies on should be thermally isolated from the substrate and 2) the support arms should carry the bridge without buckling. Apart from the detector structure, pixel size is mainly determined by the process specifications and the performance requirements of the application. Pixel size directly affects the format of the FPA that will be fabricated. If the pixel size increases large format FPAs cannot be realized.

For the optimization of the structure the most important issue is to maximize the thermal isolation of the detector. As stated in Chapter 2, the thermal conductance determines the amount of the thermal isolation of the detector from substrate. This value should be as low as possible for better thermal isolation. This can be achieved by long and thin support arms. But when the length increases and thickness decreases, the support arms become weaker, and it gets difficult to carry the active part of the detector without buckling. Also, when the support arms get longer, the *fill factor* of the detector decreases i.e., the area of the active part of the detector decreases. Figure 3.7 shows the top view of some different detector structures. The important variables are given in Figure 3.7 (a) as pixel pitch, support arm width, spacing, and active area. As the pixel pitch increases the length of the support arm and the active area can increase. But having large pixel sizes prevents fabrication of large format arrays due to process limitations and yield considerations. If the support arm width and spacing increase, the active area and support arm length decreases resulting in an increase in thermal conductance and a decrease in fill factor. The structure in Figure 3.7 (b) has short support arms resulting in high thermal conductance while the structure in Figure 3.7 (c) has small active area and more difficult fabrication process. The general trend in the literature is to design microbolometer detectors having the structure given in Figure 3.7 (a) [37, 39, 41]. So the optimizations are performed based on this structure.

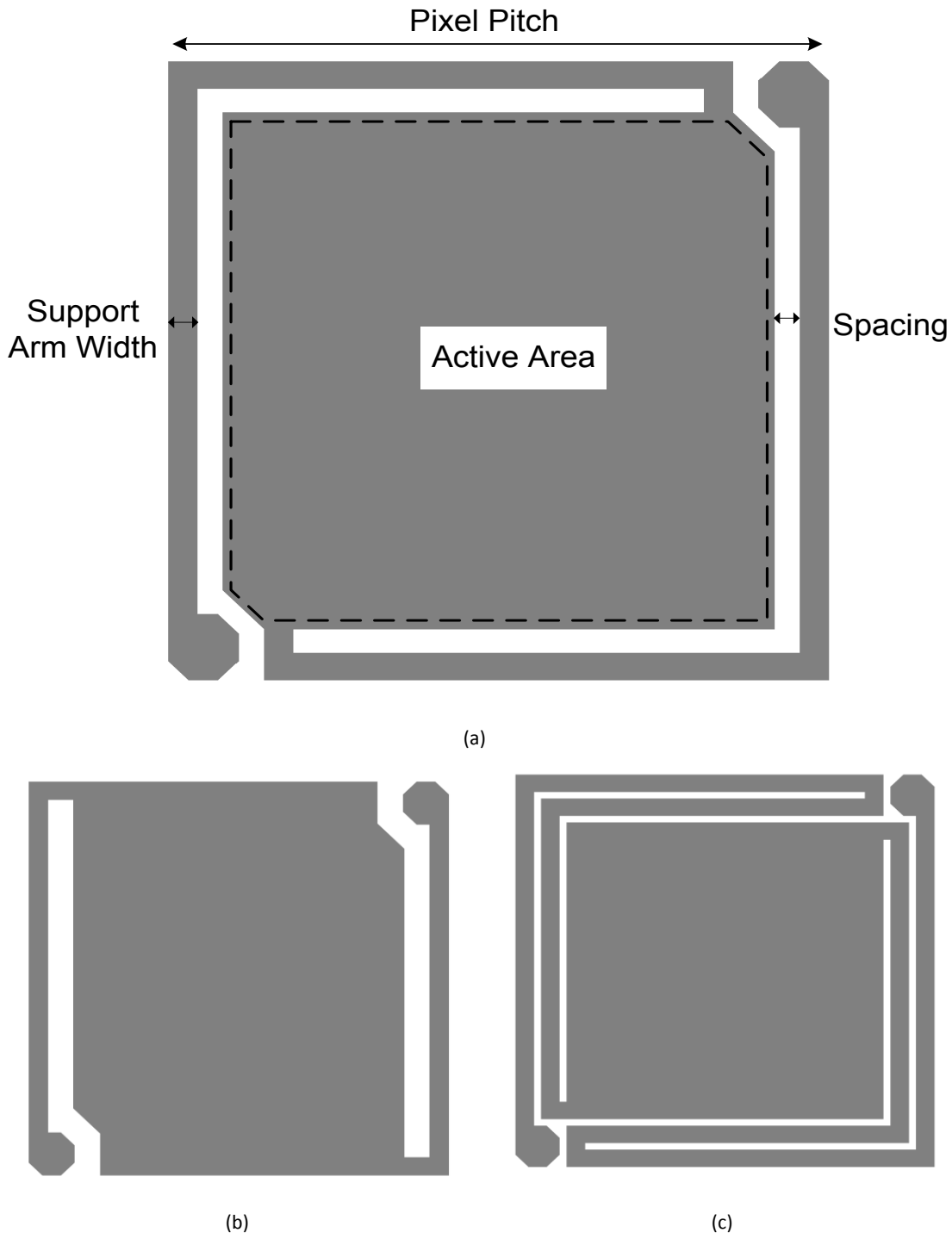



Figure 3.7: Top view of some different detector structures. The important variables are given in (a) as pixel pitch, support arm width, spacing, and active area.

The support arm width and the spacing are determined by the minimum feature size and accuracy of the fabrication process, resulting in a limitation for the maximum achievable detector performance. However, the pixel pitch of the detector can be minimized to have an NETD value proper for high performance applications. Figure 3.8 gives the variation of NETD with the pixel pitch for different minimum feature size values. In this simulation only the structural dimensions are changed according to the minimum feature size. As can be seen from the figure, for the small pixel sizes the NETD value becomes very high due to the decreased active area and increased thermal conductance. This shows that for the small pixel sizes different microbolometer structures should be designed as explained in Chapter 7. For the minimum feature size of 1.5 µm, which is the value in METU-MET facilities especially due to wet etching, the optimum pixel size is found to be larger than 45 µm if the maximum NETD limit is set to 100 mK. There are two other constraints which should be considered during the selection of the pixel size: the restriction of maximum reticle size in CMOS technologies and the image size of standard f/1 objectives. The maximum reticle size in the XFAB 0.6 µm CMOS technology is 19.5 x 19.5 $mm^2$ [97], while the image diagonal size of the standard f/1 objectives is 21 mm [98]. As a result the pixel size is chosen as 50 µm considering that the final target is to fabricate a 320x240 format microbolometer FPA on CMOS readout circuits, as stated in Chapter 1. Figure 3.9 shows the layout of the designed microbolometer detector pixel (*pixel_v1*). The metal interconnects on the support arms, the spacing and the finger size of the electrodes are designed to be 1.5 µm, which is the minimum feature size in our facilities as mentioned above. The finger type electrode structure is made as large as possible to decrease the resistance value.

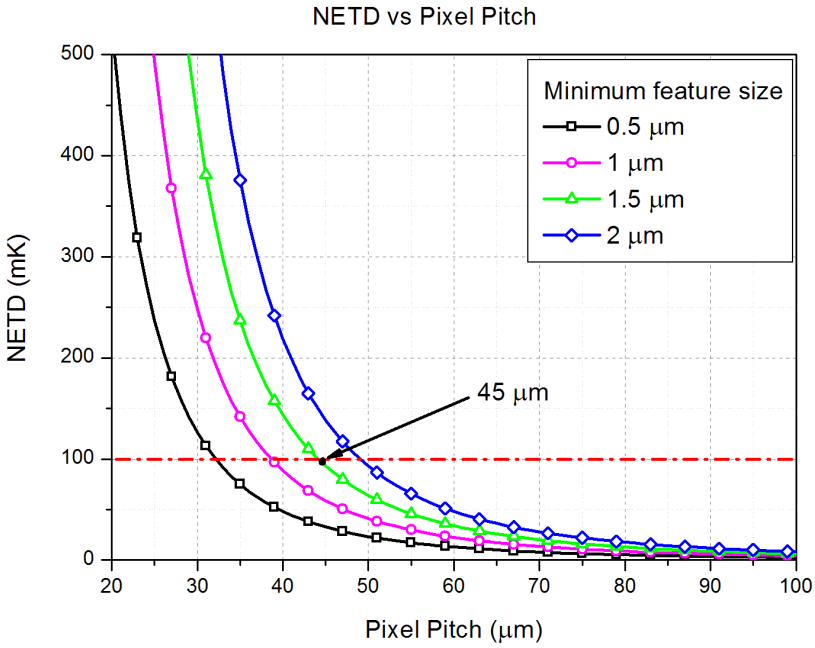



Figure 3.8: The variation of NETD with the pixel pitch for different minimum feature sizes. In this simulation only the structural dimensions are changed according to the minimum feature size.

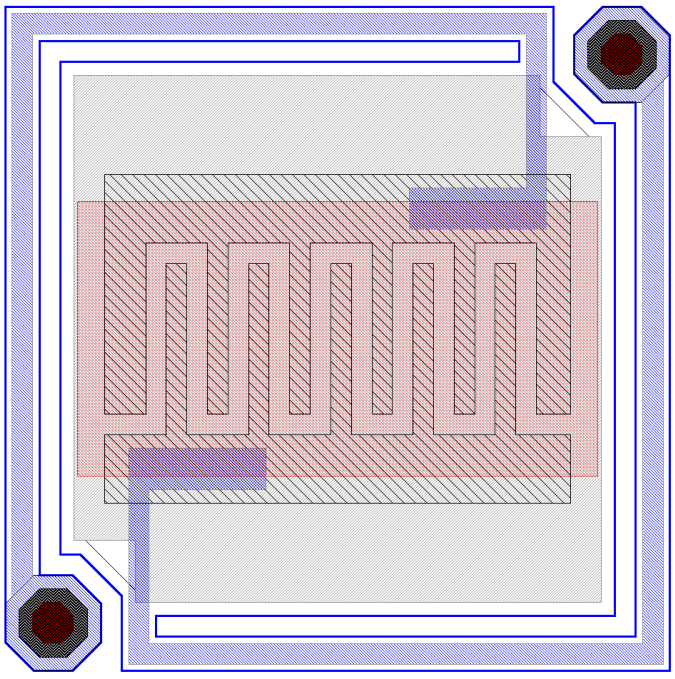


Figure 3.9: The layout of the designed microbolometer detector pixel. The metal interconnects on the support arms, the spacing and the finger size of the electrodes are designed to be 1.5 μm which is the minimum feature size in our facilities.

## 3.4. Absorption Calculations of the Detector

Infrared radiation is a part of electromagnetic spectrum as described in Chapter 1. For this reason electromagnetic laws can be applied to infrared detectors. Structures having multiple layers on top of each other can be modeled as cascaded transmission lines (CTL) [91, 92]. The CTL model approach can be applied to microbolometer detectors since they are composed of many layers each of which can be modeled as a transmission line. Figure 3.10 shows a representative perspective view of a part of a microbolometer detector and its transmission line model. The microbolometer structure includes an absorber layer, structural layers, active material, cavity, and a reflector metal.

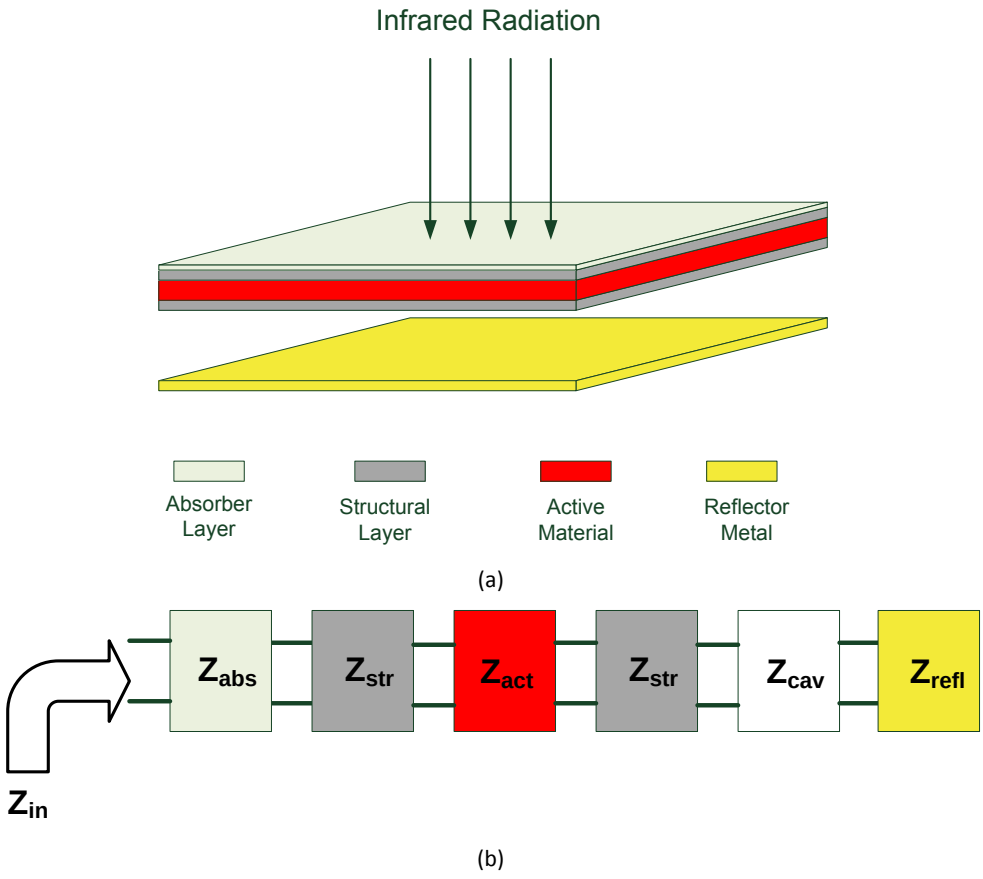



Figure 3.10: Representative perspective view of a part of a microbolometer detector (a) and its transmission line model (b).

### 3.4.1. Theory

In the transmission line model, every layer is represented by its characteristic impedance. The characteristic impedance of the free space is 377 Ω, while the characteristic impedance of a general lossy medium ($Z_0$) is given by [93]

$$Z_0 = \frac{j\omega\mu}{\gamma} \tag{3.1}$$

where $\omega$ is the radial frequency of the incident radiation, $\mu$ is the permeability of the medium which is equal to the permeability of free space for non-magnetic materials, $\gamma$ is the complex propagation constant of the medium, and $j$ is $\sqrt{-1}$. The permittivity of a lossy medium is complex and can be given as [93]

$$\varepsilon = \varepsilon^{'} - j\varepsilon^{''} \tag{3.2}$$

where $\varepsilon^{'}$ and $\varepsilon^{''}$ are the real and imaginary parts of the permittivity, respectively. These parameters can be expressed as [94]

$$\varepsilon^{'} = n^2 - k^2 \tag{3.3}$$

$$\varepsilon^{''} = 2nk \tag{3.4}$$

where $n$ is the refractive index of the material while $k$ is the extinction coefficient. These parameters are wavelength dependent and change with the deposition conditions of the materials. Using the parts of the complex permittivity, complex propagation constant can be written as

$$\gamma = \frac{\varepsilon^{''} k_0}{2\sqrt{\varepsilon^{'}}} + j\frac{k_0}{\sqrt{\varepsilon^{'}}} \tag{3.5}$$

where $k_0$ is the wavenumber of the free space which can be expressed as

$$k_0 = \omega\sqrt{\varepsilon_0\mu_0} \tag{3.6}$$

where $\omega$ is the radial frequency of the incident radiation, $\varepsilon_0$ is the permittivity of the free space which is equal to 8.85x10$^{-12}$ F/m, and $\mu_0$ is the permeability of the free space which is equal to 4πx10$^{-7}$ H/m.

The characteristic impedance of a good conductor ($Z_{cond}$) is expressed as

$$Z_{cond} = (1+j)\sqrt{\omega\mu_0/2\sigma_{cond}} \tag{3.7}$$

where $\sigma_{cond}$ is the conductivity of the conductor.

The impedance seen from the input of a medium, having a characteristic impedance of $Z$ and a load impedance of $Z_L$, is given by the *Telegrapher's Equation* [95]

$$Z_{in} = Z\frac{Z_L + Z\tanh(\gamma l)}{Z + Z_L\tanh(\gamma l)} \tag{3.8}$$

where $\gamma$ is the complex propagation constant of the medium and $l$ is the length of the medium. For example, the impedance seen from the input of the cavity in Figure 3.10 can be written as

$$Z_{in-cav} = Z_{cav}\frac{Z_{refl} + Z_{cav}\tanh(\gamma_{cav}\, l_{cav})}{Z_{cav} + Z_{refl}\tanh(\gamma_{cav}\, l_{cav})} \tag{3.9}$$

where $Z_{cav}$ is the characteristic impedance of the cavity, $Z_{refl}$ is the characteristic impedance of the reflector metal, $\gamma_{cav}$ is the complex propagation constant of the cavity, and $l_{cav}$ is the thickness of the cavity. The total input impedance of the structure in Figure 3.10 can be found by using the telegrapher equation several times.

The total impedance of the structure can be used to calculate the reflection coefficient. The reflection coefficient ($\Gamma$) of an electromagnetic wave travelling from medium 1 to medium 2 at normal incidence is expressed as [93]

$$\Gamma = \frac{Z_2 - Z_1}{Z_2 + Z_1} \tag{3.10}$$

where $Z_1$ is the characteristic impedance of the medium where the wave is coming from, and $Z_2$ is the characteristic impedance of the medium where the wave is going. The second medium is sometimes called as the load of the first medium. Using this expression the reflection coefficient ($\Gamma_{\text{inf}}$) of an infrared wave incident on a microbolometer can be found as

$$\Gamma_{inf} = \frac{Z_{in} - Z_0}{Z_{in} + Z_0} \tag{3.11}$$

where $Z_{in}$ is the input impedance of the microbolometer as shown in Figure 3.10, and $Z_0$ is the characteristic impedance of the free space (assuming that the infrared radiation is coming from free space) which is equal to 377 Ω. There is no transmission through the microbolometer structure since there is a reflector metal at the bottom. So the incident infrared radiation is either reflected or absorbed by the microbolometer structure. The ratio of the absorbed infrared power ($P_{abs}$) by the microbolometer to the incident power is given as

$$P_{abs} = 1 - P_{refl} = 1 - \left|\Gamma_{inf}\right|^2 \tag{3.12}$$

where $P_{refl}$ is the reflected power which is equal to the square of the reflection coefficient. In order to maximize the absorbed power the reflection coefficient should be minimized, i.e., the input impedance of the microbolometer structure should be close the characteristic impedance of free space.

The transmission line model given in Figure 3.10 (b) can be modified in order to simplify the calculations and optimizations. The model can be divided into two parts, the absorber layer and the remaining layers. Then the input impedance $Z_{in}$ of the model can be written as

$$Z_{in} = Z_{abs} \frac{Z_{L_abs} + Z_{abs} \tanh(\gamma_{abs} l_{abs})}{Z_{abs} + Z_{L_abs} \tanh(\gamma_{abs} l_{abs})} \tag{3.13}$$

where $Z_{abs}$ is the characteristic impedance of the absorber layer, $Z_{L_abs}$ is the equivalent characteristic impedance of the remaining layers, $\gamma_{abs}$ is the complex propagation constant of absorber layer, and $l_{abs}$ is the thickness of the absorber layer. Generally, a very thin metal film is used as the absorber layer in infrared detectors [67, 99]. Since the thickness of the layer is very small, some assumptions can be made and the input impedance can be found as [96]

$$Z_{in} = R_{s_abs} // Z_{L_abs} \tag{3.14}$$

where $R_{s_abs}$ is the surface resistance of the absorber layer and $Z_{L_abs}$ is the equivalent characteristic impedance of the remaining layers. Figure 3.11 gives the modified version of the transmission line model of the microbolometer structure. Appendix A explains the derivation of Equation 3.14.

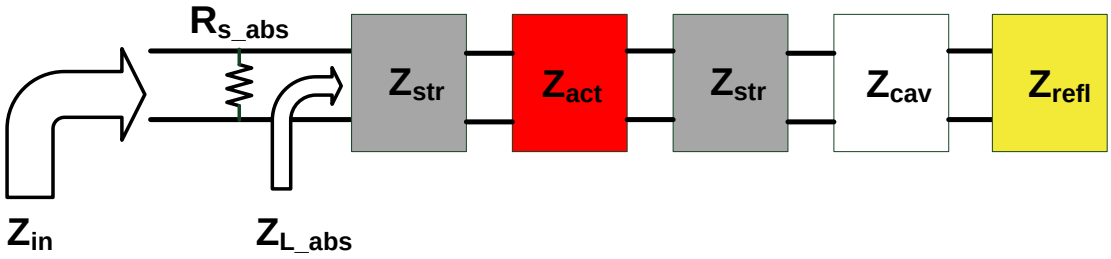



Figure 3.11: The modified version of the transmission line model of microbolometer structure after some assumptions.

Equation 3.14 shows that if $Z_{L_abs}$ and $R_{s_abs}$ are adjusted to be $\infty$ and 377 Ω, respectively, then the input impedance becomes 377 Ω and the reflection coefficient becomes zero resulting in maximum absorbed power. It is not a difficult issue to adjust the layer properties and thicknesses to have maximum absorption. But this is the case if the structure of the microbolometer is same at every point, which is practically not possible. For example, the electrodes used for the electrical contact to active material will behave as the reflector material changing the equivalent impedance at those points. For this reason, the microbolometer structure should be divided into regions having different layer combinations, and the area ratio of these regions to the total area should be used in order to calculate the total absorption. Figure 3.12 shows the regions of the microbolometer on the layout of the structure. Since the microbolometer detector has four different regions the total absorption can be written as

$$P_{tot} = P_1 \frac{A_1}{A_{tot}} + P_2 \frac{A_2}{A_{tot}} + P_3 \frac{A_3}{A_{tot}} + P_4 \frac{A_4}{A_{tot}} \tag{3.15}$$

where $P_{tot}$ is the total absorption, $A_{tot}$ is the total area of the microbolometer, $P_X$ and $A_X$ are the absorption and the area of the particular region. Table 3.1 summarizes the layer combination and areas of the regions. Total area is the sum of the areas of these regions.

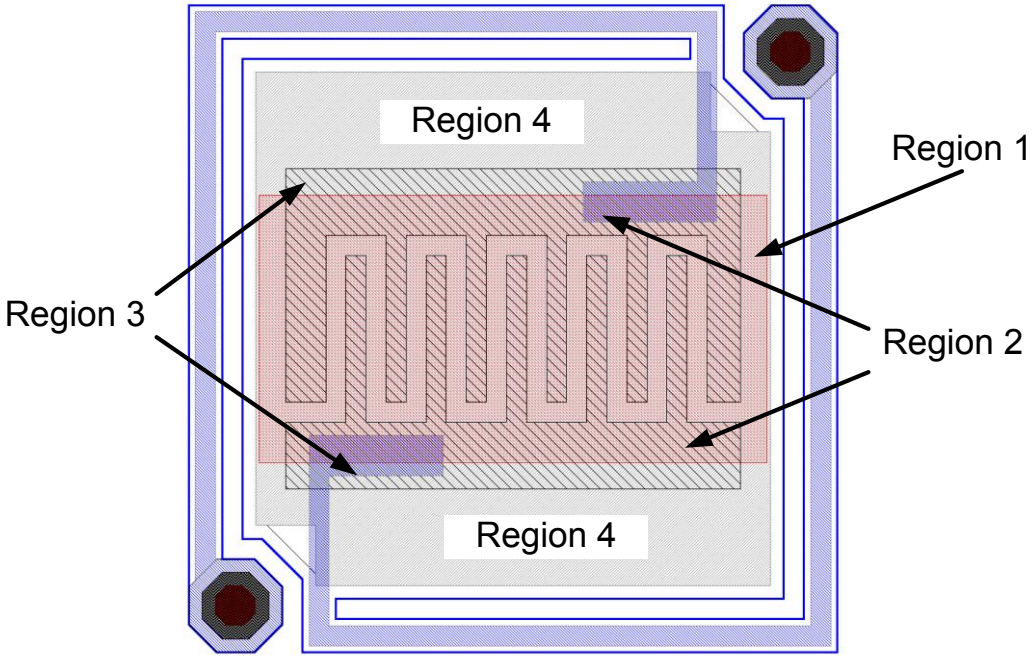



Figure 3.12: Different regions of the microbolometer detector structure.

Table 3.1: The summary of the regions, layer combinations and the areas of the regions. Total area is the sum of the areas of these regions.

| **Region** | **Layers** | **Area** |
|---|---|---|
| Region 1 | Absorber - Structural Layer - Active Material - Structural Layer- Cavity - Reflector Metal | 318.5 $\mu m^2$ |
| Region 2 | Absorber - Structural Layer - Active Material - Electrode Metal | 441.5 $\mu m^2$ |
| Region 3 | Absorber - Structural Layer - Electrode Metal | 136 $\mu m^2$ |
| Region 4 | Absorber - Structural Layer - Structural Layer - Cavity - Reflector Metal | 546 $\mu m^2$ |

The consistency of the cascaded transmission line model for the absorption simulations is tested with a pixel whose absorption is previously measured [18]. Figure 3.13 shows the layout of the pixel developed in [18]. The pixel has dimensions of 40 µm x 40 µm fabricated in 0.35 µm CMOS technology and post-CMOS processed in METU facilities. The active area has a 1 µm thick silicon dioxide layer on top and aluminum layer at the bottom. There is no optical cavity in this pixel. The refractive index and the extinction coefficient of silicon dioxide are

2.44 and 0.1, respectively [112]. The absorption of the pixel in 8-12 µm wavelength range is simulated to be 47 %, while the measured absorption in the same wavelength region is given as 45 % [18]. This result shows that the cascaded transmission line model can be used safely to find the absorption of the modeled detectors.

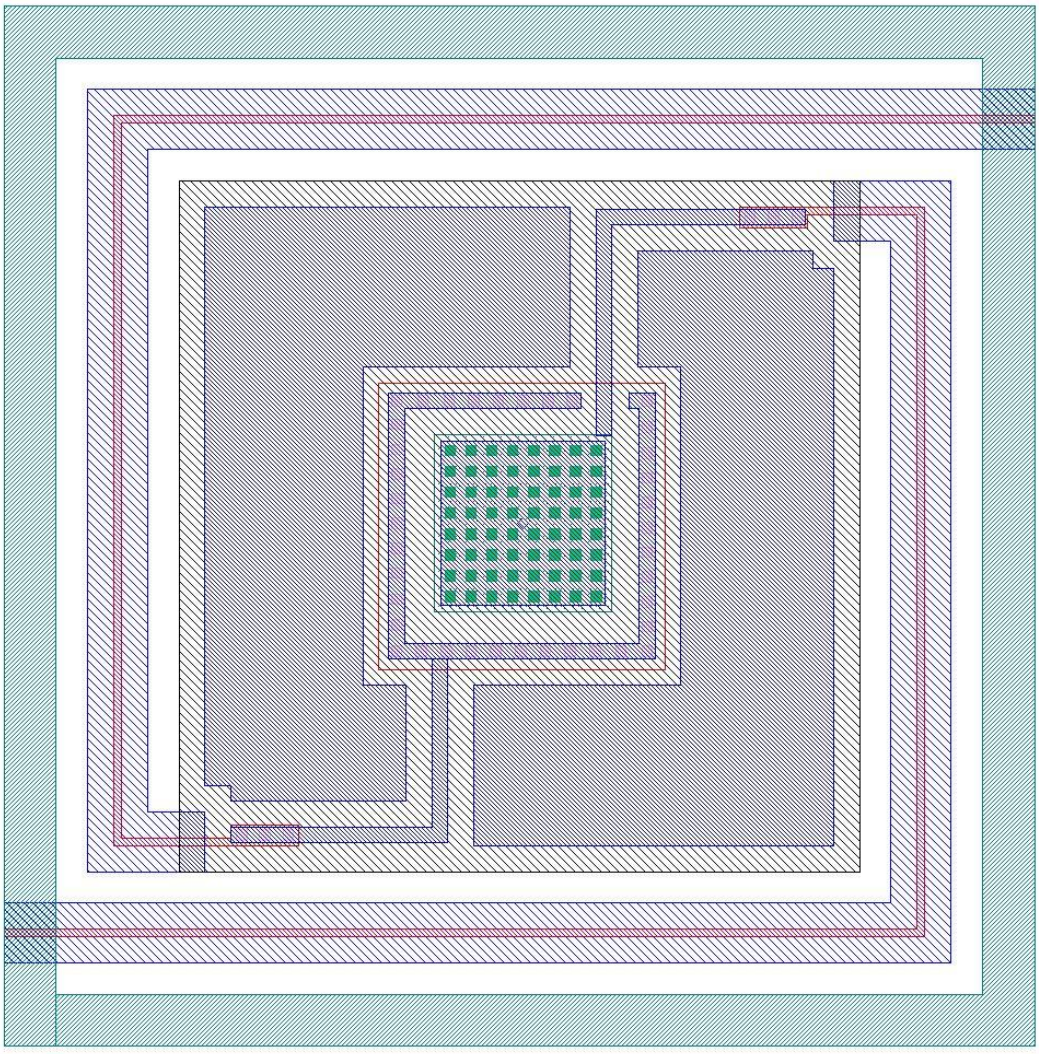


Figure 3.13: The layout of the pixel developed in [18]. The pixel has dimensions of 40 µm x 40 µm fabricated in 0.35 µm CMOS technology and post-CMOS processed in METU facilities [18].

### 3.4.2. Absorption Simulations

The microbolometer model obtained in the previous section is used to simulate the absorption of the structure and to obtain the dependency of the absorption to the layer properties. The required properties for the absorption simulation are the thicknesses and the optical constants of the layers, i.e., the refractive index and the extinction coefficient. The deposition conditions of the structural layer is selected such that the layer is stress free and the microbolometer structure remains suspended without bending and buckling. Also the active material is optimized to have a high TCR value and low resistivity. The optimizations will be explained in detail in Chapter 4. Since the deposition conditions of these layers are fixed, the optical constants are also fixed. The values of the optical constants of these layers are measured with an infrared ellipsometer. Figure 3.14 shows the measured refractive index and the extinction coefficient of the structural layer (silicon nitride, $Si_3N_4$) with the changing wavelength. Figure 3.15 shows the optical constants of the active material (YBCO) with respect to the wavelength.

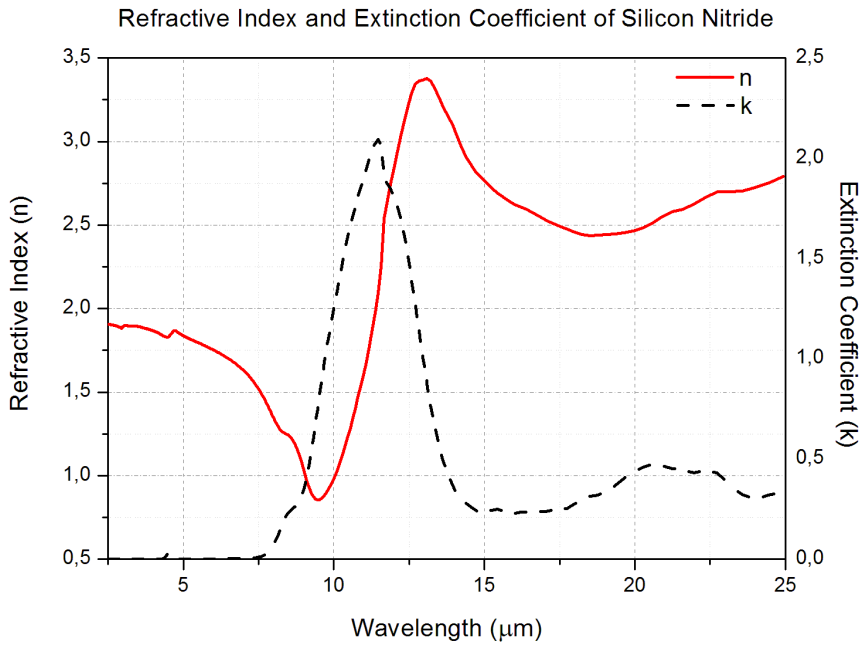



Figure 3.14: Measured refractive index and extinction coefficient of the structural layer (silicon nitride, $Si_3N_4$).

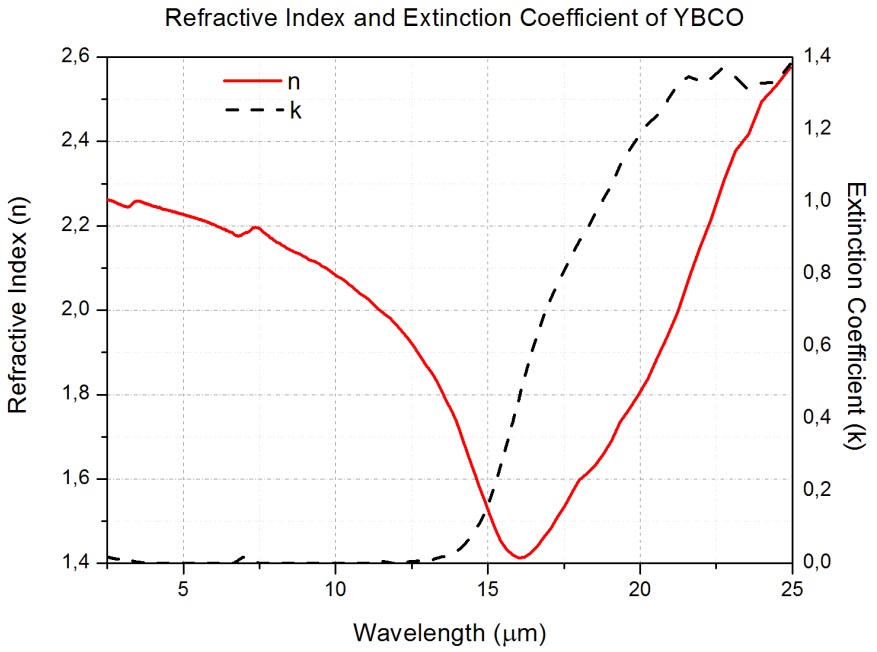



Figure 3.15: Measured refractive index and extinction coefficient of the active material (YBCO).

The absorption simulations of the microbolometer detector are carried out using the MATLAB software. The code used in the simulations is given in Appendix B. Some parameters are changed in order to see the effect on the absorption. Figure 3.16 shows the variation of the absorption with respect to the cavity and structural layer thicknesses. As can be seen from the figure, the absorption makes a peak at a cavity thickness in the range of 1.5 μm to 2 μm for the small structural layer thicknesses. The absorption increases with increasing the structural layer thickness, but this does not enhance the performance of the detector due to the rise in the thermal conductance. Figure 3.17 shows the variation of thermal conductance with the structural layer thickness. In this simulation the thickness of the interconnect metal is fixed at 0.1 μm. The thermal conductivity value of silicon nitride layer is taken as 1 W/mK which is the smallest value existing in literature [100-102]. The thermal conductance value increases by 20 % when the structural layer thickness is increased from 0.15 μm to 0.3 μm, but the absorption value increases only by 5 %. For this reason, it is not feasible to increase the structural

layer thickness too much for only increasing the absorption. Considering these and the fabrication process trials, 1.8 µm and 0.17 µm are chosen as the thicknesses of cavity layer and structural layer, respectively.

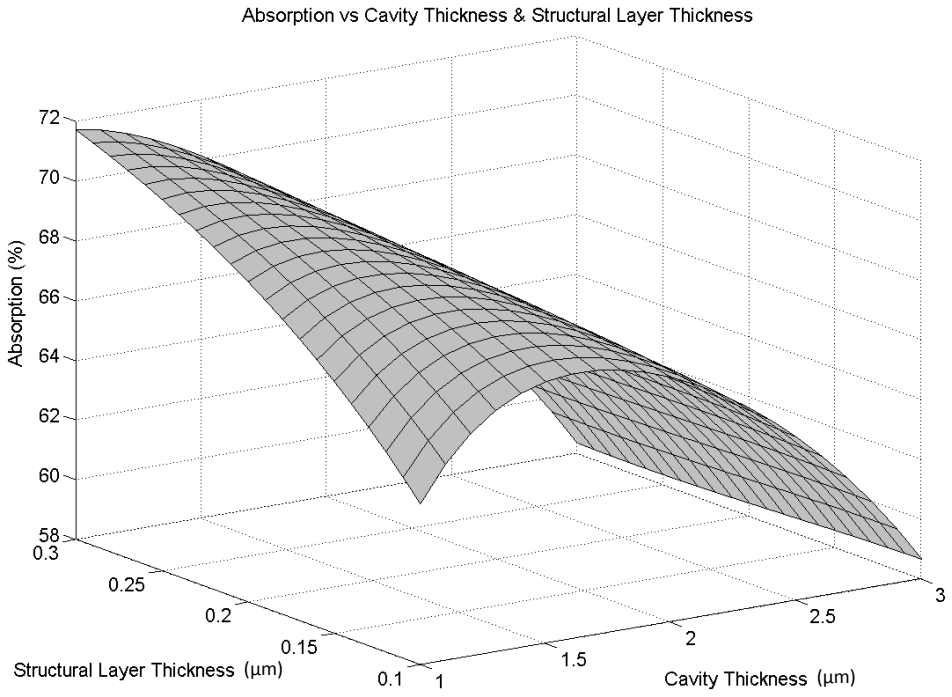



Figure 3.16: Variation of the absorption with respect to cavity and structural layer thicknesses.

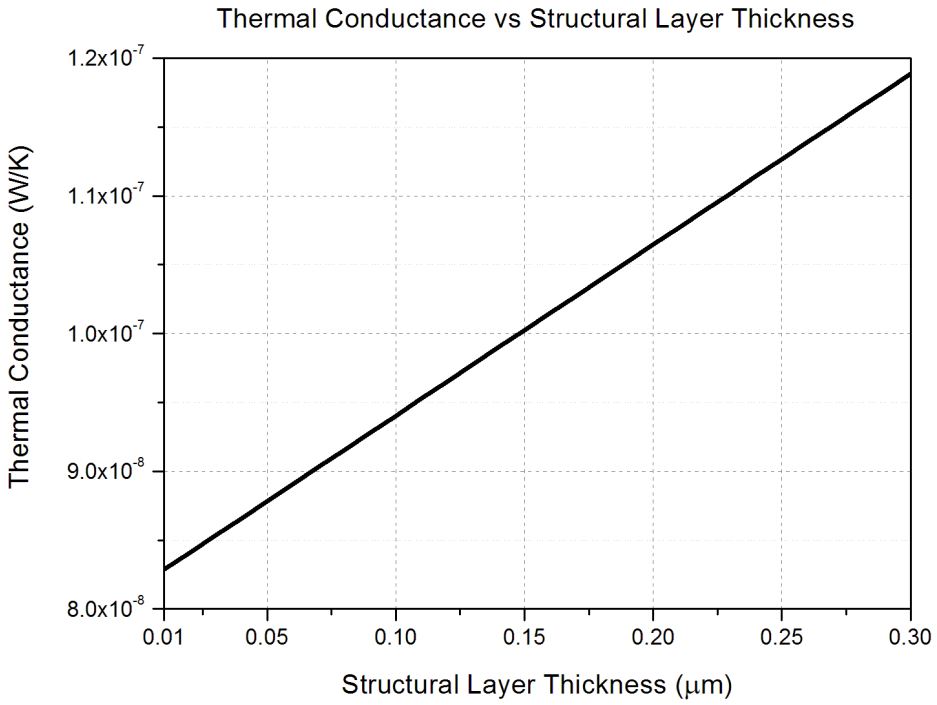



Figure 3.17: Variation of the thermal conductance with respect to structural layer thickness.

The surface resistance ($R_s$) of the absorber layer is another parameter for the absorption of the microbolometer detector. Figure 3.18 shows the variation of the absorption with the surface resistance of the absorber layer. The maximum absorption occurs when $R_s$ is around 377 Ω/□. The absorption is not effected much when $R_s$ increases. This is due to the non-zero extinction coefficient of the silicon nitride layer, which also makes absorption in the wavelength range of interest and the non-zero area of Region 2 and Region 3.

The absorption simulation of the whole microbolometer structure is performed considering all above parameters. Figure 3.19 shows the result of the absorption simulation. The absorption at 10 μm wavelength in Region 1 and Region 4 is above 85 %, while the absorption in Region 2 and Region 3 is below 35 %. Since the total area of Region 2 and 3 is around one third of the total area, the effective absorptance decreases to 66 % at around 10 μm wavelength. This absorption value

is not very low when compared to the data in literature [67], and can be increased if the areas of Region 2 and Region 3 are reduced.

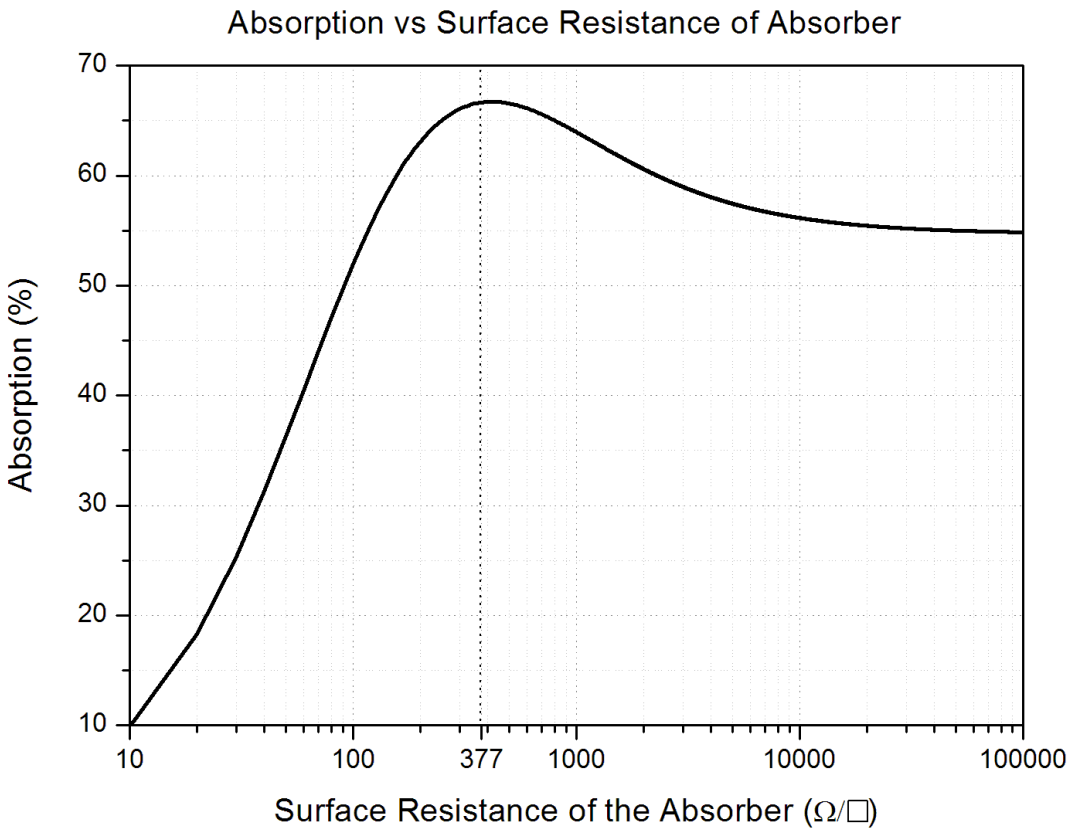



Figure 3.18: Variation of the absorption with the surface resistance of the absorber layer.

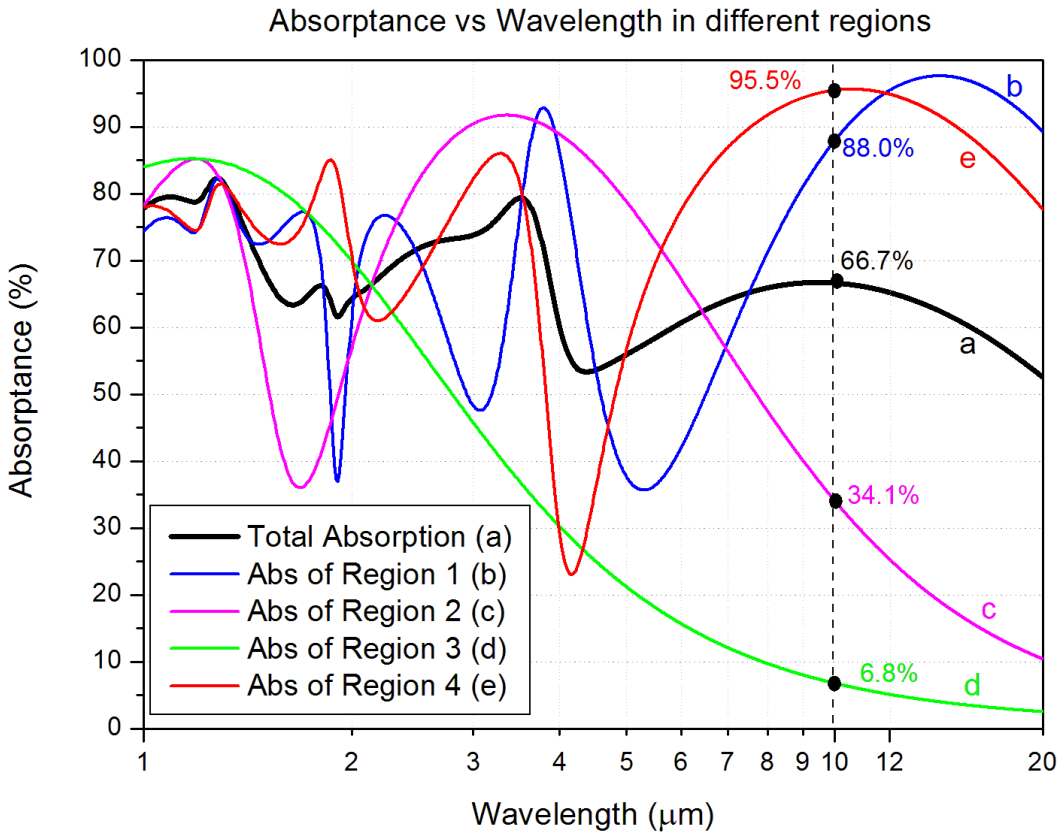



Figure 3.19: Absorption simulation of the modeled microbolometer structure. The total absorption value at 10 μm wavelength is not very low when compared with the data in literature [67] and can be increased if the areas of Regions 2 and 3 are reduced.

## 3.5. Thermal simulations

The designed microbolometer detector is thermally simulated using Coventorware software which uses Finite Element Method (FEM) for the simulations. Table 3.2 summarizes the thermal properties of the layers used in the simulations. Figure 3.20 shows the result of the thermal simulation. The temperature of the pixel increases 1061 mK with an applied power of 100 nW. This temperature increase results in a thermal conductance value of $9.4 \times 10^{-8}$ W/K which is lower than the value obtained in the MATLAB simulations. Figure 3.21 shows the variation of the pixel temperature with time. The thermal time constant of the pixel is found as 15.4 ms from this simulation result. These results are compatible with the

properties of the detectors in literature which are used in large format FPAs for infrared imaging applications.

Table 3.2: The summary of the thermal properties of the layers used in the simulations.

| | $Si_3N_4$ | Ti | Au | YBCO | TiN |
|---|---|---|---|---|---|
| Thermal Conductivity (W/cmK) | 0.01 | 0.219 | 3.2 | 0.035 | 0.192 |
| Specific Heat ($J/cm^3K$) | 2.2 | 2.36 | 2.49 | 2.65 | 2.2 |

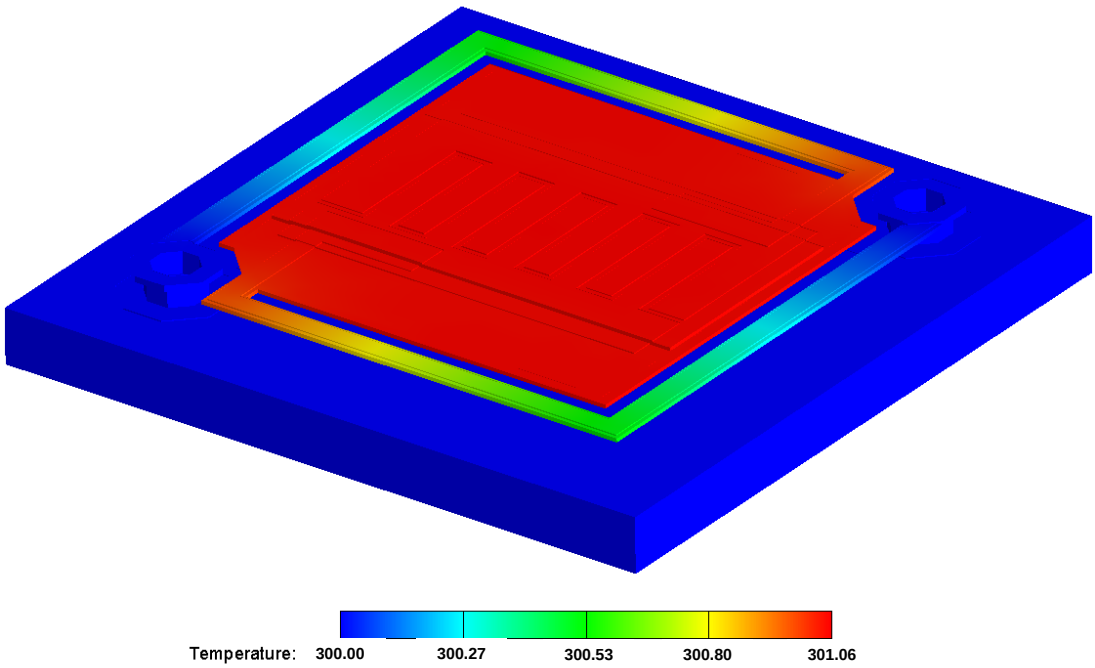



Figure 3.20: The result of the thermal simulation performed using Coventorware. The temperature of the pixel increases 1061 mK with an applied power of 100 nW. This results in a thermal conductance value of $9.4 \times 10^{-8}$ W/K.

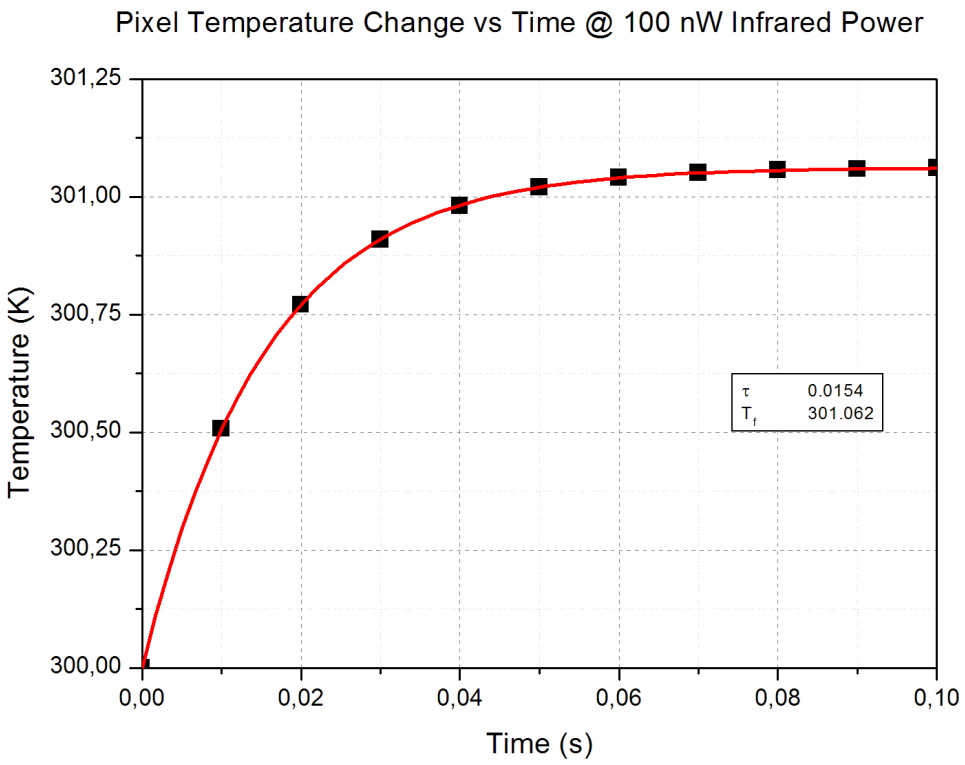



Figure 3.21: The variation of the pixel temperature with time. The thermal time constant of the pixel is found as 15.4 ms from this simulation result.

## 3.6. Mechanical Simulations

The designed microbolometer detector is mechanically simulated using Coventorware software. Table 3.3 summarizes the mechanical properties of the layers used in the support arms [103]. The properties of the other layers do not have any significance in these simulations.

Table 3.3: The summary of the mechanical properties of the layers used in the support arms.

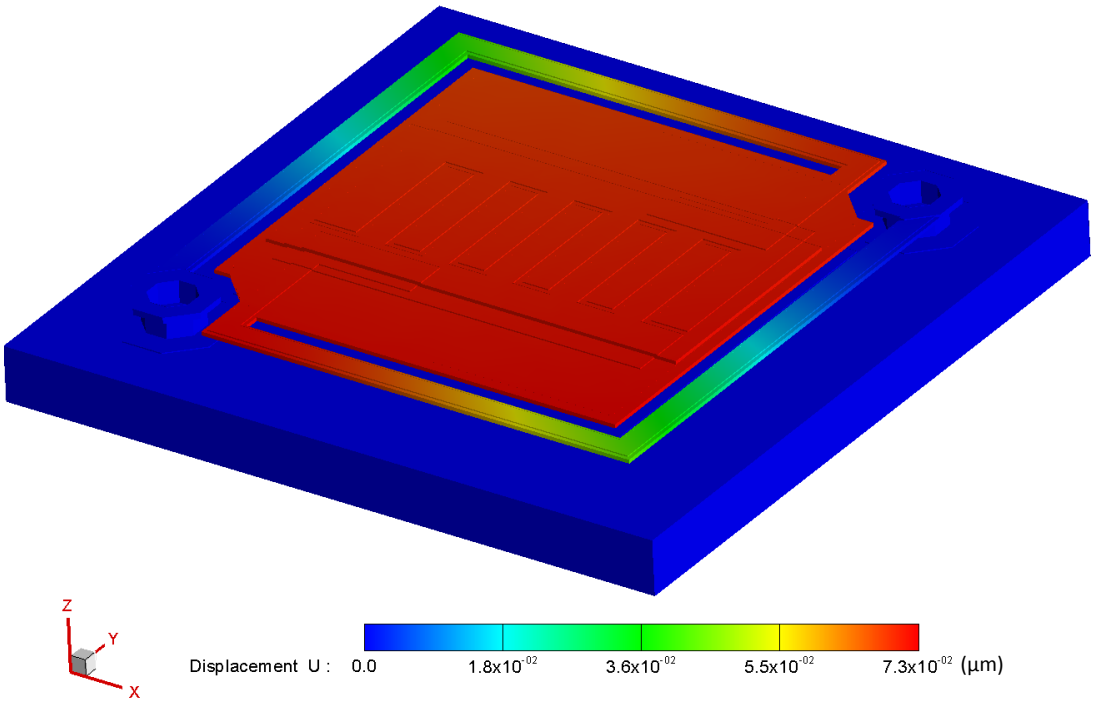
| **Property** | **Silicon Nitride ($Si_3N_4$)** | **Titanium (Ti)** |
|---|---|---|
| Young's Modulus | 222 GPa | 110 GPa |
| Poisson Ratio | 0.27 | 0.33 |

An acceleration of 1000 g is applied in all directions to the structure during the simulations, while the maximum displacement and maximum stress in the structure are observed. Figure 3.22 shows the simulation results for displacement and stress for the acceleration of 1000 g in -z direction. Table 3.4 gives maximum displacement and stress results in all directions for an acceleration of 1000 g. The maximum stress values in all directions are less than the yield strength values of silicon nitride and titanium which are 14 GPa and 170 MPa, respectively [104, 105]. This shows that the pixel is durable enough even for extreme accelerations.

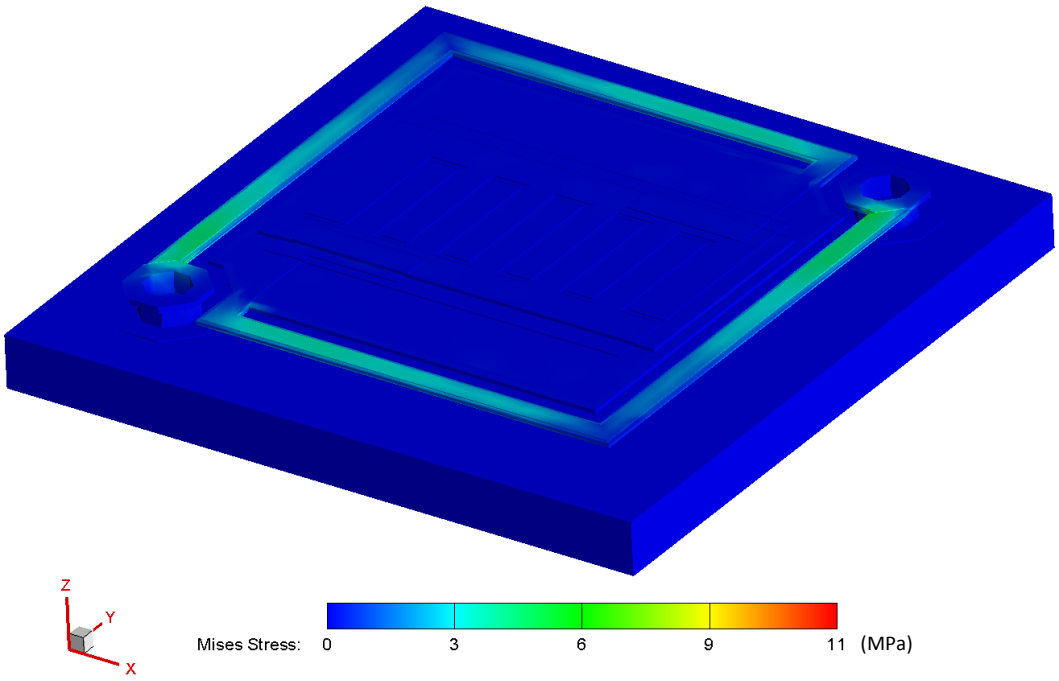
Table 3.4: The maximum displacement and stress results in all direction for an acceleration of 1000 g. The maximum stress values in all directions are less than the yield strength values of silicon nitride and titanium which are 14 GPa and 170 MPa, respectively.

| **Direction** | **+x** | **-x** | **+y** | **-y** | **+z** | **-z** |
|---|---|---|---|---|---|---|
| **Maximum Displacement (μm)** | $2.5\times10^{-3}$ | $2.5\times10^{-3}$ | $2.1\times10^{-3}$ | $2.1\times10^{-3}$ | $7.2\times10^{-2}$ | $7.2\times10^{-2}$ |
| **Maximum Stress (MPa)** | 2.3 | 2.3 | 1.6 | 1.6 | 11 | 11 |

Modal analysis is also performed to find out the resonance frequency of the microbolometer detector. In the simulations only the first 5 modes which have the lowest resonance frequencies are investigated. Table 3.5 gives the resonance frequencies and maximum displacement values of the first five modes. The results show that any mechanical input with frequency less than 60 kHz is acceptable for the designed microbolometer detector.




(a)




(b)

Figure 3.22: The simulation results for the displacement (a) and the stress (b) for the acceleration of 1000 g in -z direction.

Table 3.5: The resonance frequencies and maximum displacement values of the first five modes. The results show that any mechanical input with frequency less than 60 kHz is acceptable for the designed microbolometer detector.

| Mode Number | 1 | 2 | 3 | 4 | 5 |
|---|---|---|---|---|---|
| Resonance Frequency (kHz) | 60 | 84 | 120 | 280 | 530 |
| Maximum Displacement (μm) | 1 | 1 | 1 | 1.3 | 1 |

## 3.7. Conclusions

This chapter presented the structural design and optimization of the surface micromachined microbolometer detector pixel. The selection of the active detector material and the optimization of resistor value and resistor structure are explained. YBCO is selected as the active material and 100 kΩ is found as the optimum detector resistance. The optimization of detector size and pixel structure is given together with the absorption simulations where the detector is modeled as cascaded transmission lines. Optimum layer thicknesses are determined with these absorption simulations and the fabrication process trials. Finally, FEM simulations are performed in order to find the thermal and mechanical properties of the detector pixel. Results of all these simulations show that the designed detector pixel can be used in a large format FPA for uncooled infrared imaging applications.

# CHAPTER 4

# PROCESS OPTIMIZATION AND FABRICATION OF A SINGLE PIXEL MICROBOLOMETER

This chapter explains the process optimization and fabrication of a single pixel microbolometer detector. The microbolometer detector is resistive type and fabricated using the surface micromachined MEMS technology as stated in previous chapter. Section 4.1 presents the design of the fabrication process steps, while Section 4.2 gives the optimization details and realization of the fabrication steps. Finally, Section 4.3 summarizes the fabrication results and concludes this chapter.

## 4.1. Design of the Fabrication Process

The microbolometer detectors are generally composed of an active material, which has a high TCR value, thermally isolated from the substrate by the help of a bridge type structure. Although the structure can be explained in such a simple way, there are many parameters that should be considered during the design of the fabrication process. Some of these parameters are:

- The mirror metal at the bottom of the material should have a high conductivity value and should be shiny in order to reflect the infrared radiation.
- The sacrificial layer, which the parts of the detector will be fabricated on, should stand the pursuing process steps. Also its process should not affect the

underlying CMOS readout circuitry and its etching at the end of fabrication should be straightforward.

- The structural layer should have low thermal conductivity for good thermal isolation and should be stress free in order to prevent buckling of the detector. It should be able to carry the other parts of the detector.
- The interconnect metal on the support arms should have a low thermal conductivity and should be able to be etched without much undercut.
- There should be an electrode layer to electrically connect the interconnect metal to the active material. This layer will be patterned as finger structure as explained in the previous chapter.
- The active material should be optimized to have a high TCR value and low resistivity.
- The absorber layer should have a surface resistance of 377 Ω/□ in order to increase the infrared absorption of the detector. Since thin metal films are used as the absorber layer, the thickness should be low enough to satisfy the condition above. So the material should be able to be deposited at the desired thickness.
- The fabrication steps should be designed to have the minimum surface topography during the process.

Considering all these parameters and combining them with the experience gained during the study in University of Texas at Arlington (UTA), the process steps that will be used in the fabrication of the surface micromachined microbolometer detector are designed. Figure 4.1 shows the representative cross-sectional view of the detector after each step of the designed process flow, while Figure 4.2 shows the 3-D view of the detector pixel, which are obtained from the model used in the Coventorware software.

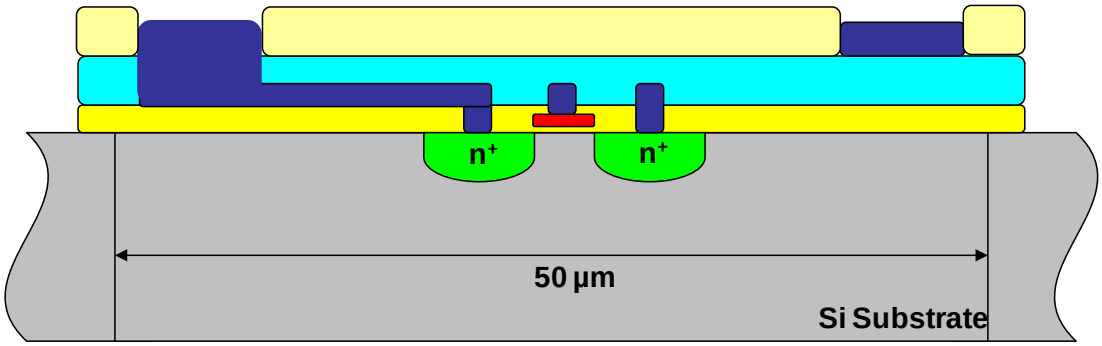



Figure 4.1 (a) The representative cross sectional view of the CMOS wafer and the circuit that will stay under the detector pixel.

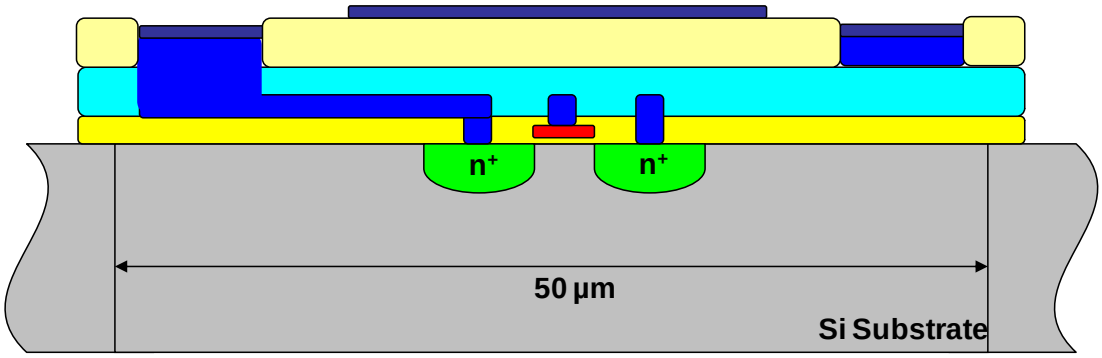



Figure 4.1 (b) The deposition and patterning of the metal layer that will be used as a mirror for the infrared radiation.

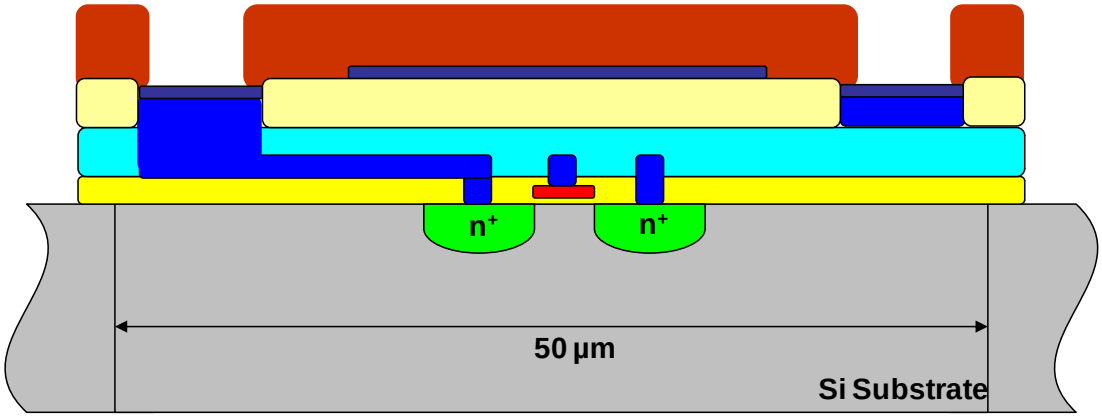



Figure 4.1 (c) Deposition and patterning of the sacrificial layer that the microbolometer structure will be built on.

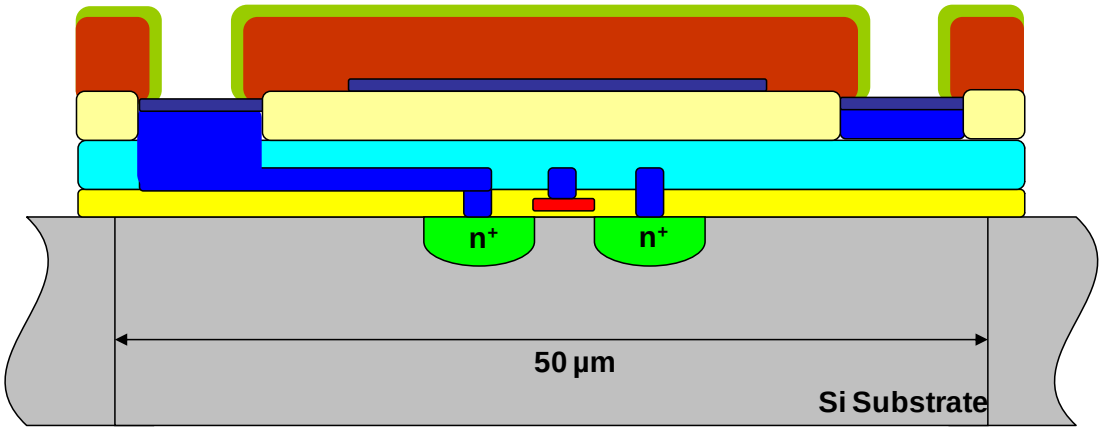



Figure 4.1 (d) Deposition of the structural layer and opening of the contact at the anchors.

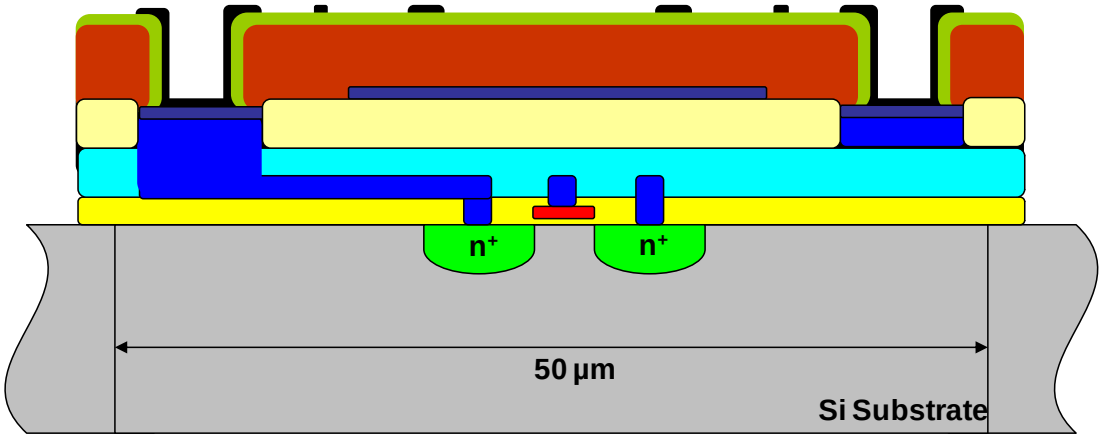



Figure 4.1 (e) Deposition and patterning of the interconnect metal on the support arms.

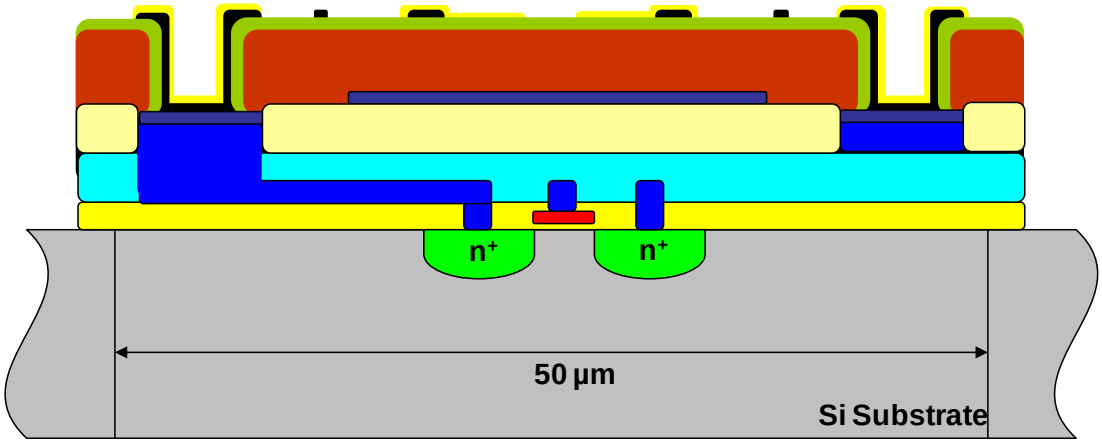



Figure 4.1 (f) Deposition of the electrode material and patterning as finger type.

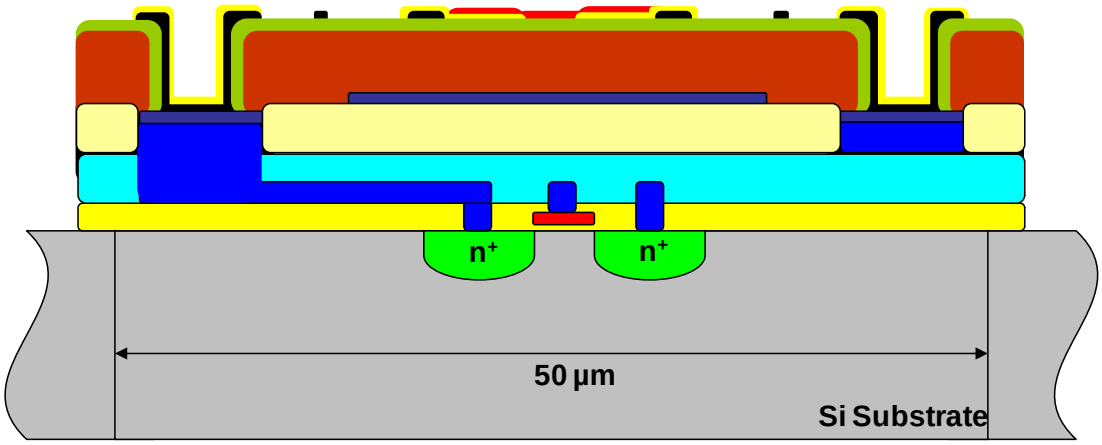



Figure 4.1 (g) Deposition and patterning of the active detector material.

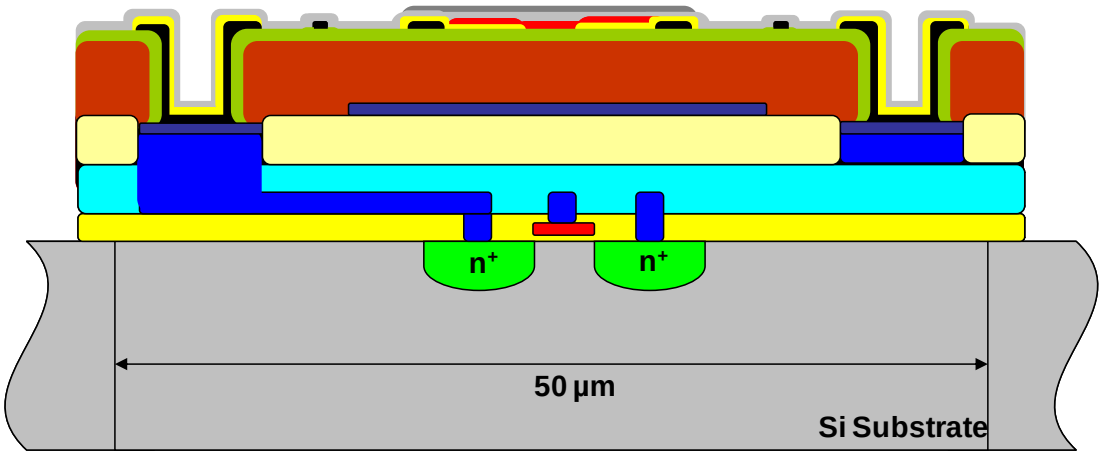



Figure 4.1 (h) Deposition of the upper structural layer followed by deposition and patterning of the absorber layer.

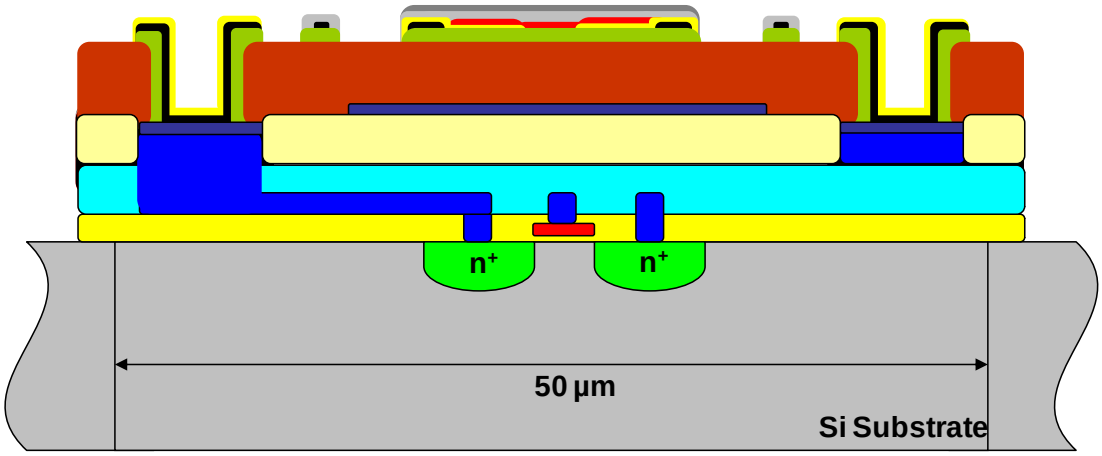



Figure 4.1 (i) Patterning of the upper structural layer to obtain the support arms and the body of the detector pixel.

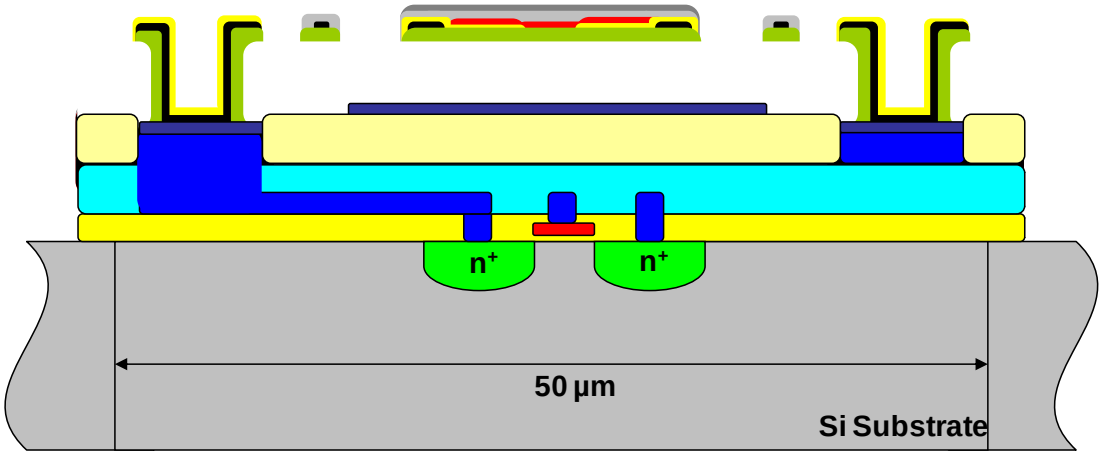



Figure 4.1 (j) Etching of the sacrificial layer and isolation of the detector pixel from the substrate.

Figure 4.1: The representative cross-sectional view of the detector after each step of the designed process flow.

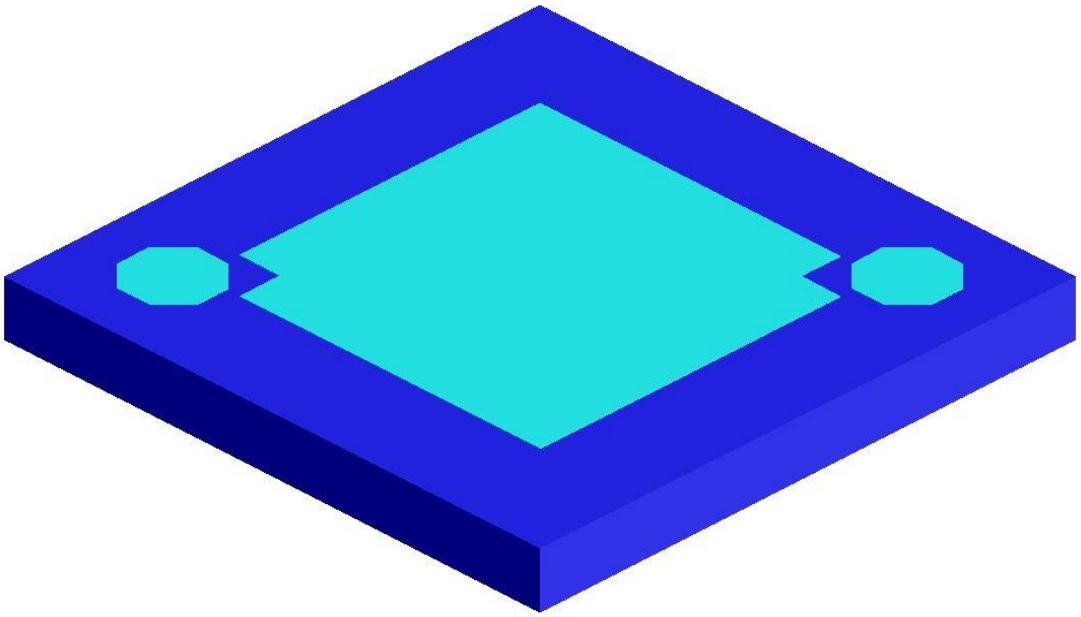


Figure 4.2 (a) The deposition and patterning of the metal layer that will be used as a mirror for the infrared radiation.

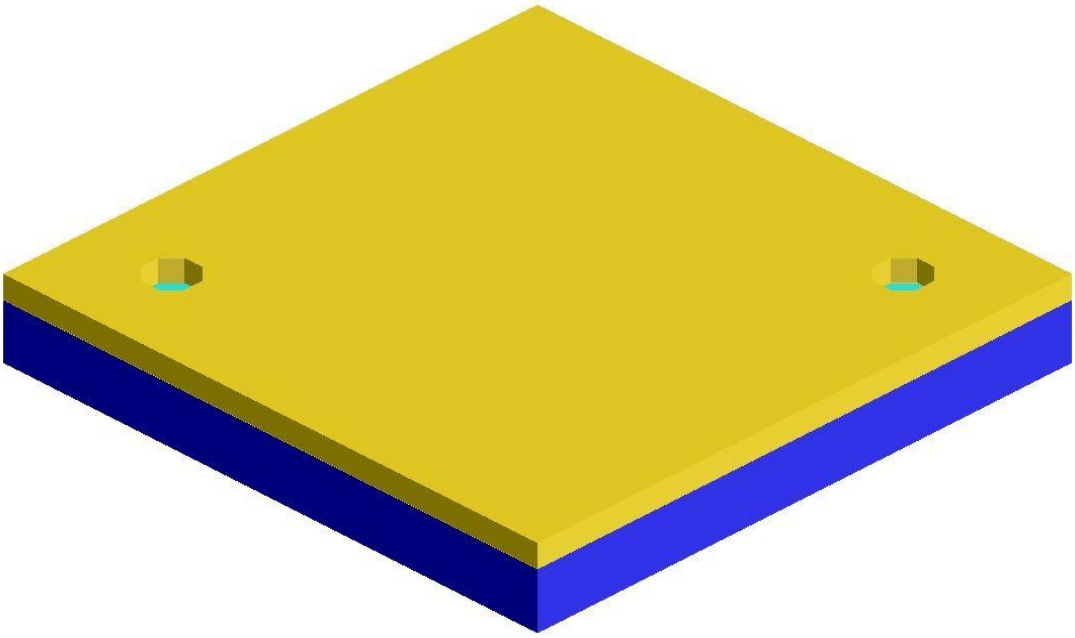


Figure 4.2 (b) Deposition and patterning of the sacrificial layer that the microbolometer structure will be built on.

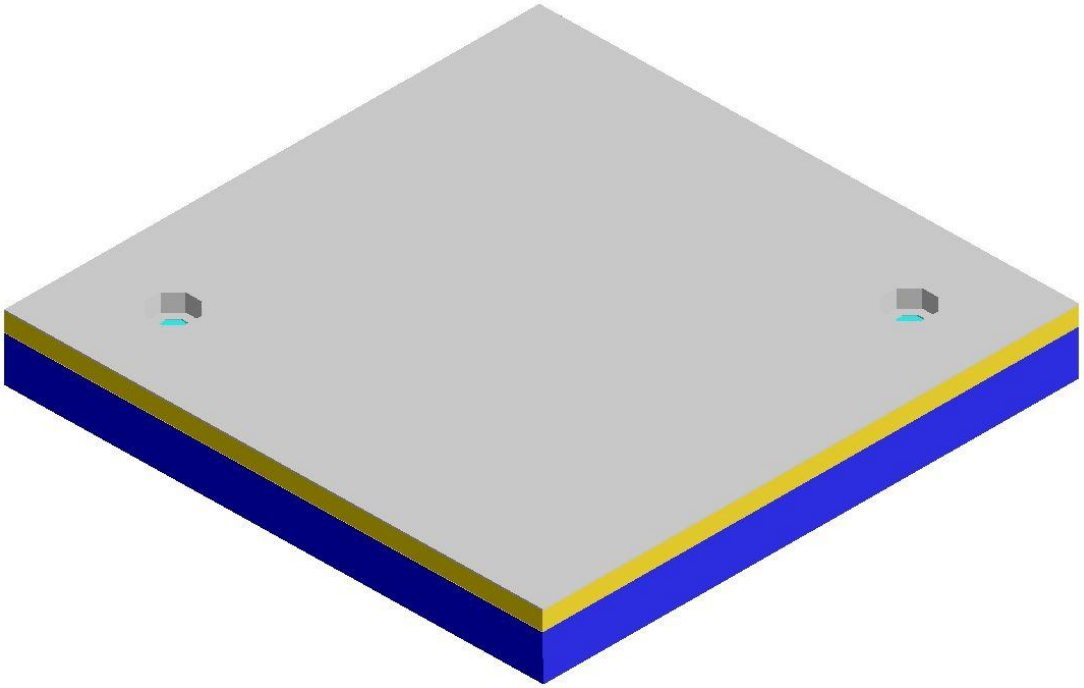


Figure 4.2 (c) Deposition of the structural layer and opening of the contact at the anchors.

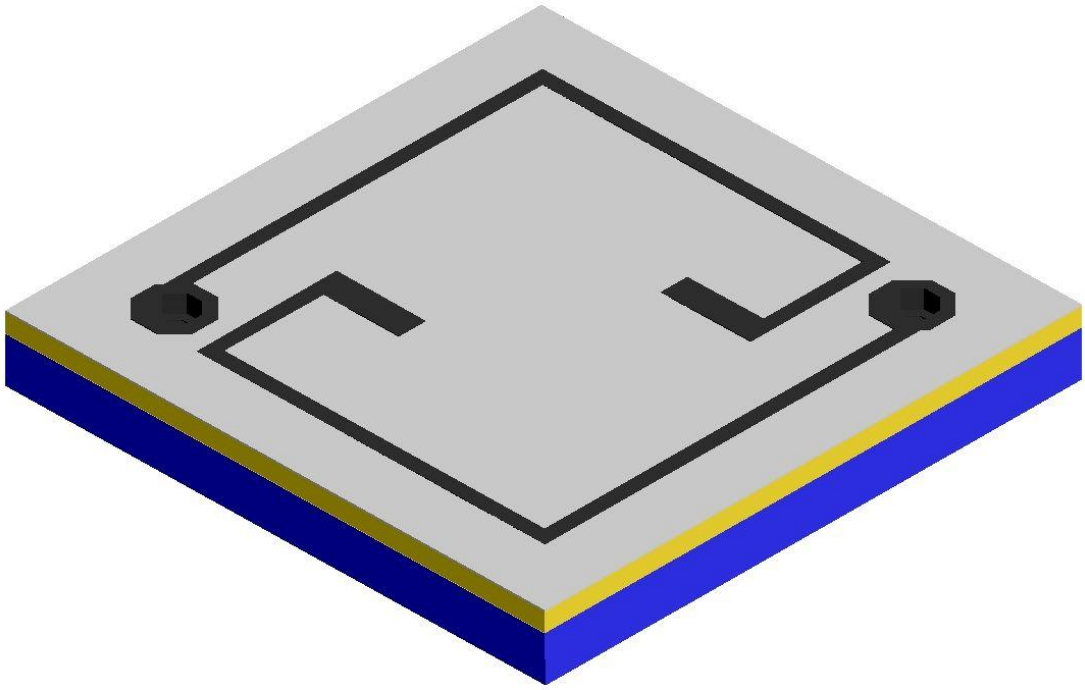


Figure 4.2 (d) Deposition and patterning of the interconnect metal on the support arms.

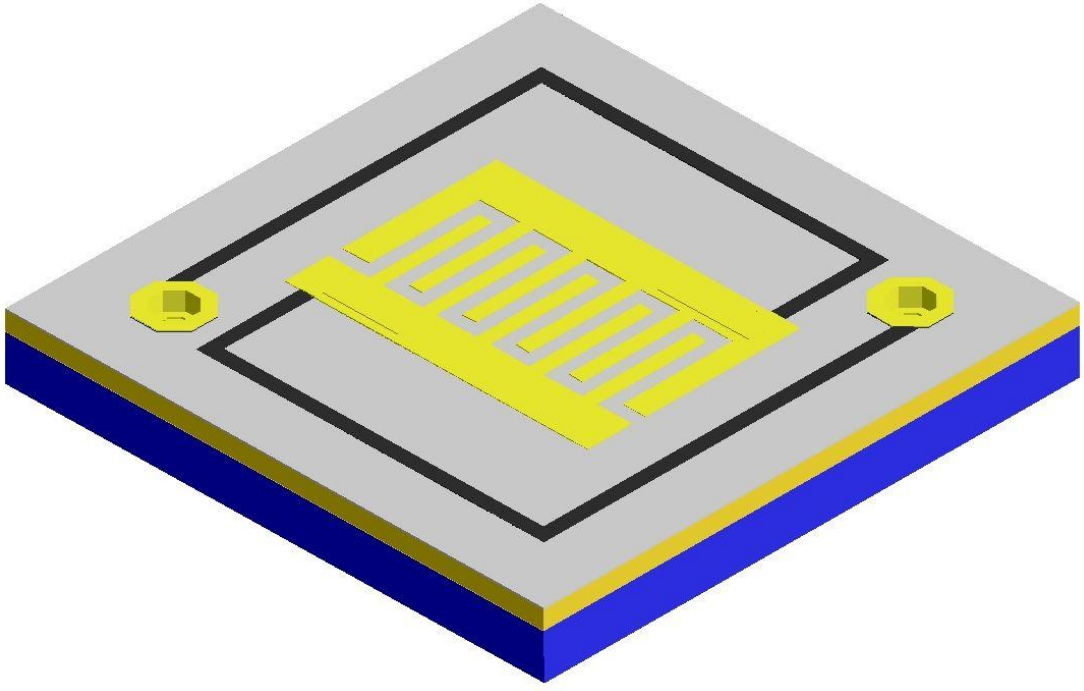


Figure 4.2 (e) Deposition of the electrode material and patterning as finger type.

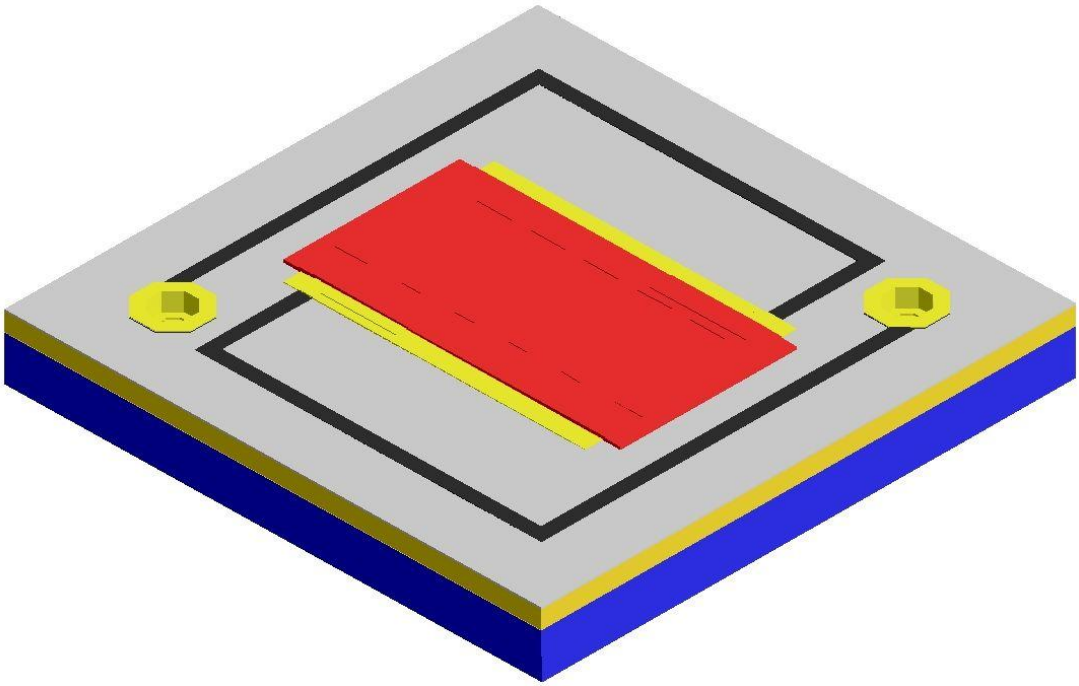


Figure 4.2 (f) Deposition and patterning of the active detector material.

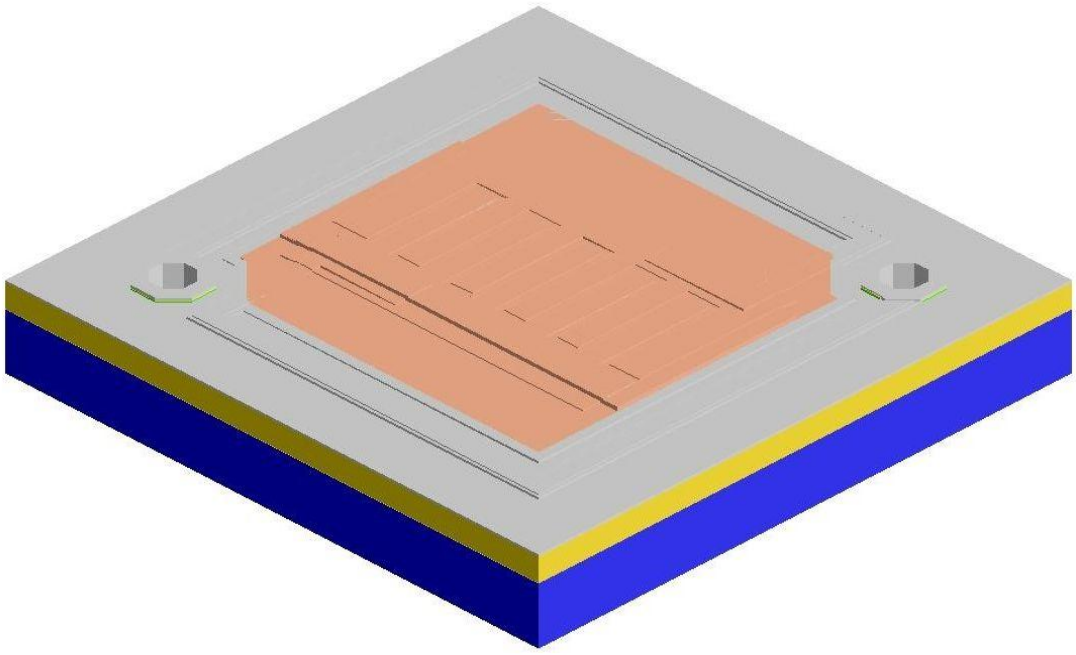


Figure 4.2 (g) Deposition of the upper structural layer followed by deposition and patterning of the absorber layer.

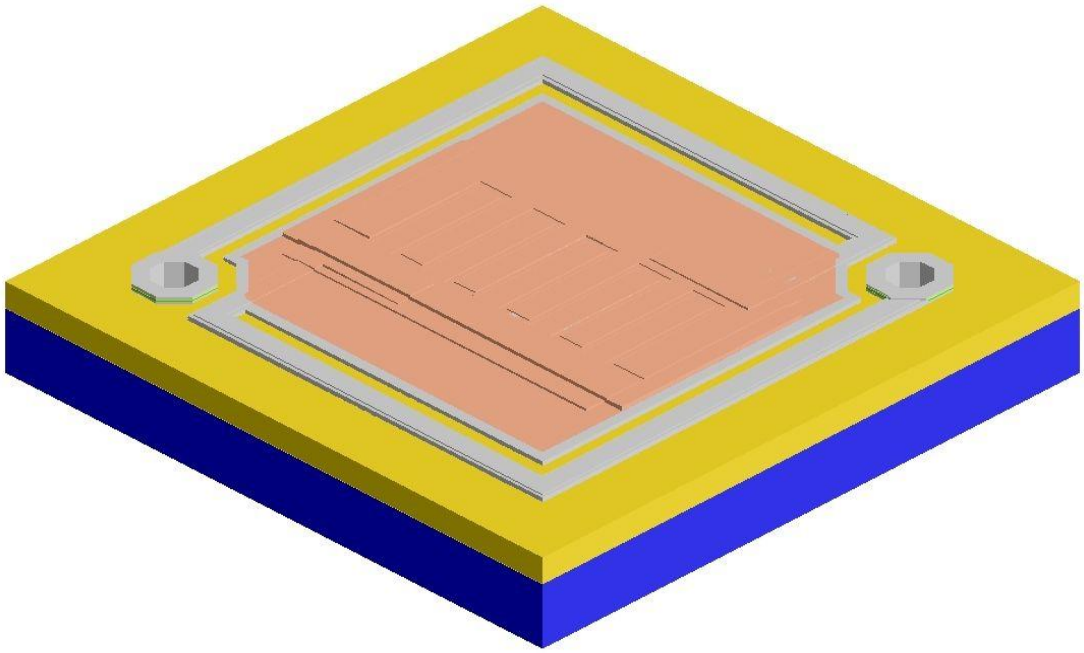


Figure 4.2 (h) Patterning of the upper structural layer to obtain the support arms and the body of the detector pixel.

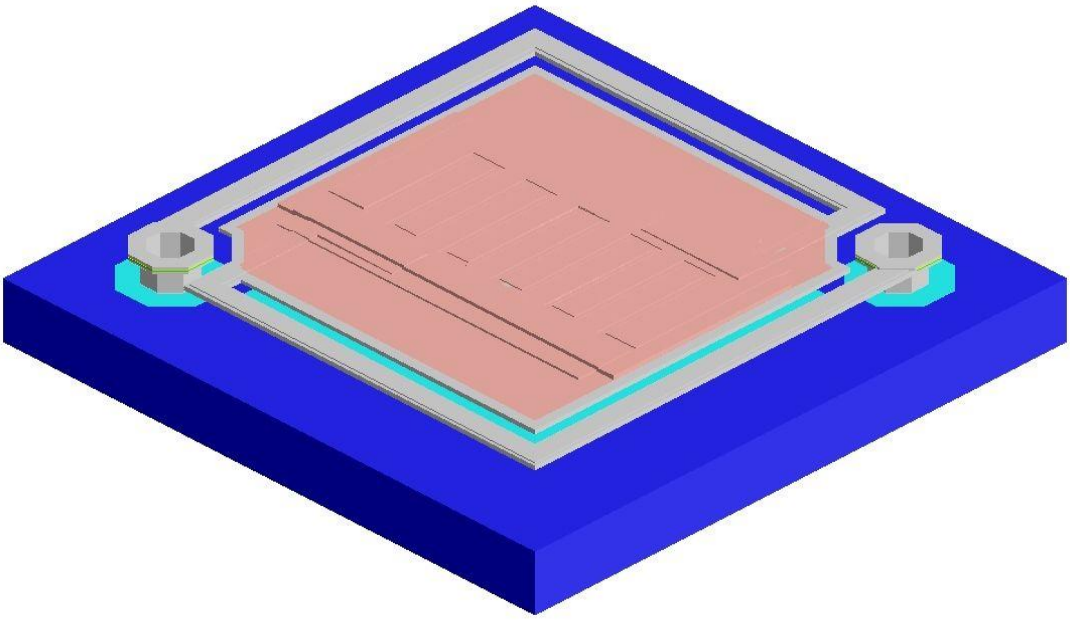


Figure 4.2 (i) Etching of the sacrificial layer and isolation of the detector pixel from the substrate.

Figure 4.2: The 3-D views of the detector pixel after each process step. The views are obtained from the model used in the Coventorware software.

## 4.2. Optimization of the Process Steps

The design of the process flow is followed by the optimization of the fabrication steps. A mask set consisting of many different pixels is designed in order to be used for the optimization of these fabrication steps. Figure 4.3 shows the layout of this mask set. This set is designed for 4" wafers and has 8 mask layers. There are three types of dies in the wafer, named as *die_v1*, *die_v2*, and *die_v3*. There are 115 of *die_v1*, 14 of *die_v2*, and 17 of *die_v3* in the mask set. *die_v1* consists of different types of pixels, while *die_v2* consists of arrays made up of these pixels. *die_v3* consists of alignment marks, characterization structures and some arrays of different pixels. Figure 4.4 gives the layouts of some of these different pixels. The optimization of each process step is explained in the following subsections. The results of the single pixel detector fabrication are given following the optimizations. The pixel given in Figure 4.4 (d) is *pixel_v2* which is used in most of the measurements due to some reasons. The reasons will be explained in detail in the following chapter.

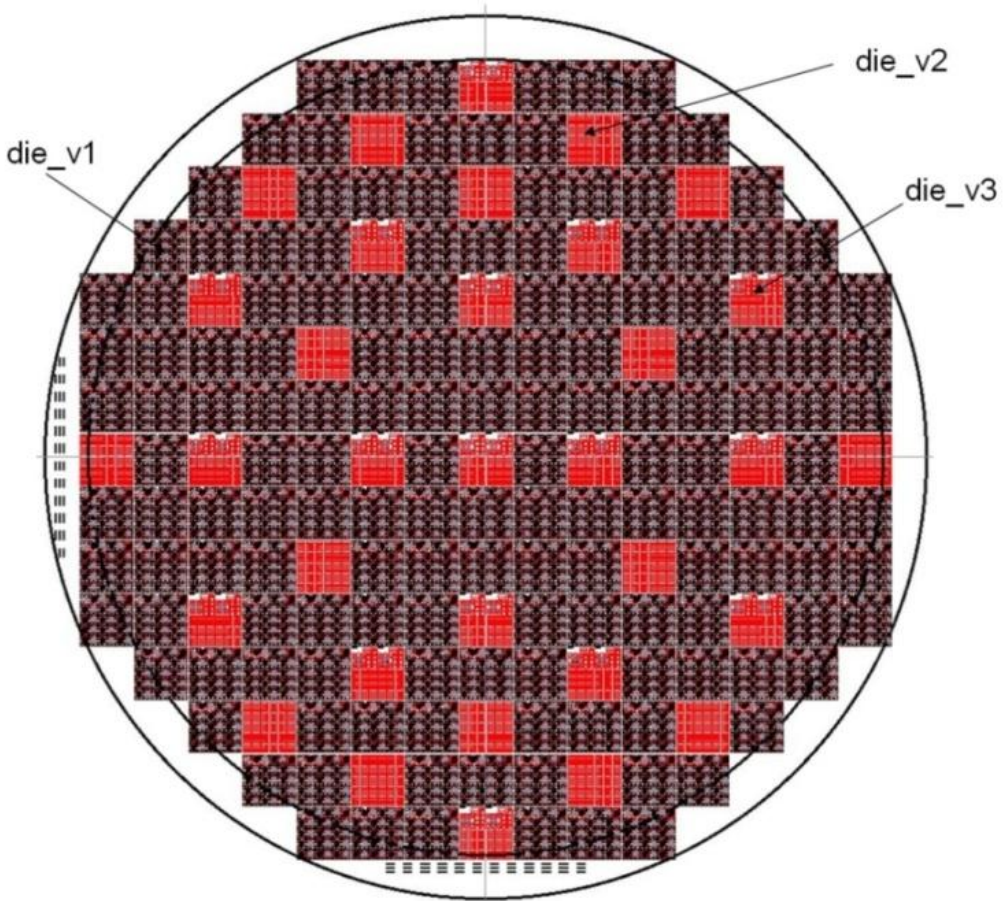



Figure 4.3: The layout of the designed mask set which is used for the optimization of the fabrication steps.

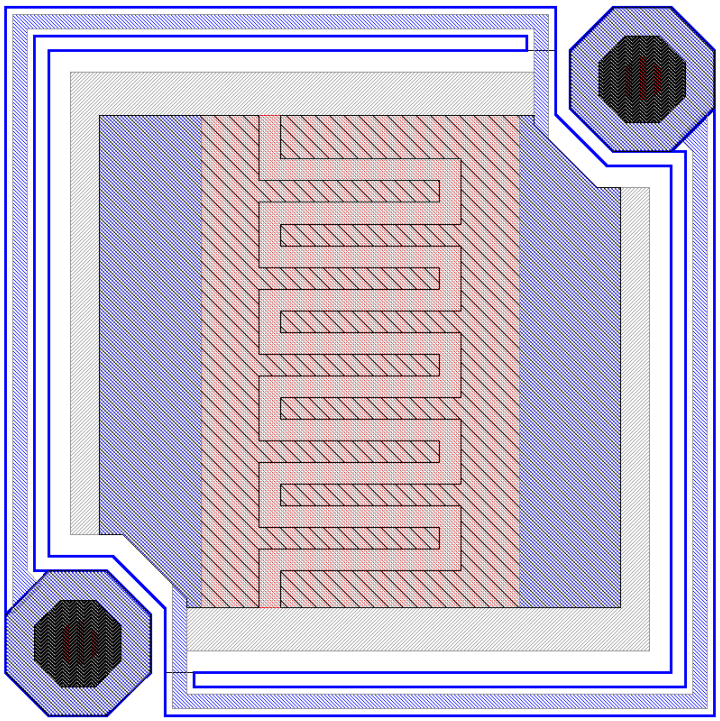


Figure 4.4 (a)

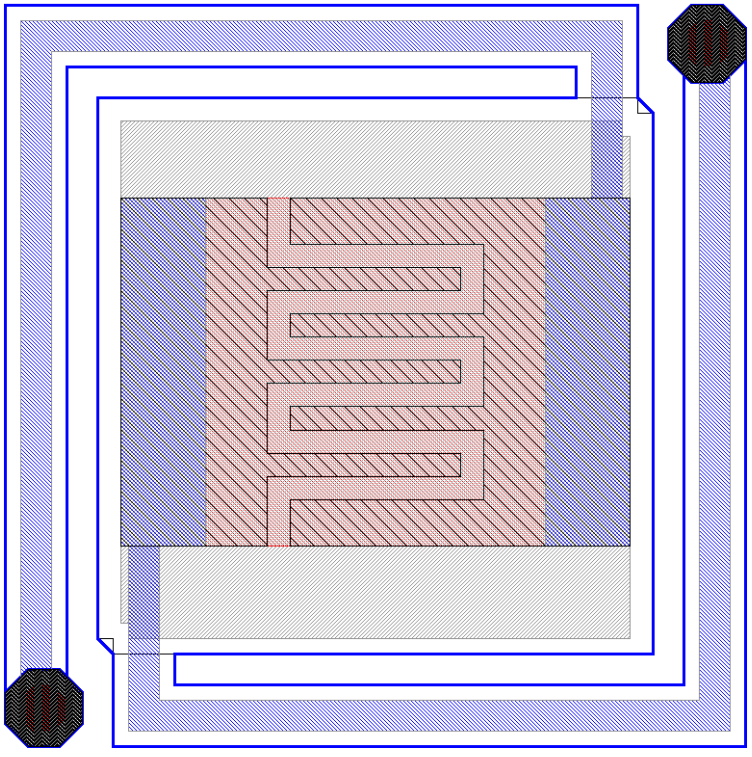


Figure 4.4 (b)

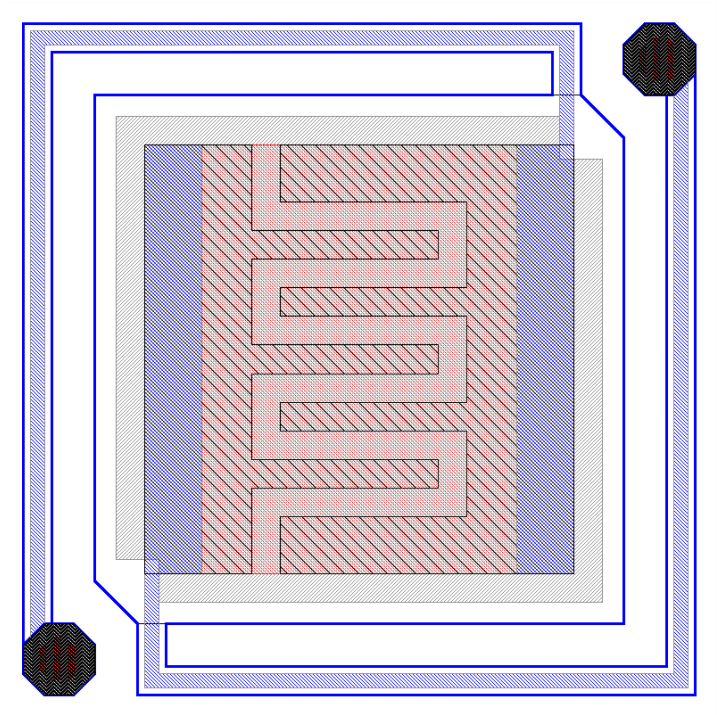


Figure 4.4 (c)

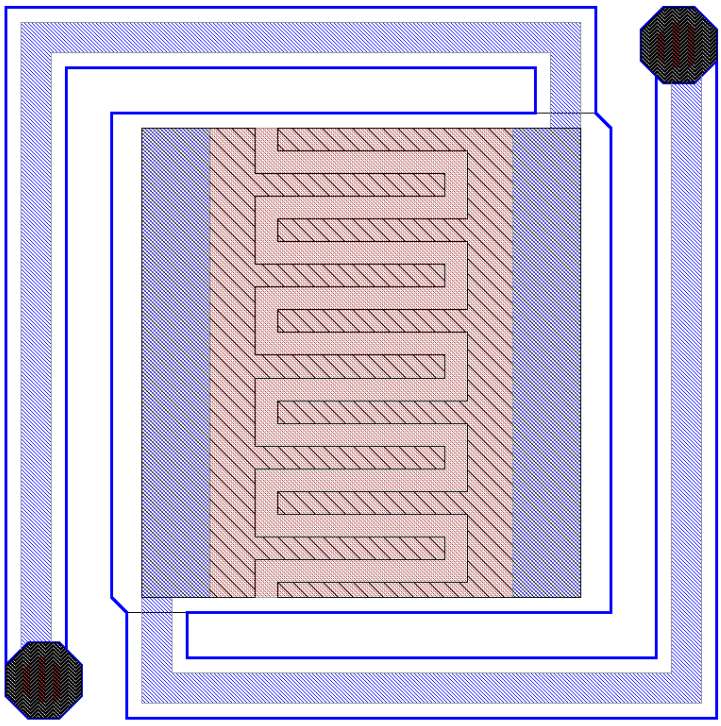


Figure 4.4 (d)

Figure 4.4: The layouts of some different pixels from the mask set.

### 4.2.1. Optimization of the Sacrificial Layer

One of the most important steps of the fabrication process is the deposition and patterning of the sacrificial layer. Mostly used sacrificial layers in the surface micromachining process are photoresist, polyimide, and amorphous-silicon (a-Si). Photoresist cannot be used in the fabrication of the microbolometers since the structural layer needs high temperature deposition conditions. So the polyimide material is the first choice as the sacrificial layer since the deposition of this material does not require any complicated system like a-Si.

Polyimide is deposited by a spin-coat process, and it is cured in an oven at 300 $^{o}$C to prevent swelling out during the structural layer deposition. Since it is cured at such a high temperature, it can only be patterned by etching it in a reactive ion etch (RIE) system. In the RIE system, a masking layer is necessary to pattern the polyimide material. Since the photoresists are organic materials like polyimides, it is difficult to find an etch recipe that has selectivity to photoresists. For this reason a hard metal like titanium, which will cause less *grassing* during RIE process, should be used as the masking layer together with the photoresist mask. After the curing of the polyimide, a titanium layer is deposited and patterned, followed by the RIE process of the polyimide layer. The photoresist and the titanium are stripped away after the RIE process. Figure 4.5 shows the SEM view of the successfully patterned polyimide layer. As can be seen from the figure the edge of the polyimide layer is vertical as desired.

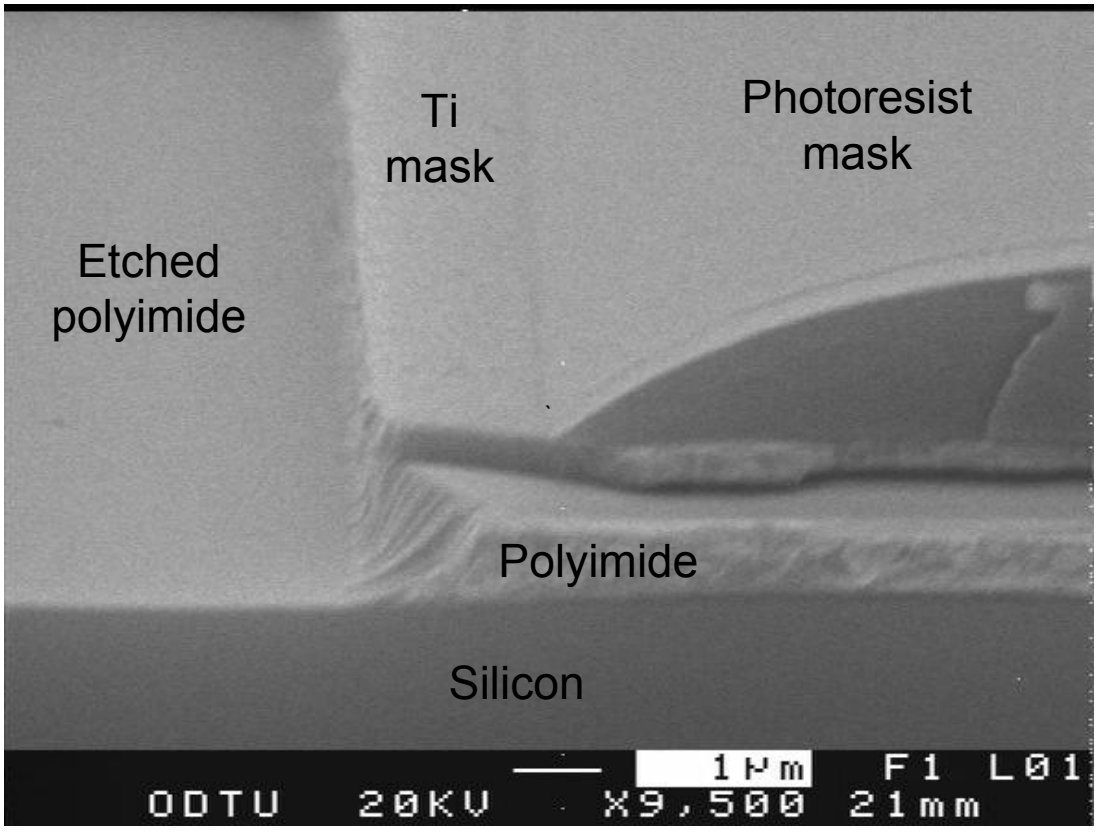
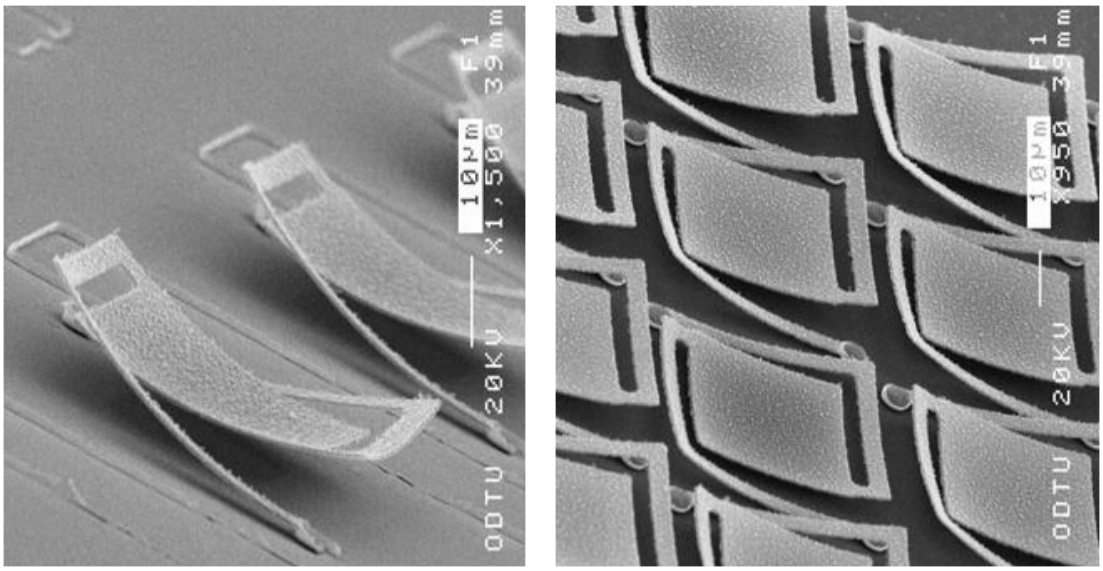



Figure 4.5: The SEM view of the successfully patterned polyimide layer. The edge of the polyimide layer is upright as desired.

The other important process related to the sacrificial layer is the etching of this layer in order to thermally isolate the detector pixel after the fabrication of the detector is completed. Aluminum bridges, which have shapes like detector pixel, are formed on the patterned polyimide layers for sacrificial etching trial of the polyimide layer. The polyimide layer underneath these bridges is etched away by using oxygen plasma, and the bridges are successfully suspended. Figure 4.6 shows the SEM views of the successfully suspended aluminum bridges. The bridges are bended due to the internal stress of the aluminum layer. The polyimide layer is decided to be used as the sacrificial layer of the microbolometer detector after all these process trials.




(a) (b)

Figure 4.6: The SEM views of the suspended aluminum bridges verifying that the polyimide layer can be successfully etched. The bridges are bended due to the internal stress of the aluminum layer.

### 4.2.2. Optimization of the Mirror Metal

The mirror metal is used to reflect the infrared signal incident on the microbolometer detector in order to increase the absorption of the detector. This metal should be shiny and should have a high conductivity, so that the assumption made in the cascaded transmission line model is acceptable. The alternatives for the mirror metal are aluminum, titanium, chromium, and gold. The first choice is aluminum because it is cheap and easy to process. It can be etched without much undercut. But it is seen during the process trials that, the aluminum layer is etched away during the strip process of the titanium layer which is used as the mask of the polyimide. Due to this reason aluminum and titanium are decided not to be used as the mirror metal. Chromium is the second choice because it has good adhesion properties and it is not etched in titanium etchant during the strip process of titanium. But chromium is etched away in oxygen plasma during the etching of the polyimide at the end of the process. Considering all these effects gold is chosen as

the mirror metal. Since it does not have good adhesion properties to silicon dioxide and silicon nitride a thin layer of chromium is deposited under the gold layer. Figure 4.7 shows successfully patterned chromium/gold mirror of the microbolometer pixel.

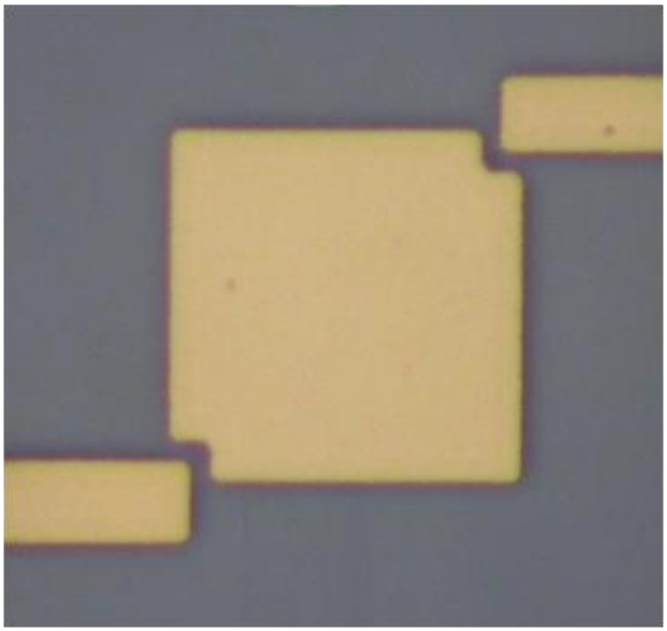
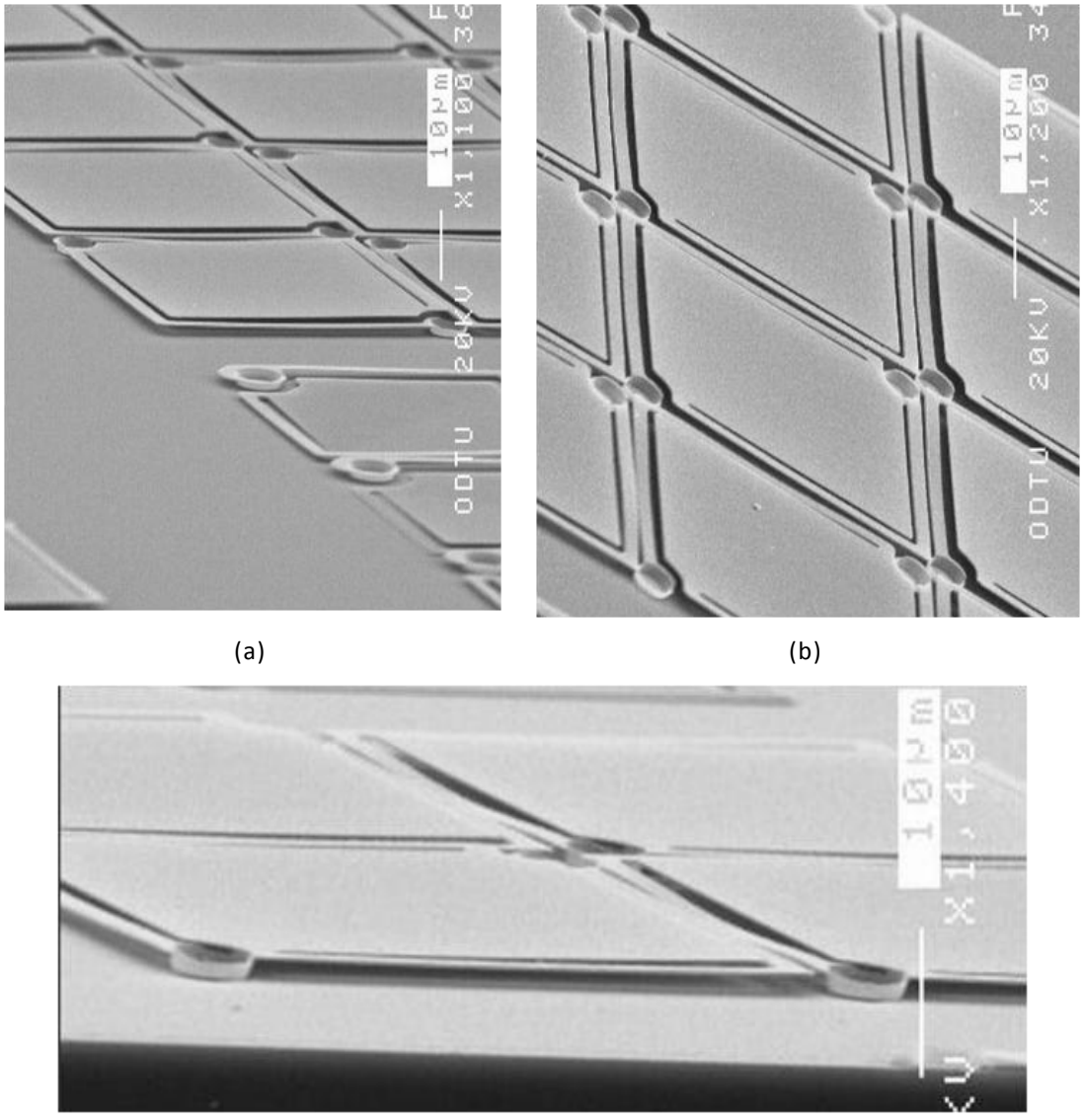


Figure 4.7: Successfully patterned chromium/gold mirror of the microbolometer pixel.

### 4.2.3. Optimization of the Structural Layer

Another important layer in the microbolometer detector is the structural layer that the other parts of the detector will stand on. The important properties of this layer are given in the previous section so will not be repeated here. The alternatives for the structural layer are silicon dioxide ($SiO_2$) and silicon nitride ($Si_3N_4$). As mentioned in Chapter 3, silicon nitride layer has a low thermal conductivity value [100-102] as opposed to the general knowledge [105]. Therefore, there is not much difference between silicon nitride and silicon dioxide when the thermal conductivity is considered. Since it is very difficult to make a stress free silicon dioxide layer,

silicon nitride is chosen as the structural layer. The nitride layer can be deposited with a PECVD system at low temperatures with dual frequency configuration to be stress free. Figure 4.8 shows the SEM pictures of the suspended nitride bridges patterned in detector shape. As can be seen from the figure, the layer is stress free and can be used as the structural layer of the detector.




(a) (b)

(c)

Figure 4.8: The SEM pictures of the suspended nitride bridges patterned in detector shape. As can be seen the layer is stress free and can be used as the structural layer of the detector.

### 4.2.4. Optimization of Interconnect Metal and the Electrode Metal

There should be an electrically conductive layer on the support arms to carry the electrical signal from the active material to the readout circuit. This layer should have a high electrical conductivity value to have low arm resistance and low thermal conductivity to have good thermal isolation. The width and the thickness of this layer should be able to be made as narrow as possible for better thermal isolation. Titanium has a relatively low thermal conductance when compared with aluminum, chromium, and gold. It can also be deposited with sputter to have small thickness values, and its etchant makes little undercut. All these properties show that narrow and thin lines can be patterned using titanium. So titanium is decided to be used as the interconnect material in the detectors. Figure 4.9 shows the successfully patterned titanium lines.

There should be an electrode metal that will electrically connect the YBCO layer to the interconnect material. Titanium cannot be used directly because it does not make ohmic contact to YBCO layer. There are three metals that can make ohmic contact to YBCO layer with a low contact resistance, which are gold, platinum, and silver [64]. The process of gold is easier than the other metals, so gold is selected as the electrode metal.

The electrode metal should be patterned as finger structure due to the high resistivity of the YBCO layer as explained in the previous chapter. The number of the fingers should be increased to decrease the resistance value, so the width of the fingers should be small. Also, the distance between the fingers should be decreased. The commercial gold etchant has a high undercut value, and it is not possible to have narrow fingers and small distances between the fingers. Due to this reason, a new gold etchant which has very low undercut values is developed by diluting “Aqua Regia”. Using this etchant gold fingers are successfully patterned as the electrode material. Figure 4.9 shows successfully patterned gold fingers.

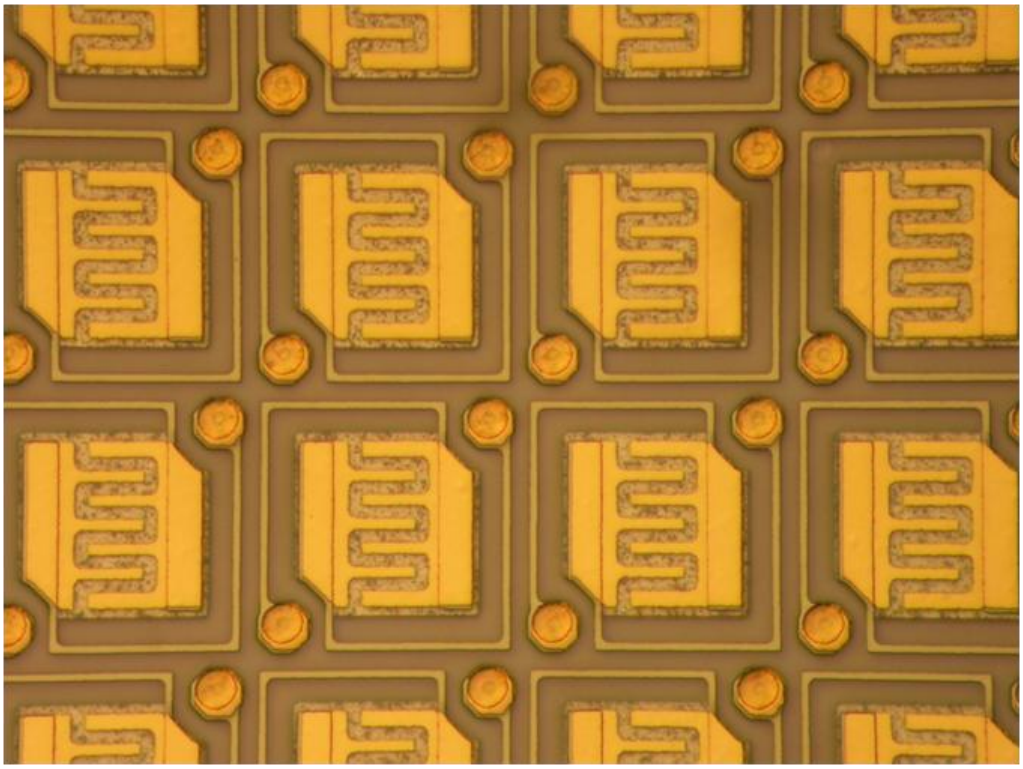


Figure 4.9: Successfully patterned titanium as the interconnect metal and the gold fingers as the electrode metal.

### 4.2.5. Optimization of the YBaCuO Layer

YBaCuO material is a relatively new material as a microbolometer active layer. When it is deposited in crystal form it can be used as a superconductor, while in the amorphous form it can be used as a semiconductor with a high TCR value. The layer's reported TCR values are generally higher than the other common microbolometer materials like $VO_X$ and a-Si [63, 67] as stated in the previous chapter. But, it is also reported that the resistivity of this material depends highly on the oxygen amount in the material and can be high resulting in large resistance values [67]. For this reason, the resistivity of this layer is tried to be reduced as much as possible by changing the oxygen ratio in the gas environment during the deposition process in sputter system. The resistivity of each deposited YBCO layer

is measured with by using two resistances whose dimensions are different and known. Figure 4.10 shows the measured variation of the resistivity of the YBCO layer with the oxygen ratio change. A minimum resistivity of 255 Ω-cm is obtained for an oxygen ratio of 5 %. This resistivity value is larger than the data in literature (90 Ω-cm), due to the oxygen amount of the YBCO target used in the sputter system. This resistivity value is also suitable to be used in high performance detectors, although it is higher than the values in literature.

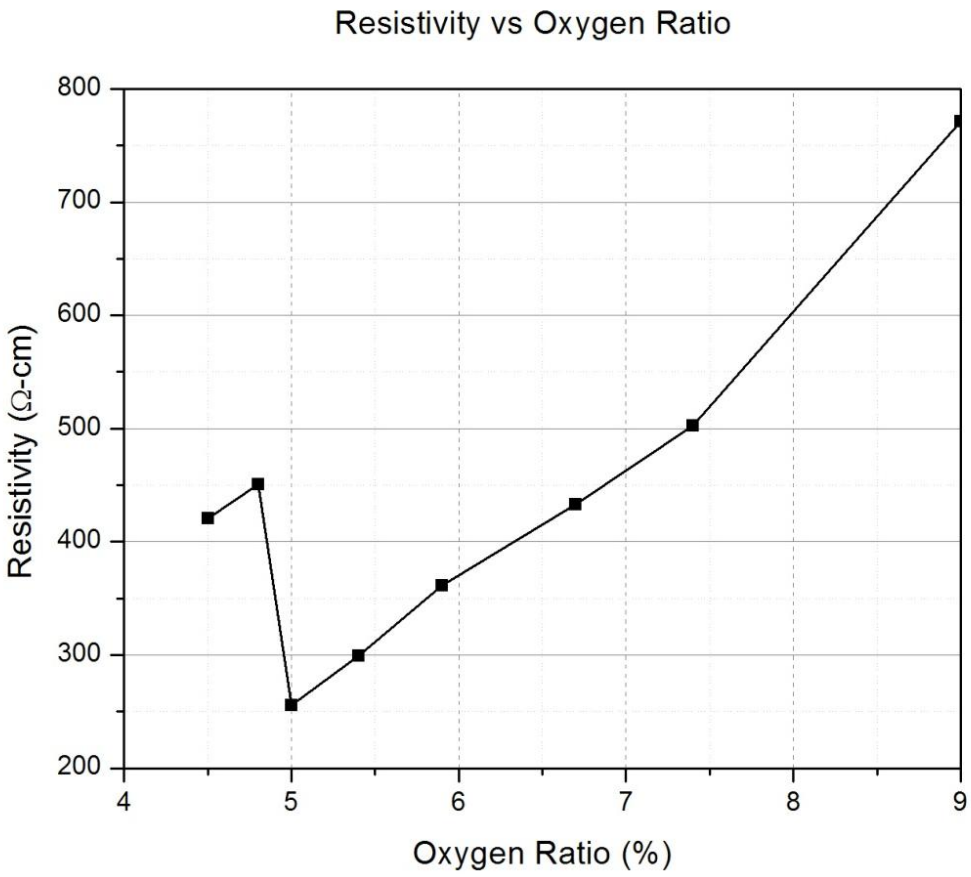



Figure 4.10: The variation of the resistivity of YBCO layer with the oxygen amount change. A minimum resistivity of 255 Ω/cm is obtained for an oxygen amount of 5 %.

The TCR of the YBCO layer is also measured with the change of the oxygen amount in the sputter environment. The details of the measurement setup are given in Section 5.1. Figure 4.11 shows the change of the TCR value of the YBCO layer with the oxygen amount variation. As can be seen from the figure, the TCR values are very close to each other. The highest measured TCR value is -3.6 %/K with an oxygen ratio of 7.4 %. On the other hand, YBCO at this oxygen ratio has a resistivity of 500 Ω-cm. When compared with the oxygen ratio of 5%, there is an increase of 6 % in the TCR value, while the resistivity increases 100 % making the overall performance to decrease since the resistance will increase and the bias current will decrease. Figure 4.12 shows the variation of NETD with the oxygen ratio calculated using the measured resistivity and the TCR values. As can be seen from the figure, the optimum oxygen amount to have the highest performance is 5 % for the finger type electrodes when the resistivity and TCR of the YBCO layer are considered together. The performance can increase further with the deposition environment of a 7.4 % oxygen ratio, if a different electrode structure is designed to decrease the resistance value.

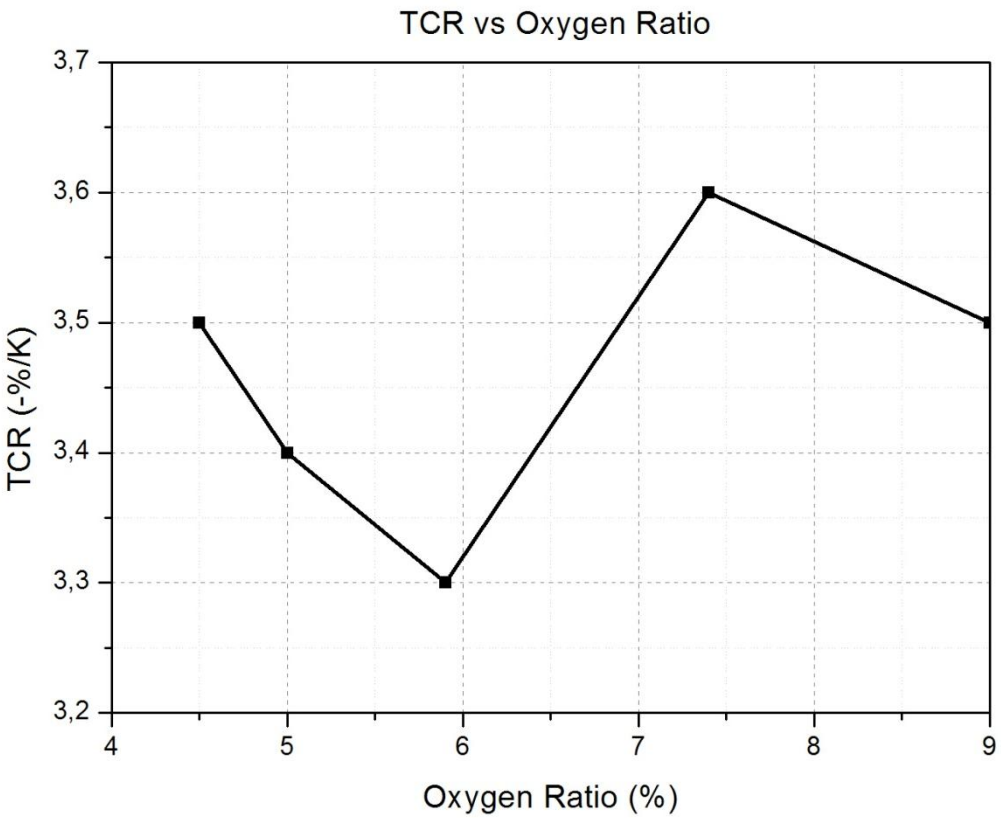



Figure 4.11: The change of the TCR value of the YBCO layer with the oxygen amount variation. As can be seen from the figure the TCR values are very close to each other. The highest measured TCR value is -3.6 %/K with an oxygen ratio of 7.4 %.

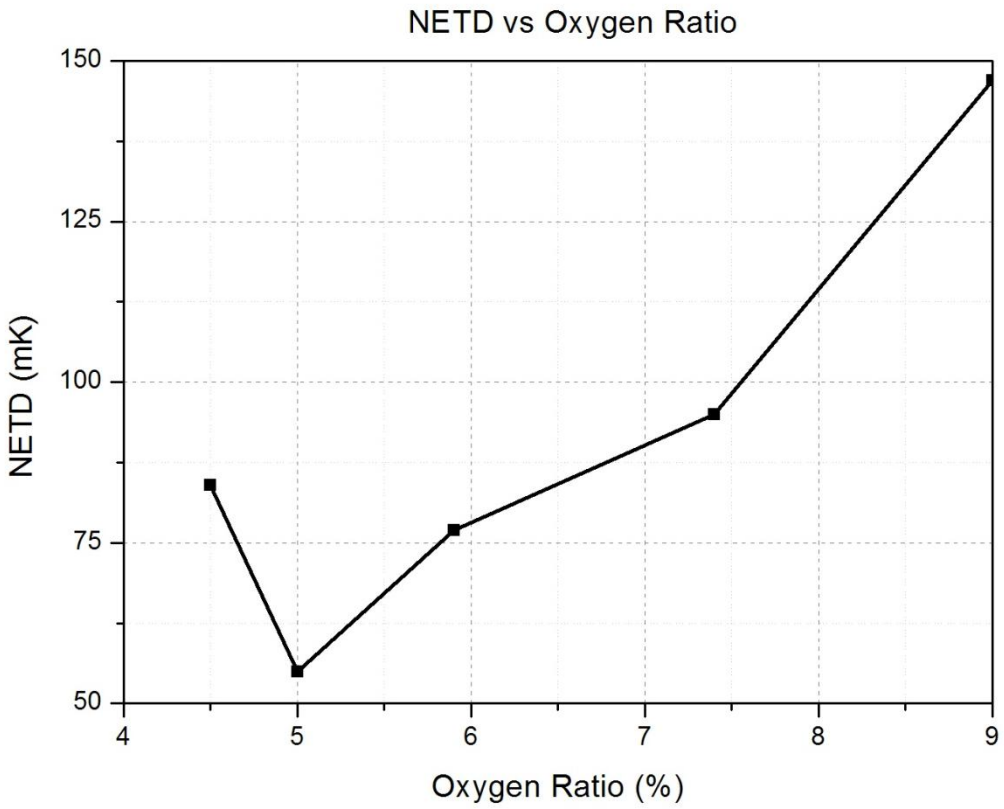



Figure 4.12: The change of the NETD value with the oxygen amount variation. As can be seen from the figure, the optimum oxygen amount to have the highest performance is 5 % for the finger type electrodes when the resistivity and TCR of the YBCO layer are considered together.

### 4.2.6. Optimization of the Absorber Layer

The absorber layer is used to increase the absorptance of the detectors and increase the performance. Thin film metallic layers like titanium nitride (TiN), goldblack, and nichrome (NiCr) are generally used as the absorber layer in the microbolometer detectors [67, 109, 110]. The sheet resistance of this layer should be adjusted to 377 Ω/□ in order to obtain the maximum absorption value as explained in the previous chapter. The layer should also be compatible with the other processes and layers of the microbolometer detector. Considering all these, the TiN layer is chosen as the absorber layer, and a sheet resistance of 377 Ω/□ is

obtained for a thickness of 5-7 nm. This thickness value is compatible with the data in the literature.

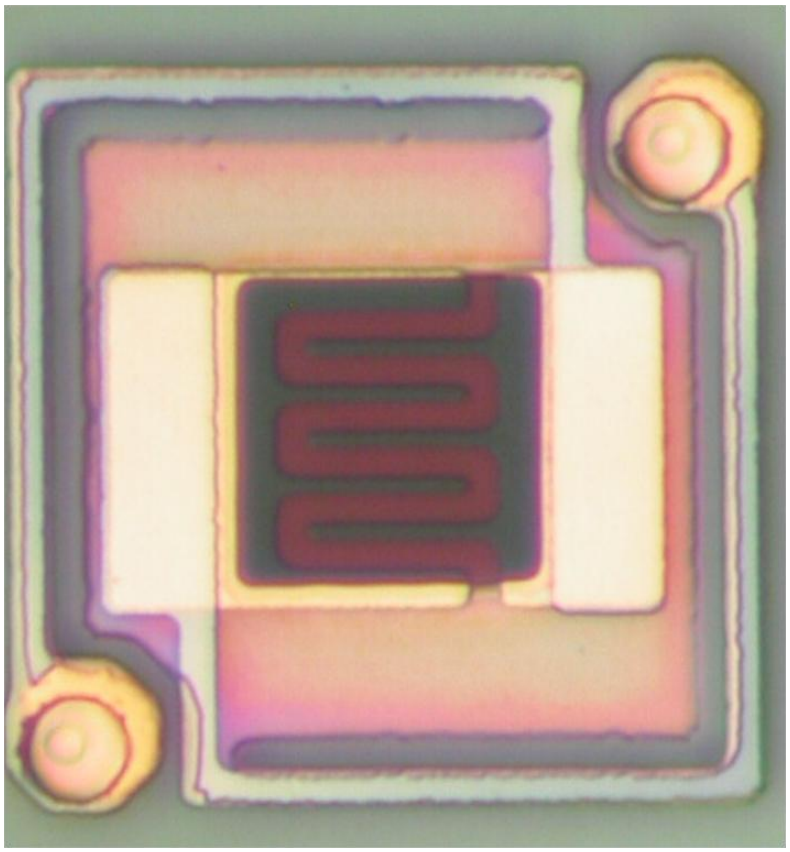


Figure 4.13: Microscopic view of a successfully fabricated microbolometer detector.

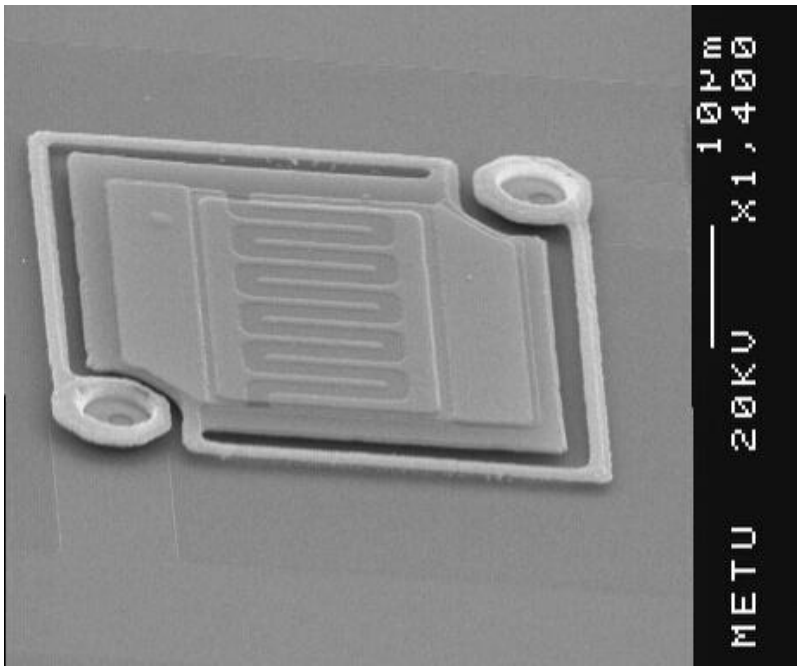
### 4.2.7. Fabrication Results of the Single Pixel Microbolometer Detector

The optimizations of the steps are followed by the realization of the fabrication process. This realization is performed by using the mask set explained in previous sections. Many different pixels are fabricated. The fabrication of the microbolometer detectors starts with the formation of the mirror underneath the pixel. The sacrificial and the structural layer are deposited and patterned. Following these layers interconnect metal, electrode metal and active material are

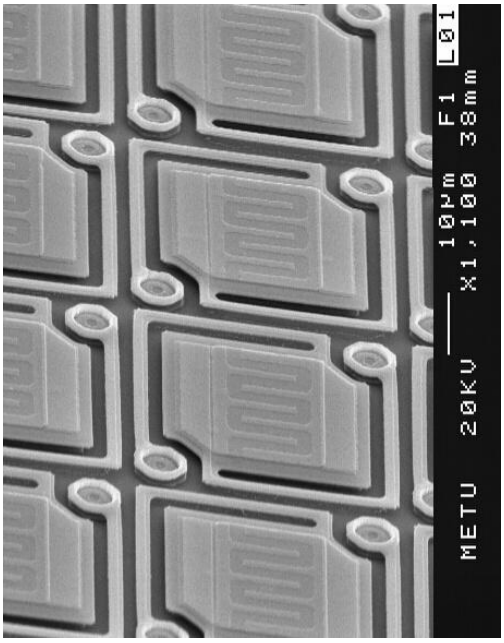
formed. The absorber layer is patterned, and it is followed by the etching of the sacrificial layer in order to thermally isolate the detector pixel. The details of the fabrication are given in Appendix C. Figure 4.13 shows the microscopic view of a fabricated microbolometer detector pixel, while Figure 4.14 shows the SEM views of the fabricated detectors. As can be seen from the SEM views, the detectors are suspended and thermally isolated from the substrate. Also the detectors are standing without any buckling since there is no stress in the arms due to the stress free nitride layer.

## 4.3. Conclusions

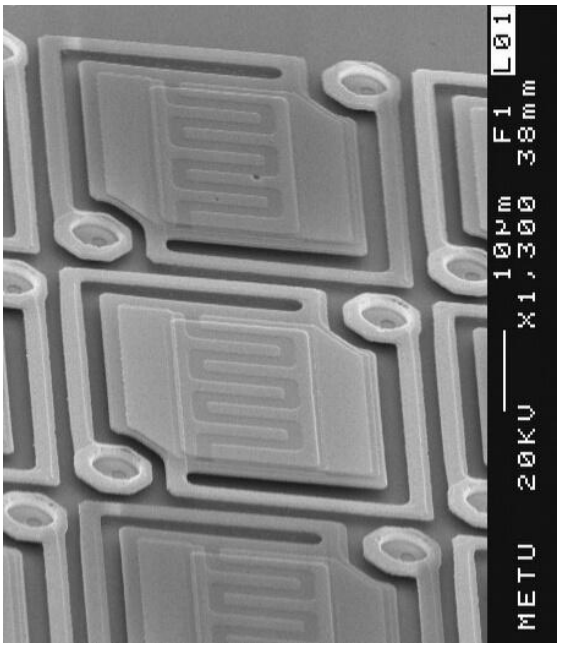
The process optimization and fabrication of a single pixel microbolometer detector are explained in this chapter. The microbolometer detector is resistive type and fabricated using the surface micromachined MEMS technology as stated in previous chapter. The design of the fabrication steps and the optimization of the each layer that are used in these steps are explained. The realization of the fabrication of the detectors is presented. As a result it can be stated that the single pixel detectors are successfully fabricated and ready to be tested.




(a)




(b)




(c)

Figure 4.14: The SEM views of the fabricated detectors. As can be seen from the views, the detectors are suspended and thermally isolated from the substrate. Also the detectors are standing without any buckling since there is no stress in the arms due to the stress free nitride layer.

# CHAPTER 5

# TEST RESULTS OF FABRICATED SINGLE PIXEL MICROBOLOMETER DETECTORS

This chapter presents the test results of the fabricated single pixel microbolometer detectors. Section 5.1 gives the procedure and results of the TCR measurements while Section 5.2 defines a method and a mathematical formulation to measure the thermal conductance and gives the results of the thermal conductance measurements. Section 5.3 presents the noise measurement results. Section 5.4 explains the responsivity measurement and presents the measured results. These results include responsivity values and the absorptance of the detector pixel. Section 5.5 summarizes the measurement results, gives expected performance values and concludes the chapter.

## 5.1. TCR Measurements

TCR is one of the most important parameters of the microbolometer material as explained in Chapter 2. The measurement of TCR is performed in a Tenney environmental chamber by using an unsuspended detector in order to eliminate the effect of the electrical heating. The change in the environment temperature is measured by a temperature sensor (AD590) which gives the absolute temperature directly at the output. The temperature of the environmental chamber is changed from 19 to 31 °C, and the voltage of the detector is measured while it is biased with a constant current. The resistance change with the temperature is fitted into a

polynomial, and the TCR value is found using the expression of the polynomial. Figure 5.1 shows the picture of the sample and the temperature sensor used in TCR measurements. Figure 5.2 shows the resistance and TCR variation with the changing temperature. The TCR value at the room temperature (25 $^{o}$C) is measured approximately as -3.4 %/K. This TCR value is higher than the TCR values of the common microbolometer materials like $VO_x$ and a-Si, and it is one of the highest values reported among YBCO materials which have reasonable resistivity values [63, 67].

## 5.2. Thermal Conductance Measurements

Thermal conductance is the measure of the thermal isolation of the detector from the substrate as explained in Chapter 2. The sacrificial layer underneath the detector structure should be etched away, and the detector should be in vacuum for the thermal conductance measurements. The detectors are thermally isolated from the substrate as explained in the previous chapter, and they are placed in an in-house built vacuum dewar for the thermal conductance measurements. Figure 5.3 shows the pictures of this vacuum dewar.

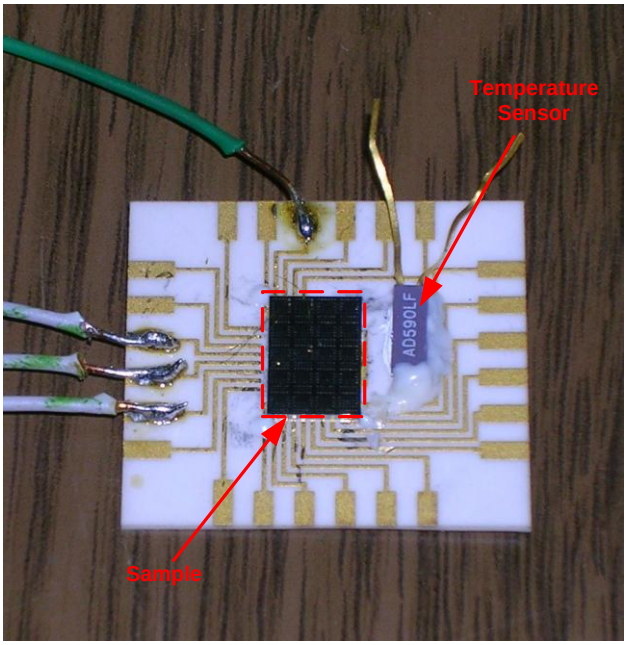



Figure 5.1: The sample and the temperature sensor used in TCR measurements.

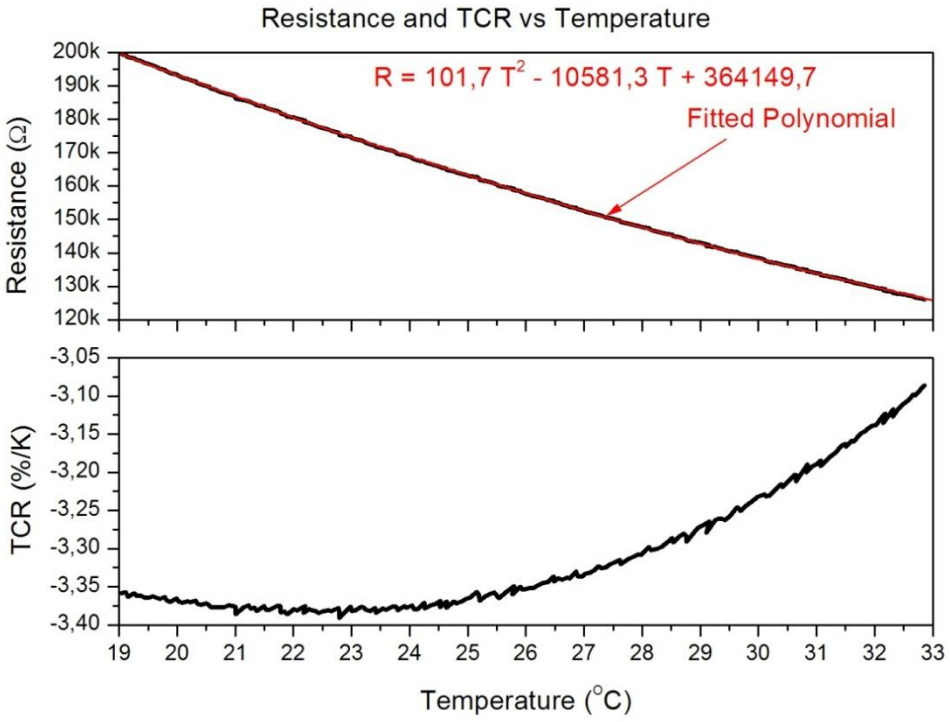
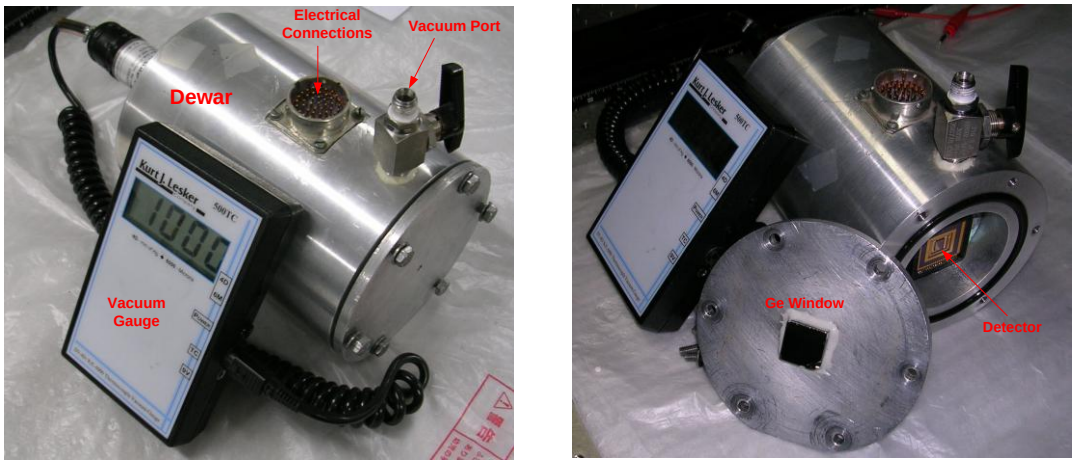



Figure 5.2: Resistance and TCR variation with the changing temperature. The TCR value at the room temperature (25 °C) is measured approximately as -3.4 %/K.




(a) (b)

Figure 5.3: The vacuum dewar used in the thermal conductance measurements.

In order to measure the thermal conductance, a constant current is applied to the detector under atmospheric pressure, and the voltage is measured. This voltage is divided by the applied current, and the detector resistance is calculated. This is the real resistance of the detector, because, at atmospheric pressure it is assumed that the detector is not heated up with the applied electrical power. Then, the dewar is vacuumed, the same constant current is applied, and the voltage of the detector is measured again. This time the resistance is different because the detector is heated up with the applied electrical power. By using Equation 2.1 the resistance under the vacuum environment can be written as

$$R = R_0(1 - \alpha t_u)^n \tag{5.1}$$

where $R$ is the detector resistance under vacuum, $R_0$ is the detector resistance at atmospheric pressure, $\alpha$ is the TCR of the detector resistance, $t_u$ is the unit temperature change, and $n$ is the number of units that the temperature changes in order obtain $R$ value. The total temperature change in the detector is given as

$$\Delta T = nt_u \tag{5.2}$$

The target of the measurement is to find the total temperature change in order to calculate the thermal conductance value. If the natural logarithm of both sides of Equation 5.1 is taken and some arrangements are performed, the expression becomes

$$nln(1-\alpha t_u) = ln(\frac{R}{R_0}) \tag{5.3}$$

and the value of $n$ can be found as

$$n = \frac{ln(\frac{R}{R_0})}{ln(1-\alpha t_u)} \tag{5.4}$$

Using this equation the total temperature change can be written as

$$\Delta T = t_u \frac{ln(\frac{R}{R_0})}{ln(1-\alpha t_u)} \tag{5.5}$$

If the unit temperature change is reduced the total temperature change can be calculated more accurately. So taking the limit of $nt_u$ as $t_u$ approaches 0 gives

$$\Delta T = \lim_{t_u \to 0} nt_u = \lim_{t_u \to 0} t_u \frac{ln(\frac{R}{R_0})}{ln(1-\alpha t_u)} = \lim_{t_u \to 0} \frac{ln(\frac{R}{R_0})}{(-\alpha/1-\alpha t_u)} = -ln(\frac{R}{R_0}).\frac{1}{\alpha} \tag{5.6}$$

Using this equation the thermal conductance value of the pixel can be found as

$$G_{th} = \frac{P_{elec}}{\Delta T} = \frac{I^2 R}{ln(\frac{R}{R_0}).\frac{1}{\alpha}} = \frac{I^2 R\,\alpha}{ln(\frac{R}{R_0})} \tag{5.7}$$

where $G_{th}$ is the thermal conductance of the detector, $P_{elec}$ is the applied electrical power, $\Delta T$ is the total temperature change, $R$ is the detector resistance under vacuum, $R_0$ is the detector resistance at atmospheric pressure, $\alpha$ is the TCR of the

detector resistance, and $I$ is the applied bias current. This method gives more accurate results than the methods in literature [102, 111] which uses the TCR equation directly to find the temperature change. It is possible to use the TCR equation directly when the temperature change is very small since the applied current is very low. But total temperature change deviates from the correct result as the applied current is increased, since the TCR value is a ratio of the initial resistance to the final resistance, and it becomes obligatory to use Equation 5.7 to find the thermal conductance value.

The thermal conductance value of one of the fabricated single pixel detectors is measured using the method above. The measured detector (*pixel_v2*) is different than the one given in Figure 3.9 (*pixel_v1*), since the detector designed in Chapter 3 could not be tested as a single pixel due to some problems. The main problem is the sticking of the pixel to the substrate before the test is completed. This sticking problem is not due to the stress on the arms or the mass of the detector, but is probably due to the charging of the pixels during the long etching of the sacrificial layer in RIE system. It is anticipated that, the sticking problem is going to be solved with an oxygen plasma system that has high polyimide etch rates and does not charge the etched devices. The other problem is that the readout circuit of the FPA does not allow the pixels to be tested independently, so the detectors that are fabricated in the FPAs could not be tested. Figure 5.4 shows the layout of the pixel that is used during the thermal conductance measurements (the pixel is also given in Figure 4.4 (d)). This pixel also has a pixel pitch of 50 µm, but the support arm width and the spacing are different than the pixel used in the array. The support arm width is 4 µm where the interconnect metal width is 2 µm and the spacing is 3 µm. The length of the arms is 80 µm which is 0.5 µm shorter than the pixel used in the array.

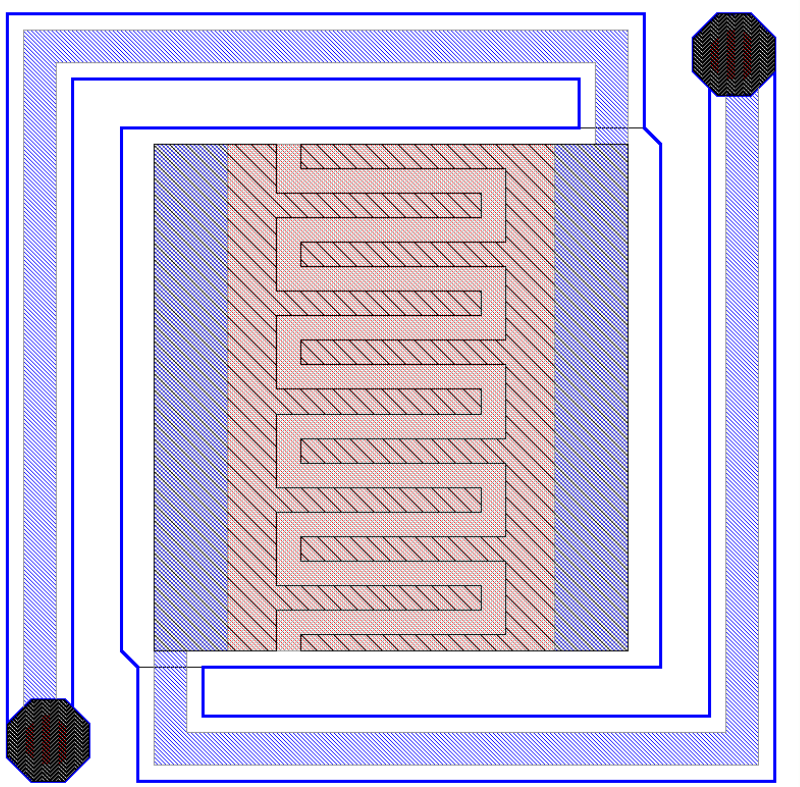


Figure 5.4: The layout of the pixel used in thermal conductance measurements (*pixel_v2*). This pixel also has a pixel pitch of 50 µm, but the support arm width and the spacing is different than the pixel used in the array. The support arm width is 4 µm where the interconnect metal width is 2 µm and the spacing is 3 µm. The length of the arms is 80 µm which is 0.5 µm shorter than the pixel used in the array.

Figure 5.5 shows the result of the thermal simulation of *pixel_v2* performed using the Coventorware software. The thermal conductance value is simulated as $1.35 \times 10^{-7}$ W/K which is higher than the simulated value of *pixel_v1* ($9.4 \times 10^{-8}$ W/K) due to the wider support arms. Figure 5.6 shows the thermal conductance value of *pixel_v2* with the changing vacuum level. The minimum measured thermal conductance is $1.27 \times 10^{-7}$ W/K which is smaller than the simulated value. This can be due to the different thermal conductivities of the layers used in the detector. Using the ratio of the simulations the real thermal conductance value of *pixel_v1* can be assumed as $9.0 \times 10^{-8}$ W/K. This value is the smallest value compared to all reported YBCO based microbolometers.

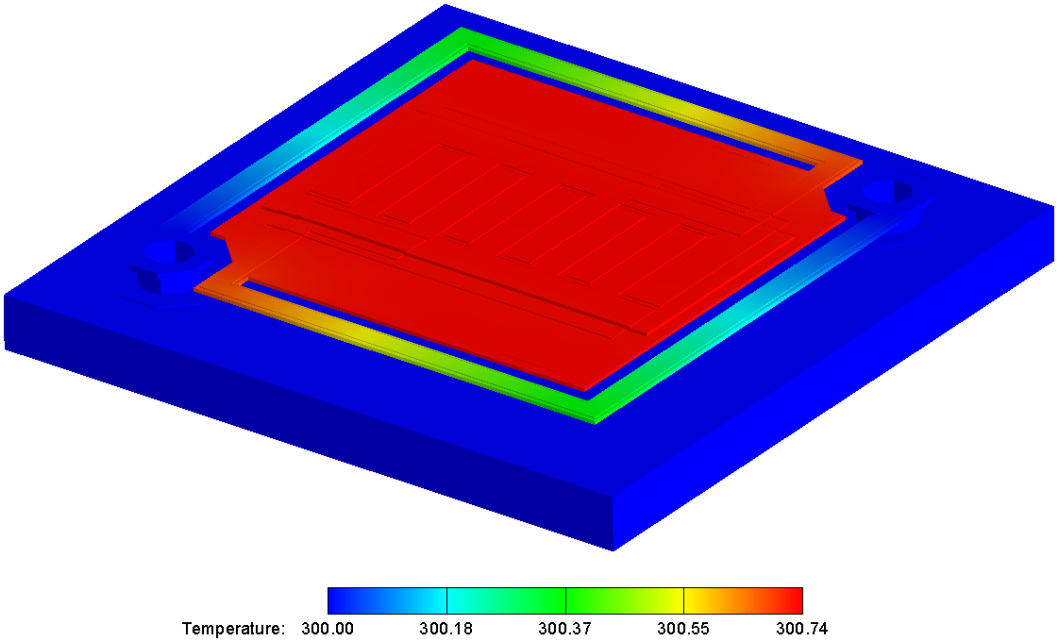



Figure 5.5: The result of the thermal simulation of *pixel_v2* performed using Coventorware software. The thermal conductance value is simulated as $1.35 \times 10^{-7}$ W/K which is higher than the simulated value of *pixel_v1* due to the wider support arms.

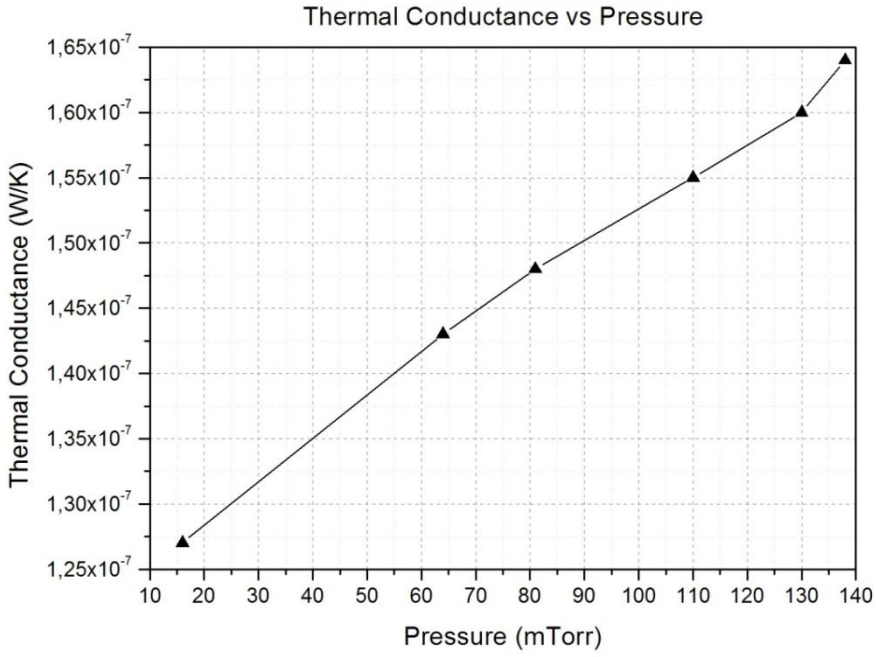



Figure 5.6: The thermal conductance value of *pixel_v2* with the changing vacuum level. The minimum measured thermal conductance is $1.27 \times 10^{-7}$ W/K which is smaller than the simulated value.

## 5.3. Noise Measurements

The noise of the detector resistance is a key parameter for the performance of the microbolometer detectors. Every resistance has a thermal noise under bias or no-bias conditions and has 1/f noise under bias conditions as explained in Chapter 2. The frequency at which these two noises become equal is called the *1/f corner frequency*. This frequency should be as low as possible in order for the noise to be low and the detector to have high performance. Figure 5.7 shows the power spectral density of a detector having 106 kΩ resistance at room temperature (this measurement is done by Mr. Murat Tepegöz). The measurement is performed with the setup suggested in [18] and two identical resistances are used to make the input DC point of the amplifier zero. The measurement is made at different bias values to see the effect of the bias on the noise value. As can be seen from the figure, there is no 1/f noise if no bias is applied to the detector. The corner frequency increases as the applied bias value increases. The corner frequencies for 27 μA and 54 μA are 1.6 kHz and 4.3 kHz, respectively. These values are a bit higher than the values in literature [67], but still can be used in high performance detectors.

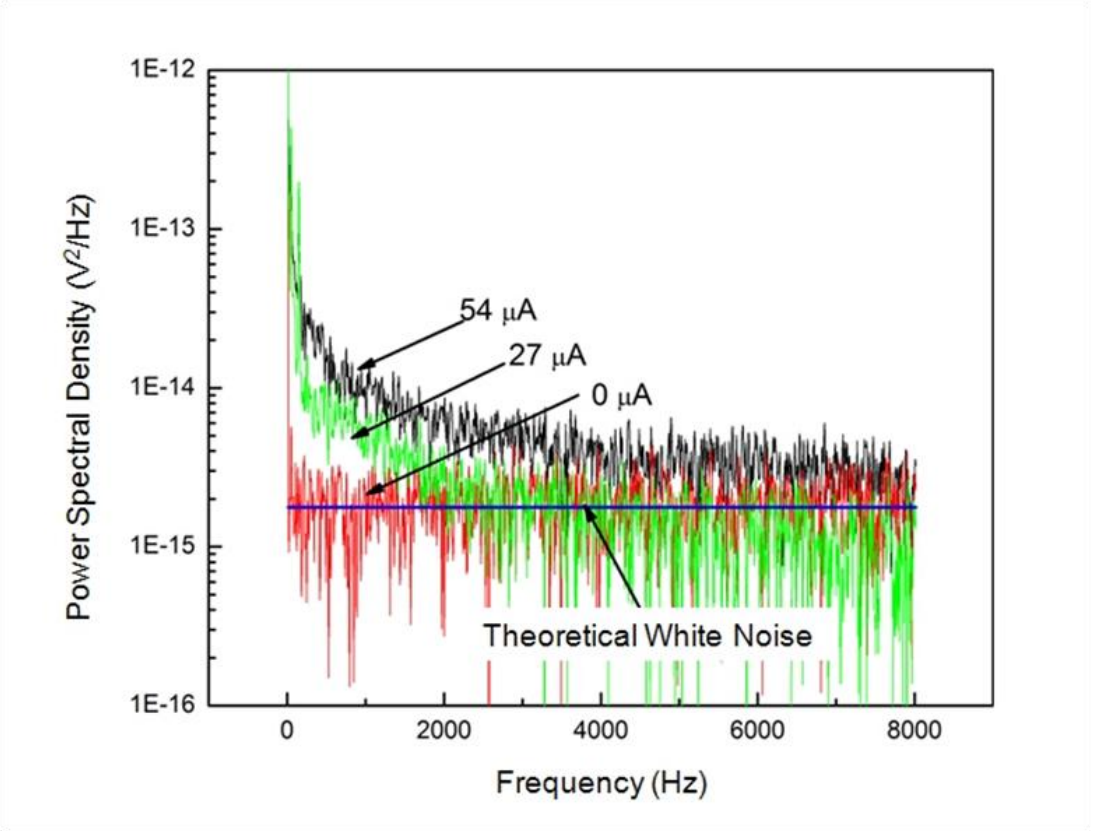



Figure 5.7: The power spectral density of a detector having 106 kΩ resistance at room temperature (this measurement is done by Mr. Murat Tepegöz). The corner frequencies for 27 μA and 54 μA are 1.6 kHz and 4.3 kHz respectively.

## 5.4. Responsivity Measurements

Responsivity is another important parameter for the microbolometer detectors. It is simply the output signal change with the incident infrared power. Chapter 2 gives the details of the responsivity and they will not be repeated here. Figure 5.8 shows the test setup that is used to measure the responsivity of the fabricated detector. The detector is placed in a vacuum dewar in order to eliminate the thermal conductance of air and to increase the performance of the detector. There is a germanium (Ge) window in front of the dewar for the infrared radiation to enter the dewar. The blackbody is heated to 1000 °C, and the radiation coming from the blackbody is modulated by the help of a frequency controlled chopper. A reference

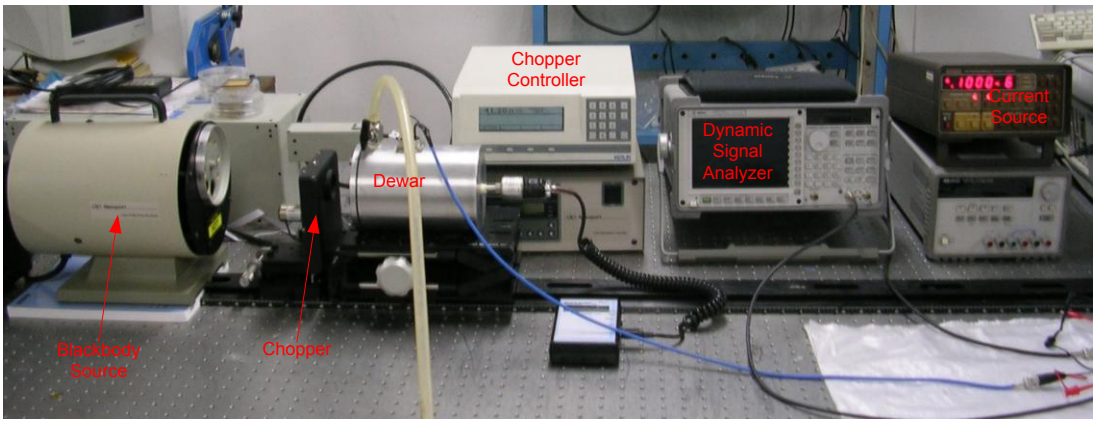
detector is used to measure the power of the infrared radiation. The detector is biased at constant current (0.1 μA in this test in order to eliminate the self-heating effect) with a current source and the voltage across the detector is measured with dynamic signal analyzer (Agilent 35670A). The signal at the chopping frequency gives the voltage value on the detector due to the infrared radiation. The ratio of this voltage to the incident infrared power gives the voltage responsivity of the detector at that frequency. The voltage responsivity of a microbolometer detector ($\Re$) can be expressed as

$$\Re = \frac{\Re_{DC}}{\sqrt{1+(\omega\tau)^2}} \tag{5.8}$$

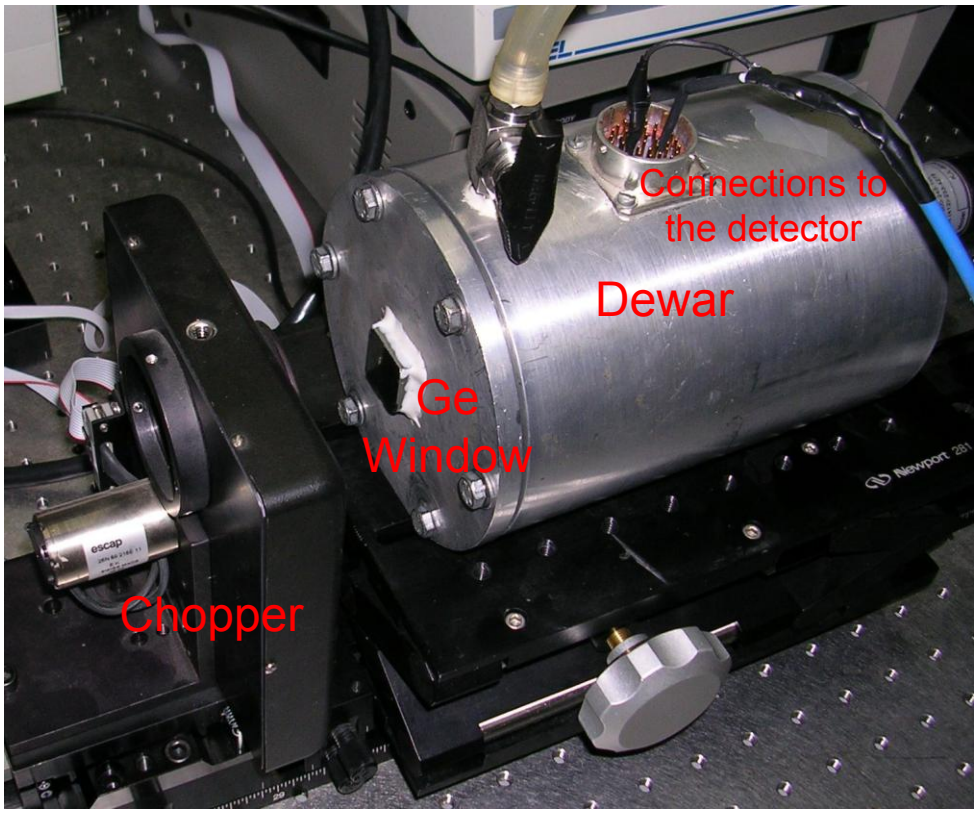
where $\Re_{DC}$ is the DC responsivity where the incident infrared radiation is not modulated, $\omega$ is the modulation frequency of the infrared signal, and $\tau$ is the time constant of the detector. Combining Equation 2.9 and 5.8, the DC responsivity ($\Re_{DC}$) can be found as

$$\Re_{DC} = \frac{\eta I_d \alpha R_d}{G_{th}} \tag{5.9}$$

where $\eta$ is the absorptance (absorption efficiency) of the detector, $I_d$ is the bias current, $\alpha$ is the TCR, $R_d$ is the detector resistance, and $G_{th}$ is the thermal conductance of the detector. The DC responsivity of the detector can be extracted from the responsivity measurements at different modulation frequencies, and TCR and $G_{th}$ can be measured with the methods explained above. So the absorptance ($\eta$) of the detector can be calculated since the bias current and the detector resistance is also known.




(a)




(b)

Figure 5.8: The test setup that is used to measure the responsivity of the fabricated detector. (a) shows the whole setup while (b) shows the zoomed view of the dewar and chopper.

The responsivity measurements are performed using *pixel_v2* for the same reason as the thermal conductance measurements. The detector is biased with a constant current of 0.1 μA. Figure 5.9 gives the result of the responsivity measurements and the fitted curve. The DC responsivity of the detector is found as 665.2 V/W from the fitting. This result will increase as the bias current increases. The absorptance of the detector pixel is calculated using Equation 5.9 as 0.153. This means that this detector absorbs the 15.3 % of the incident infrared radiation. This value is compatible with the simulated absorption. Figure 5.10 gives the result of the absorption simulation performed using the cascaded transmission line method suggested in Chapter 3. As can be seen from the figure the absorptance at 10 μm is 21.5 %. This pixel have high area ratio of Region 2 and Region 3, so the absorptance of the pixel at 10 μm is low. The discrepancy between the measurements and simulations comes from the fabricated thicknesses of the layers. From these measurement and simulation results we can assume the absorptance of *pixel_v1* is around 60 %. Then the responsivity of *pixel_v1* can be extracted as 4000 V/W at 0.1 μA current bias due to larger active area, higher absorptance, and lower thermal conductance.

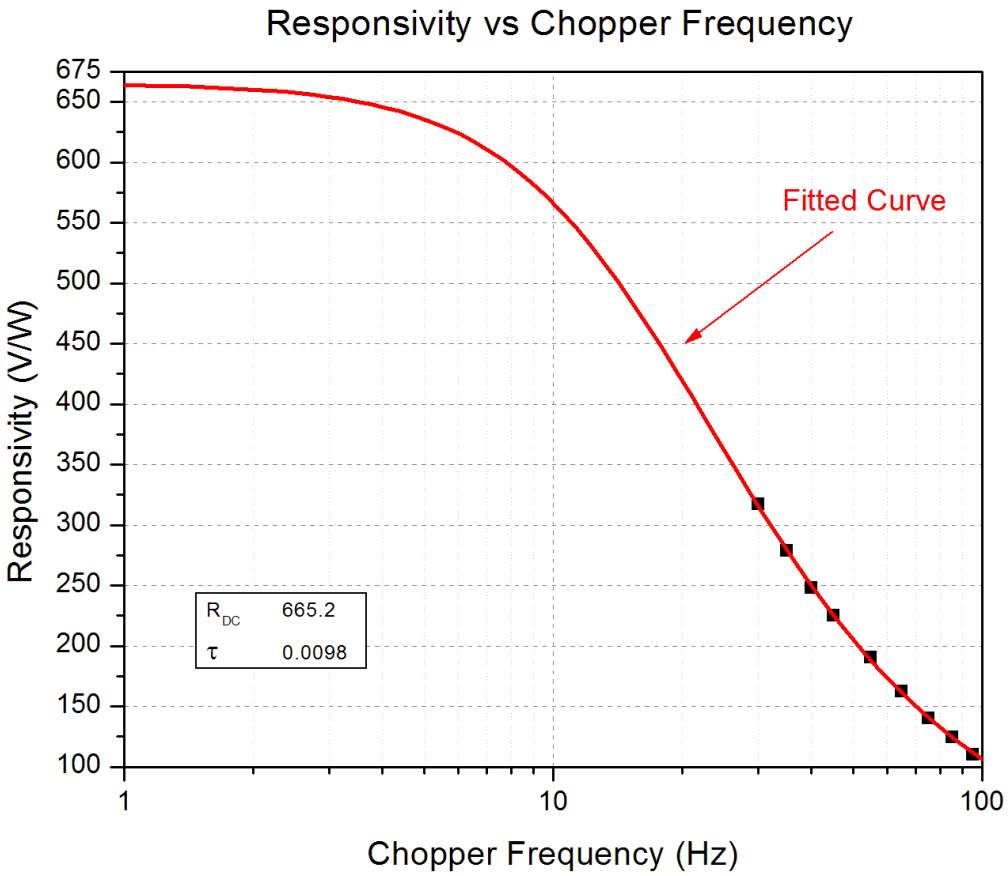



Figure 5.9: The responsivity measurement of *pixel_v2* and the fitted curve. The DC responsivity of the detector is found as 665.2 V/W from the fitting.

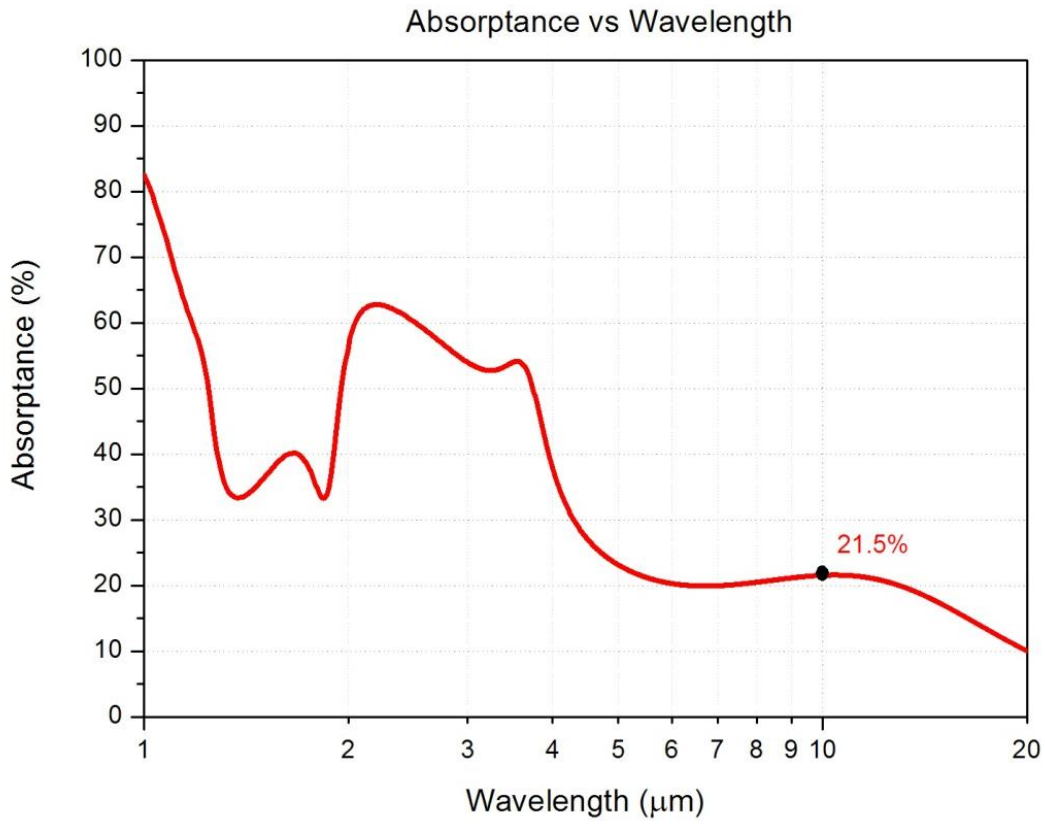



Figure 5.10: The result of the absorption simulation performed using cascaded transmission line method. The absorptance at 10 μm is 21.5 %. This pixel have high area ratio of Region 2 and Region 3, so the absorptance of the pixel at 10 μm is low. The discrepancy between the measurements and simulations comes from the fabricated thicknesses of the layers

## 5.5. Conclusions

This chapter presents the measurements performed using the fabricated detectors. The measured properties are TCR, thermal conductance, noise, and responsivity. The TCR of the detector resistor is measured as -3.4 %/K, which is one of the highest values for YBCO material having reasonable resistivity. The thermal conductance value of *pixel_v2* is measured as $1.27 \times 10^{-7}$ W/K, and the thermal conductance of *pixel_v1* is extracted as $9.0 \times 10^{-8}$ W/K from these measurements. This value is the smallest thermal conductance value obtained with YBCO microbolometers. The absorptance of *pixel_v2* is calculated as 15 % from the responsivity measurements. This result is in accordance with the simulations resulting in an absorptance value of

60-65 % for *pixel_v1*. Table 5.1 summarizes the properties of *pixel_v1* and gives some expected performance values of a 320x240 FPA consisting of this type of pixel. As can be seen from the table, the 320x240 FPA is estimated to have high performance values and can be used in applications requiring high performances.

Table 5.1: Summary of the properties of *pixel_v1* and expected performance values.

| **Parameter** | **Value** |
|---|---|
| Pixel Type | Surface micromachined resistive microbolometer |
| Pixel Area | 50 µm x 50 µm |
| Resistance | 150 kΩ |
| Fill Factor | 64 % |
| TCR | -3.4 %/K |
| Thermal Conductance | $9.0 \times 10^{-8}$ W/K |
| DC Responsivity (single pixel) | 4000 V/W @ 0.1 µA bias |
| DC Responsivity (in array) | 400000 V/W @10 µA bias |
| Absorptance (Absorption efficiency) | 60 % |
| Time Constant | 15.4 ms |
| FPA Size | 320x240 |
| Electrical Bandwidth @ 30 fps | 4.8 kHz |
| Detector Noise | 10.0 µVrms |
| Detectivity | $1.0 \times 10^{10}$ cm$\sqrt{}$Hz/W |
| NETD (using an f/1 lens) | 55 mK (including the effect of reference detector) |

# CHAPTER 6

# FABRICATION OF 320X240 MICROBOLOMETER FOCAL PLANE ARRAY AND INITIAL MEASUREMENTS

This chapter presents the fabrication of 320x240 microbolometer FPAs and the initial tests that have been performed using these FPAs. Section 6.1 explains the fabrication process where the process is almost same as the fabrication of the single pixel detectors and gives the results of the fabrication. Section 6.2 introduces the system used to test the fabricated FPAs and gives the NETD measurement results together with the initial infrared images obtained using the system. Section 6.3 summarizes the results and concludes the chapter.

## 6.1. Fabrication of 320x240 FPAs

The detector array of 320x240 FPAs are fabricated directly on CMOS wafers for monolithic integration with its CMOS readout circuitry. The CMOS readout circuitry is designed in XFAB 0.6 µm standard CMOS technology in the framework of another Ph.D. thesis. The Ph. D. study for the development of the CMOS readout circuitry is currently being conducted by Mr. Murat Tepegöz. Figure 6.1 shows the 6" CMOS wafer fabricated in the XFAB facilities and a zoomed view of one of the readouts. There are 30 readout chips in a fabricated 6" wafer, each of which occupies an area of 19.3 x 18 $mm^2$.

A new mask set is designed for the fabrication of the detectors on the 6” wafers monolithically with the CMOS readout circuits. Figure 6.2 shows the layout of the designed mask set. There are 8 masks in the set since the process steps are the same as the process of the single pixel microbolometer detector. Figure 6.3 (a)-(g) show the microscope views of the detectors after each process step.

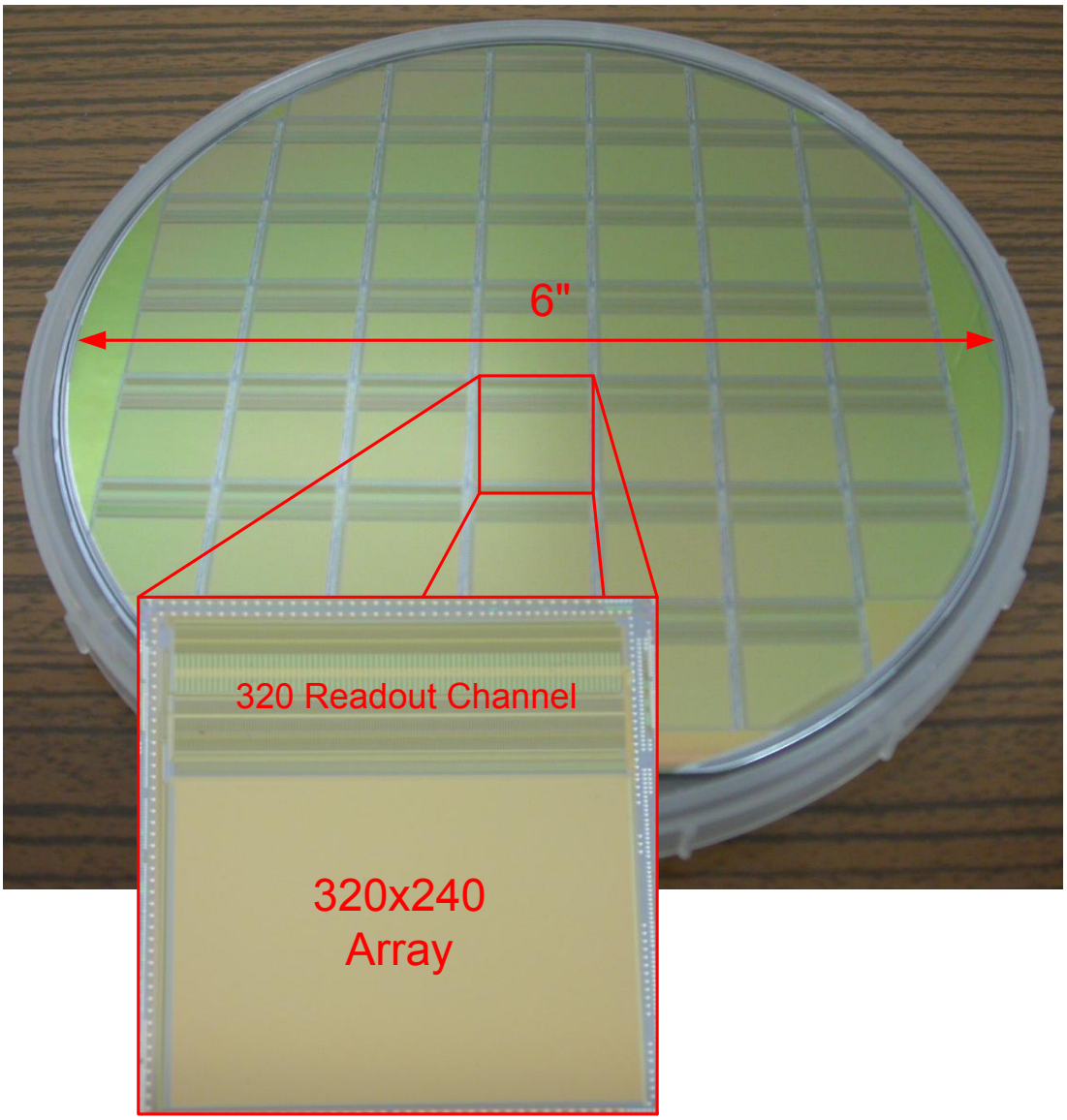



Figure 6.1: The 6” CMOS wafer and a zoomed view of one of the readouts. There are 30 readout chips in a 6” wafers.

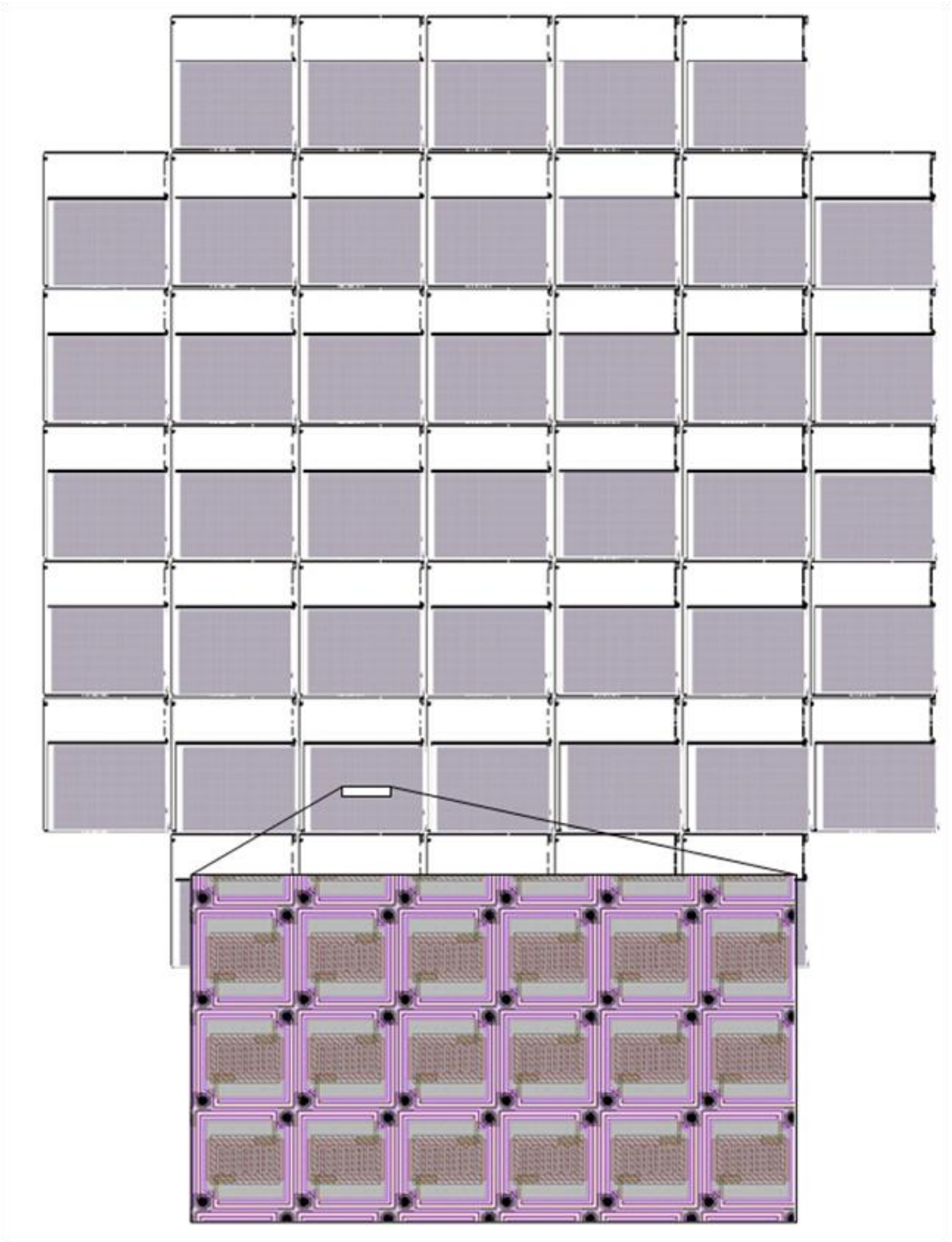


Figure 6.2: The layout of the designed mask set for fabrication of 320x240 FPAs on 6" wafers. There are 8 masks in the set since the process steps are the same as the process of the single pixel microbolometer detector.

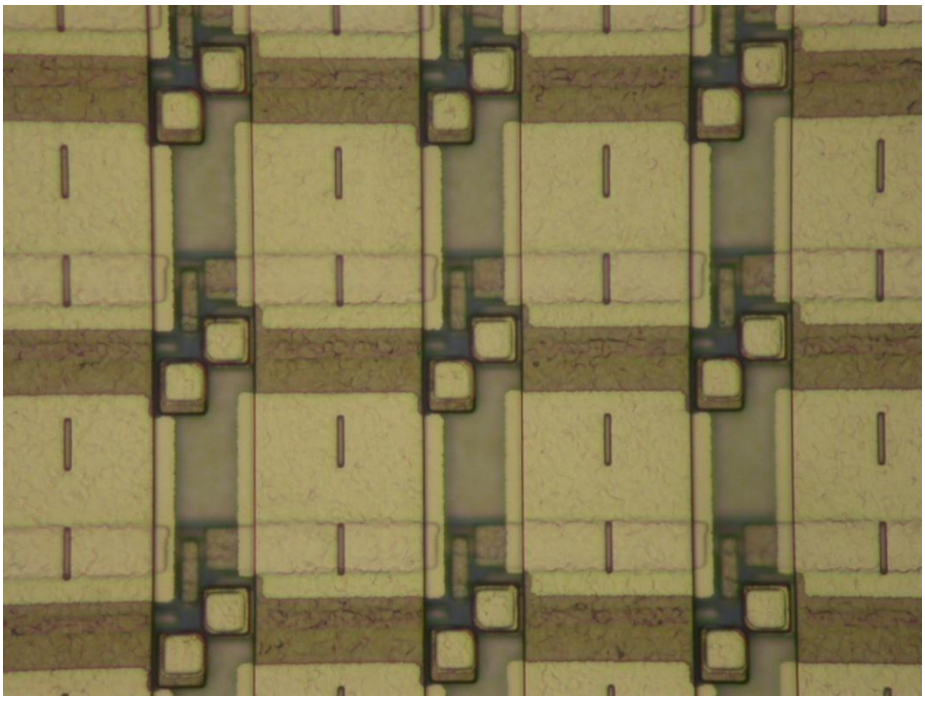


Figure 6.3 (a) Deposition and patterning of the mirror metal layer (Cr/Au)

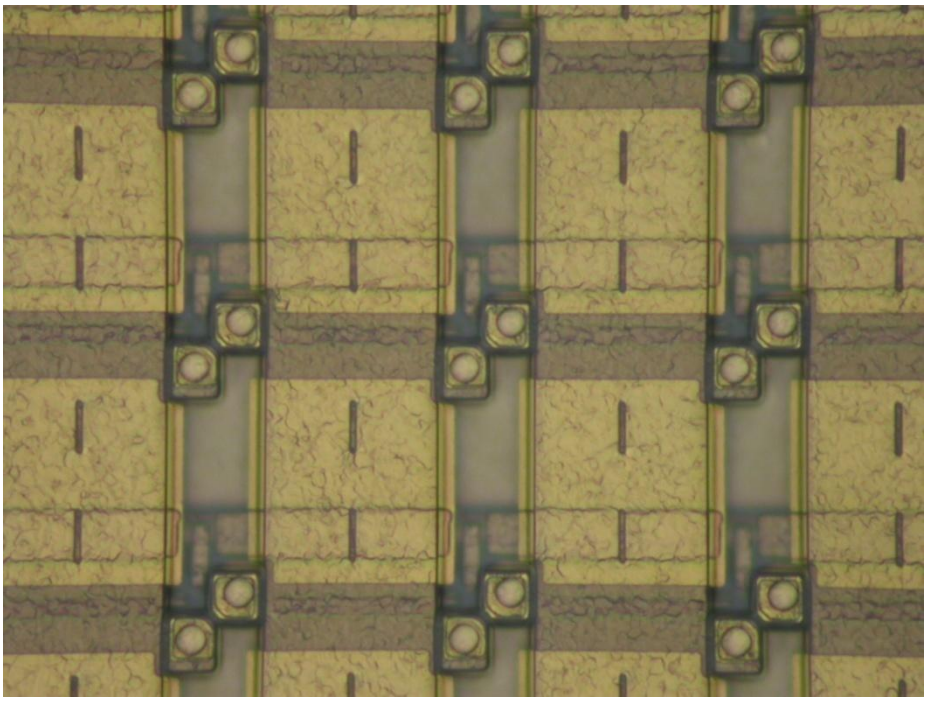


Figure 6.3 (b) Deposition and patterning of sacrificial layer (polyimide)

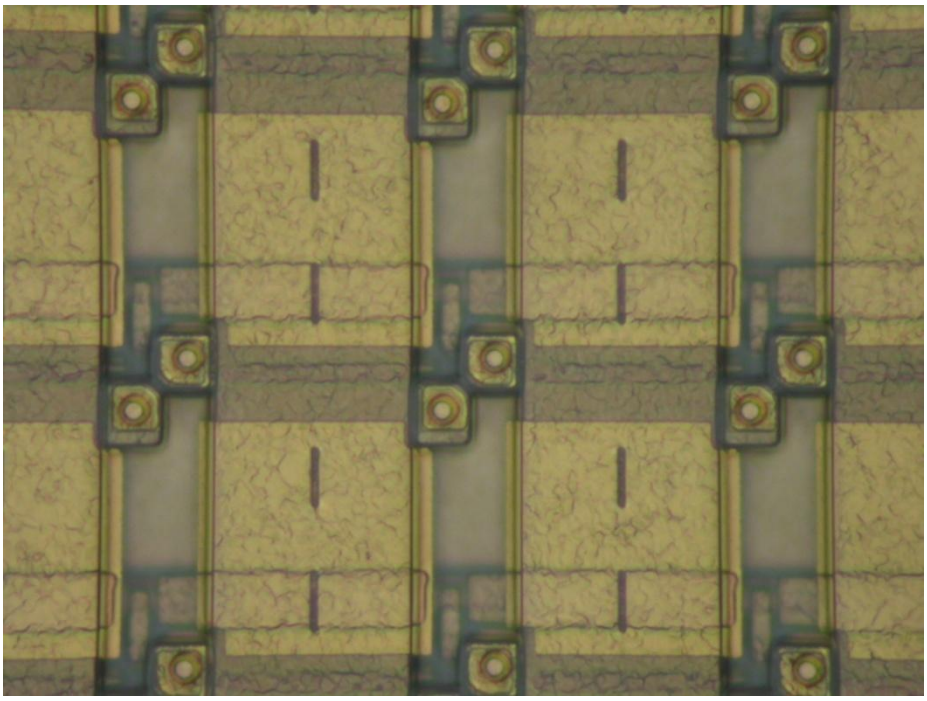


Figure 6.3 (c) Deposition and patterning of the structural layer (silicon nitride)

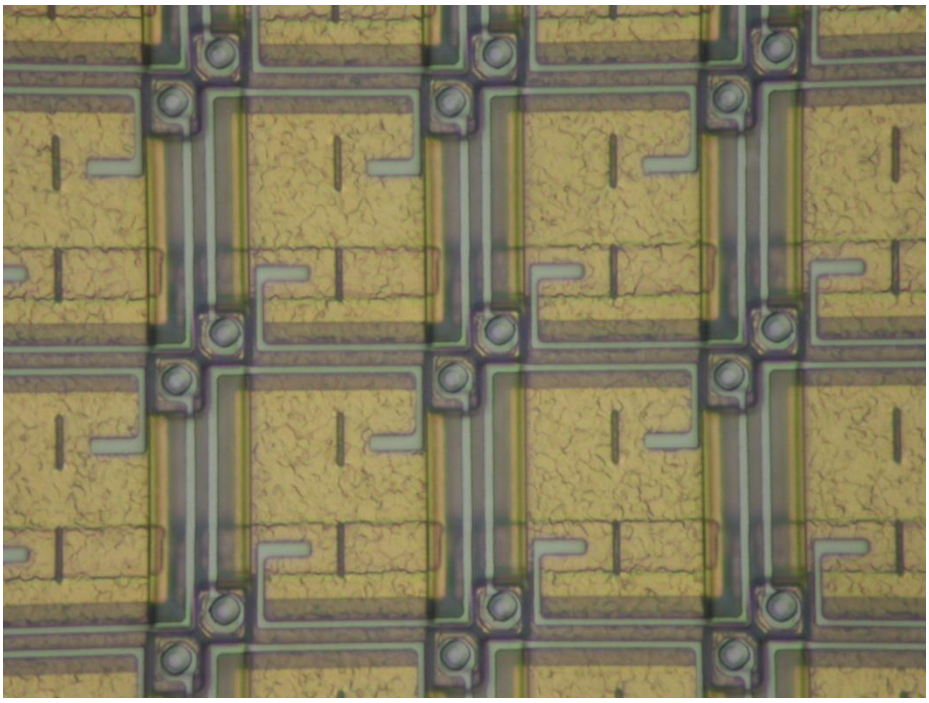


Figure 6.3 (d) Deposition and patterning of the interconnect metal (Ti)

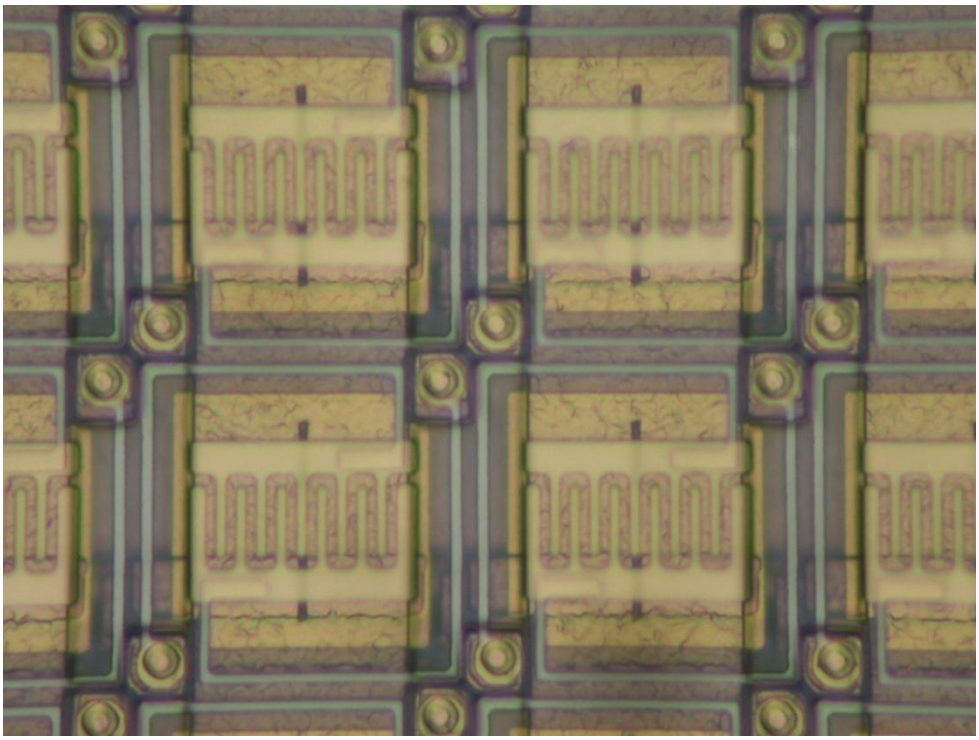


Figure 6.3 (e) Deposition and patterning of the electrode metal in finger shape (Cr/Au)

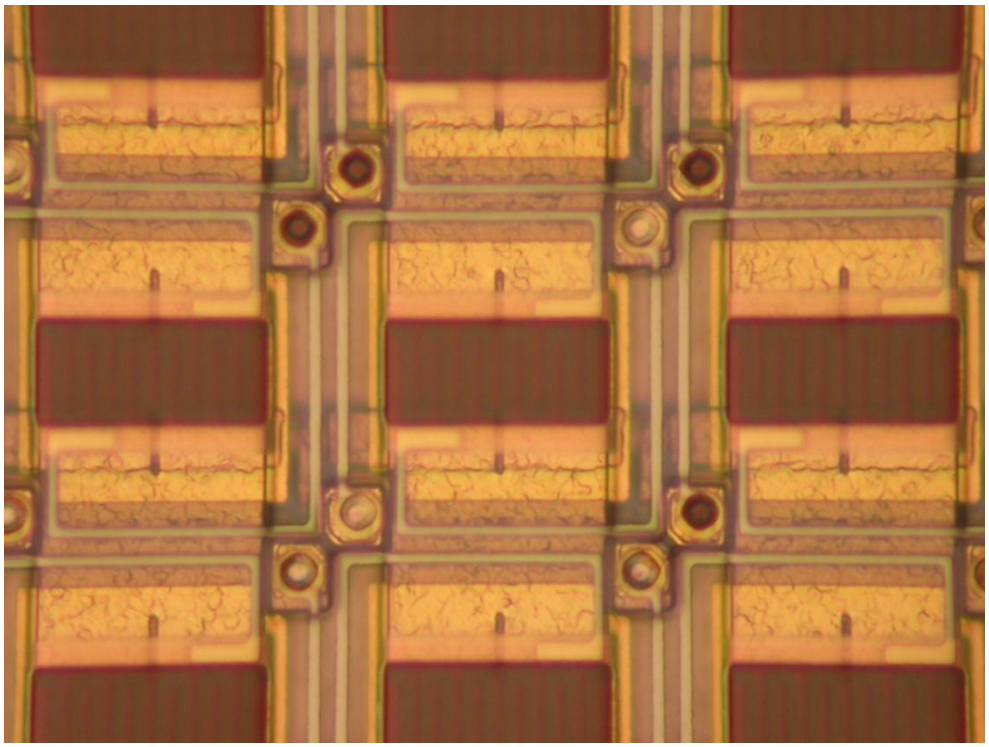


Figure 6.3 (f) Deposition and patterning of the active material (YBCO)

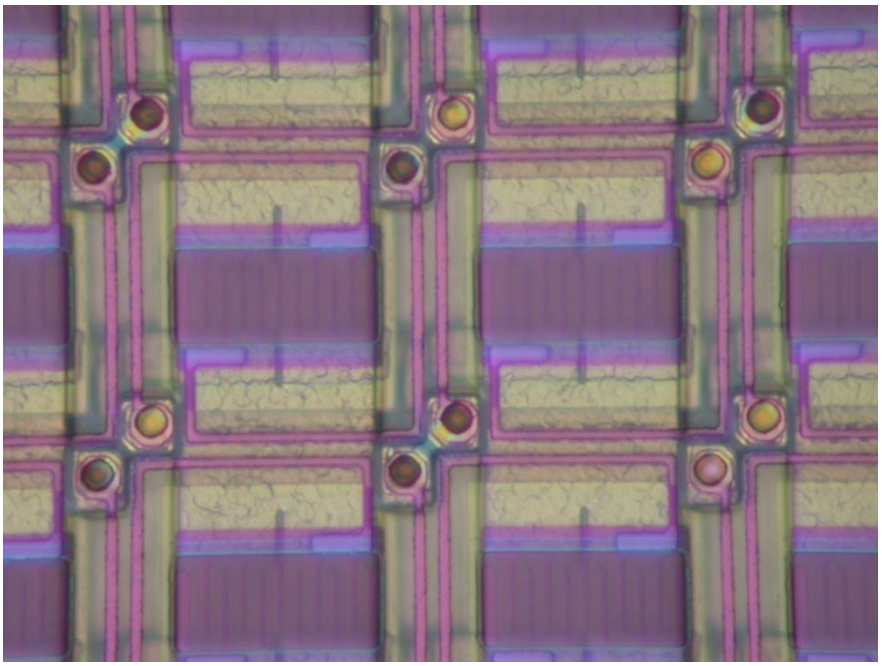


Figure 6.3 (g) Deposition of the upper structural layer (silicon nitride) and deposition and patterning of the thin metallic film absorber layer (TiN)

Figure 6.3: The microscope views of the detectors after each process step.

Following the fabrication, the wafer is diced before the releasing process of the microbolometer detector arrays from the substrate. Figure 6.4 (a)-(e) give the SEM views of the successfully released detectors in 320x240 FPAs. The FPAs are released separately since the dicing is a wet process and if performed after the release step, the detectors can stick to the substrate due to the surface tension of water. Instead of an oxygen plasma system, the release process is performed in RIE system, with addition of a little $CF_4$ gas into the oxygen environment. The oxygen plasma system in METU-MET facilities is not successful to etch the polyimide underneath the pixels after the whole fabrication is completed. The fabrication consists of the thermal processes like dehydration, photoresist curing, and nitride deposition, therefore polyimide is additionally cured during these processes. That is the reason for the usage of the RIE system to etch the polyimide underneath the pixel. But the usage of RIE system causes the sticking of the detectors to the substrate due to charging. This problem can be solved with the use of a new oxygen plasma system which does not cause charging on the devices.

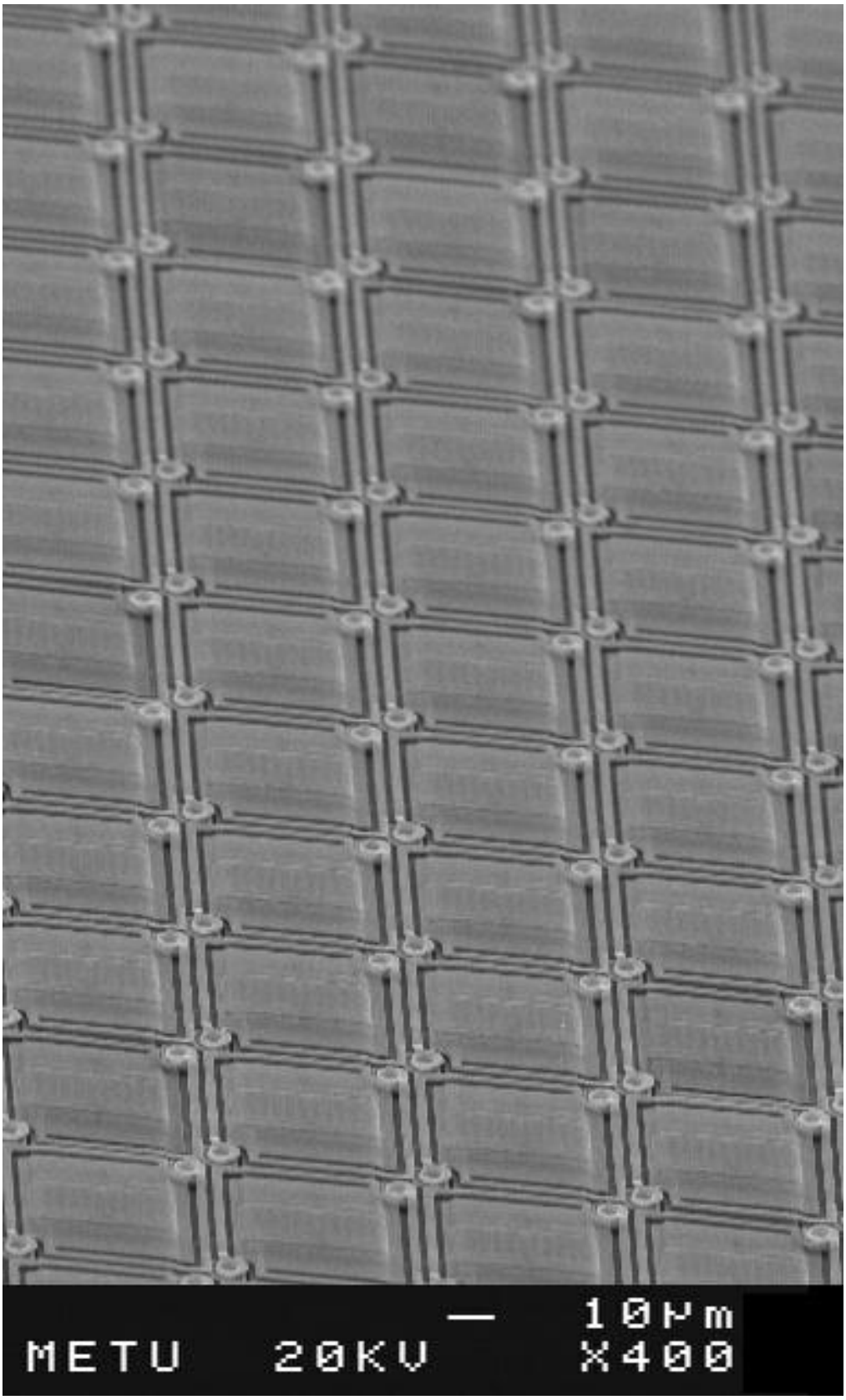



Figure 6.4 (a)

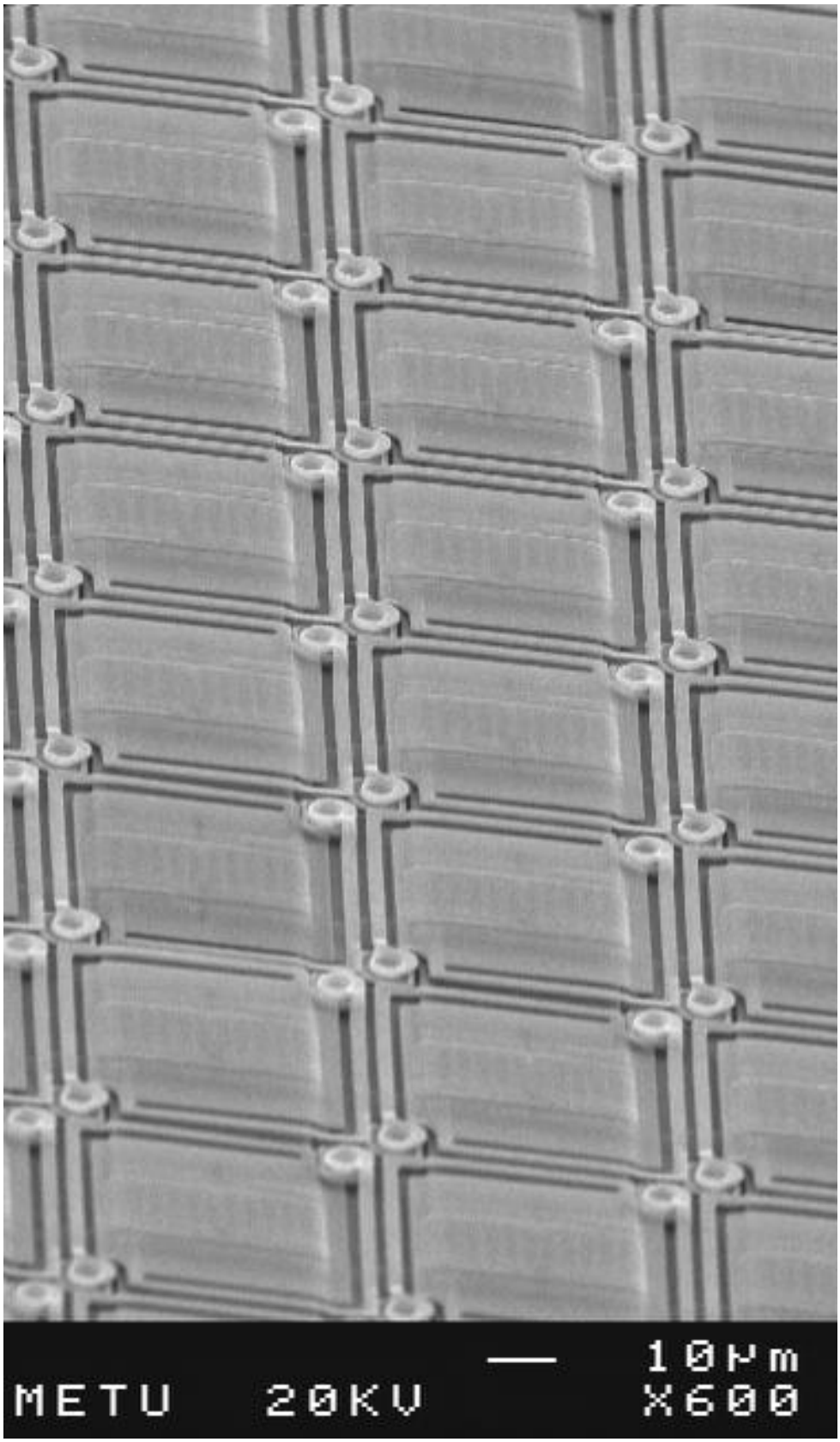



Figure 6.4 (b)

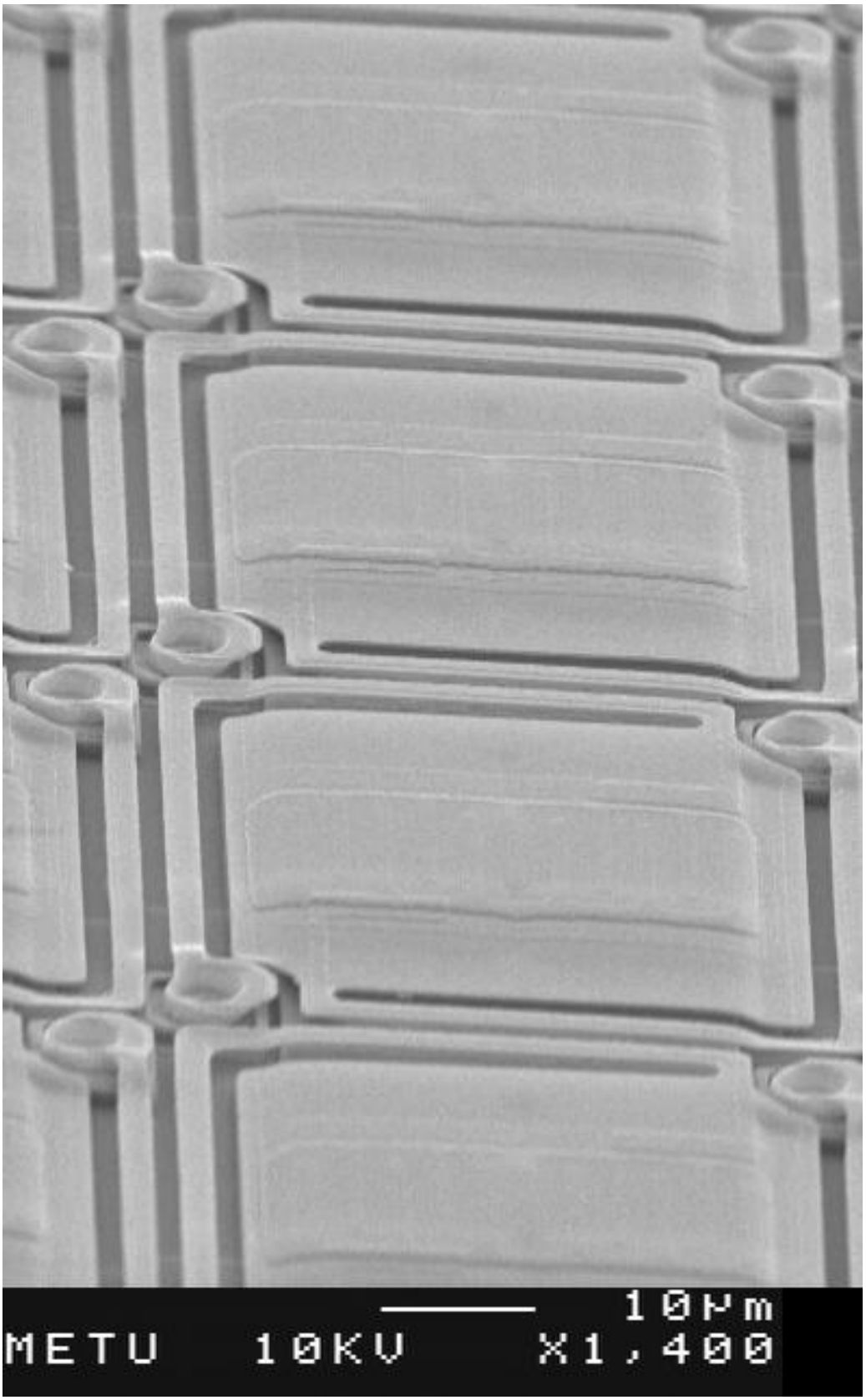



Figure 6.4 (c)

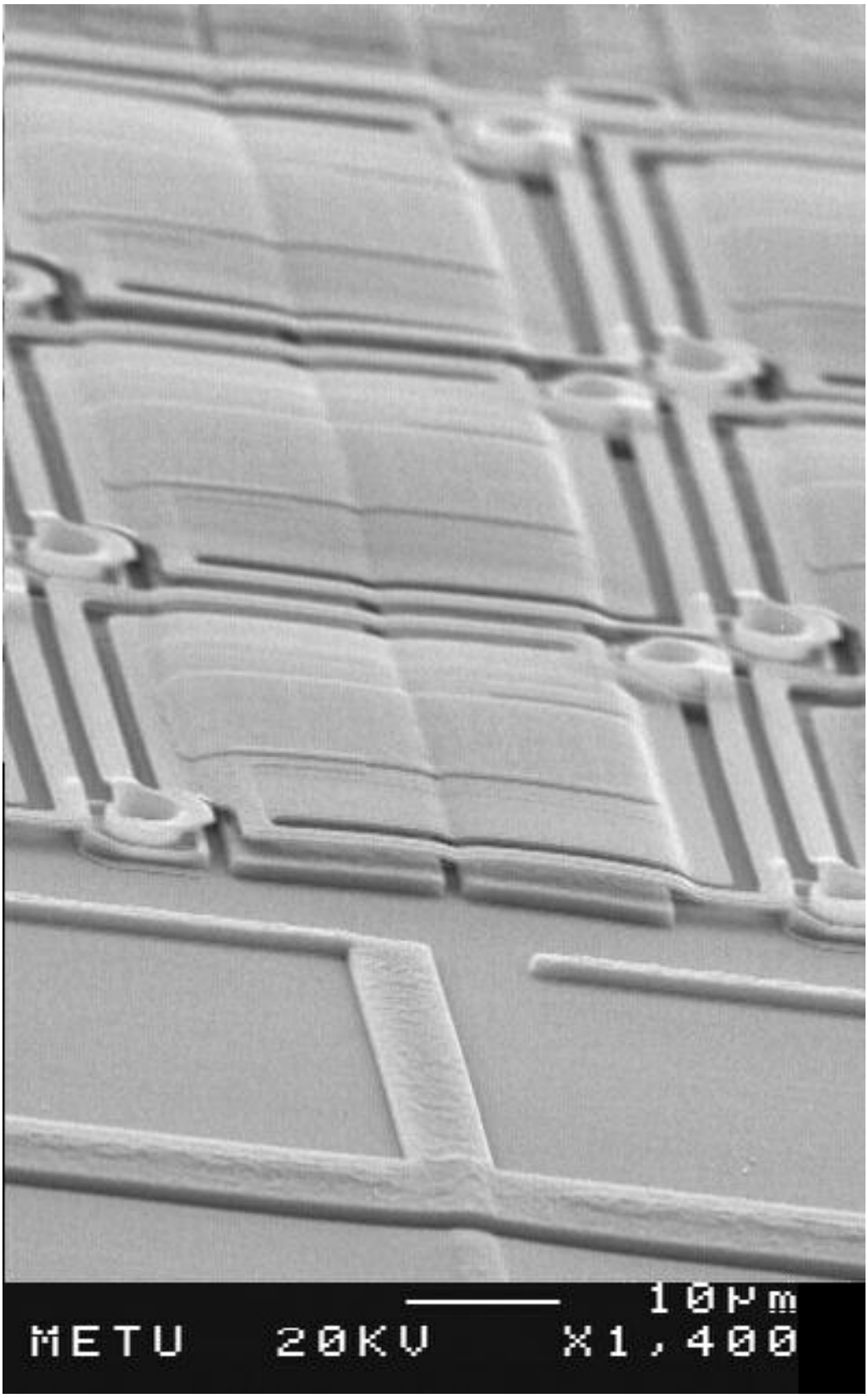



Figure 6.4 (d)

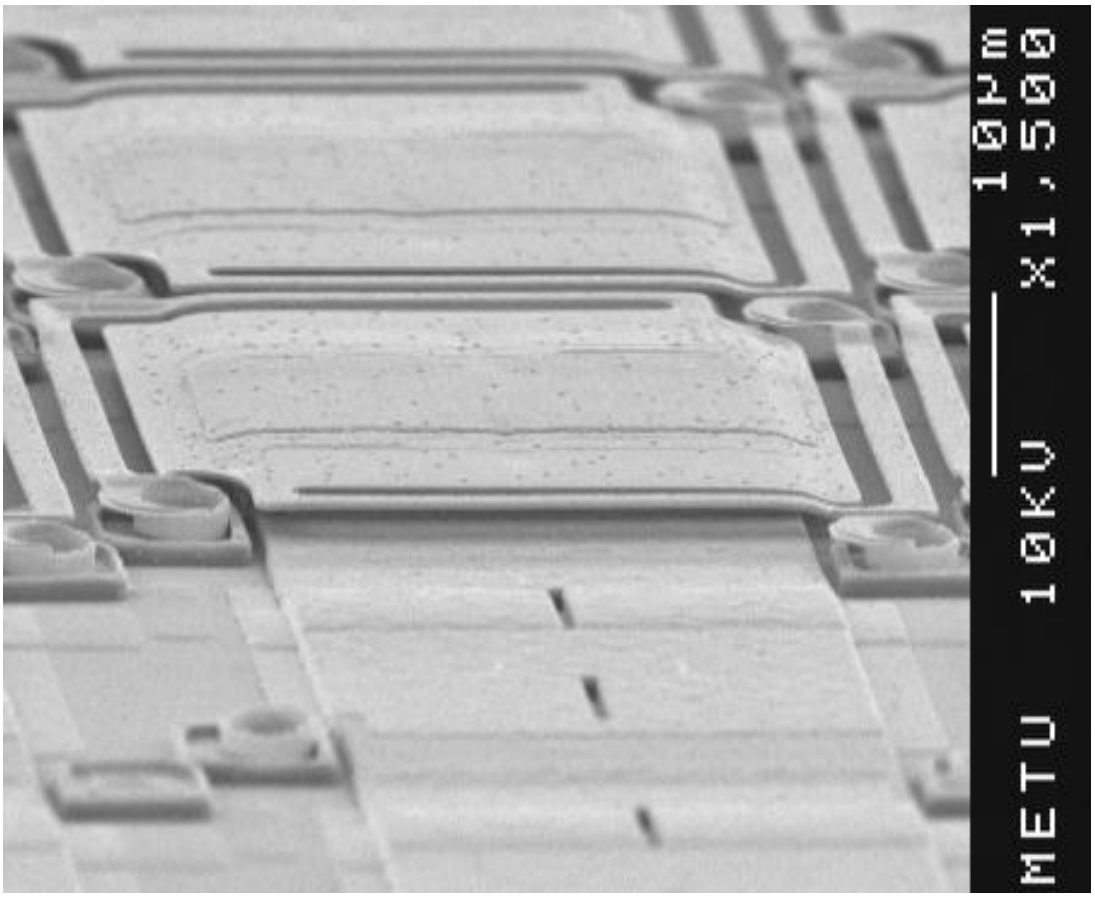



Figure 6.4 (e)

Figure 6.4: The SEM views of the successfully released detectors in 320x240 FPAs.

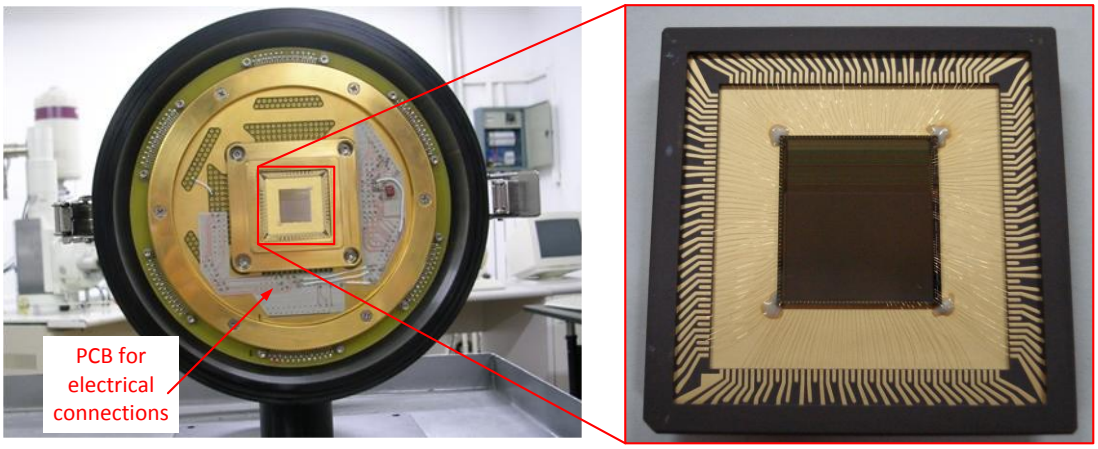
As can be seen from the views the detectors are thermally isolated from the substrate, and they are standing as desired without any buckling. The only difference of these detectors from the fabricated single pixel detectors is the effect of the surface topography of the CMOS circuits and routing lines. This topography comes from the last metal layer of the CMOS process and directly affects the shape of the detectors. This shape deformation can be solved by the use of a chemical mechanical polishing (CMP) system during the fabrication. The CMOS substrates can be polished before the detector fabrication starts and the surface topography can be minimized.

## 6.2. Initial Measurements and the First Images from 320x240 FPA

The fabrication process of the FPAs is followed by the initials measurements performed in order to demonstrate the operation of the detectors together with the readout circuit and to observe the performance parameters. A different vacuum dewar is used for the tests since the chip size is large and the package (PGA180) that the FPA chip is wirebonded to does not fit into the dewar given in Figure 5.3. Also this chip needs more electrical connections than the dewar can handle, and the use of an infrared lens is necessary for imaging applications. This new vacuum dewar is big enough so that the package fits into it, has enough connections to operate the FPA chip, includes a thermoelectric cooler (TEC) to stabilize the temperature of the tested device, and a lens can be mounted in front of the dewar. Figure 6.5 shows the pictures of the dewar used for the initial tests and the wirebonded FPA chip. The inputs to the FPA are applied by the help of some outside circuitry, and the outputs of the FPA are fed into the computer through a data acquisition card. A printed circuit board (PCB) is placed inside the dewar for the electrical connections from the FPA to the pins of the dewar. Due to lack of space in the dewar, the PCB cannot be large enough to handle all the connections to the FPA. For this reason the FPA cannot be operated at full performance. Also, due to some problems in readout circuit, the pixels cannot be measured independently, and many tests like resistance uniformity, thermal conductance of the pixels, and responsivity of the pixels cannot be measured. The only measurable parameter is the noise equivalent temperature difference.




(a)




(b)

Figure 6.5: The dewar used for the initial tests and the wirebonded FPA chip.

The noise equivalent temperature difference (NETD) of the FPA is measured by the help of a large area blackbody source. This blackbody source has a reference plate and a hotplate that is heated with respect to the reference. First the reference plate is placed in front of the dewar, and the FPA data is measured for a large number of frames. Then the hotplate is placed, and the FPA data is measured for the same number of frames. The average and the rms value of the data are calculated for every pixel for both conditions. The rms value of the data gives the noise of the pixels. The difference between the average values of the data obtained from reference plate and hotplate gives the response of the pixels to the temperature change. Then, by simple proportion, NETD i.e., the temperature change which causes a response equal to the noise value, can be calculated. Figure 6.6 gives the NETD measurement results for the FPA. The mean value of NETD is measured as 450 mK. This value is much higher than the estimated NETD value given in Table 5.1, which is 55 mK. This is mostly due to the noise coupling from the environment and operation of the chip below its full performance. The performance is expected to increase when the setup and testing conditions are improved.

Figure 6.7 shows the infrared images obtained from several FPAs. These images are raw images, and only one point correction is applied. Figure 6.8 shows filtered version of one of the images (the filtering process is done by Emre Kültürsay). The single dead pixels are replaced by the surrounding pixels and the background noise is eliminated by some software filtering in this image. As can be seen from the images a human can easily be detected. The quality of the images will increase as the setup, the testing conditions, and the correction method are improved. These images show that the detector pixels are successfully fabricated on the readout circuit, and the circuit and the detector array are successfully working together.

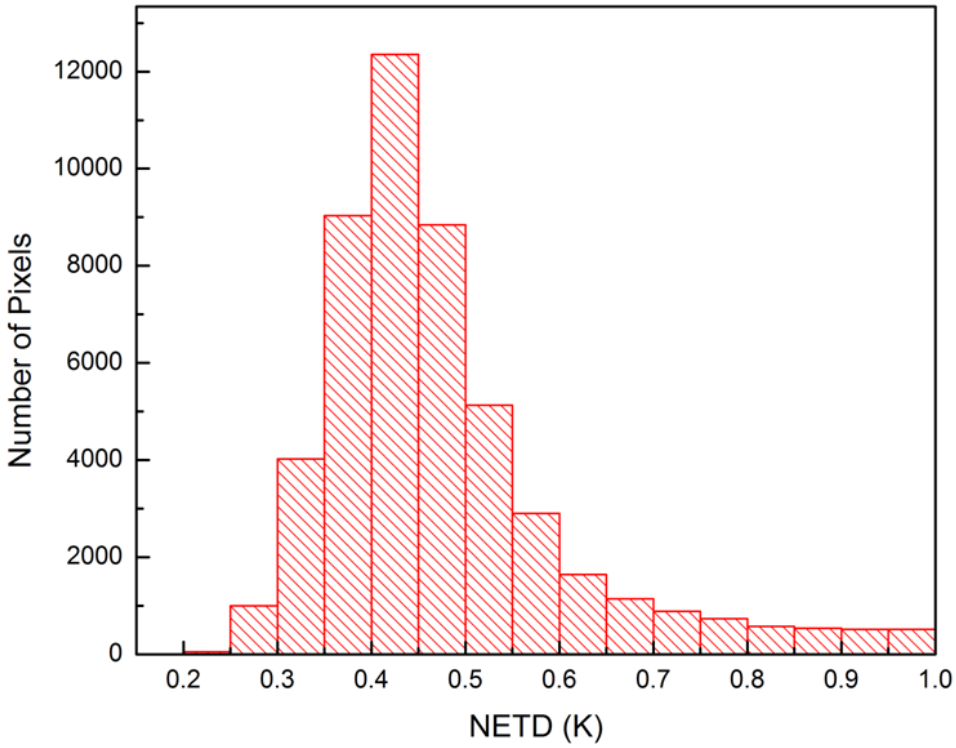



Figure 6.6: NETD measurement result for the FPA. The mean value of NETD is measured as 450 mK.



Figure 6.7 (a)

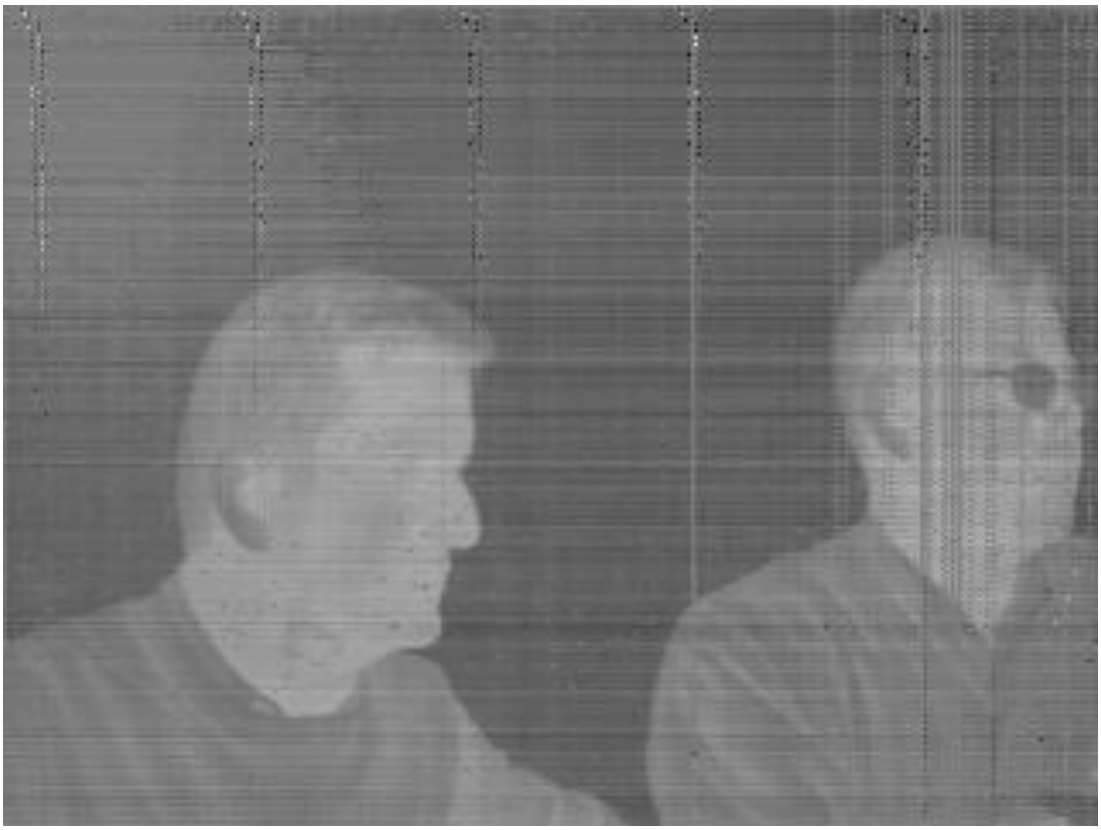


Figure 6.7 (b)



Figure 6.7 (c)

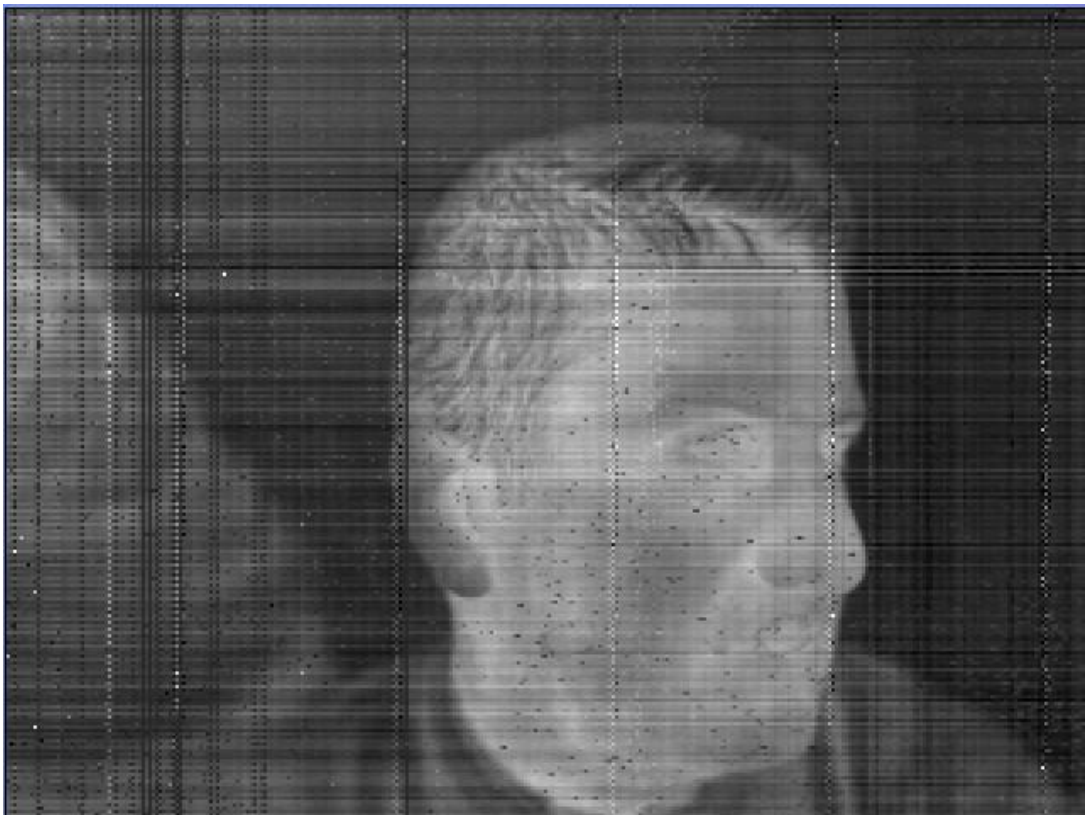


Figure 6.7 (d)

Figure 6.7: Infrared images obtained from several FPAs. These images are raw images and only one point correction is applied.



Figure 6.8: Filtered version of Figure 6.7 (b). The single dead pixels are replaced by the surrounding pixels and the background noise is eliminated by some software filtering. (the image processing is performed by Emre Kültürsay)

## 6.3. Conclusions

This chapter presents the fabrication of 320x240 microbolometer FPAs and the initial tests that have been performed using these FPAs. The fabrication process is explained, and the results of the fabrications are presented. It can be seen from the results that the detectors are successfully fabricated monolithically with the CMOS readout circuitry. The vacuum dewar used in the test setup for the measurements of the FPAs is presented. The results of the NETD measurements performed using the FPAs, and the test setup is given. The mean NETD value is measured as 450 mK, which is higher than the expected value of 55 mK. This is due to the noise coupling from the environment and operation of the chip below its full performance. The first images obtained from different FPAs are also presented. These images show that the detector pixels are successfully fabricated on the readout circuit, and the circuit and the detector array are successfully working together. The performance of the FPAs and the quality of the images will increase as the setup and the testing conditions are improved.

# CHAPTER 7

# CONCLUSIONS AND FUTURE WORK

The research performed in the framework of this study involves the development of a high performance surface micromachined uncooled infrared resistive type microbolometer detector that can be used in large format FPAs and the implementation of a 320x240 FPA that consists of the developed detectors. The design, fabrication and tests of the detectors are successfully completed. The measured results are compatible with the calculation and simulation values showing that the detectors are successfully modeled during the design. The fabrication and NETD tests of the 320x240 FPAs are demonstrated and first infrared images are obtained using the fabricated FPAs. The measured mean NETD of the FPA is 450 mK mostly due to the measurement setup and should decrease under 100 mK when the setup is improved.

The achievements and results obtained throughout this Ph. D. research can be summarized as follows:

1. The detector type that is going to be used in a large format uncooled infrared FPA is investigated. The microbolometer type detector is chosen to be used among the other alternatives like pyroelectric detectors, thermopiles, and microcantilevers due to its advantages such as high performance, high yield, and monolithic integration with the CMOS readout circuitry.

2. The types of the microbolometers are determined to be surface micromachined and bulk micromachined microbolometers. Bulk micromachined microbolometers developed previously at METU facilities are not suitable to be used in targeted FPAs since the performance of these detectors is not high enough. So surface micromachined microbolometers are decided to be used for the targeted FPAs.

3. The active material that is going to be used in the surface micromachined detectors is determined as YBaCuO due to its advantages when compared with the other materials such as $VO_x$ and a-Si. YBaCuO has a TCR value higher than the other materials, it does not require any high temperature process, and it is not commercially patented and information about the deposition and process exist in literature. Also it is relatively a new material when $VO_x$ and a-Si are considered. Collaboration is made with University of Texas at Arlington and some YBaCuO samples are taken in order to make some measurements and process trials.

4. The resistance value of the detector and the electrode structure to be used are optimized. The performance of the detector increases as the resistance value decreases if the self-heating effect is not taken into account. When the effect of self-heating is considered the highest performance is achieved for a resistance value of 100 kΩ. Finger shaped electrodes are specially designed to obtain this resistance value since the resistivity of YBCO layer is high.

5. The pixel size and the structure of the detector pixel are also optimized considering the minimum feature size and the accuracy of the fabrication process in METU-MET facilities. The minimum feature size that can be obtained is 1.5 μm since the etching of the metals is performed using wet etch. The support arm structure is chosen to be double folded considering the thermal and mechanical properties.

6. The layers of the detector are modeled as cascaded transmission lines in order to calculate the absorption efficiency of the detector. The model is demonstrated to work for a previously fabricated and tested detector. Then the model is applied to the newly designed detectors. The dependence of the absorptance on the layer properties is investigated. A **newly proposed method** to find the total absorptance of the detectors is dividing the detectors into 4 regions in which the combination of the layers is different. The absorption of each region is calculated separately, and the ratio of the areas of the regions to the total absorbing area is used to find the total absorption efficiency. It is seen that the regions including electrode metals have lower absorption efficiencies than the other regions causing a decrease in the overall absorptance. The overall absorptance for the designed detector pixel is calculated as 66 % in the wavelength region of 8-12 μm, which is not a very low value. It is possible to increase the absorptance if the areas of such regions are decreased.

7. The thermal and mechanical simulations of the designed detector are performed in order to find the thermal conductance, thermal time constant, the stress on the detector under extreme accelerations, and the minimum resonance frequency of the detector. The thermal conductance is simulated as $9x10^{-8}$ W/K while the time constant is found to be 15.4 ms. The maximum stress on the detector under 1000 g acceleration is simulated to be 11 MPa which is much lower than the yield strength of titanium and silicon nitride. The minimum resonance frequency of the detector is simulated as 60 kHz showing that any mechanical input with frequency less than 60 kHz is acceptable for the designed microbolometer detector.

8. The process layers in the detector are individually optimized for the fabrication. The mirror metal is chosen to be Cr/Au after some process trials. The etching of the sacrificial polyimide is optimized using titanium as mask layer in the RIE system. The structural layer is chosen as silicon nitride since it is easier to

fabricate stress free nitride when compared with stress free oxide. The interconnect metal and the electrode metal is determined as Ti and Au, respectively. The etching of Au layer is performed in diluted "Aqua Regia" solution which is specifically used for the fabrication of the fingers. The surface resistance of the absorber layer is optimized to be 377 Ω/□ as found in the absorptance simulations.

9. YBCO layer is optimized for the detector to have the highest performance. The resistivity and the TCR of the YBCO layer are investigated while the oxygen ratio in the deposition environment is varied. The resistivity is tried to be minimized in order to decrease the detector resistance. The resistivity of the YBCO layer is minimum for an oxygen ratio of 5 % and it is measured as 255 Ω-cm. At this oxygen amount the TCR value is measured as -3.4 %/K. The maximum TCR value is obtained as -3.6 %/K with a resistivity of 500 Ω-cm at an oxygen ratio of 7.4 %. Using all these results the **optimum** oxygen ratio for the deposition of YBCO layer for finger shape electrode structure is found as 5 %. If a different electrode structure can be developed to decrease the resistance value, then oxygen ratio of 7.4 % can be used in order to increase the TCR of the detector.

10. The performance parameters of the fabricated detectors are measured. The TCR of the detector is measured as -3.4 %/K which is one of the **highest** value obtained with YBCO material having reasonable resistivity. The thermal conductance, noise, responsivity, and the absorptance of a different pixel are measured since the designed pixel could not be tested due to some problems. The main problem is the sticking of the pixel to the substrate before the test is completed, and the other problem is that the readout circuit of the FPA does not allow the pixels to be tested independently. A methodology, which is **more accurate** than the ones in literature, is **firstly** introduced in this thesis to measure the thermal conductance of the detectors. All the measured values

are compatible with the simulation results. If the simulation results for the designed pixel are used, the NETD value becomes 55 mK for a 320x240 FPA.

11. The fabrication of 320x240 FPA consisting of the designed pixels is successfully completed. The NETD of the array is measured and some infrared images are obtained using the fabricated FPA in a self-formed imaging system. The NETD of the FPA is measured as 450 mK which is higher than the expected result due to the current test setup. The NETD will decrease, and the quality of the images will increase when the setup is improved.

Although an enormous effort has been spent to reach the major objectives of this Ph. D. research, there are still various items that need to be studied. These items can be explained as follows:

1. The sticking problem of the pixels to the substrate should be further investigated and solved. An oxygen plasma system which has a high polyimide etch rate and does not charge the etched devices can be used for the etching of the sacrificial layer instead of RIE system. So, the etching time will be shortened and the charging of the pixels will be avoided.

2. The setup used for tests of the FPAs should further be improved in order to determine the real performance parameters of the FPAs.

3. The optical properties of the layers can be further optimized, without affecting the mechanical properties, to increase the absorptance of the detectors.

4. A new resistance structure, which can be a *sandwich type* resistance, is needed to be designed to further decrease the resistance value. This decrease in the resistance value will allow the TCR value to increase, since the oxygen ratio of the deposition environment will be changed. Also the new resistance structure will be used in pixels having smaller pitch values since the finger shape electrodes is not suitable for small pixel sizes.

5. The pixel size of the detectors should be decreased in order to enlarge the FPA format due to the limitations of the CMOS foundries. Decreasing the pixel size using the same detector structure, i.e., having a single sacrificial layer will result in a low fill factor for the detectors. So detectors having double sacrificial layers to form an umbrella structure should be designed in order to decrease the pixel size and enlarge the FPA format while having a high fill factor. Also the thermal conductance value of the small pixels should be low enough to have high performance values. In order to achieve low thermal conductance values the thickness and the width of the support arms should be lowered which needs some improvements and more optimizations in the fabrication processes.

6. The detectors need vacuum environment to have higher performance values. This vacuum environment can be obtained via different methods. First method is the usage of a vacuum dewar as suggested in this thesis. This method can only be used for testing of the FPAs. For the FPAs to be used in the field the chips should be packaged in a vacuum environment. This can be either done in special vacuum packages where the chip is placed inside the package and the package is vacuumed through a port, or the FPAs can be packaged wafer level. The second option is cheaper and more reliable but needs more process optimizations.

This work is a very important example of the development of MEMS and infrared imaging systems in Turkey. There are 5 more countries, which are USA, United Kingdom, France, Japan, and Israel, that have developed microbolometer FPAs. United Kingdom and Israel use the technology of USA, so Turkey is the **4$^{th}$ country** that has developed its own technology to fabricate uncooled microbolometer FPAs. The fabricated FPA is the **first** surface micromachined uncooled infrared microbolometer array in Turkey which can be used for applications requiring high performance.

# REFERENCES


[1] Y. Zhao, "Optomechanical Uncooled Infrared Imaging System," *Dissertation for the Degree of Doctor of Philosophy*, University of California at Berkeley, Department of Mechanical Engineering, 2002.

[2] M.Y. Tanrıkulu, "A High Fill Factor CMOS Uncooled Infrared Microbolometer Detector," *Dissertation for the Degree of Master of Science*, Middle East Technical University, Department of Electrical and Electronics Engineering, 2002.

[3] http://www.maxtech-intl.com/irnews.htm, reached on 24.6.2007.

[4] A. D. Dave, "Micromachined Infrared Sensors with Device-Level Encapsulation," *Dissertation for the Degree of Master of Science*, University of Texas at Arlington, Department of Electrical Engineering, May 2005.

[5] http://www.theses.ulaval.ca/2005/23016/apb.html, reached on 24.6.2007.

[6] http://en.wikipedia.org/wiki/Infrared, reached on 24.6.2007.

[7] E. L. Dereniak and G. D. Boreman, "*Infrared Detectors and* Systems", John Wiley & Sons Inc., Academic Press, 1996.

[8] http://www.newport.com/Laws-of-Radiation/381843/1033/catalog.aspx, 24.6.2007.

[9] P. W. Kruse and D. D. Skatrud, *"Uncooled Infrared Imaging Arrays and Systems,"* Semiconductor and Semimetals, vol. 47, Academic Press, 1997.

[10] M. Henini and M. Razeghi, *"Handbook of Infrared Detection Technologies,"* Elsevier Science Ltd., 2002.

[11] S. Özer, "InSb and InAsSb Infrared Photodiodes on Alternative Substrates and InP/InGaAs Quantum Well Infrared Photodetectors: Pixel and Focal Plane Array Performance," *Dissertation for the Degree of Doctor of Philosophy*, Middle East Technical University, Department of Electrical and Electronics Engineering, 2005.

[12] A. Rogalski, "Infrared Detectors: An Overview," *Infrared Physics and Technology*, vol. 43, pp. 187-210, June 2002.

[13] S. Özer and C. Beşikçi, “Assessment of InSb Photodetectors on Si Substrates,” *Journal of Physics D: Applied Physics*, vol. 36, pp. 559-563, February 2003.

[14] İ. Kimukin, N. Bıyıklı, T. Kartaloğlu, O. Aytür, and E. Özbay, “High-Speed InSb Photodetectors on GaAs for Mid-IR Applications,” *IEEE Journal of Selected Topics in Quantum Electronics*, vol. 10, no. 4, pp. 766-770, July/August 2004.

[15] A. Rogalski, “Quantum Well Photoconductors in Infrared Detector Technology,” *Journal of Applied Physics*, vol. 93, no. 8, pp. 4355-4391, April 2003.

[16] O. O. Cellek, S. Özer, and C. Beşikçi, “High Responsivity InP–InGaAs Quantum-Well Infrared Photodetectors: Characteristics and Focal Plane Array Performance,” *IEEE Journal of Quantum Electronics*, vol. 41, no. 7, pp. 980-985, July 2005.

[17] H. Mohseni and M. Razeghi, “Long-Wavelength Type-II Photodiodes Operating at Room Temperature,” *IEEE Photonics Technology Letters*, vol. 13, no. 5, pp. 517-519, May 2001.

[18] S. Eminoğlu, “Uncooled Infrared Focal Plane Arrays with Integrated Readout Circuitry Using MEMS and Standard CMOS Technologies,” *Dissertation for the Degree of Doctor of Philosophy*, Middle East Technical University, Department of Electrical and Electronics Engineering, 2003.

[19] http://www.infraredsolutions.com/html/technology/thermalSensorsF.shtml, reached on 1.7.2007.

[20] Z. Olgun, “Infrared Thermopile Structures Using Any Standard CMOS Integrated Circuit Process,” *Dissertation for the Degree of Master of Science*, Middle East Technical University, Department of Electrical and Electronics Engineering, 1998.

[21] http://en.wikipedia.org/wiki/Thermopower, reached on 26.7.2007.

[22] H. Baltes, O. Brand, G.K. Fedder, C. Hierold, J. Kornivk, and O. Tabata, *“CMOS-MEMS: Advanced Micro and Nanosystems,”* Wiley-VCH, 2005.

[23] A. Schaufelbühl, N. Schneeberger, U. Münch, M. Waelti, O. Paul, O. Brand, H. Baltes, C. Menolfi, Q. Huang, E. Doering, and M. Loepfe, “Uncooled Low-Cost Thermal Imager Based on Micromachined CMOS Integrated Sensor Array,” *IEEE Journal of Microelectromechanical Systems*, vol. 10, no. 4, pp. 503-510, December 2001.

[24] T. Akın, Z. Olgun, O. Akar, and H. Külah, “An Integrated Thermopile Structure with High Responsivity Using Any Standard CMOS Process,” *Sensors and Actuators A*, vol. 66, pp. 218-224, April 1998.

[25] A.D. Oliver and K.D. Wise, “A 1024-element Bulk-Micromachined Thermopile infrared imaging array,” *Sensors and Actuators A*, vol. 73, pp. 222-231, March 1999.

[26] T. Kanno, M. Saga, S. Matsumoto, M. Uchida, N. Tsukamoto, A. Tanaka, S. Itoh, A. Nakazato, T. Endoh, S. Tohyama, Y. Yamamoto, S. Murashima, N. Fujimoto, N. Teranishi, “Uncooled Infrared Focal Plane Array Having 128 × 128 Thermopile Detector Elements,” *Proc. of SPIE, Infrared Technology XX,* vol. 2269, pp. 450-459, July 1994.

[27] W. G. Baer, T. Hull, K. D. Wise, K. Najafi, and K. D. Wise, “A Multiplexed Silicon Infrared Imaging Sensor,” *International Conference on Solid State Sensors and Actuators (TRANSDUCERS’ 91),* pp. 631-634, June 1991.

[28] C.Calaza, N.Viarani, G.Pedretti, M.Gottardi, A.Simoni, V.Zanini, and M.Zen, “An Uncooled Infrared Focal Plane Array for Low-Cost Applications Fabricated with Standard CMOS Technology,” *Sensors and Actuators A*, vol. 132, pp. 129-138, November 2006.

[29] M. Hirota, Y. Nakajima, M. Saito, and M. Uchiyama, “120×90 Element Thermoelectric Infrared Focal Plane Array with Precisely Patterned Au-black Absorber,” *Sensors and Actuators A*, vol. 135, pp. 146-151, March 2007.

[30] A. Rogalski, “Infrared Detectors: Status and Trends,” Progress in Quantum Electronics, vol. 27, pp. 59-210, 2003.

[31] M. Kohli, C. Wuethrich, K. Brooks, B. Willing, M. Forster, P. Muralt, N. Setter, and P. Ryser, “Pyroelectric Thin-Film Sensor Array,” *Sensors and Actuators A*, vol. 60, pp. 147-153, May 1997.

[32] P. W. Kruse, *“Uncooled Thermal Imaging Arrays, Systems, and Applications,”* SPIE Press, 2001.

[33] http://www.thermal-eye.com/9/PRODUCTS.htm, reached on 26.6.2007.

[34] D. Sabuncuoğlu Tezcan, “A CMOS Compatible Uncooled Detector Focal Plane Array for Night Vision Applications Using MEMS Technology,” *Dissertation for the Degree of Doctor of Philosophy*, Middle East Technical University, Department of Electrical and Electronics Engineering, 2002.

[35] http://en.wikipedia.org/wiki/Bolometer, reached on 27.6.2007.

[36] P. L. Richards, “Bolometers for Infrared and Millimeter Waves,” *Journal of Applied Physics*, vol. 76, no. 1, pp. 1-24, July 1994.

[37] R. A. Wood, “Uncooled Thermal Imaging with Monolithic Silicon Focal Arrays,” *Proc. of SPIE*, *Infrared Technology XIX,* vol. 2020, pp. 322-329, July 1993.

[38] R. A. Wood, “Use of Vanadium Oxide in Microbolometer Sensors,” US. Patent No. 5450053, 1995.

[39] D. Murphy, A. Kennedy, M. Ray, R. Wyles, J. Wyles, J. Asbrock, C. Hewitt, D. Van Lue, T. Sessler, J. Anderson, D. Bradley, R. Chin, H. Gonzales, C. Le Pere, and T. Kostrzewa, “Resolution and Sensitivity Improvements for VOx Microbolometer FPAs,” *Proc. of SPIE, Infrared Technology and Applications XXIX,* vol. 5074, pp. 402-413, April 2003.

[40] D. Murphy, M. Ray, A. Kennedy, J. Wyles, C. Hewitt, R. Wyles, E. Gordon, T. Sessler, S. Baur, D. Van Lue, S. Anderson, R. Chin, H. Gonzalez, C. Le Pere, S.Ton, and T. Kostrzewa, “Expanded Applications for High Performance VOx Microbolometer FPAs,” *Proc. of SPIE, Infrared Technology and Applications XXXI,* vol. 5783, pp. 448-459, March 2005.

[41] B. S. Backer, N. Butler, M. Kohin, M. Gurnee, J. T. Whitwam, and Tom Breen, “Recent Improvements and Developments in Uncooled Systems at BAE Systems North America,” *Proc. of SPIE, Infrared Detectors and Focal Plane Arrays VII*, vol. 4721, pp. 83-90, April 2002.

[42] P. W. Norton, S. Cox, B. Murphy, K. Grealish, M. Joswick, B. Denley, F. Feda, L. Elmali, and M. Kohin, “Uncooled Thermal Imaging Sensor and Application Advances,” *Proc. of SPIE, Infrared Technology and Applications XXXII,* vol. 6206, pp. 620617-1 – 620617-7, April 2006.

[43] A. Fraenkel, U. Mizrahi, L. Bikov, A. Adin, E. Malkinson, A. Giladi, D. Seter, and Z. Kopolovich, “VOx-Based Uncooled Microbolometric Detectors: Recent Developments at SCD,” *Proc. of SPIE, Infrared Technology and Applications XXXII*, vol. 6206, pp. 62061C-1 - 62061C-11, April 2006.

[44] U. Mizrahi, L. Bikov, A. Giladi, A. Adin, N. Shiloah, E. Malkinson, T. Czyzewski, D. Seter, A. Amsterdam, Y. Sinai, and A. Fraenkel, “Large format and high sensitivity VOx microbolometer detectors at SCD,” *Proc. of SPIE, Infrared Technology and Applications XXXIII*, vol. 6542, pp. 65421X-1 - 65421X-7, April 2007.

[45] B. Terre, B. Cannata, P. Franklin, A. Gonzalez, E. Kurth, H. Ly, B. Parrish, K. Peters, T. Romeo, and B. VanYsseldyk, “Microbolometer Development and Production at Indigo Systems,” *Proc. of SPIE, Infrared Technology and Applications XXIX,* vol. 5074, pp. 518-526, April 2003.

[46] P.E. Howard, J.E. Clarke, A.C. lonescu, C. Li, and J.C. Stevens, “DRS U6000 640x480 VOx Uncooled IR Focal Plane,” *Proc. of SPIE, Infrared Detectors and Focal Plane Arrays VII*, vol. 4721, pp. 48-55, April 2002.

[47] S. Tohyama, M. Miyoshi, S. Kurashina, N. Ito, T. Sasaki, A. Ajisawa, and N. Oda, “New Thermally Isolated Pixel Structure for High-Resolution Uncooled Infrared FPAs,” *Proc. of SPIE, Infrared Technology and Applications XXX,* vol. 5406, pp. 428-436, April 2004.

[48] K. Egashira, T. Yamamoto, K. Kawano, Y. Tanaka, K. IIda, T. Fujishima, T. Kakimoto, and N. Oda, “Infrared Sensor Modules Using Uncooled 320x240 / 640x480 Detector,” *Proc. of SPIE, Infrared Technology and Applications XXXIII*, vol. 6542, pp. 65421R-1 - 65421R-11, April 2007.

[49] D. Murphy, M. Ray, J. Wyles, C. Hewitt, R. Wyles, E. Gordon, K. Almada, T. Sessler, S. Baur, D. Van Lue, and S. Black, “640 x 512 17 µm Microbolometer FPA and Sensor Development,” *Proc. of SPIE, Infrared Technology and Applications XXXIII,* vol. 6542, pp. 65421Z-1 - 65421Z-10, April 2007.

[50] R. J. Blackwell, T. Bach, D. O’Donnell, J. Geneczko, and M. Joswick, “17 µm pixel 640 x 480 Microbolometer FPA Development at BAE Systems,” *Proc. of SPIE, Infrared Technology and Applications XXXIII*, vol. 6542, pp. 65421U-1 - 65421U-4, 2007.

[51] C. Li, G. D. Skidmore, C. Howard, C. J. Han, L. Wood, D. Peysha, E. Williams, C. Trujillo, J. Emmett, G. Robas, D. Jardine, C-F. Wan, and E. Clarke, “Recent Development of Ultra Small Pixel Uncooled Focal Plane Arrays at DRS,” *Proc. of SPIE, Infrared Technology and Applications XXXIII,* vol. 6542, pp. 65421Y-1 - 65421Y-12, April 2007.

[52] http://www.defense-update.com/newscast/0407/news/110407_fpa.htm, reached on 27.6.2007.

[53] http://www.thermal-eye.com/default.asp?NodeId=202, reached on 27.6.2007.

[54] J.-L. Tissot, J.-L. Martin, E. Mottin, M. Vilain, J.-J. Yon, and J. P. Chatard, “320x240 Microbolometer Uncooled IRFPA Development,” *Proc. of SPIE, Infrared Technology and Applications XXVI,* vol. 4130, pp. 473-479, July 2000.

[55] C. Trouilleau, A. Crastes, O. Legras, J.L. Tissot, and J.P. Chatard , “35 µm Pitch at ULIS, a Breakthrough,” *Proc. of SPIE, Infrared Technology and Applications XXXI,* vol. 5783, pp. 578-585, March 2005.

[56] J.L. Tissot, B. Fieque, C. Trouilleau, P. Robert, A. Crastes, C. Minassian, and O. Legras, “First Demonstration of 640 x 480 Uncooled Amorphous Silicon IRFPA with 25 µm Pixel Pitch,” *Proc. of SPIE, Infrared Technology and Applications XXXII,* vol. 6206, pp. 620618-1 - 620618-4, April 2006.

[57] C. Trouilleau, B. Fieque, J. L. Tissot, P. Robert, A. Crastes, C. Minassian, O. Legras, B. Dupont, A. Touvignon, S. Tinnes, J. J. Yon, and A. Arnaud, “Uncooled Amorphous Silicon 160 x 120 IRFPA with 25 µm Pixel-Pitch for Large Volume Applications,” *Proc. of SPIE, Infrared Technology and Applications XXXIII*, vol. 6542,pp. 65421V-1 - 65421V-8, April 2007.

[58] T. Schimert, N. Cunningham, G. Francisco, R. Gooch, J. Gooden, P. McCardel, B. Neal, B. Ritchey, J. Rife, A. J. Syllaios, J. Tregilgas, J. Brady, J. Gilstrap, and S. Ropson, “Low Cost, Low Power Uncooled 120x160 a-Si-based Micro Infrared Camera for Law Enforcement Applications,” *Proc. of SPIE, Enabling Technologies for Law Enforcement and Security,* vol. 4232, pp. 187-194, November 2000.

[59] V. N. Leonov, Y. Creten, P. De Moor, B. Du Bois, C. Goessens, B. Grietens, P. Merken, N. A. Perova, G. Ruttens, C. Van Hoof, A. Verbist, and J. Vermeiren, “Small Two-Dimensional and Linear Arrays of Polycrystalline SiGe Microbolometers at IMEC-XenICs,” *Proc. of SPIE, Infrared Technology and Applications XXIX,* vol. 5074, pp. 446-457, April 2003.

[60] S. Sedky, P. Fiorini, M. Caymax, C. Baert, L. Hermans, and R. Mertens, “Characterization of Bolometers Based on Polycrystalline Silicon Germanium Alloys,” *IEEE Electron Device Letters*, vol. 19, no. 10, pp. 376-378, October 1998.

[61] H.-K. Lee, J.-B. Yoon, E. Yoon, S.-B. Ju, Y.-J. Yong, W. Lee, and S.-G. Kim, “A High Fill-Factor Infrared Bolometer Using Micromachined Multilevel Electrothermal Structures,” *IEEE Transaction on Electron Devices*, vol. 46, no. 7, pp. 1489-1491, July 1999.

[62] J.-S. Shie, Y.-M. Chen, M. Ou-Yang, and B. C. S. Chou, “Characterization and Modeling of Metal-Film Microbolometer,” *Journal of Microelectromechanical Systems*, vol. 5, no. 4, pp. 298-306, December 1996.

[63] P. C. Shan, Z. Çelik-Butler, D. P. Butler, A. Jahanzeb, C. M. Travers, W. Kula, and R. Sobolewski, “Investigation of Semiconducting YBaCuO Thin Films: A New Room Temperature Bolometer,” *Journal of Applied Physics*, vol. 80, no. 12, pp. 7118-7123, December 1996.

[64] C. M. Travers, A. Jahanzeb, D. P. Butler, and Z. Çelik-Butler, “Fabrication of Semiconducting YBaCuO Surface-Micromachined Bolometer Arrays,” *Journal of Microelectromechanical Systems,* vol. 6, no. 3, pp. 271-276, September 1997.

[65] A. Yıldız, Z. Çelik-Butler, and D. P. Butler, “Microbolometers on a Flexible Substrate for Infrared Detection,” IEEE Sensors Journal, vol. 4, no.1, pp. 112-117, February 2004.

[66] H. Wada, T. Sone, H. Hata, Y. Nakaki, O. Kaneda, Y. Ohta, M. Ueno, and M. Kimata, “YBaCuO Uncooled Microbolometer IRFPA,” *Proc. of SPIE, Infrared Technology and Applications XXVII,* vol. 4369, pp.297-304, April 2001.

[67] H. Wada, T. Sone, H. Hata, Y. Nakaki, O. Kaneda, Y. Ohta, M. Ueno, and M. Kimata, “YBaCuO Uncooled Microbolometer IRFPA,” *Sensors and Materials*, vol. 12, no. 5, pp. 315-325, 2000.

[68] T. Ishikawa, M. Ueno, Y. Nakaki, K. Endo, Y. Ohta, J. Nakanishi, Y. Kosasayama, H. Yagi, T. Sone, and M. Kimata, “Performance of 320 x 240 Uncooled IRFPA with SOI Diode Detectors,” *Proc. of SPIE, Infrared Technology and Applications XXVI,* vol. 4130, pp. 1-8, July 2000.

[69] M. Ueno, Y. Kosasamaya, T. Sugino, Y. Nakaki, Y. Fujii, H. Inoue, K. Kama, T. Seto, M. Takeda, and M. Kimata, “640 x 480 pixel uncooled infrared FPA with SOI diode detectors,” *Proc. of SPIE, Infrared Technology and Applications XXXI*, vol. 5783, pp. 566-577, March 2005.

[70] M. Kimata, M. Ueno, M. Takeda, and T. Seto, “SOI diode uncooled infrared focal plane arrays,” *Proc. of SPIE, Quantum Sensing and Nanophotonic Devices III*, vol. 6127, pp. 61270X-1 - 61270X-11, April 2006.

[71] H. Torun and H. Ürey, “Uncooled Thermo-mechanical Detector Array with Optical Readout,” *Opto-electronics Review*, vol.14, no. 1, pp. 55-60, 2006.

[72] S. R. Hunter, R. A. Amantea, L. A. Goodman, D. B. Kharas, S. Gershtein, J. R. Matey, S. N. Perna, Y. Yu, N. Maley, and L. K. White, “High Sensitivity Uncooled Microcantilever Infrared Imaging Arrays,” *Proc. of SPIE, Infrared Technology and Applications XXIX,* vol. 5074, pp. 469-480, April 2003.

[73] S. R. Hunter, G. Maurer, L. Jiang, and G. Simelgor, “High Sensitivity Uncooled Microcantilever Infrared Imaging Arrays,” *Proc. of SPIE, Infrared Technology and Applications XXXII,* vol. 6206, pp. 62061J-1 - 62061J-12, April 2006.

[74] N.V. Lavrik, D. Grbovic, S. Rajic, P. G. Datskos, D. Forrai, E. Nelson, J. Devitt, and B. McIntyre, "Uncooled Infrared Imaging Using Bimaterial Microcantilever Arrays," *Proc. of SPIE, Infrared Technology and Applications XXXII,* vol. 6206, pp. 62061K-1 - 62061K-8, April 2006.

[75] M. Wu, J. Cook, R. DeVito, J. Li, E. Ma, R. Murano, N. Nemchuk, M. Tabasky, and M. Wagner, "Novel low-cost uncooled infrared camera," *Proc. of SPIE, Infrared Technology and Applications XXXI*, vol. 5783, pp. 496-505, March 2005.

[76] M. Wagner, E. Ma, J. Heanue, and S. Wu, "Solid state optical thermal imagers," *Proc. of SPIE, Infrared Technology and Applications XXXIII,* vol. 6542, pp. 65421P-1 - 65421P-10, April 2007.

[77] D. Sabuncuoğlu Tezcan, F. Koçer, and T. Akın, "An Uncooled Microbolometer Infrared Detector in any Standard CMOS Technology," *The 10th Int. Conf. on Solid-State Sensors and Actuators (TRANSDUCERS'99)*, vol. 1, pp. 610-613, June 1999.

[78] D. Sabuncuoğlu Tezcan, S. Eminoğlu, O. Ş. Akar, and T. Akın, "A Low Cost Uncooled Infrared Microbolometer Focal Plane Array Using the CMOS N-Well Layer," *IEEE International MicroElectroMechanical Systems Conf. (MEMS 2001)*, pp. 566-569, January 2001.

[79] D.Sabuncuoğlu Tezcan, S. Eminoğlu, O. Ş. Akar, and T. Akın, "An Uncooled Microbolometer Infrared Focal Plane Array in Standard CMOS," *Proc. of SPIE, Photodetector Materials and Devices VI*, vol. 4288, pp. 112-121, January 2001.

[80] S. Eminoğlu, D. Sabuncuoğlu Tezcan, and T. Akın, "CMOS N-Well Microbolometer FPA with Temperature Coefficient Enhancement Circuitry," *Proc. of SPIE, Infrared Technology and Applications XXVII,* vol. 4369, pp. 240-249, April 2001.

[81] D. Sabuncuoğlu Tezcan, S. Eminoğlu, and T. Akın, "A Low Cost Uncooled Infrared Microbolometer Detector in Standard CMOS Technology," *IEEE Transaction on Electron Devices*, vol. 50, no. 2, pp. 494-502, February 2003.

[82] S. Eminoğlu, M. Y. Tanrıkulu, D. Sabuncuoğlu Tezcan, and T. Akın, "A Low Cost, Small Pixel Uncooled Infrared Detector for Large Focal Plane Arrays using a Standard CMOS Process," *Proc. of SPIE, Infrared Technology and Applications XXVIII*, vol. 4721, pp. 111-121, April 2002.

[83] S. Eminoğlu, D. Sabuncuoğlu Tezcan, M. Y. Tanrıkulu, and T. Akın, "Low-Cost Uncooled Infrared Detectors in CMOS Process," *The 16$^{th}$ European Conference on Solid-State Transducers (EUROSENSORS XVI)*, vol. 2, pp. 263-264, September 2002.

[84] S. Eminoğlu, M. Y. Tanrıkulu, and T. Akın, "Low-Cost Uncooled Infrared Detector Arrays in Standard CMOS," *Proc. of SPIE, Infrared Technology and Applications XXIX*, vol. 5074, pp. 425-436, April 2003.

[85] S. Eminoğlu, M. Y. Tanrıkulu, and T. Akın, "Low-Cost 64×64 Uncooled Infrared Detector Arrays in Standard CMOS," *The 12th International Conference on Solid-State Sensors and Actuators (TRANSDUCERS'03)*, vol. 1, pp. 316-319, June 2003.

[86] S. Eminoğlu, D. Sabuncuoğlu Tezcan, M. Y. Tanrıkulu , and T. Akın, "Low-Cost Uncooled Infrared Detectors in CMOS Process," *Sensors and Actuators A*, vol. 109/1-2, pp. 102-113, December 2003.

[87] K. Ş. Demirci, "A Low-Cost 16x16 Uncooled Infrared Detector FPA Using Standard CMOS and Wafer Level MEMS Processes," *Dissertation for the Degree of Master of Science*, Middle East Technical University, Department of Electrical and Electronics Engineering, 2005.

[88] E. Alpman, "Development of Low-Cost Uncooled Infrared Detector Arrays in Standard CMOS and SOI-CMOS Processes," *Dissertation for the Degree of Master of Science*, Middle East Technical University, Department of Electrical and Electronics Engineering, 2005.

[89] M. Almasri, D. P. Butler, and Z. Çelik-Butler, "Self-Supporting Uncooled Infrared Microbolometers with Low-Thermal Mass," *Journal of Microelectromechanical Systems*, vol. 10, no.3, pp. 469-476, September 2001.

[90] D. P. Butler, Z. Çelik-Butler, and P-C. Shan, "Uncooled YBaCuO Thin Film Infrared Detector," US. Patent No: 5572060, 1996.

[91] R. F. Harrington, *"Time Harmonic Electromagnetic Fields,"* The IEEE Press Series on Electromagnetic Wave Theory, John Wiley & Sons, 2001.

[92] C. A. Balanis, *"Advanced Engineering Electromagnetics,"* John Wiley &Sons, 1989.

[93] D. M. Pozar, *"Microwave Engineering,"* John Wiley &Sons, 2005.

[94] M. Kerker, *"Scattering of Light and Other Electromagnetic Radiation,"* Academic Press, 1969.

[95] D. K. Cheng, *"Fundamentals of Engineering Electromagnetics,"* Prentice Hall, 1993.

[96] H. Bosman, Y. Y. Lau, and R. M. Gilgenbach, "Microwave Absorption on a Thin Film," *Applied Physics Letters*, vol. 82, no. 9, pp. 1353-1355, March 2003.

[97] Personal communication with hotline department of XFAB.

[98] http://www.janostech.com/thermal_image_lenses/tyto, 10.7.2007.

[99] A. S. Weling, P. F. Henning, D. P. Neikirk, and S. Han, "Antenna-Coupled Microbolometers for Multi-Spectral Infrared Imaging," *Proc. of SPIE, Infrared Technology and Applications XXXII,* vol. 6206, pp. 62061F-1 - 62061F-8, April 2006.

[100] J. Kuntner, A. Jachimowicz, F. Kohl, and B. Jakoby, "Determining the thin-film thermal conductivity of low temperature PECVD silicon nitride," *19th European Conf. on Solid-State Transducers (EUROSENSORS XIX),* vol. 2, pp. 388-389, 2006.

[101] M. von Arx, O. Paul, and H. Baltes, "Process-Dependent Thin-Film Thermal Conductivities for Thermal CMOS MEMS," *Journal of Microelectromechanical Systems*, vol. 9, no. 1, 136-145, March 2000.

[102] P. Eriksson, J. Y. Andersson, and G. Stemme, "Thermal Characterization of Surface-Micromachined Silicon Nitride Membranes for Thermal Infrared Detectors," *Journal of Microelectromechanical Systems*, vol. 6, no. 1, 55-61, March 1997.

[103] Coventorware material property database.

[104] http://www.feppd.org/ICB-Dent/campus/biomechanics_in_dentistry/ldv_data/mech/basic_titanium.htm, 14.7.2007.

[105] T. Akın, "*Integrated Sensors and Sensor Systems Course Notes*", Middle East Technical University, Department of Electrical and Electronics Engineering, 2007.

[106] C. M. Hanson, "Barriers to Background-Limited Performance for Uncooled IR Sensors," *Proc. of SPIE, Infrared Technology and Applications XXX,* vol. 5406, pp. 454-464, April 2004.

[107] M. Kohin and N. Butler, "Performance Limits of Uncooled VOx Microbolometer Focal Plane Arrays," *Proc. of SPIE, Infrared Technology and Applications XXX,* vol. 5406, pp. 447-453, April 2004.

[108] P. W. Kruse, "Can the 300 K Radiating Background Noise Limit Be Attained By Uncooled Thermal Imagers?," *Proc. of SPIE, Infrared Technology and Applications XXX,* vol. 5406, pp. 437-446, April 2004.

[109] R. R. Neli, I. Doi , J. A. Diniz, and J. W. Swart, "Development of Process for Far Infrared Sensor Fabrication," *Sensors and Actuators A*, vol. 132, pp. 400-406, November 2006.

[110] M. Almasri, B. Xu, and J. Castracane, “Amorphous Silicon Two-Color Microbolometer for Uncooled IR Detection,” *IEEE Sensors Journal*, vol. 6, no. 2, pp. 293-300, April 2006.

[111] A. Jahanzeb, C. M. Travers, Z. Çelik-Butler, D. P. Butler, and S. G. Tan, “A Semiconductor YBaCuO Microbolometer for Room Temperature IR Imaging,” IEEE Transaction on Electron Devices, vol. 44, no. 10, pp. 1795-1801, October 1997.

[112] WVASE32 IR materials model library.

# APPENDIX A

# DERIVATION FOR EQUATION 3.14

In this part of the thesis the derivation of Equation 3.14 is explained in detail. The derivation starts with Equation 3.13 and makes some approximations to obtain Equation 3.14.

$$Z_{in} = Z_{abs} \frac{Z_{L_abs} + Z_{abs} \tanh(\gamma_{abs} l_{abs})}{Z_{abs} + Z_{L_abs} \tanh(\gamma_{abs} l_{abs})} \tag{10}$$

Since $\gamma_{abs} l_{abs}$ is very small when compared with the wavelength of interest

$$\tanh(\gamma_{abs} l_{abs}) \cong \gamma_{abs} l_{abs} \tag{11}$$

So Equation 1 becomes

$$Z_{in} = Z_{abs} \frac{Z_{L_abs} + Z_{abs} (\gamma_{abs} l_{abs})}{Z_{abs} + Z_{L_abs} (\gamma_{abs} l_{abs})} \tag{12}$$

Characteristic impedance and complex propagation constant of a conductor can be written as

$$Z_{cond} = \sqrt{\frac{\mu}{\varepsilon - j\frac{\sigma}{\omega}}} = \sqrt{\frac{\mu}{\varepsilon_c}} \tag{13}$$

$$\gamma_{cond} = j\omega\sqrt{\mu\varepsilon_c} \tag{14}$$

where $\mu$ is the permeability, $\varepsilon$ is the permittivity, and $\sigma$ is the conductivity of the conductor. Then Equation 3 becomes

$$Z_{in} = \sqrt{\frac{\mu}{\varepsilon_c}} \frac{Z_{L_abs} + \sqrt{\frac{\mu}{\varepsilon_c}} j\omega\sqrt{\mu\varepsilon_c} l_{abs}}{\sqrt{\frac{\mu}{\varepsilon_c}} + Z_{L_abs} j\omega\sqrt{\mu\varepsilon_c} l_{abs}} = \sqrt{\frac{\mu}{\varepsilon_c}} \frac{Z_{L_abs}\sqrt{\frac{\varepsilon_c}{\mu}} + j\omega\sqrt{\mu\varepsilon_c} l_{abs}}{1 + Z_{L_abs} j\omega\varepsilon_c l_{abs}} \tag{15}$$

The term $j\omega\sqrt{\mu\varepsilon_c} l_{abs}$ is very small since the thickness of the absorber layer is much smaller than the wavelength of interest. So Equation 6 becomes

$$Z_{in} = \frac{Z_{L_abs}}{1 + Z_{L_abs} j\omega\varepsilon_c l_{abs}} = \frac{Z_{L_abs}}{1 + Z_{L_abs} j\omega(\varepsilon - j\frac{\sigma}{\omega}) l_{abs}} \tag{16}$$

For a good conductor $\varepsilon \ll j\,\sigma/\omega$ so the expression can be written as

$$Z_{in} = \frac{Z_{L_abs}}{1 + Z_{L_abs}\sigma l_{abs}} = Z_{L_abs} // \frac{1}{\sigma l_{abs}} = Z_{L_abs} // R_{s_abs} \tag{17}$$

where $R_{s_abs}$ is the sheet resistance of the absorber layer.

# APPENDIX B

# MATLAB CODE FOR ABSORPTION SIMULATIONS

```
% Microbolometer absorption simulation file
% Created by M. Yusuf TANRIKULU


% the speed of light m/s----------------------------
c = 3e8;

% permeability of air H/m-----------------------
mu_0 = 4e-7*pi;

% permittivity of air  F/m----------------------------
eps_0 = 8.85e-12;

% conductivity of Al  S/m   wikipedia-------------------------
cond_Au = 4.52e7;

% wavelength  m-------------------------------------
lambda=1e-9*(1000:10:100000);

% frequency Hz----------------------------
f=c./lambda;

% angular frequency w----------------------
w = 2*pi*f;

% k0 of air---------------------------------
k0_air = w*sqrt(eps_0*mu_0);

 % thickness of sacrificial layer  m
l_sac = 1.8e-6;

% sheet resistance of TiN ohm-cm
res_TiN = 377;

% YBCO
% refractive index of YBCO
n_YBCO = 2;

% extinction coefficient of YBCO
k_YBCO = 0;

% thickness of YBCO m
l_YBCO=0.3e-6;

% relative permittivity' of YBCO
eps_prime_YBCO = n_YBCO^2-k_YBCO^2;

% relative permittivity'' of YBCO
eps_dprime_YBCO = 2*n_YBCO*k_YBCO;
```

```
 % SiN
% refractive index of SiN
n_nit = 1;


% extinction coefficient of SiN
k_nit = 0;

%thickness of nitride layer   m
l_nit=0.17e-6;

% relative permittivity' of nitride layer
eps_prime_nit=n_nit^2-k_nit^2;

%relative permittivity'' of nitride layer
eps_dprime_nit=2*n_nit*k_nit;



% alpha YBCO
alpha_YBCO = eps_dprime_YBCO*k0_air/(2*sqrt(eps_prime_YBCO));

% beta YBCO
beta_YBCO = k0_air*sqrt(eps_prime_YBCO);

% alpha nitride
alpha_nit = eps_dprime_nit*k0_air/(2*sqrt(eps_prime_nit));

% beta nitride
beta_nit = k0_air*sqrt(eps_prime_nit);

% impedance of Air (vacuum)
Z0_air=377;


% impedance of Au
Z0_Au = (1+j)*sqrt(w*mu_0/(2*cond_Au));

% gamma YBCO
gamma_YBCO = alpha_YBCO+j*beta_YBCO;

% impedance of YBCO
Z0_YBCO = j*w*mu_0./gamma_YBCO;

% gamma nitride
gamma_nit = alpha_nit+j*beta_nit;

% impedance of nitride
Z0_nit = j*w*mu_0./gamma_nit;


%Region1 TiN-SiN-YBCO-SiN-Sac-Met

% impedance seen from the sacrificial layer, Z0_Au is the load impedance
Z_sac1=Z0_air*(Z0_Au+j*Z0_air*tan(k0_air*l_sac))./(Z0_air+j*Z0_Au.*tan(k0_air*l_sac));

% impedance seen from the first nitride layer, Z_sac1 is the load impedance
Z_nit11=Z0_nit.*(Z_sac1+Z0_nit.*tanh(gamma_nit*l_nit))./(Z0_nit+Z_sac1.*tanh(gamma_nit*l_nit));

% impedance seen from the YBCO layer, Z_nit11 is the load impedance
Z_YBCO=Z0_YBCO.*(Z_nit11+Z0_YBCO.*tanh(gamma_YBCO*l_YBCO))./(Z0_YBCO+Z_nit11.*tanh(gamma_YBCO*l_YBCO));

% impedance seen from the second nitride layer, Z_YBCO is the load impedance
Z_nit12=Z0_nit.*(Z_YBCO+Z0_nit.*tanh(gamma_nit*l_nit))./(Z0_nit+Z_YBCO.*tanh(gamma_nit*l_nit));
```

```
% impedance seen from the input, parallel impedance of Znit12 and TiN
Z_in1= Z_nit12.*res_TiN./(Z_nit12+res_TiN);

 %Region2 TiN-SiN-YBCO-Met
% impedance seen from the YBCO layer, Z0_Au is the load impedance
Z_YBCO2=Z0_YBCO.*(Z0_Au+Z0_YBCO.*tanh(gamma_YBCO*l_YBCO))./(Z0_YBCO+Z0_Au.*tanh(gamma_YBCO*l_YBCO));

% impedance seen from the nitride layer, Z_YBCO2 is the load impedance
Z_nit2=Z0_nit.*(Z_YBCO2+Z0_nit.*tanh(gamma_nit*l_nit))./(Z0_nit+Z_YBCO2.*tanh(gamma_nit*l_nit));

% impedance seen from the input, parallel impedance of Znit2 and TiN
Z_in2= Z_nit2.*res_TiN./(Z_nit2+res_TiN);


%Region3 TiN-SiN-Met

% impedance seen from the YBCO layer, Z0_Au is the load impedance
Z_nit3=Z0_nit.*(Z0_Au+Z0_nit.*tanh(gamma_nit*l_nit))./(Z0_nit+Z0_Au.*tanh(gamma_nit*l_nit));

% impedance seen from the input, parallel impedance of Znit3 and TiN
Z_in3= Z_nit3.*res_TiN./(Z_nit3+res_TiN);


%Region4 TiN-SiN-SiN-Sac-Met

% impedance seen from the sacrificial layer, Z0_Au is the load impedance
Z_sac4=Z0_air*(Z0_Au+j*Z0_air*tan(k0_air*l_sac))./(Z0_air+j*Z0_Au.*tan(k0_air*l_sac));

% impedance seen from the first nitride layer, Z_sac4 is the load impedance
Z_nit41=Z0_nit.*(Z_sac4+Z0_nit.*tanh(gamma_nit*l_nit))./(Z0_nit+Z_sac4.*tanh(gamma_nit*l_nit));

% impedance seen from the second nitride layer, Z_nit41 is the load impedance
Z_nit42=Z0_nit.*(Z_nit41+Z0_nit.*tanh(gamma_nit*l_nit))./(Z0_nit+Z_nit41.*tanh(gamma_nit*l_nit));

% impedance seen from the input, parallel impedance of Znit42 and TiN
Z_in4= Z_nit42.*res_TiN./(Z_nit42+res_TiN);


% reflection coefficient Part1
refl_1=(Z_in1-Z0_air)./(Z_in1+Z0_air);

% reflection coefficient Part1
refl_2=(Z_in2-Z0_air)./(Z_in2+Z0_air);

% reflection coefficient Part1
refl_3=(Z_in3-Z0_air)./(Z_in3+Z0_air);

% reflection coefficient Part1
refl_4=(Z_in4-Z0_air)./(Z_in4+Z0_air);



% reflected power Part1
refl_power_1=abs(refl_1).^2;

% reflected power Part2
refl_power_2=abs(refl_2).^2;

% reflected power Part3
refl_power_3=abs(refl_3).^2;

% reflected power Part4
refl_power_4=abs(refl_4).^2;



% absorbed power Part1
```

```
abs_power_1=1-refl_power_1;


% absorbed power Part2
abs_power_2=1-refl_power_2;

% absorbed power Part3
abs_power_3=1-refl_power_3;

% absorbed power Part4
abs_power_4=1-refl_power_4;


%  Total absorbed power
abs_power=(abs_power_1*318.5+abs_power_2*441.5+abs_power_3*136+abs_power_4*545.75)/1441.75;

% abs_power
abs_power_per=abs_power*100;

semilogx(lambda*1000000,abs_power.*100);
hold;
semilogx(lambda*1000000,abs_power_1.*100, 'm');
semilogx(lambda*1000000,abs_power_2.*100, 'g');
semilogx(lambda*1000000,abs_power_3.*100, 'c');
semilogx(lambda*1000000,abs_power_4.*100, 'r');
grid;
```

# APPENDIX C

# DETAILED FABRICATION PROCESS FLOW

| | | |
|---|---|---|
| **1** | OXIDE COATED SILICON WAFERS OR CMOS WAFERS | 4" or 6" Wafers |
| | | |
| **2a** | **CHROMIUM SPUTTERING** | Dehydration, $N_2$, 110°C, 15 min. |
| | | Flow: 9 sccm Ar (Pressure: $10^{-3}$ mbar) |
| | | Power: 600 W Distance: 130 mm |
| | | End Point Thickness: 50 A |
| | | Meas: ~ 200 A thickness |
| | | |
| **2b** | **GOLD SPUTTERING** | Flow: 6.2 sccm Ar (Pressure: $5.2x10^{-3}$ mbar) |
| | | Power: 300 W Distance 130 mm |
| | | Time: 80 secs |
| | | Meas: ~1000 A |
| | | |
| **3** | **LITHOGRAPHY** | 1. Dehydration, $N_2$, 110°C 20 min. |
| | MASK #1 for **Cr/Au** | 2. Primer(HMDS), 500rpm 7 sec. + 4000rpm 30 sec. |
| | Mask name: **MET1** | 3. S1813 PR, 500rpm 7 sec. + 4000rpm, 30 sec. |
| | | 4. Softbake 115°C, 70 secs. hotplate |
| | | 5. Align & Expose, 4.2 sec (Constant Power) |
| | | 6. Develop, MF-319, 60 sec. |
| | | 7. DI-Water Rinse, 3 min+1.5min. |
| | | 8. Dry by $N_2$ |
| | | 9. Inspect alignment marks |
| | | 10. O2 plasma at 300 W 0.2 Torr |
| | | 11. Hardbake start at room temperature raise the temperature to 110°C, total 15 min |
| | | |
| **4a** | **GOLD ETCH** | 1. Etch in Au Etchant (Duration depends on the etchant, ~11 secs) |
| | | 2. DI-water rinse |
| | | 3. Dry by $N_2$ |
| | | 4. Inspection (Check the metals on the anchors) |
| | | |
| **4b** | **CHROMIUM ETCH** | 1. Etch in Cr Etchant (~40-45 secs) |
| | | 2. Rinse in 2% $H_2SO_4$ (10 secs) (80ml $H_2SO_4$: 4000ml DI) |
| | | 3. DI-water rinse |
| | | 4. Dry by $N_2$ |
| | | 5. Inspection (Check the metals on the anchors) |

| | | |
|---|---|---|
| **5** | **STRIP PHOTORESIST** | 1. ACE 10 min. |
| | | 2. IPA 2 min. |
| | | 3. DI-water rinse . |
| | | 4. Dry by $N_2$ |
| | | 5. Inspection |
| | | 6. 5 min O2 plasma 1 Torr 300 W |
| | | |
| **6** | **POLYIMIDE SPIN (PI 2610)** | 1. Dehydration, $N_2$, 120°C 30 min. |
| | | 2. Primer(Diluted VM651), 500rpm 20 sec. + 2500rpm 60 sec. |
| | 1 ml VM651 to 1000ml DI | 3. Bake for 60 secs @ 130° C on hotplate (on aluminum foil) |
| | | 4. PI 2610 (pour directly from bottle), 500rpm 20 sec. + 2500rpm 60 sec. |
| | | 5. Bake for 5 min @ 130° C on hotplate (on aluminum foil) |
| | Use the oven in etching | 6. Using oven start at 50° C raise to 150° C hold for 5 min at 150° C. |
| | | 7. Proceed to 230° C and hold for 5 min at 230° C. |
| | | 8. Proceed to 250° C and hold for 5 min at 250 °C |
| | | 9. Proceed to 300° C and hold for 40 min at 300° C. |
| | | 10. Cool down to 120 °C in oven (natural cool down). |
| | | |
| **7** | **TITANIUM SPUTTERING** | Dehydration, $N_2$, 110°C, 15 min. (skip if continously done after previous step) |
| | | Flow: 2 sccm Ar (Pressure: 2.1e-3 mbar) |
| | | Power: 300 W Distance: 130 mm |
| | | End Point Thickness: 80 A |
| | | |
| **8** | **SPR220-3 SPIN** | 1. Dehydration, $N_2$, 110°C 15 min. (skip if continously done after previous step) |
| | For front side protection | 2. Primer(HMDS), 500rpm 7 sec. + 2000rpm 30 sec. |
| | | 3. SPR220-3 PR, 500rpm 7 sec. + 2000rpm, 30 sec. |
| | | 4. Softbake 115°C, 90 sec., hotplate |
| | | 5. Hardbake 110° C 5 min in oven |
| | | |
| **9** | **O2 Plasma** | 1. 1 Torr 300 W O2 plasma for 15 min+ 15 min + 10 min + 10 min |
| | For backside PI cleaning | 2. Inspect backside for PI clean. |
| | | |
| **10** | **STRIP PHOTORESIST** | 1. ACE 10 min. |
| | | 2. IPA 2 min. |
| | | 3. DI-water rinse . |
| | | 4. Dry by $N_2$ |
| | | 5. Inspection |
| | | |
| **11** | **LITHOGRAPHY** | 1. Dehydration, $N_2$, 110°C 15 min. |
| | MASK #2 for **Sacrificial Layer** | 2. Primer(HMDS), 500rpm 7 sec. + 2000rpm 30 sec. |
| | Mask name: **PAD DARK** | 3. SPR220-3 PR, 500rpm 7 sec. + 2000rpm, 30 sec. |
| | | 4. Softbake 115°C, 70 secs hotplate. |
| | | 5. Align & Expose, 7.5 sec. |
| | | 6. Develop, MF-24A, 60 sec. |
| | | 7. DI-Water Rinse, 3 min+1.5min. |
| | | 8. Dry by $N_2$ |
| | | 9. Inspect alignment marks and openings in the anchors |
| | | 10. O2 plasma at 300 W 0.2 Torr Time depends on the number of |
| | | 11. Hardbake start at room temperature raise the temperature to 110°C, total 90 min *** |

| | | |
|---|---|---|
| **12** | **TITANIUM ETCH** | 1. Etch in Ti Etchant (1:1:640 HF:H2O2:DI) for ~5-5.5 min |
| | | 2. DI-water rinse |
| | | 3. Dry by $N_2$ |
| | | 4. Inspection (Check the openings in the anchors) |
| | | *** Continue hardbake for 30 min (start from room temperature |
| | | |
| **13** | **PI RIE** | 1. Etch PI in RIE for 50+5+5+3.5 min with PI RIE recipe |
| | | 2. Inspection (Check the openings in the anchors) |
| | | |
| **14** | **STRIP PHOTORESIST** | 1. ACE 10min. |
| | | 2. IPA 2 min. |
| | | 3. DI-water rinse . |
| | | 4. Dry by $N_2$ |
| | | 5. Inspection |
| | | |
| **15** | **TITANIUM STRIP** | 1. Etch in Ti Etchant (1:1:640 HF:H2O2:DI) for ~10 min |
| | | 2. DI-water rinse |
| | | 3. Dry by $N_2$ |
| | | 4. Inspection |
| | | |
| **16** | **PECVD NITRIDE DEPOSITION** | 1. Dehydration, $N_2$, 120°C 30 min. |
| | | 2. Deposit 0.2 μm SiN (15 min 20 secs) mixed frequency stress free |
| | | 3. Meas thickness: 1800 A |
| | | |
| **17** | **LITHOGRAPHY** | 1. Dehydration, $N_2$, 120°C 30 min. |
| | MASK #3 for **Contact Opening** | 2. Primer(HMDS), 500rpm 7 sec. + 4000rpm 30 sec. |
| | Mask name: **CONT** | 3. S1813 PR, 500rpm 7 sec. + 4000rpm, 30 sec. |
| | | 4. Softbake 115°C, 70 secs, hotplate |
| | | 5. Align & Expose, 12 secs. |
| | | 6. Develop, MF-319, 50 secs. |
| | | 7. DI-Water Rinse, 3 min+1.5min. |
| | | 8. Dry by $N_2$. |
| | | 9. Inspect the openings in the anchors |
| | | 10. O2 plasma at 300 W 0.2 Torr |
| | | 11. Hardbake start at room temperature raise the temperature to 100°C, total 15 min |
| | | |
| **18** | **NITRIDE RIE** | 1. Etch SiN in RIE for 70 secs with SiN RIE recipe |
| | | 2. Inspection (Check the openings in the anchors) |
| | | |
| **19** | **STRIP PHOTORESIST** | 1. ACE 10 min. |
| | | 2. IPA 2 min. |
| | | 3. DI-water rinse . |
| | | 4. Dry by $N_2$ |
| | | 5. Inspection |
| | | 6. 5 min $O_2$ plasma 0.7 Torr 300 W |
| | | 7. Inspection (if not stripped continue $O_2$ plasma for at most 10 more minutes) |

| | | |
|---|---|---|
| **20** | **TITANIUM SPUTTERING** | Dehydration, $N_2$, 110°C 15 min. |
| | | Flow: 2 sccm Ar (Pressure: $2.1x10^{-3}$ mbar) |
| | | Power: 300 W Distance: 130 mm |
| | | Time: 320 secs |
| | | |
| **21** | **LITHOGRAPHY** | 1. Dehydration, $N_2$, 120° C 30 min. |
| | MASK #4 for **Metal in the** | 2. Primer(HMDS), 500rpm 7 sec. + 4000rpm 30 sec. |
| | Mask name: **MET2** | 3. S1813 PR, 500rpm 7 sec. + 4000rpm, 30 sec. |
| | | 4. Softbake 115°C, 70secs, hotplate |
| | | 5. Align & Expose, 3.3 secs (Constant Power) |
| | | 6. Develop, MF-319, 40 sec. |
| | | 7. DI-Water Rinse, 3 min+1.5 min. |
| | | 8. Dry by $N_2$ |
| | | 9. Inspection |
| | | 10. O2 plasma at 300 W 0.2 Torr |
| | | 11. Hardbake start at room temperature raise the temperature to 110°C, total 15 min |
| | | |
| **22** | **TITANIUM ETCH** | 1. Etch in Ti Etchant (1:1:640 HF:H2O2:DI) for ~6-7 min |
| | | 2. DI-water rinse |
| | | 3. Dry by $N_2$ |
| | | 4. Inspection (especially the 1 µm arms) |
| | | |
| **23** | **STRIP PHOTORESIST** | 1. ACE 10 min. |
| | | 2. IPA 2 min. |
| | | 3. DI-water rinse . |
| | | 4. Dry by $N_2$ |
| | | 5. Inspection (especially the 1 µm arms) |
| | | 6. 5 min O2 plasma 0.7 Torr 300 W |
| | | 7. Inspection (if not stripped continue $O_2$ plasma for at most 10 more minutes) |
| | | |
| **24a** | **CHROMIUM** | Dehydration at 110 C for 15 min |
| | | Flow: 9 sccm Ar (Pressure: $10^{-3}$ mbar) |
| | | Power: 600 W Distance: 130 mm |
| | | End Point Thickness: 20 A |
| | | Meas: ~ 300 A thickness |
| | | |
| **24b** | **GOLD SPUTTERING** | Flow: 6.2 sccm Ar (Pressure: $5.2x10^{-3}$ mbar) |
| | | Power: 300 W Distance 130 mm |
| | | Time: 70 secs |
| | | Meas: ~850-900 A |
| | | |
| **25** | **LITHOGRAPHY** | 1. Dehydration, $N_2$, 120°C, 30 min. |
| | MASK #5 for Fingers | 2. Primer(HMDS), 500rpm 7 sec. + 4000rpm 30 sec. |
| | Mask name: **MET3** | 3. S1813 PR, 500rpm 7 sec. + 4000rpm, 30 sec. |
| | | 4. Softbake 115°C, 70 secs,hotplate |
| | | 5. Align & Expose, 5 secs |
| | | 6. Develop, MF-319, 40 sec. |
| | | 7. DI-Water Rinse, 3 min+1.5 min. |
| | | 8. Dry by $N_2$ |
| | | 9. Inspection (especially the finger and openings) |
| | | 10. O2 plasma at 300 W 0.2 Torr Time depends on the number of wafers |
| | | 11. Hardbake start at room temperature raise the temperature to 110°C, total 15 min |

| | | |
|---|---|---|
| **26** | **GOLD ETCH** | 1. Etch in Diluted Aqua Regia (Depend on the etch rate of the day |
| | Aqua Regia (AR) (1200ml:400ml | 2. DI-water rinse |
| | Wait ~15 min then mix 1300 AR: 2600 DI | 3. Dry by $N_2$ |
| | | 4. Inspection (Check the fingers) |
| | | |
| **27** | **STRIP PHOTORESIST** | 1. ACE 10 min. |
| | | 2. IPA 2 min. |
| | | 3. DI-water rinse . |
| | | 4. Dry by $N_2$ |
| | | 5. Inspection |
| | | 6. If not stripped 15 min O2 plasma 0.7 Torr 300 W |
| | | 7. Inspection |
| | | |
| **28** | **CHROMIUM ETCH** | 1. Etch in Cr Etchant |
| | | 2. Rinse in 2% $H_2SO_4$ (10 secs) (30ml $H_2SO_4$: 1500ml ) |
| | | 3. DI-water rinse |
| | | 4. Dry by $N_2$ |
| | | 5. Inspection (Check the fingers) |
| | | |
| **29** | **YBCO SPUTTERING** | Dehydration, $N_2$, 110°C 30 min. |
| | | Flow: 3.8 sccm Ar / 0.2 sccm $O_2$ (Pressure: $2x10^{-3}$ mbar) |
| | | Power: 600 W Distance: 98 mm (manipulator 7.5mm) |
| | | Time2: 2000s |
| | | Sputter YBCO with the same conditions for at least 1 dummy wafer |
| | | |
| **30** | **LITHOGRAPHY** | 1. SPR220-3 PR, 500rpm 7 sec. + 6000rpm, 30 sec. |
| | MASK #6 for YBCO | 4. Softbake 115°C, 70 secs.,hotplate |
| | Mask name: **DIFF** | 3. Align & Expose, 12 sec |
| | | 4. Develop, MF-24A, 90 sec. |
| | | 5. DI-Water Rinse, 3 min+3 min (change both of the waters in every wafer). |
| | | 6. Dry by $N_2$ |
| | | 7. Inspect |
| | | |
| **31** | **YBCO ETCHING** | 1. Etch in diluted YBCO Etchant (40-45 secs) |
| | (YBCO Etchant 16:1:13 | 2. DI-water rinse |
| | mix 60 ml YBCO Etchant with 4000 ml DI | 3. Dry by $N_2$ |
| | | 4. Inspection |
| | | |
| **32** | **STRIP PHOTORESIST** | 1. ACE 10 min. |
| | | 2. IPA 2 min. |
| | | 3. DI-water rinse. |
| | | 4. Dry by $N_2$ |
| | | 5. Inspection |
| | | |
| **33** | **PECVD NITRIDE DEPOSITION** | 1. Dehydration, $N_2$, 110°C 15 min. |
| | | 2. Deposit 0.2 um SiN (15 min 20 secs) mixed frequency stress |
| | | 3. Meas thickness: 1700 A |

| | | |
|---|---|---|
| **34** | **TiN SPUTTERING** | Dehydration at 110 C for 15 min |
| | | Flow: 1.5 sccm Ar (Pressure: 2.2e-3 mbar) |
| | | Power: 600 W Distance: 155 mm |
| | | Time: 80 secs |
| | | Meas: ~ 377 ohm/sq |
| | | |
| **35** | **LITHOGRAPHY** | 1. Dehydration, $N_2$, 110°C 20 min. |
| | MASK #7 for Absorber | 2. Primer(HMDS), 500rpm 7 sec. + 4000rpm 30 sec. |
| | Mask name: **NWELL** | 3. S1813 PR, 500rpm 7 sec. + 4000rpm, 30 sec. |
| | | 4. Softbake 115°C, 70 secs, hotplate |
| | | 5. Align & Expose, 8 sec. |
| | | 6. Develop, MF-319, 40 sec. |
| | | 7. DI-Water Rinse, 3 min+1.5min. |
| | | 8. Dry by $N_2$ |
| | | 9. Inspect the openings between arms and the body |
| | | 10. O2 plasma at 300 W 0.2 Torr |
| | | 11. Hardbake start at room temperature raise the temperature to 110°C, total 15 min |
| | | |
| **36** | **TiN ETCHING** | 1. Etch in $H_2O_2$ at 55 °C (2.5 min) |
| | | 2. DI-water rinse |
| | | 3. Dry by $N_2$ |
| | | 4. Inspection |
| | | |
| **37** | **STRIP PHOTORESIST** | 1. ACE 10 min. |
| | | 2. IPA 2 min. |
| | | 3. DI-water rinse . |
| | | 4. Dry by $N_2$ |
| | | 5. Inspection |
| | | |
| **38** | **LITHOGRAPHY** | 1. Dehydration, $N_2$, 110°C 20 min. |
| | MASK #8 for Pixel | 2. Primer(HMDS), 500rpm 7 sec. + 4000rpm 30 sec. |
| | Mask name: **PWELL** | 3. S1813 PR, 500rpm 7 sec. + 4000rpm, 30 sec. |
| | | 4. Softbake 115°C, 70 secs, hotplate |
| | | 5. Align & Expose, 7 sec. |
| | | 6. Develop, MF-319, ~40 sec. |
| | | 7. DI-Water Rinse, 3 min+1.5min. |
| | | 8. Dry by $N_2$ |
| | | 9. Inspect the openings between arms and the body |
| | | 10. O2 plasma at 300 W 0.2 Torr |
| | | 11. Hardbake start at room temperature raise the temperature to 110°C, total 15 min |
| | | |
| **39** | **NITRIDE RIE** | 1. Etch SiN in RIE for 70+70+70 secs with SiN RIE recipe |
| | | 2. Inspection (Check the openings between arms and the body) |
| | | |
| **40** | **DICING** | 1. Dice the wafers |
| | | |
| **41** | **SUSPENSION in RIE** | 1. Etch PI in RIE for 30 + 30 + 30 + 15 + 10 +15 min in RIE. |
| | | 2. Inspection |

# CURRICULUM VITAE

## Personal Information

| | |
|---|---|
| *Surname, Name* | TANRIKULU, M. Yusuf |
| *Date of birth* | 14.5.1978 |
| *Place of birth* | Tarsus/TURKEY |
| *Nationality* | Turkish (TC) |
| *Current Position* | Ph. D. student and Research Assistant in Middle East Technical University Department of Electrical and Electronics Engineering |
| *Phone* | +90 312 2104409/ +90 532 2510817 |
| *Home Address* | İnceark Mah. Muvaffak Uygur Cad. Emek Apt. 11/5 33440 Tarsus/Mersin |
| *Phone* | +90 324 6241383 |

## Education

| | |
|---|---|
| *2002-* | Ph. D. Department of Electrical and Electronics Engineering, Middle East Technical University, Ankara, TURKEY (Cum. GPA: 3.81/4.00 ) |
| *2000-2002* | MSc. Department of Electrical and Electronics Engineering, Middle East Technical University, Ankara, TURKEY (Cum. GPA: 3.64/4.00) |
| *1996-2000* | B.Sc. Department of Electrical and Electronics Engineering, Middle East Technical University, Ankara, TURKEY (Cum. GPA: 3.57/4.00) |
| *1989-1996* | Tarsus Abdülkerim Bengi Anadolu Lisesi (Cum. GPA: 4.87/5.00) |

## Work Experience

| | |
|---|---|
| *July 2000-* | *Research and Teaching Assistant*, Department of Electrical and Electronics Engineering, Middle East Technical University, Ankara, TURKEY |
| *Summer 1999* | *Intern*, Turkish Aerospace Industries (TAI), Ankara, TURKEY |
| *Summer 1998* | *Intern*, BOSSA T.A.Ş, Adana , TURKEY |

## Foreign Languages

Advanced English

## Hobbies

TaeKwon Do (1st Dan Black Belt Certificate), soccer, volleyball, table tennis, reading, movies.

## International Journal Publications

1. S. Eminoğlu, D. Sabuncuoğlu Tezcan, **M. Y. Tanrıkulu**, and T. Akın, "Low Cost Uncooled Infrared Detectors in CMOS Process," *Sensors and Actuators A,* vol. 109/1-2, pp. 102-113, December 2003.

2. S. Eminoğlu, **M. Y. Tanrıkulu**, and T. Akın, "A Low-Cost 128x128 Uncooled Infrared Detector Array In CMOS Process," *Submitted to Journal Microelectromechanical Systems*, 2007.

## International Conference Publications

1. S. Eminoğlu, **M.Y. Tanrıkulu**, and T. Akın, "Low-Cost 64×64 Uncooled Infrared Detector Arrays in Standard CMOS," *The 12$^{th}$ Int. Conf. on Solid-State Sensors and Actuators (TRANSDUCERS'03)*, vol. 1, pp. 316-319, 2003.

2. S. Eminoğlu, **M. Y. Tanrıkulu**, and T. Akın, "Low-Cost Uncooled Infrared Detector Arrays in Standard CMOS," *Proc. of SPIE*, *Infrared Technology and Applications XXIX,* vol. 5074, pp. 425-436, 2003.

3. S. Eminoğlu, D. Sabuncuoğlu Tezcan, **M. Y. Tanrıkulu**, and T. Akın, "Low-cost Uncooled Infrared Detectors in CMOS Process," *The 16$^{th}$ European Conf. on Solid State Transducers (EUROSENSORS XVI)*, vol. 2, pp 263-264, 2002.

4. S. Eminoğlu, **M. Y. Tanrıkulu**, D. Sabuncuoğlu Tezcan, and T. Akın, "A Low Cost, Small Pixel Uncooled Infrared Detector for Large Focal Plane Arrays using a Standard CMOS Process," *Proc. of SPIE, Infrared Technology and Applications XXVIII*, vol. 4721, pp. 111-121, 2002.